Western Graduate&PostdoctoralStudies

Electronic Thesis and Dissertation Repository

9-13-2016 12:00 AM

Formation and Past Evolution of the Meteoroid Complex of Comet 96P/Machholz

Abedin Yusein Abedin
The Univerisity of Western Ontario

Supervisor
Prof. Paul A. Wiegert
The University of Western Ontario Joint Supervisor
Prof. Peter G. Brown
The University of Western Ontario

Graduate Program in Astronomy
A thesis submitted in partial fulfillment of the requirements for the degree in Doctor of Philosophy
© Abedin Yusein Abedin 2016

Follow this and additional works at: https://ir.lib.uwo.ca/etd

Part of the The Sun and the Solar System Commons

Abstract

The past dynamical evolution of the meteoroid streams associated with comet 96P/Machholz is investigated. The goal is to obtain a coherent picture of the past capture of this large comet into a short period orbit, and its subsequent breakup hierarchy. In particular, the aim is to constrain the earliest epoch that this large first precursor started to supply meteoroids into the interplanetary space. The fragments and meteoroid streams of that past cometary decay constitute a wide multiplex of interplanetary bodies, knows as the 96P/Machholz complex. The largest presently surviving fragment is comet 96P/Machholz, followed by a large amount of debris including the Marsden and Kracht group of sungrazing comets, as well as at least one object of asteroidal appearance e.g., asteroid 2003 EH_1.

It has been recognized that comet 96P/Machholz can give rise to eight different meteor showers within one Kozai secular cycle. These are the Quadrantids, daytime Arietids, Southern and Northern δ-Aquariids, κ-Velids, θ-Carinids, α-Cetids and the Ursids. The first four showers are strong and well defined. The remaining four showers are weaker and less well constrained. In fact, while the activity of the Southern and Northern δ-Aquariids and κ-Velids, θ-Carinids stands well above the sporadic meteor background, the existence of the α-Cetids and the Ursids, and their association with comet 96P/Machholz is uncertain.

Recently, some of these meteor showers have been associated with the Marsden group of sunskirting comets, based on orbital similarity and past dynamical evolution. The fact that these meteoroid streams are associated with more than one parent strongly suggest a possible genetic relationship between these bodies.

Using large-scale numerical simulations, the formation and past evolution of each individual meteoroid stream, associated with comet 96P/Machholz and the Marsden group of comets, is explored. Then the simulated shower characteristics are compared with observed ones as constrained by different meteor detection surveys (radar, TV, video, photographic and visual).

In the first part of this work, the formation and likely age of the Quadrantids, the strongest among the eight meteor showers, is examined. The Quadrantids are unusual with their very short duration of maximum activity (~17 hours) superimposed over a long-lasting weaker activity. The short duration of the peak activity indicates a narrow stream which on the other hand suggest that it must be young. Using numerical simulations it is demonstrated that the core of the Quadrantids is only 200 years old and is associated with asteroid 2003 EH_1, while the broader activity is associated with comet 96P/Machholz. The possible nature of the parent, as a dormant or recently extinct comet, is emphasized.

The second part of the work focuses on the age and likely parent of the daytime Arietids meteor shower. Due to their daytime peak activity, the observational characteristics of the Arietids are mostly constrained by radar surveys. The association of the shower with comet

96P/Machholz, and more recent linkage to the Marsden group of sunskirters is examined. Numerical simulations fits to observations suggest that the the Marsden group of comets can not be the dominant parent of the stream, though they contribute to the peak of the shower. The major parent is comet 96P/Machholz and the age of the daytime Arietids is at least 10000 years.

The last part of this study investigates the origin and ages of the less-well constrained showers, the Southern and Northern δ-Aquariids, κ-Velids, θ-Carinids, and the mis-associated α-Cetids and Ursids with comet 96P/Machholz. It is demonstrated that the gross features of the observed characteristics of the first four showers can be explained by comet 96P/Machholz while the Marsden group of comets contribute a small fraction to the peak activity of these showers. Furthermore, the association of the Northern δ-Aquariids with the Marsden group of comets, as previously suggested by several authors, is not supported by this study. Instead the bulk contributor to the shower is comet 96P/Machholz, and possibly another minor parent or parents not considered in this work. Furthermore, two showers were established as potential candidates for the misidentified α-Cetids and Ursids. These showers are the daytime λ-Taurids and the much weaker December α-Draconids, though the last shower spatially overlaps with the November ι-Draconids, where their separation as individual showers is difficult. Lastly, the derived ages of all showers vary between 12000-20000 years, much older than previous estimates. When these shower age estimates are put into perspective, the observed characteristics of showers are consistent with a scenario of a capture of a large first precursor of the 96P complex circa 20000 BC and its subsequent fragmentation with a major break occurring around 100 AD as origin of the sunskirting comets.

Copyright and Permissions

This thesis consists of three papers, listed in the Co-Authorship Statement, which are published, in press or submitted to the *Icarus* journal.

The journal grants first authors an explicit permission to use their work as part of their Ph.D. thesis (personal communications with the journal's support team).

Co-Authorship Statement

This thesis dissertation is based on several published or submitted manuscripts which are listed as follows:

- **Chapter 2**
Age and Formation Mechanism of the Core of the Quadrantid Meteoroid Stream: Published in *Icarus*, (2015), Vol. 261, pp. 100-117. **Authors**: Abedin, Abedin; Spurný, Pavel; Wiegert, Paul; Pokorný, Petr; Borovička, Jiří; Brown, Peter:

I prepared the initial conditions for integration of the equations of motion of 8 high-precision photographic Quadrantid backwards in time. Next, I numerically integrated backwards the equations of motion of each photographic Quadrantid along with 10000 clones and the orbit of 2003 EH_1, which was the presumed parent body in this work. The aim was to identify the epoch when the distance between the orbits of the clones and the parent was minimum. I then used that epoch as meteoroid ejection onset time and propagated the orbits of the parent and synthetic meteoroid streams forward in time, until the present. I then collected a graphed the output from the simulations. The results of the simulations were interpreted with the help of Dr. Paul Wiegert, Dr. Peter Brown and Dr. Petr Pokorny. I then prepared and submitted the manuscript to the Icarus journal. Finally, I edited the manuscript in accordance with the reviewers' comments and suggestions. At that time we figured the necessity of toolkit, designed to automate the illustration of the results of simulation for future works, whose graphic interpretation would be similar to the current work. At that point, I started developing a toolkit, which would take the results of simulations as an input and output the results in illustrative form ready to be interpreted.

Dr. Paul Wiegert contributed to this work with providing a numerical integration package and numerous of advices and comments as to how the problem has to be tackled. He also actively participated in the preparation of the manuscript providing useful comments and suggestions as to how the text can be improved. Drs. Pavel Spurný and Jiří Borovička were mainly involved in the observations, data gathering and processing of seven high-precision photographic Quadrantids. Without their effort, this work would not be possible. Dr. Petr Pokorný contributed with useful comments on this work. Dr. Peter Brown was involved in the radar detection of the meteor showers and has kindly provided observational data on five high-precision radar Quadrantids.

- **Chapter 3**

  The age and the probable parent body of the daytime Arietid meteor shower: Submitted to *Icarus* and in Press, (2016). **Authors**: Abedin, Abedin; Wiegert, Paul; Pokorný, Petr; Brown, Peter:

  In the course of preparing this work, I spent a substantial amount of work to modify my toolkit, so more complicated problems can be solved. At this stage the toolkit was already more advanced. I prepared the initial conditions for backward integrations of the equations of motion of the two presumed parent bodies, comet 96P/Machholz and comet P/1999 J6 that represented the Marsden group of comets. I numerically integrated the equations of motion backwards in time, along with 10000 clones for each parent. I used the integration package provided by Dr. Paul Wiegert. I analyzed the results from backward numerical integrations with the help of Dr. Paul Wiegert, Dr. Peter Brown and Dr. Petr Pokorny. Using the results from these simulations, we selected an appropriate meteoroid ejection onset time and forward numerical integrations of the orbits of both parents and their synthetic meteoroid streams, until the present. I prepared and ran the simulations on the large computer cluster - the Shared Hierarchical Academic Research Computing Network (SHARCNet). I streamed the results of the forward integrations through my numerical toolkit, which provided a direct comparison of the results of simulations with the observed characteristics of the daytime Arietids shower. I interpreted and analyzed the results from the simulations with the help of Dr. Paul Wiegert, Dr. Peter Brown and Dr. Petr Pokorny. I then prepared and submitted the manuscript after incorporating useful suggestions and comments from Dr. Paul Wiegert, Dr. Peter Brown and Dr. Petr Pokorny. Finally, I revised and re-submitted the manuscript in accordance with the reviewers' comments.

  Dr. Paul Wiegert contributed to this work with providing a numerical integration package and with many comments and suggestions as to how the problem may be solved. In addition, he spent some time to verify some of the calculations. Dr. Petr Pokorný contributed with useful comments on this work, related to the preparation and analysis of the numerical simulations. Dr. Peter Brown was involved in radar registration and data processing pertinent to the observations of the daytime Arietids. In addition, he also provided useful comments on how to improve that work.

- **Chapter 4**

  Formation and past evolution of the showers of 96P/Machholz complex: Submitted to

At this stage, my numerical toolkit was already rather advanced. It allowed for numerical simulations initiation and their redistribution across multiple computing nodes. Dr. Paul Wiegert kindly provided the integration package. I prepared the set of initial conditions for backward integrations of the orbits of comet 96P/Machholz and comet P/1999 J6 that represented the Marsden group fo comets. I fed these initial conditions to my toolkit, which using the numerical integration package, ran the jobs on multiple CPUs on SHARCNet. I used again my toolkit, which took as input the raw data from simulations and output a graphical representation of the results. At that point myself, Dr. Paul Wiegert, Dr. Peter Brown and Dr. Petr Pokorny determined the initial meteoroid ejection onset epochs for forward integration of the orbits of both presumed parent bodies along with large set of particles, representing synthetic meteoroid streams of each parent. I prepared the initial conditions for the forward simulations and using my toolkit the jobs were initiated on the SHARCNet computer cluster. Once again, the raw data from the forward simulations was input by myself to my toolkit, which compared the results of the simulations directly with the observed characteristics of the resulting meteor showers of each parent body. Moreover, the toolkit provided graphical representations of the fits from the simulations, which I interpreted with help of Dr. Paul Wiegert, Dr. Peter Brown and Dr. Petr Pokorny. Finally, I prepared and submitted initial manuscript to the Icarus journal. Subsequently, I revised the initial manuscript, along with Dr. Paul Wiegert, Dr. Peter Brown and Dr. Petr Pokorny, in accordance with the reviewers' comments and I re-submitted the final version of the manuscript.

Dr. Diego Janches is the person who has contributed to the establishment of the Southern Argentina Agile Meteor Radar (SAAMER), which is now operational in the southern hemisphere of the Earth. Dr. Janches has also actively participated in data gathering and processing of meteor showers registered by SAAMER and associated with comet 96P/Machholz. These showers are observable from the southern hemisphere only. Without his great contribution, this work would not be possible. Dr. Paul Wiegert contributed to this work with providing a numerical integration package and with many comments and suggestions on meteoroid stream dynamics and interpretation of results from numerical simulations.

Dr. Petr Pokorný contributed substantially to this work by analyzing the observational characteristics of the showers obtained by CMOR and SAAMER. In addition, he has

Contents

List of Figures

xvi

List of Tables

List of Appendices

List of Abbreviations and Symbols

AD   From Latin "Anno Domini". Refers to after Christ
AU   Astronomical Unit, equals to mean Sun-Earth distance
BC   Before Christ
CAI   Calcium-Aluminum rich Inclusions
CAMS   Cameras for All-sky Meteor Surveillance
CMOR   Canadian Meteor Orbit Radar
Dec.   Declination
DMS   Dutch Meteor Society
EN   European fireball Network
ESA   European Space Agency
FWHM   Full-Width-Half-Maximum
HTC   Halley-Type comet
IAU   International Astronomical Union
IDP   Interplanetary Dust Particle
IMO   International Meteor Organization
in-situ   Latin word for "locally" or "on-site"
JFC   Jupiter-Family Comet
JPL   Jet Propulsion Laboratory
KBO   Kuiper Belt Object
LONEOS   Lowell Observatory for Near Earth Object Search
LPC   Long Period Comet
MAB   Main Asteroid Belt
MDC   Meteor Data Center
MMR   Mean Motion Resonance
MOID   Minimum Orbit Intersection Distance
NASA   National Aeronautics and Space Administration
NEA   Near-Earth Asteroid
NEO   Near-Earth Object
R.A.   Right Ascension
SAAMER   Southern Argentina Agile Meteor Radar
SOHO   Solar and Heliospheric Observatory
SOMN   Southern Ontario Meteor Network
SPC   Short Period Comets

TNO	Trans-Neptunian Object
TV	Television
UT	Universal Time
ZHR	Zenith-Hourly Rate
a	Semi-major axis
α	Celestial right ascension
α_g	Geocentric right ascension
A	Cross-section **or** geometric albedo
b	Ecliptic latitude
β	Ratio of solar radiation pressure to solar gravity
c	Speed of light
C_K or C	Kozai energy
δ	Celestial declination
δ_g	Geocentric declination
d	Diameter
D'	Drummond's orbital similarity criterion
D_{SH}	Southworth and Hawkins orbital similarity criterion
e	Eccentricity
ϵ	Obliquity of the Earth's equator to the ecliptic
ϕ	Geographic latitude
F_{eff}	Effective force
F_G	Solar gravitational force
F_R	Solar radiation pressure
h	Altitude
H	Absolute visual magnitude
i	Inclination
km	Kilometer
ξ_j	Column vector of random numbers
$L_\odot$	Luminosity of the Sun
L_Z	The "Z-th" component of the orbital angular momentum
Λ_{kj}	matrix of eigen-values
λ	Geographic longitude
$\lambda_\odot$	Solar longitude
$\lambda_{\odot start}$	Solar longitude of the beginning of the activity profile

$\lambda_{\odot max}$	Solar longitude of the maximum of the activity profile
$\lambda_{\odot end}$	Solar longitude of the end of the activity profile
$\lambda - \lambda_\odot$	Sun-centered ecliptic longitude
m or m_o	Mass of meteoroid
$M_\oplus$	Mass of the planet Earth
$M_\odot$	Mass of the Sun
mm	Millimeter
μm	Micrometer
ν_6	Secular orbital resonance due to Jupiter and Saturn
ω	Argument of perihelion
Ω	Longitude of the ascending node
P	Orbital period
$P(V - V_{ej})$	Parabolic probability distribution of meteoroid ejection speeds
q	Perihelion distance
Q	Aphelion distance
Q_{PR}	Light scattering efficiency
r or r_o	Heliocentric distance (Distance from the Sun)
R_c	Radius of comet nucleus
ρ	Bulk density
ρ_c	Bulk density of comet nucleus
σ	Standard deviation
s	Meteoroid radius **or** mass index
θ	True anomaly
θ_c	True anomaly of comet
T	Period of some periodic event
T_J	Tisserand parameter with respect to Jupiter
V_{ej}	Ejection speed of meteoroids from the surface of a comet
V_{obs}	Observed (in-atmosphere) speed of meteoroid
$\vec{V_g}$	Geocentric velocity vector
$\vec{V_m}$	Heliocentric velocity of meteoroid
$\vec{V_E}$	Heliocentric velocity of the Earth
V_∞	Speed at "infinity"
w or W_s	Weighting factor of meteoroids by their perihelion distance at time of ejection
W_r	Weighting factor of meteoroids by their size
X	the "X" component of the heliocentric radius vector

$\dot{X}$	the "X" component of the heliocentric velocity vector
Y	the "Y" component of the heliocentric radius vector
$\dot{Y}$	the "Y" component of the heliocentric velocity vector
Z	the "Z" component of the heliocentric radius vector
$\dot{Z}$	the "Z" component of the heliocentric velocity vector

Chapter 1

Introduction

The aim of this work is to explain the formation and past evolution of the interplanetary complex of bodies associated with comet 96P/Machholz. The goal is to obtain a self-consistent scenario of the fragmentation history of a single large progenitor, whose fragments and meteoroid streams constitute the complex. We will concern ourselves with obtaining a broad coherent picture as to the relative contribution of these fragments to the associated meteoroid streams, and thus establishing the dominant parent body of the complex. In particular, we attempt to answer the question as to the earliest epoch when the first large progenitor might have been captured in a short period orbit, as a proxy of the age of the entire complex. For that purpose, we perform detailed modelling of the meteoroid streams, released from multiple parent bodies and fit our simulations to the observed showers characteristics, obtained by various meteor detection surveys (radar, photographic, TV and visual).

In the following sections we will review how meteoroids are related to their parents, and how they are liberated from comets and asteroids, and how a meteoroid stream is formed. Next, we will discuss what are the forces that meteoroids are subject to, upon release from a parent body, and how these particles evolve over time.

1.1   Small Solar System Bodies. Motivation

Asteroids, comets and *meteoroids* are leftovers from the formation of the Solar System about 4.6×10^9 years ago (e.g., Bouvier and Wadhwa, 2010), and are collectively known as *small Solar System bodies* ("small bodies" hereafter), to distinguish them from their larger counterparts, the planets. Over the history of the Solar System, the planets have been physically and chemically altered due to large-scale impacts, geological processes and weathering. Conversely, the small Solar System bodies are relatively pristine with little processing. Furthermore, the asteroids and comets have been extensively linked to the origin of life on the Earth. Shortly after the

planets had accreted most of their mass ($\sim$ 4 billion years ago), their surfaces were constantly reshaped by heavy bombardments with the leftover debris of planet formation. It is believed that during that period water and carbon-based molecules may have been delivered on the Earth (Martins et al., 2013).

Without delving into a great detailed review of Solar System formation, a few key points should be noted in an attempt to outline the significance of the study of asteroids, comets and meteoroids. Asteroids are rock or metal based small bodies, believed to have condensed from the Solar nebula in the region of the terrestrial planets, Mercury, Venus, Earth and Mars (e.g., Bottke et al., 2006a; Crida, 2009). Observations suggest that some of the asteroids have been melted and differentiated (where heavier elements such as iron and nickel sunk to the center of the planetesimal, while lighter elements surrounded the core and formed the crust or the mantle of the asteroid). However, the bulk of the asteroids have never been heated to their melting point and are believed to be pristine and constitute a class of asteroids known as *chondrites*. These asteroids are made of three main components: Calcium-Aluminum rich Inclusions (CAI) (millimeter sized grains of refractory material - mostly Calcium and Aluminum), *chondrules* (millimeter sized silicate spherules, 2 million years older than the CAI (e.g., Amelin et al., 2002; Bizzarro et al., 2004), and a matrix holding everything together. The chondrites are believed to be the key to understanding the early chemical composition and physical process of the early matter in the region of the terrestrial planets.

In contrast, comets are icy bodies with embedded solid dust particles within (Whipple, 1950, 1951). They are believed to have coalesced near the orbits of the *Giant planets*, Jupiter, Saturn, Uranus and Neptune (e.g., Fernández, 1997), where the temperatures were low enough to allow for volatiles to condense. The most important feature of the physical and dynamical evolution of the comets is that, unlike asteroids, the comets have never been heated up above 50 K, and thus are believed to have preserved even better the footprint of the primordial mixture in the region of the giant planets.

Dynamical models of the formation of the Solar System strive to understand the redistribution and evolution of the matter throughout the history of the Solar System, with the aim of establishing its locus of origin. Combined with ground-based observations or in-situ explorations this study provides crucial information as to the physical and chemical processes that took place 4.6 billion years ago.

The concept of a collision of the Earth with an asteroid or comet, as a potential life threatening hazard, has been becoming more and more popular, not only among scientists but also for the general public. These events have happened before, evidenced by numerous craters covering planetary surfaces and their moons. Among the most well-known past and present such collision events are:

1. The Chicxulub crater in the Yucatan peninsula. With dimensions more than 180 km wide and 20 km deep, the crater is believed to have formed in a catastrophic collision of the Earth with an asteroid about 66 million years ago (Renne et al., 2013). The event is associated with the *Cretaceous-Paleogene* mass extinction event (the extinction of the dinosaurs) (e.g., Schulte et al., 2010).

2. The largest documented impact in the history of mankind is the *Tunguska event*, in which a massive explosion on June 30, 1908 devastated $\sim$ 2000 km^2 a remote forest area in Russia (Ben-Menahem, 1975). The scientific investigations provide evidence for an explosion of a small asteroid or comet (a few tens of meters across) at an altitude of $\approx$ 10 km in the Earth's atmosphere (Vasilyev, 1998). Kresak (1978) argued that the impactor may be a fragment of comet 2P/Encke, which is associated with the Taurid meteoroid complex (see Asher (1991) for an extensive review).

3. On February 15, 2013, a 20 meter size asteroid (Brown et al., 2013) entered the Earth's atmosphere and exploded at an altitude of $\approx$ 30 km over the Russian city of Chelyabinsk. Over 1000 people were reportedly injured by shattered windows due to the blast wave (Popova et al., 2013). The energy deposition in the explosion was estimated to be $\approx$500 kilotons (Brown et al., 2013), equivalent to 20-30 times the energy released in the detonation of the Hiroshima atomic bomb. Silber et al. (2009) argued that the impact probability from objects in the size range 10 - 50 m, equivalent to the Chelyabinsk event asteroid is by an order of magnitude higher than initially thought.

Presently, scientists strive to constrain the size distribution, composition and orbits of the *Near-Earth Objects* (NEOs) and understand their dynamics for numerous of reasons. For example:

1. Modelling of the dynamical evolution of small bodies may provide a crucial information as to the formation of the planets, their physical and dynamical evolution and the birth regions of asteroids and comets.

2. Determine a suitable candidate and time for *in-situ* exploration via space mission.

3. Predict if a an object is moving on a collision course with the Earth, and develop mitigation strategies.

On the other hand, meteoroids are the smaller counterpart of the asteroids and comets. The Earth is constantly hit by these small particles whose interaction with the Earth's atmosphere can be detected if the meteoroid is large enough (see Sec. 4.2 for details). In general, that interaction is accompanied by a streak of light in the sky, a phenomenon known as a *meteor*. Over the history of modern meteor observations, there have been several definitions of the term meteoroid. In the most common sense, meteoroids are solid interplanetary bodies orbiting the Sun, though substantially smaller than the asteroids and comets. The International Astronom-

ical Union (IAU) assembly in 1958, adopted the definition of a meteoroid as: "*A solid object moving in the interplanetary space, of a size considerably smaller than asteroid and considerably larger than an atom*" (Millman, 1961). That definition is vague and immediately raises the question "what is the lower limit of the term asteroid?". Beech and Steel (1995) suggested that meteoroid should be defined as any solid interplanetary object with size greater than 100 μm and less than 10 m. According to that definition, objects larger than 10 m are considered asteroids, while particles less than 100 μm are regarded as dust particles. More recently, Rubin and Grossman (2010) proposed a new definition, where meteoroids should be considered interplanetary bodies with size between 10 μm and 1 m, where solid particles between 10 μm and 2 mm are referred to as *micro-meteoroids*. Any particle less than 10 microns is considered *Interplanetary Dust Particle* (IDP). Although there is no a rigorous boundary between the size of a meteoroid and asteroid, the above definitions nevertheless provides a basic sense as to the size of these objects. Figure 1.1 illustrates the size and masses of some known objects, including the asteroids, comets and meteoroids.
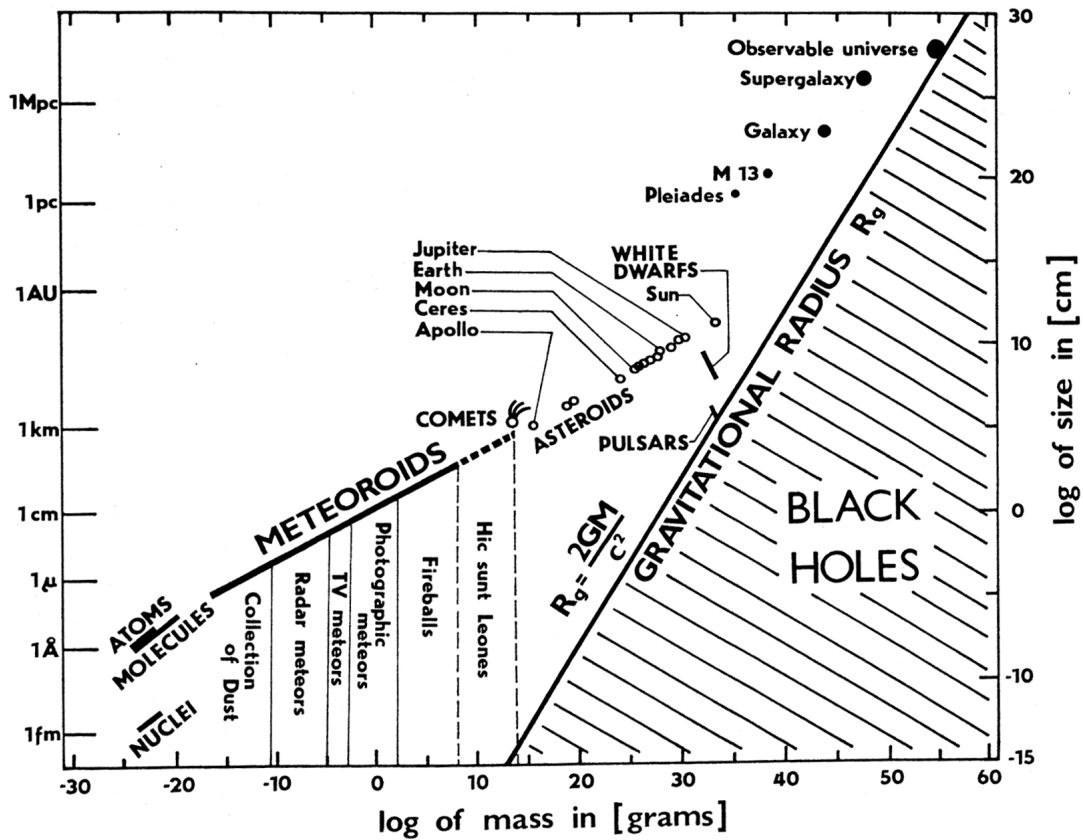
Figure 1.1: Illustration of size-mass distribution of some known objects. Adapted from Ceplecha et al. (1998).

Meteoroid study is scientifically important for numerous of reasons, though the most important ones within the scope of this work are:

1. Meteoroids are proxies of their parent bodies - the comets and asteroids (Sec. 1.2). Fortunately, comets and asteroids rarely intersect the Earth's orbit, whereas our planet is constantly hit with small debris. The linkage of meteoroids to their parent is thus of a crucial importance. It allows us to sample their parent asteroids or comets from the Earth, while *in-situ* explorations are generally expensive.

2. Even the smallest meteoroids approaching the Earth may pose a hazard to the Earth's artificial satellites, where a hypervelocity impact could damage spacecraft components. In fact, on the night of August 12, 1993, astronauts on-board of the *Mir* station reported audible impact noise on the craft's exterior, which was later verified that the space station had been hit by ~ 2000 meteoroids, which damaged the solar panels (e.g., Beech et al., 1995).

1.2 Parent bodies of meteoroids

1.2.1 Comets

We have briefly discussed in Sec. 1.1 that comets are icy bodies with embedded solid dust particles within and have formed in the region of the giant planets. However for a full understanding of how meteoroids are related to comets, a few additional definitions and facts need to be presented.

An active comet consists of four distinct features - the *nucleus*, *coma*, *dust tail* and *ion or gas tail*, respectively. Whipple (1950) suggested a comet model often referred to as the *dirty snowball* model or the *icy conglomerate* model, which describes a comet nucleus as irregularly shaped solid body consisting of a mixture of frozen volatiles with embedded dust particles within. Figure 1.2 shows an illustration of what a comet nucleus interior is believed to look like. Greenberg (1998) argued that roughly 26% of the nucleus mass is contained in refractory silicate particles, 23% in complex organic refractory material (dominated by carbon), and the remainder being occupied by frozen volatiles. The most abundant among the volatiles is the $\sim 30\%$ with a mixture of other frozen gases such as, CO, CO_2, CH_3OH, CH_4, NH, etc, each contributing by about 2% by mass. At their reservoirs (Sec. 1.1), comets orbit the Sun in regions of extremely low temperatures, so the cometary ices are in solid state.

Occasionally, some comets are perturbed away from their reservoirs by various mechanisms, depending on source region (see Sec. 1.2.1) which may cause a comet to attain an orbit that brings it in the planetary neighborhood. During its course towards the inner Solar System, the Sun's heat causes the temperature of the comet nucleus to rise, resulting in sub-
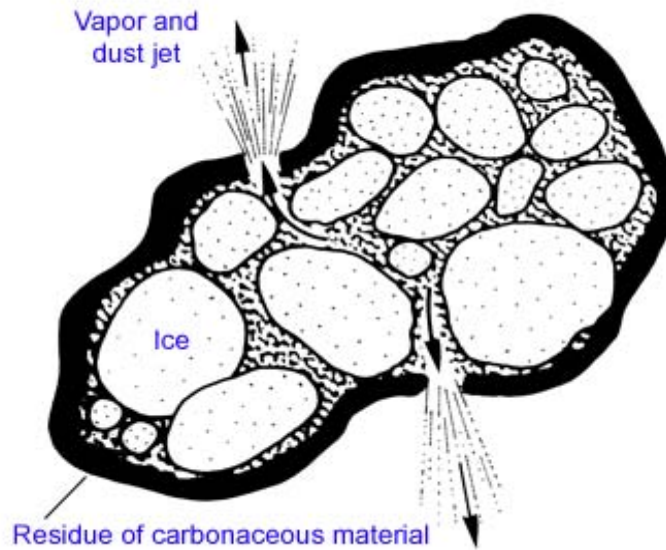
Figure 1.2:   Illustration of an assumed structure of a comet nucleus.   Image credit: *http://explanet.info/Chapter14.htm*

limation (direct transition of a solid ice into a gas) of the the frozen volatiles. The distance at which the cometary ices begin to sublimate is a strong function of the composition of the volatiles. Delsemme (1982) calculated that water ice can sublimate at a heliocentric distance (distance from the Sun) of $\approx$ 3 AU, whereas more volatile substances such as CO_2 and CO begin to evaporate even further, at distances beyond 5 AU. During sublimation, the escaping gas expands almost radially outwards, dragging away trapped dust particles of different size (submicron - centimeter sized), within the ice. Generally, the smaller particles are more abundant than millimeter and centimeter particles. Upon release, the particles are subjected to the minuscule nucleus gravity and Solar radiation pressure (Sec. 1.4.2) that is strictly size and mass dependent. The photon pressure drags the smaller (micron and sub-micron) particles radially opposite to the Sun's direction, forming an extended envelope of gas and dust (micron sized particles), called the *dust tail* of the comet (see Fig. 1.3). The gas and dust surrounding the nucleus is referred to as the *coma*. Furthermore, the Sun's energetic UV radiation ionizes some of the coma atoms while the solar wind pushes the ions in direction opposite to the Sun, resulting in a narrow and long structure known as the *ion or gas tail*. The released larger particles (hundreds of microns to centimeter) are meteoroids and will be reviewed in Sec. 1.3 and Sec. 1.4.

Finally, our understanding of comets has significantly improved in the last three decades, owing to the era of space exploration. The *Giotto* spacecraft of the European Space Agency (ESA) and former USSR space probes *Vega 1 and Vega 2* made a rendezvous with comet
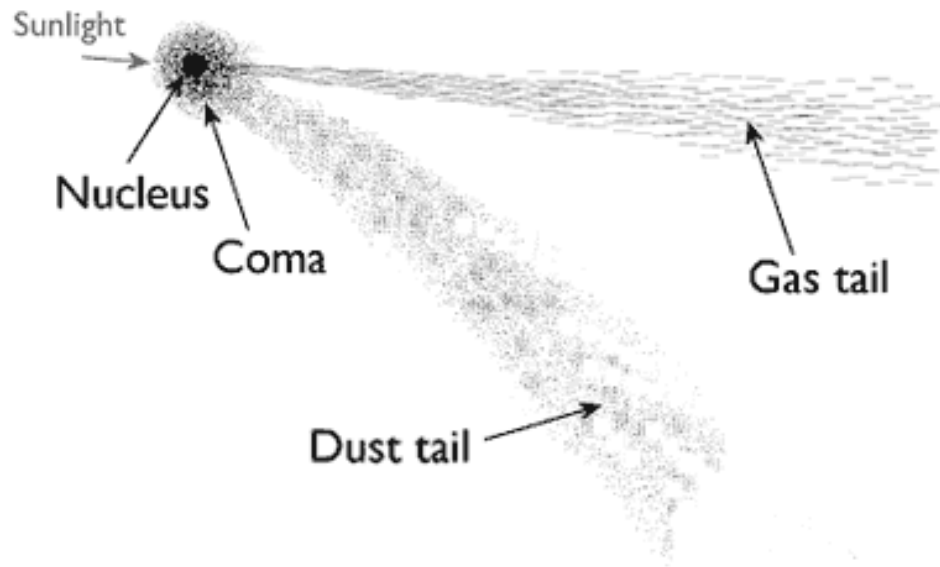
Figure 1.3: Illustration of the main components of an active comet. Image credit: *https://lcogt.net*

1P/Halley in 1986. That was the first ever direct imaging and measurement of comet's nucleus size. The results showed that the size of the nucleus is roughly 15 km long, 7 km to 10 km wide and it was darker than previously thought, being covered by a thick layer of dust. Only about 15% of the nucleus surface was active. The estimated nucleus density was ~ 0.6 g.cm^{-3} (Sagdeev et al., 1988), with the mass of the ejected material being 80% water ice and 10% of CO. Figure 1.4 shows the sizes and shapes of a few comets which have been visited by spacecraft.

On November 12, 2014, for first time a space probe landed on comet surface. The *Philae* lander, of the ESA's *Rosetta* mission, made a successful touch on the surface of comet 67P/Churyumov-Gerasimenko.The preliminary results indicated that the surface of the comets is rich in carbon-based compounds and similar to other comets its surface is extremely dark with geometric albedo (the ratio of reflected to incident light) of $A \approx 0.06$ (Capaccioni et al., 2015). Just for a comparison the latter value almost corresponds to a pure charcoal. Among other cometary missions are e.g., the *Deep Impact* mission to comet 9P/Temple, the *Stardust* mission with an aim of collecting dust from the coma of comet 81P/Wild.

Comet reservoirs and orbital classifications

During the formation of the giant planets, they underwent a complex dynamical evolution, migrating inwards and outwards relative to their present location as a result of the interaction with the protoplanetary disk, as well as their mutual gravitational influence. About 99% of the
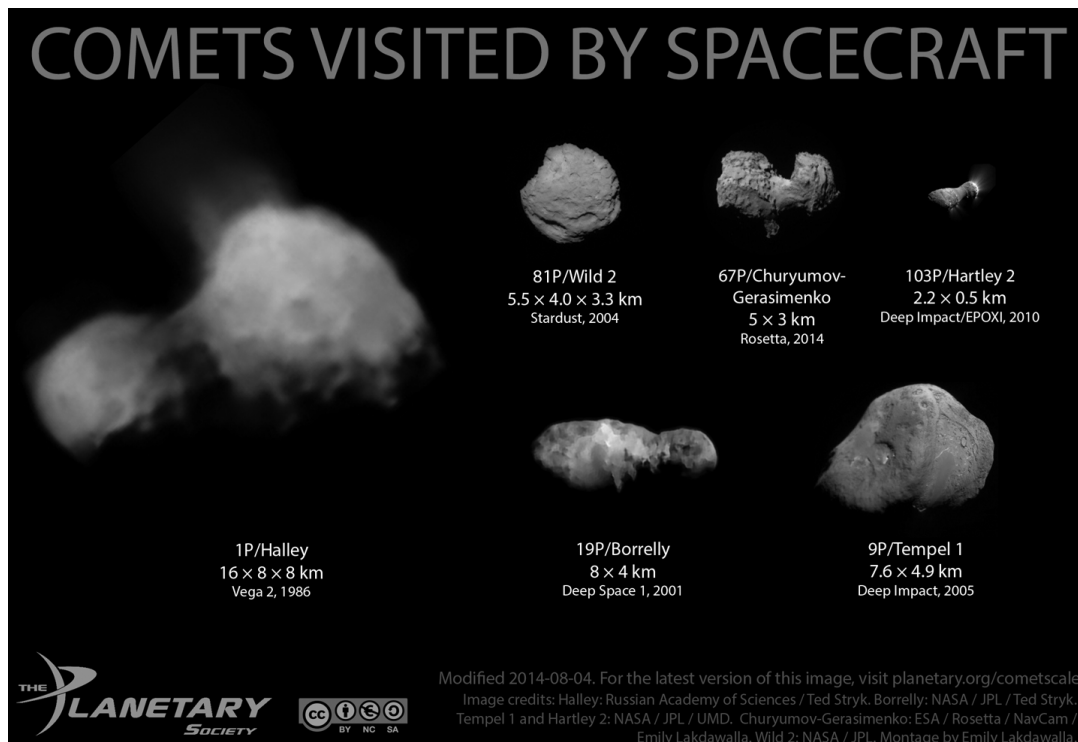
Figure 1.4: Illustration of the shapes and sizes of some comets, visited by spacecrafts. Image credit: *https://cumbriansky.wordpress.com/*

icy planetesimals in that region, were scattered away during that dynamical instability leaving only about 1% of the initial icy population beyond the orbit of Neptune (Morbidelli et al., 2005; Levison et al., 2008). Sometimes these objects are referred to as *trans-Neptunian objects* (TNOs). Presently, this region is recognized as the *Kuiper belt* (Edgeworth, 1949) or sometimes also called the *Edgeworth-Kuiper belt* which roughly extends from 35 AU - 50 AU (Stern and Colwell, 1997) (see also Fig. 1.5). It was named after the Dutch-American astronomer Gerard Kuiper, though he did not actually predict its existence. The Kuiper belt is believed to supply the *short period comets* (SPC), comets with orbital period of $P < 200$ years, into the inner Solar System.
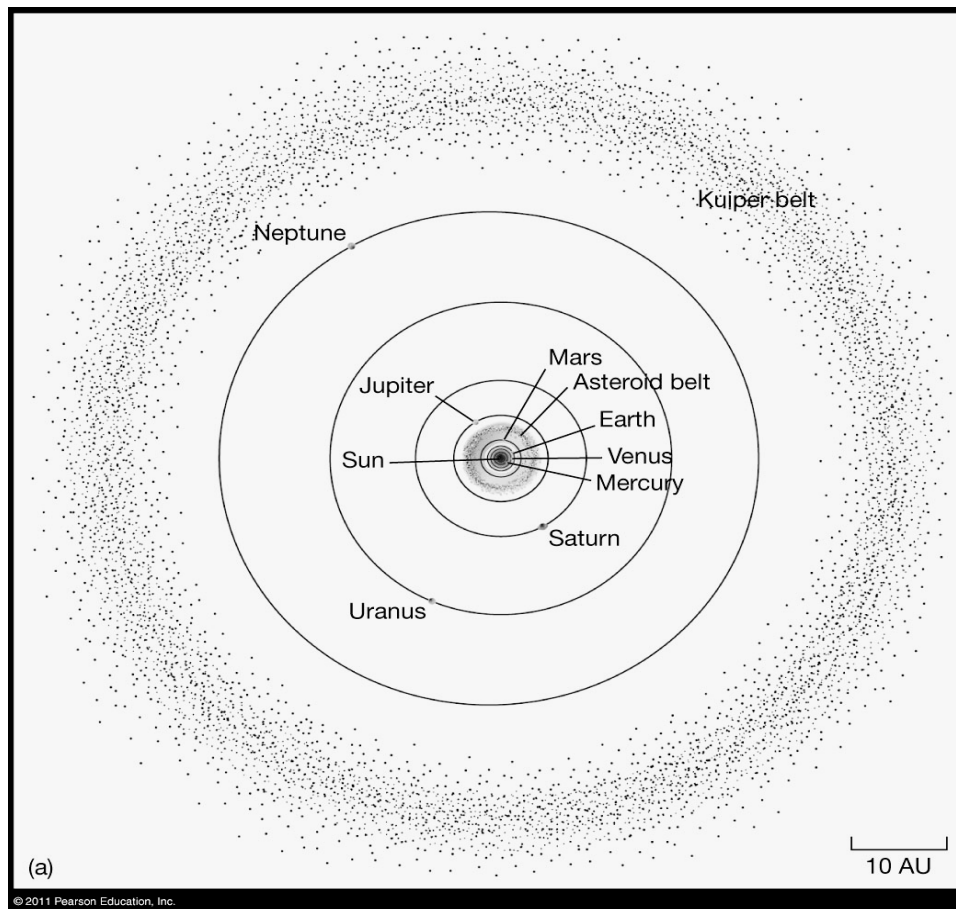
Figure 1.5: Location of the Kuiper belt, relative to planetary orbits. Image credit: *Pearson Education. Inc.*

The rest of the scattered planetesimals during that instability period, were ejected out of the planetary region to nearly interstellar distances, where these comets form a spherical shell of $10^{12} - 10^{13}$ comets, surrounding the Solar System. This shell is named the *Oort cloud* after the Dutch astronomer, Ian Oort (Oort, 1950), who first hypothesized its existence.

Although far away from the planetary region, the Oort cloud undergoes occasional pertur-
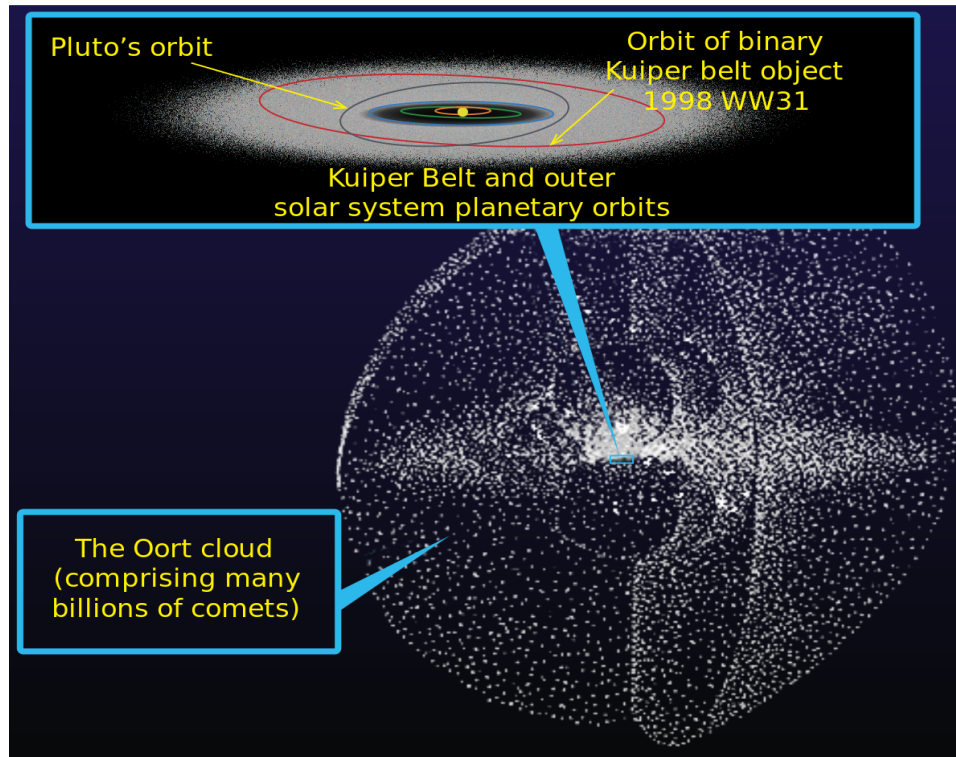
Figure 1.6: Location of the Oort cloud, relative to planetary orbits. Image credit: *Pearson Education. Inc.*

bation by close passing stars, giant molecular clouds or galactic tides. These perturbations are thought as the mechanism of delivering the *long-period comets* (LPC), comets with periods ($P > 200$ years) into the planetary region (e.g., Duncan, 2008). The process is complicated and involves dynamical capture of these comets by the giant planets which are subsequently "handed-in" to the next planet, until its perihelion distance reaches a value below 5 AU (approximately the extent of Jupiter's orbit) where it can become an active comet.

1.2.2   Main Asteroid Belt

Most of the known asteroids (also referred to as *minor planets*) orbit the Sun between the orbits of planets Mars and Jupiter (see Fig. 1.7), or roughly between 2 AU and 4 AU, known as the *Main Asteroid Belt* (MAB hereafter). Their size vary greatly from a few kilometers to a few hundreds of kilometers. The largest asteroid is *1 Ceres* (now referred to as a dwarf planet) which has a diameter $d \approx 950$ km, followed by asteroids *4 Vesta* - $d \approx 525$ km (Russell et al., 2012), *2 Pallas* (Pitjeva, 2005) and *10 Hygiea*. Presently estimated mass of MAB is $M_{MAB} \approx 5 \times 10^{-4} M_{\oplus}$ (1 $M_{\oplus} \approx 6 \times 10^{24}$ kg is the mass of the Earth), where half of this mass is contained in the four largest asteroids. Moreover, numerical simulations show that present

mass of the belt is only 0.1% of the original mass (e.g., Petit et al., 2001), the bulk being ejected or accumulated by the planets.

The orbits of most asteroids in the MAB are relatively stable with a few regions which are heavily disturbed by the gravitational influence of Jupiter. In those regions the asteroids' orbital periods are synchronously locked to the orbital period of Jupiter, a mechanism known as a *Mean Motion resonance* (MMR hereafter). That is evidenced by apparent depletion of asteroids in those regions, known as the *Kirkwood gaps*, which have been scattered away by Jupiter. These gaps are approximately found near heliocentric distances of 2.5 AU, 2.83 AU and 3.27, respectively, corresponding to 3:1, 5:2 and 2:1 MMR with Jupiter. An additional and more complex perturbing mechanism also responsible for asteroid scatter is the ν_6 secular resonance region, due to the combined perturbation by Jupiter and Saturn.
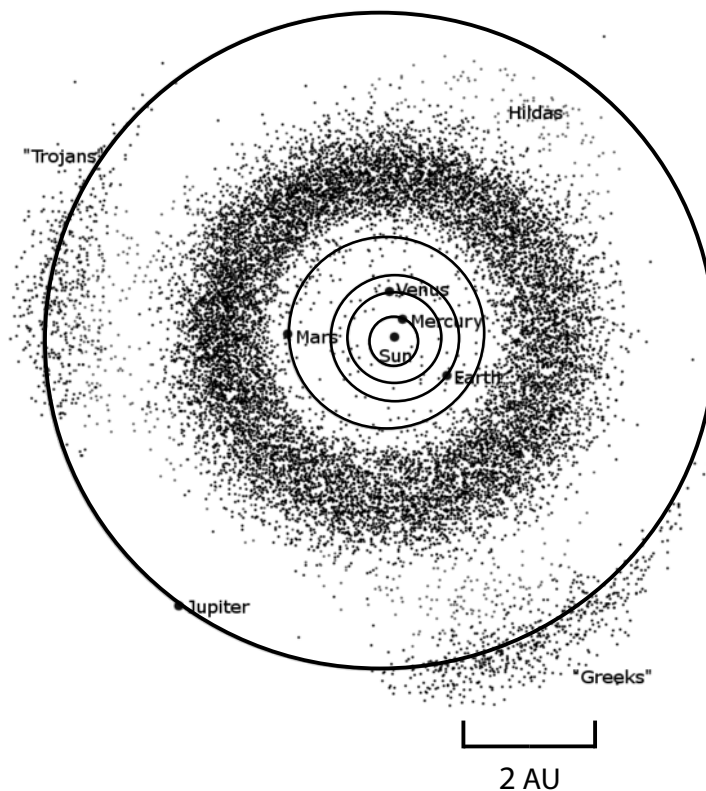
Figure 1.7: Location of the Main Asteroid Belt, relative to planetary orbits. Image credit: *https://en.wikipedia.org*

Delivery of asteroids to the near-Earth space.

Asteroids in these MMR regions are heavily perturbed by the Jupiter and Saturn and their orbital eccentricities are increased, so they attain orbits which may bring them to Venus and Earth-crossing orbits (Morbidelli et al., 2002). Once on such orbits, these asteroids are called *Near-Earth Objects* (NEOs hereafter). Strictly speaking, NEOs are defined as having orbital perihelion distance $q < 1.3$ AU and aphelion distance $Q > 0.983$ AU.

Once in the planetary region, the dynamical evolution of NEOs is controlled by Jupiter and to a lesser degree by close encounters with the terrestrial planets. The dynamical lifetime of NEOs is shorter than the age of the Solar System, so the fact that we still observe them today strongly suggests that they are replenished (Gladman et al., 2000; Morbidelli et al., 2002). Numerical simulations indicate that the majority of the NEOs are supplied from the MAB, while only $\approx 6\%$ originate from Jupiter Family Comets (JFCs) (Bottke et al., 2002). However, as discussed in Sec. 1.2.2 the resonance regions in the MAB are almost depleted, so there must be a way of transporting asteroids from nearly stable orbits to these "escape hatches".

It has been shown that radiation forces from the Sun, such as the *Yarkovsky effect* (see e.g., Bottke et al., 2006b) can increase the orbital semi-major axis, and once the body reaches these resonance regions, it may well be injected in the terrestrial planets region. It's been demonstrated that the Yarkovsky effect is an efficient mechanism of pushing meteoroids and asteroids (up to 10 km in size) to these "escape hatches" and subsequently producing NEOs (Bottke et al., 2000; Vokrouhlický and Farinella, 2000; Morbidelli et al., 2002). It is noteworthy that the Yarkovsky effect was measured for first time in 2003 for the near-Earth and potentially hazardous asteroid 6489 "Golevka" (Chesley et al., 2003).

1.3   Formation of meteoroid streams

1.3.1   Cometary origin

Presently, formation of cometary meteoroid streams is a relatively well understood process (e.g., Whipple, 1951; Kresak, 1976; Williams, 1992; Vaubaillon et al., 2005). The breakthrough in understanding this process originated from Whipple's icy conglomerate model of comet nuclei (Whipple, 1950).

Far away from the Sun, the comet nucleus is inactive (greater than 5 AU), with some exceptions depending on the volatile composition of the nucleus. However, when a comet approaches the Sun, the volatiles begin to sublimate and drag along the embedded dust particles. Different volatiles sublimate at different heliocentric distances. The most volatile compound, found among cometary ices, is CO which has been shown to sublimate beyond $r = 12$ AU (e.g., Davis

and Richter, 2005), whereas CO_2 roughly begins to sublimate at $r \approx 5$ AU. However, generally the abundance of these gases are low compared to the water ice (Greenberg, 1998), and most likely the evaporation of these ices lifts up only the smallest particles off the surface of the comet. In order for larger particles to be lifted and accelerated, more violent cometary activity is expected. Generally, meteoroid production is associated with sublimation of water ice, roughly corresponding to $r = 3$AU, partly due to the greater gas production rate and the greater molecular weight of the water vapor. In fact, a particle can only leave the surface of the comet if the gas drag force overcomes the nucleus gravity. A typical upper limit as to particles' sizes, released by water sublimation from comets is a few tens of centimeters. The latter is a strong function of the particle's size and density which may vary anywhere between $\rho = 500$ kg.m^{-3} for ice particles to $\rho = 3000$ kg.m^{-3} for silicate particles.

Ejection speeds

When the particles are ejected from the comet nucleus the gas drag accelerates the particles approximately radially outward from the nucleus. At about ten nucleus radii the particles reach a terminal speed, which typically does not exceed 1 km.s^{-1}. A that point the particles follow a trajectory independent of the parent and are referred to as meteoroids (see also Sec. 1.1).

The magnitude of the ejection speed is strictly a function of the heliocentric distance, the size of the nucleus as well as the size and density of the ejected particle. As a result of his icy-conglomerate comet model, Whipple (1951) derived for the ejection speed of a spherical particles, the expression:

$$V_{ej} \approx 8.3 r^{-1.125} R_c^{1/2} m^{-1/6} \rho^{-1/3} f, \qquad (1.1)$$

where V_{ej} is the ejection speed of the meteoroid in m.s^{-1}, r is the heliocentric distance in AU, R_c is the radius of the comet nucleus in km, m is the mass of the meteoroid in grams, ρ is the bulk density of the meteoroid in (g.cm^{-3}) and f is the fraction of the solar radiation available for sublimation (usually taken as unity). Using the above expression for a typical meteoroid, equivalent to a visual meteor, of $\rho = 0.7$ g.cm^{-3} and mass of $m = 3 \times 10^{-3}$ grams, ejected from a comet nucleus of size $R_c = 5$ km at a heliocentric distance of $r = 1$ AU, the magnitude of the ejection speed is $V_{ej} \approx 55$ m.s^{-1}.

Jones (1995) noticed some shortcomings in Whipple's expression, and allowed for additional effects such as cooling of the comet's surface due to the sublimation of the ice, and adiabatic expansion of the escaping gases. The author ended up with an expression, similar to the one obtained by Whipple, given by:

$$V_{ej} \approx 10.2 r^{-1.038} R_c^{1/2} m^{-1/6} \rho^{-1/3} f, \tag{1.2}$$

where the variables are the same as in Eq. 1.1. The only difference in the latter equation is the modified dependence on the heliocentric distance, though the overall magnitude of the ejection speed does not differ much from Whipple's expression. Indeed, using the same values for the meteoroid size and density and size of the comet as in Eq. 1.1 the resulting ejection speed is $V_{ej} \approx 67$ m.s^{-1}.

Over the last decades there have been several revisions of the Whipple's original expression, with accounting for various effects. Gustafson (1989a) explored the ejection speeds as a function of the meteoroids' shape, considering particles of "flakes" and "needle"-like shapes. Hughes (2000) considered the scenario that ejected meteoroids contain frozen ices where upon particle ejection, the residual ices may continue to sublimate and produce a "rocket"-like force increasing the speed of the meteoroid. However, the overall result would agree that the ejection speeds are small and are less than the speed of the escaping gas (less than 1 km.s^{-1}) (Hughes, 2000).

The heliocentric (orbiting the Sun) speed of a body is given by:

$$V_h = \sqrt{GM_\odot \left(\frac{2}{r} - \frac{1}{a} \right)}, \tag{1.3}$$

where G is the standard gravitational constant in units (m^{3}kg^{-1}s^{-2}), $M_\odot \approx 2 \times 10^{30}$ kg is the mass of the Sun, r is the heliocentric distance of the body in meters and a is the body's orbital semi-major axis in meters (see Appendix A for definition of the orbital elements). Assuming a comet with orbital semi-major axis of $a = 3$ AU (a typical value for JFC), located at a heliocentric distance of $r = 1$ AU, its heliocentric speed will be $V_h \approx 47$ km.s^{-1}. We compare that speed to the ejection speed $V_{ej} \approx 50$ m.s^{-1} of a $s = 1$ mm meteoroid of mass $m = 3 \times 10^{-3}$ grams, from the surface of a comet of radius $R_c = 5$ km at a heliocentric distance of $r = 1$ AU. It is evident that the meteoroid ejection speeds will be much lower than the heliocentric speed of the comet. Hence, upon ejection the meteoroids are expected to initially move along a path close to the parent's orbit. Assuming that the comet produces meteoroids of different sizes they will have different ejection speed as per Eq. 1.2. These ejection speeds relative to the comet nucleus will cause the meteoroids to spread along the orbit of the parent in the form of a torus. Williams (1992) showed that it takes roughly 100 orbital revolutions for the meteoroids to completely spread along the parent orbit. Thus, for a comet with an orbital period of 5 years, the meteoroids will be uniformly distributed along the orbit within 500 years. Their subsequent dynamical evolution will be governed by the gravitational perturbations from the

planets as well as non-gravitational forces (Sec. 1.4).

Evolution of comets into asteroids

Levison and Duncan (1997) calculated that the physical lifetime of short-period comets is ~ 12000 years, which is significantly lower than their dynamical lifetime $\sim 4.5 \times 10^7$ years. That implies that cometary nuclei "fade" (disappear due to a breakup or become inactive) before they are ejected from the inner Solar System. Whitman et al. (2006) argued that there is a greater probability of a comet nucleus becoming inactive rather than being completely disrupted. There a few mechanisms that are believed to lead to "demise" of comets.

1. Weissman et al. (1989) argued that comets lose roughly 0.01 - 0.1% of their mass on each perihelion return. Thus, cometary activity can not be sustained indefinitely, especially active comets. Eventually, over many revolutions around the Sun, the cometary volatiles will deplete and only refractory inert material will remain (e.g., Whipple, 1950; Weissman et al., 1989). Weissman (1980) estimated lifetimes of ~ 600, 4500, and 4×10^5 returns for 1 km radius water ice spheres with surface albedo of 0 and density of 0.6 g.cm^{-3}, for long-period comets with perihelia of 1, 2, and 3 AU, respectively. The lifetimes of short-period comets will be lower due to their lower semi-major axis and eccentricity. Observationally, the "dead" comet nucleus will be dark indistinguishable from an asteroid. This is referred to as an *extinct comet*. However, the complete de-volatilization of a comet nucleus is not a well understood process. Weissman (1980) argued that comets are likely to develop an inert crust (see below) of their surface, which would prevent further sublimation and thus subsequent lost of volatiles.

2. Another mechanism which may lead to low or no cometary activity is development and inert crust (mantle) on the surface of a comet. This mechanism was proposed by Whipple (1950) as a consequence of his "icy-conglomerate nucleus" model. Rickman et al. (1990) noted that during cometary activity only the lightest particles can escape the nucleus gravity. The larger silicate particles and boulders remain on the surface or are lifted up and eventually fall back onto the surface. Over time, this material will form a "blanket" of inert crust on the cometary surface, suppressing or ceasing the activity. This is referred to as a *dormant comet*. Similar to the case with extinct comet, the nucleus of a dormant comet would be difficult to be differentiated from an asteroid. However, occasionally a passage of dormant comet close to some of the planets, the tidal forces may produce cracks in the mantle which may reactivated the comet for a short time (Jenniskens, 2006).

The existence of such inert crust on cometary surfaces is evidenced for example by space fly-by missions to comets. Nucleus observations of comet Halley showed that only ~15% of the surface was active, a similar case observed for most of the comets (Sec. 1.2.1). Finally, investigations suggest that extinct or dormant comets are maybe comprise approximately 5-10

% of the NEO population (Fernández et al., 2001; Bottke et al., 2002).

1.3.2   Asteroidal origin

Presently, there are only two meteor showers associated with asteroids. The core of the Quad-rantid meteoroid streams is asteroid 2003 EH$_1$ (e.g., Jenniskens, 2004; Wiegert and Brown, 2005; Neslušan et al., 2013), whereas the Geminids meteor shower has been linked to asteroid 3200 Phaeton (Gustafson, 1989b; Williams and Wu, 1993; Ryabova, 2016). However, the ex-istence of dormant or extinct comets (Sec. 1.3.1) makes it difficult to link meteoroid streams to asteroids, for one obvious reason: A comet may have produced a meteoroid stream in the past, during its active period (see Sec. 1.3.1), and later has become dormant or extinct. If the stream is not tremendously old, the particles can still be linked to the parent body. But the parent will presently be dormant and thus it will be recognized as an asteroid which will lead to association of the resulting stream with an asteroid.

Although, there have been a number of studies (e.g., Steel, 1995; Jopek et al., 2002; Porubčan et al., 2004) dedicated to establishing a child-parent relationship of meteoroid stream with an asteroid, the subject is still debatable. Nevertheless, below is presented a few mecha-nisms which may lead to mass shedding from the surface of an asteroid.

Mass loss from asteroids

1. *Collision* - In 2010, a peculiar object was discovered, named P/2010 A2, showing evidence of mass loss. Computed orbital elements revealed that the object is a member of the MAB (Jewitt et al., 2010). Furthermore, observations of the near nucleus environment suggested that the mass loss is different from cometary water-ice sublimation. Follow-up calculations of dust and fragment dispersal indicated that the mass loss was likely due to a collision with another body, results consistent with the mean asteroid velocity dispersion in the MAB ($\Delta V \approx 5\,\mathrm{km.s^{-1}}$) (Bottke et al., 1994) and with models of catastrophic collision between rocky bodies (Benz and Asphaug, 1999). However, the work of Benz and Asphaug (1999) suggests that the ejection speeds of fragments in a collision are low and thus a direct injection of meteoroids from the MAB into Earth-crossing orbit is unlikely.

2. *Spin-up disintegration* - There is evidence that some asteroids (D < 10 km) (Harris, 1996; Pravec et al., 2002) may be an agglomeration of fragments "rubble-pile", as a result of a catastrophic collision and subsequent re-accumulation (e.g., Michel et al., 2001). These asteroids are believed to be held together solely due to their mutual gravity, with almost zero tensile strength. When that is combined with increase or decrease of the spin rate of asteroids, due to the Yarkovsky-O'Keefe-Radzievskii-Paddack (YORP) effect (Rubincam, 2000), that

may explain the lack of fast rotating asteroids of size ~ 10 km, suggesting that they disintegrate when they reach the spin limit ~ 2.2 hours (Pravec et al., 2002). Thus, all fast rotating asteroids with absolute magnitude of H<22 (roughly 150 m) must be monolithic (Pravec et al., 2002). This mass-shedding mechanism is also believed to produce the observed binary asteroids (e.g., Walsh et al., 2008), which account for 15% among the NEO and MAB population. The YORP spin-up was measured for first time in 2007 for near-Earth asteroid 2000 PH5 (Lowry et al., 2007).

Finally, it is not clear whether the above mentioned mechanisms can explain the formation of the Geminids or the Quadrantids. We recall that, Gustafson (1989b) showed that the activity of Geminids can be explained if Phaeton was an active comet ~ 1000 years ago and then it gradually ceased activity. Similar work was done by Abedin et al. (2015) who showed that the timing and duration of the core of the Quadrantids can be explained by cometary activity from the surface of 2003 EH$_1$ some 200 years ago, which later similar to Phaeton perhaps has gone dormant or extinct.

1.4 Dynamical evolution of meteoroid streams

1.4.1 Gravitational and secular evolution

All Solar System bodies move under the dominant central force of the Sun, with planets acting as perturbers. Hence, the orbits of the bodies to a first approximation are Keplerian (the two body problem), with planets impinging small but significant disturbances on their Keplerian motion (the *N*-body problem). The most massive planet in the Solar System is Jupiter, so it is expected to be the main perturber, where Saturn, Uranus and Neptune will also have a substantial effect. In addition, smallest meteoroids (micrometer - centimeter) will be also affected by non-gravitational forces (see Sec. 1.4.2).

It is well known fact the the *N*-body problem is not integrable in analytic functions (in a closed form), though the motion of a body can be approximated as infinite series of polynomials (Murray and Dermott, 2000). Simulations of the dynamical evolution of meteoroid streams in the past were performed by hand, where the myriad of particles (meteoroids) were replaced by a few particles only (Williams, 1992). Often scientists had to resort to analytical secular methods, where the gravitational influence of the planets were averaged over a complete orbit. Nowadays with the advancement of computational technologies these tasks are easily achievable and the problems can be solved numerically.

Fortunately, meteoroids' parent bodies rarely intersect the Earth which would imply a collision. However, even if a comet moves away from the Earth's orbit its meteoroid stream may

still hit the Earth. In Sec. 1.2.1 we discussed that meteoroids are ejected with non-zero speeds with respect to the parent comet nucleus. These speeds will cause the meteoroids to attain slightly different orbits from the parent. Thus, the planetary perturbations will also be slightly different on the meteoroids compared to the parent. The small differences in the net force accumulate over time and may cause the meteoroids to approach, while the parent may avoid a planet. The stronger gravitational perturbations from the planet on the meteoroids, may alter their trajectories in a way such that they intersect the Earth's orbit, though the parent may still move far from the Earth's path. Over longer time periods (centuries) the stream may evolve substantially away from its parent so that establishing a genetic relationship between the two may be difficult.

In the last century, problems involving long-term dynamical evolution of small Solar System bodies were tackled by employing a secular evolution analysis, as mentioned above. Perhaps the most extensively used secular method is the "Gauss-Halphen-Goryachev" technique, utilized by many scientists to investigate the long-term dynamics of Solar System bodies (e.g., Plavec, 1950). A major prediction of the secular method is the progression or regression of the orbital nodes (see Appendix A for description of orbital elements), where the orbital line of apsides regresses for an object in a prograde orbit (orbital inclination $i < 90°$), but progresses for a retrograde orbiter (orbital inclination $90° < i < 180°$).

Another effect of the secular evolution of the orbits is the well-known *Kozai mechanism* or sometimes referred to as the *Kozai-Lidov mechanism* (Kozai, 1962; Lidov, 1962; Gronchi and Milani, 1999). This effect is stronger for orbits with initial orbital inclination close $i \approx 90°$) and perihelion distance $q \approx 2$ AU. The Kozai mechanism manifests itself in a distinct correlation between some the orbital elements, where the longitude of the ascending node and argument of perihelion circulate from $0° - 360°$ with a period T. Within that period the perihelion distance and inclination of the orbit complete two in-phase oscillation cycles, where as the eccentricity oscillates out-of-phase with a period $T/2$. The out-of-phase oscillation of i and e approximately preserves the orbital semi-major axis and the Z-component of the orbital angular momentum $L_Z = \sqrt{1 - e^2} \cos i$, a situation often seen in sungrazing comets (Bailey et al., 1992). Furthermore, the angle 2ω (ω = argument of perihelion) and the eccentricity e approximately conserve the quantity C_K - *Kozai energy* and is given by Kinoshita and Nakai (1999) as:

$$C_K = (2 + 3e^2)(3\cos^2 i - 1) + 15e^2 \sin^2 i \cos 2\omega \qquad (1.4)$$

where e is the orbital eccentricity, i and ω are the orbital inclination and argument of perihelion respectively.

For example, the orbit of comet 96P/Machholz and Marsden group of sunskirters are in

a Kozai-type secular evolution, which causes the orbital nodes of the comets to intersect the Earth's orbit at eight different locations and thus give rise to eight different meteor showers. That, along with cascading fragmentation of the parent is an efficient way of creating a complex of interplanetary objects, a situation also seen the well-known Taurid complex, associated with comet 2P/Encke and multiple other fragments (Asher, 1991).

1.4.2 Non-gravitational forces

Non-gravitational forces play a crucial role in the dynamics of meteoroids and streams. They act on small dust meteoroids ($\sim \mu m - cm$) once they leave their parent bodies. The magnitude of these non-gravitational forces are strictly dependent on particles' size and mass with smaller meteoroids being affected the most. The most important non-gravitational forces acting on small meteoroids are, solar radiation pressure, *Poynting-Robertson drag* (PR hereafter), the Lorentz force and Solar wind corpuscular drag. However, for particles under consideration in this work, the Lorentz force and the solar wind are ~ 1000 times smaller than the Solar radiation pressure and PR drag, and hence they will be ignored.

Solar radiation pressure

Solar radiation pressure is a radial force directed outwards from the Sun. Thus, the net effect is weakening of the Solar gravity. In meteoroid stream dynamics, the effect of the Solar radiation pressure force is often expressed as the standard β-parameter, being the ratio of the radiation pressure to solar gravity and is given by Burns et al. (1979) as:

$$\beta = \left(\frac{F_R}{F_G}\right) \approx 5.7 \times 10^{-4} \frac{Q_{pr}}{\rho s}, \tag{1.5}$$

where the effective force on a meteoroid is given by:

$$F_{eff} = F_G - F_R = F_G\left(1 - \frac{F_R}{F_G}\right) = F_G(1 - \beta) = \mu F_G, \tag{1.6}$$

In the Eq. 3.3, Q_{pr} is the light scattering efficiency of the particle often taken as unity, ρ is the meteoroid's bulk density in kg.m^{-3} and s is the radius of the particle in meters. The radiation pressure force, similar to gravity, depends on the heliocentric distance as $(1/r^2)$, so the β-parameter will be constant for a particle of given mass and size.

Using some typical meteoroid values, equivalent to a visual meteor, $\rho = 2000$ kg.m^{-3} and $s = 1$ mm or 0.001 m, the ratio of the radiation pressure to the solar gravity will be $\beta = 2.3 \times 10^{-4}$. For a typical radar meteor $s = 100 \mu$m, the above ratio evaluates to $\beta = 2.3 \times 10^{-3}$.

Thus, it is evident that smaller particles are affected more than larger particles, where for a meteoroid of sizes $s = 1 - 10$ cm the solar radiation pressure is virtually zero. Whether a particle will remain on a bound orbit about the Sun, depends on its orbital energy upon ejection. Kresak (1976) provides the expressions:

$$
\begin{aligned}
\beta &\lesssim \frac{r_o}{2a_o} \\
m &\gtrsim 6.5 \times 10^{-12} \frac{a_o^3}{\rho^2 r_o^3},
\end{aligned}
\tag{1.7}
$$

where a_o is the semi-major axis the orbit from which a particles has been released, r_o is the heliocentric distance of of the particle, and m and ρ are the particle's mass and bulk density. From Eq. 1.4.2 it is evident that $\beta > 1$ is not the sole condition for a meteoroid to be ejected from the solar system. In fact, meteoroids can easily attain hyperbolic orbits, if ejected from a parent on a loosely bound orbit. The second equation in Eq. 1.4.2 provides an approximate mass of a particle (as a function of its density and initial orbit) that is required for it to remain bound to the Sun or to escape the Solar system.

Poynting - Robertson drag

The PR drag arises from absorption of solar thermal photons by a particle, and followed by anisotropic emission of the radiation in the reference frame of the Sun. A particle in a heliocentric orbit around the Sun will absorb the solar radiation and will emit it isotropically in its own reference frame. In the inertial frame of the Sun, the absorbed energy will be emitted preferentially in the direction of motion of the particle, leading to dissipation of its energy and angular momentum. That will result in a particle to slowly spiral towards the Sun, gradually "damping" its eccentricity (circularize the orbit). The evolution of the orbital semi-major axis and eccentricity for a spherical meteoroid are given by (e.g., Wyatt and Whipple, 1950) as:

$$
\frac{da}{dt} = -\frac{L_\odot Q_{pr} A}{4\pi c^2 a} \frac{(2 + 3e^2)}{(1 - e^2)^{3/2}},
$$

$$
\tag{1.8}
$$

$$
\frac{de}{dt} = -\frac{L_\odot Q_{pr} A}{4\pi c^2 a^2} \frac{5e}{(1 - e^2)^{1/2}},
$$

where $L_\odot$ is the luminosity of the Sun, Q_{pr} is the particle's light scattering efficiency, A is the the cross section of the particle, a and e are the semi-major axis and eccentricity of the orbit and c is the speed of light. Wyatt and Whipple (1950) also provide an expression for the time (in years) needed to change the semi-major axis of a spherical particle, from initial value a_0 to

some other value a, as:

$$(t - t_o) = 3 \times 10^7 \frac{(1 - e^2)^{3/2}}{(2 + 3e^2)} (a_o^2 - a^2)\rho s, \tag{1.9}$$

where e is the meteoroid's orbital eccentricity, s and ρ are the particles size and bulk density in cgs units. Using the same typical meteoroid characteristics values $s = 1$ mm, $\rho = 2.5$ g.cm^{-3} and $e = 0.5$, $a = 3AU$ and $a_o = 2AU$, the time required for the semi-major axis to decay by $1\ AU$, is $(t - t_o) \sim 10^6$ years, whereas for a radar meteor of $s = 100\ \mu$m, the decay time is $(t - t_o) \sim 10^5$ years. The latter results underline the significance of the radiation forces in meteoroid stream dynamics. Meteoroids cannot survive the age of the Solar System, so they must be continuously replenished.
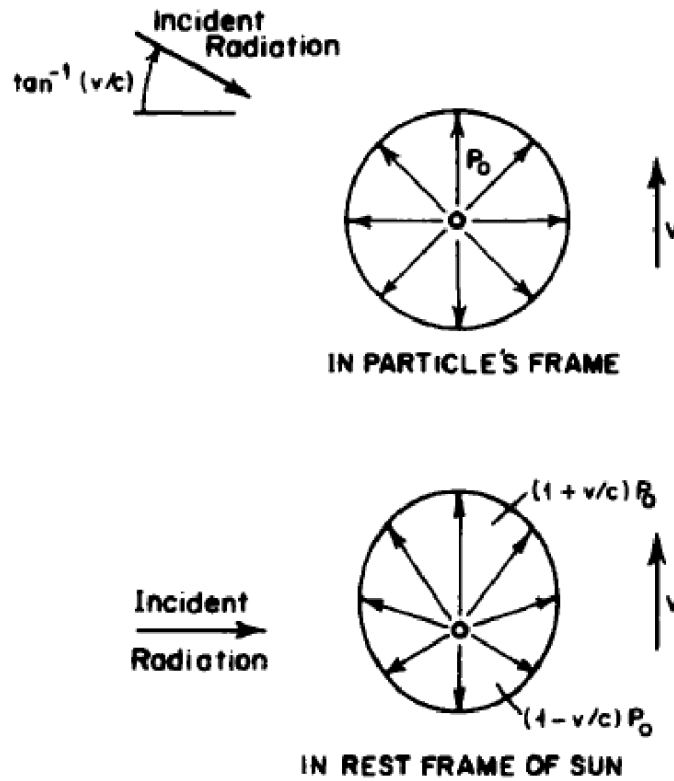
Figure 1.8: Illustration of the Poynting-Robertson effect. Particle in a heliocentric orbit absorbs the solar radiation and radiates it isotropically in its own reference frame. In the reference frame of the Sun, the particles emits the radiation preferentially in the direction of particle's motion, resulting in a dissipation of the orbital angular momentum. Adapted from Burns et al. (1979).

1.5   Meteor detections and observations

Meteoroids can enter the Earth's atmosphere with speeds between $11.2\,\mathrm{km.s^{-1}}$ and $73.6\,\mathrm{km.s^{-1}}$, depending on the encounter geometry. Indeed, strictly speaking the speed is a vector quantity (has a direction and magnitude) called a *velocity* while its magnitude is known as *speed*. The above speeds are derived from two effects:

1. The encounter geometry - Assuming a meteoroid and the Earth have different orbits, they will also have different heliocentric speeds V_m and V_E respectively. Thus, the relative velocity of a meteoroid with respect to the Earth (assuming the Earth is massless) is called *geocentric speed* and is $\vec{V_g} = \vec{V_m} - \vec{V_E}$, and hence the geocentric speed is just $V_g = |\vec{V_g}|$. Thus, depending on the encounter geometry, the geocentric speed can vary from $V_g = 0$ for meteoroid moving on the same orbit as the Earth, and just catching up behind it (see Fig. 1.9 panel (a)). The maximum geocentric speed is obtained for a meteoroid moving on a parabolic orbit in the ecliptic, whose perihelion distance coincides with the perihelion of the Earth (see Fig. 1.9 panel (b)). The meteoroid and the Earth will meet at point P with parallel but opposite velocity vectors, corresponding to a head-on collision. This will correspond to $V_g = 72.6\,\mathrm{km.s^{-1}}$, being the vector sum of the Earth's heliocentric speed at perihelion $V_E \approx 30\,\mathrm{km.s^{-1}}$ and the parabolic speed at the meteoroid's perihelion of $V_m \approx 42.2\,\mathrm{km.s^{-1}}$.

2. The Earth's gravity - The meteoroid's speed is further modified once it falls into Earth's gravitational well and is accelerated. This speed is referred to as V_∞ generally taken at the top of the Earth's atmosphere and is related to the speed a particle can fall in the Earth's gravity well, known as the Earth's escape speed $V_{esc} \approx 11.2\,\mathrm{km.s^{-1}}$. Thus, a particle encountering the Earth with a $V_g = 0$ will free-fall due to the Earth's gravity and the maximum speed it can attain is $V_\infty = \sqrt{V_g^2 + V_{esc}^2} = \sqrt{0^2 + 11.2^2} = 11.2\,\mathrm{km.s^{-1}}$. Conversely, a head-on collision with a meteoroid will correspond to $V_\infty = \sqrt{V_g^2 + V_{esc}^2} = \sqrt{72.6^2 + 11.2^2} = 73.4\,\mathrm{km.s^{-1}}$.

During a meteor shower, for an observer on Earth, all meteors seem to emerge from a single point in the sky, called the *radiant*. This is a optical illusion, similar to parallel lines seeming to intersect at infinity. The radiant location is given in geocentric equatorial reference frame, with coordinates (α, δ) or (R.A., Dec)(see Appendix B). However, that coordinate system does not account for the diurnal motion of the Earth, which results in a diurnal radiant drift. A preferred coordinate system is the sun-centered ecliptic system, which accounts for the Earth's orbital motion, and will be used throughout this work. However, back and forth conversion between the sun-centered ecliptic and geocentric equatorial systems is presented in (Appendix B). Given the radiant and the speed of a meteor, the orbit is completely determined.
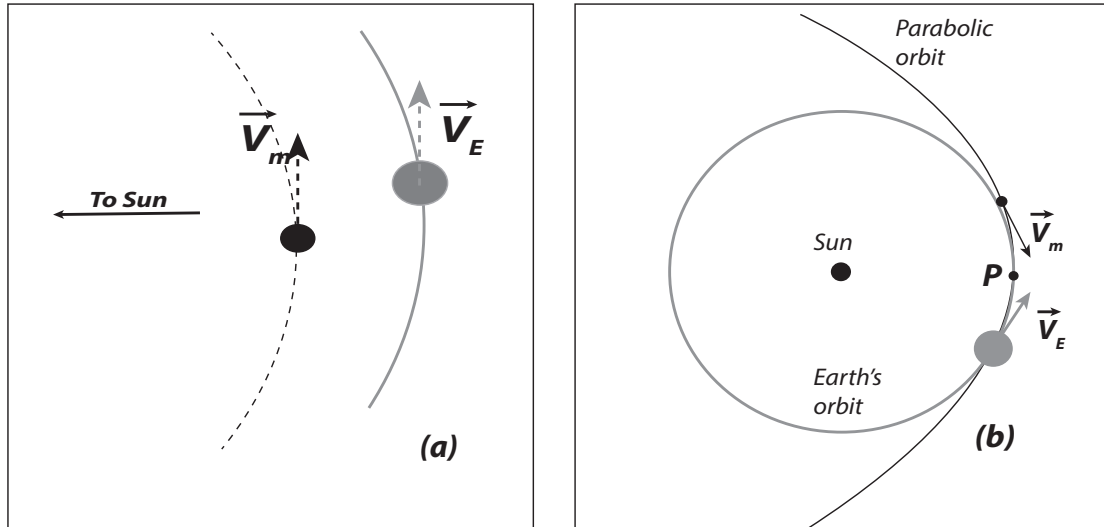
Figure 1.9: Illustration of the geometry of a meteoroid encountering the Earth. The minimum geocentric speed of the meteoroid will be observed when it moves on an orbit, similar to an Earth-like orbit, and just catching up behind the Earth(panel a). The maximum geocentric speed will result from a head-on collision e.g., meteoroid moving on a parabolic heliocentric orbit (panel b).

When a meteoroid intersects the Earth's path, it interacts with the upper atmosphere (between $\sim$ 80 km - 100 km) and, if sufficiently large (millimeter sized) and fast enough, it will ablate and can be observed visually or detected by optical techniques as a meteor. However, if the meteoroid is small it will likely be too faint to be detected by optical instruments, though the created plasma train, from the ionized atmospheric and meteoric atoms, can be registered by radar. We continue this section by reviewing the various techniques used to detect meteors.

1.5.1 Visual observations

Meteors have been observed since ancient times, evidenced by a number of records on wood carvings and paintings, which renders the method as the oldest (e.g., Jenniskens, 2006). The only instrument needed is the human's eyes or a telescope with a large aperture. Apart from meteors seen by a random person, nowadays there are large number of amateur astronomers and organizations whose contribution is crucial and complements other meteor detection techniques. During an enhanced meteor activity (meteor shower), meteor observers from different locations on the globe report on the strength of the observed meteor shower. Generally, this is from the *Zenith Hourly Rate* (ZHR) - the number of meteors that have been observed within one hour, looking towards the zenith (the point on the sky directly above the observer). Then, using the ZHR and meteor population index (the brightness distribution of meteors) a meteoroid flux (number of meteors per unit time per unit area in the sky) can be calculated. That is

is usually done by large number of observers and different groups, which significantly increase the statistical significance of the results. Finally, often during meteor observations the meteor color is reported, which is a proxy to the meteoroid approximate composition, though due to the subjectivity of color perception by different individuals, the meteoroids' chemistry is less well constrained by visual observations.

1.5.2 Photographic observations

Photographic observation of meteors is the second oldest method after the visual. It involves obtaining a photographic image of a meteor in the upper atmosphere. Generally, photographic observations are very precise and have been used to calculate meteoroid orbits. However, to do that information about the atmospheric trajectory of the meteoroid is needed, which is achieved by obtaining at least two images of the same meteor, from two remote stations. In essence, this consists of defining two planes, each containing the meteor trajectory and the station, with the meteoroid trajectory being the intersection of the two planes (Ceplecha, 1987). Then, through simple algebraic manipulations, initial heliocentric orbit of the meteoroid can be reconstructed (Ceplecha, 1987).

To obtain information on the deceleration of the meteoroid in the atmosphere, its trajectory on the image is interrupted (marked) at equal time intervals, thus yielding information on the velocity between successive time marks. This has been achieved by mounting rotating shutters near the focal plane of the cameras, rotating at a constant angular speed. Thus, the deceleration of the meteoroid along with the atmospheric trajectory, corrected for the gravitational attraction from the Earth, allows for determination of a few important parameters. These are the equatorial coordinates (position) of the apparent radiant (α_R, δ_R), the pre-atmospheric velocity V_∞ and initial height. Detailed explanation on the observational data reduction techniques and obtaining the latter parameters can be found in Ceplecha (1987).

Having obtained all the parameters above, along with the time of observation, allows for the calculation of the heliocentric position X, Y, Z and velocity $\dot{X}, \dot{Y}, \dot{Z}$ components, as well as the heliocentric orbital elements $a, e, i, \omega, \Omega, M$ (see Appendix C). The orbital elements can be used to study the future or past dynamical evolution of the meteoroid.

The largest currently operating photographic meteor observation network is the "*European Fireball Network*" (Oberst et al., 1998) which began in 1963. It consists of more than 34 all-sky and fish-eye cameras, located about 100 km apart from each other, thus covering $\sim 10^6$ km^2 sky area. The cameras are situated in Germany, the Czech and Slovak Republics, as well as some parts of Belgium, Switzerland and Austria. On average the network provides ~ 10000 photographic images of meteors per year, corresponding on average to 1200 h of clear sky.

One of the largest past photographic observations network was the "*Prairie Network*" founded in 1964 and terminated in 1975. It consisted of 16 stations situated $\approx$ 250 km apart, on the territory of the USA (Midwestern United States) and having approximately 11×10^5 km^2 sky coverage. Each station was equipped with four long focal-length photo cameras with a main goal of detecting bright meteors and subsequently (if impacted on the ground) recovery of the associated meteorites. The precisions of those instruments were better than 1% for the velocity along the trajectory and even better for meteoroid's angular position on the sky (McCrosky and Boeschenstein, 1965).

1.5.3   Video observation

In terms of sensitivity, video and television (TV) meteor observations are intermediate between photographic and sensitive radar techniques, with limiting apparent meteor magnitudes down to about $+9^m$ (Ceplecha et al. (1998)), where the word "magnitude" refers to the apparent brightness of a meteor. The method essentially makes use of low light level television (LLLT) methods for the study of meteors. These television based detectors have fields of view of roughly 15° and this coupled with the sensitivity threshold provides sporadic meteor rates of approximately 15-20 meteors per hour (Hawkes, 1993). Video meteor observations could be either fully automated, partially automated or non-automated, where the former requires no user intervention for control, event detection and data reduction analysis (Weryk and Brown (2012)). However, the downside of video meteor observations is the poor signal-to-noise ratio and the small field of view (about 15°). The latter could result in a number of partial trails observed, which could complicate the light-curve and atmospheric trajectory analyzes Hawkes (1993).

1.5.4   Radar observations

As a meteoroid enters the Earth's atmosphere, at higher altitudes where the free molecule regime holds, the meteoroid is heated by collision with air molecules. As it further descends through the atmosphere to altitudes of about 100 km, the meteoric atoms are released by evaporation from the meteoroid surface. The inelastic collisions of the vaporized atoms with the air molecules cause ionization and production of an ionization trail of free electrons until the latter are removed by chemical reactions (Ceplecha et al., 1998). Radar observations involve specular reflection of emitted radio waves from the ionized trail created by the meteoroid entry, and subsequent registration of the reflected waves by receivers on the ground.

One of the main advantages of the radar meteor observations over the photographic or video observations is that the radar system can operate and detect meteors during day-time and

overcast weather. In addition, it can detect smaller meteoroids ($\sim 100 \mu m$ and larger), whereas video and photographic observations are typically restricted to $\sim$ mm-cm sized particles. Using the radar meteor observation can aid to estimate more accurately the total influx of material onto the Earth (especially the smaller population), and in the Solar system. Furthermore, it allows the linking of meteoroid streams which peak during day-time, and which can not be observed by other observational techniques. Also, the observations of meteors by photographic and video techniques are biased towards larger meteoroids (mm-cm sized), by utilizing radar techniques that bias can be corrected.

1.6   The meteoroid complex of comet 96P/Machholz

1.6.1   Comet 96P/Machholz

Comet 96P is unusual among the short-period comets. It has an extremely low perihelion distance, grazing the Sun at a distance of 0.123 AU or roughly $26.5 R_{\odot}$, and has been associated with a number of other comets and objects of asteroidal appearance. In particular, it is well known that 96P shares a genetic relationship with the *Marsden* and *Kracht* group of sunskirting comets and the *Kreutz* sungrazers (e.g., Sekanina and Chodas, 2005; Jenniskens, 2006). It is also associated with up to eight different meteor showers, the Quadrantids, daytime Arietids, Southern and Northern δ-Aquariids, α-Cetids, κ-Velids, θ-Carinids and the Ursids (e.g., Babadzhanov and Obrubov, 1992; Neslušan et al., 2013). This ensemble of interplanetary bodies is referred to as the *Machholz interplanetary complex* and is believed to have originated from a single split of a larger progenitor prior to 950 AD (Sekanina and Chodas, 2005). Despite the association of 96P with the aforementioned bodies, some of their present orbital elements differ noticeably, owing to the differential planetary perturbations (mainly due to Jupiter). Presently, the Marsden sunskirters approach the Sun within $8-11 R_{\odot}$ and have mean orbital inclination of $\approx 26°$, whereas the Kracht group of comets have perihelia in the range $6.7-11.6 R_{\odot}$ and inclination of $\approx 13°$. For comparison, the present inclination of 96P is $i \approx 58°$ and perihelion distance of 0.123 AU. Furthermore, 96P is interesting among other comets as it has anomalous molecular abundances (e.g., A'Hearn et al., 1995; Schleicher, 2008), being relatively depleted in CN, C_2, C_3 compared to the OH abundance. That indicates that 96P has either formed in a region of the early Solar system with unusual conditions or is interstellar in origin.

Comet 96P was mentioned for first time in the context of meteor astronomy by McIntosh (1990). The author noted the similar orbital evolution of 96P and the Quadrantid meteoroid stream, though their evolutionary cycles were offset by 4000 years. That led McIntosh (1990)

to suggest a sibling rather than child-parent relationship.

Numerical simulations of the long-term evolution of the orbit of 96P were performed by Babadzhanov and Obrubov (1992). They were the first to suggested that within one circulation cycle of the longitude of the ascending node Ω and the argument of perihelion ω (≈ 8200 years), the comet may give rise to eight different meteor showers. The Earth intersects four of these showers at their descending nodes and four at their ascending nodes. The authors identified these showers as the Quadrantids, daytime Arietids, Southern and Northern δ-Aquariids, Ursids, κ-Velids, Carinids and the α-Cetids. The first four showers are well known and constrained. The existence of the rest of the other showers has remained uncertain, partly due to the lack of systematic meteor surveys from the Southern hemisphere.

Jones and Jones (1993) argued that if comet 96P had been captured by close approach with Jupiter, about 2200 years ago, there has been sufficient time for the comet to produce most of the observed characteristics of the Quadrantids, the daytime Arietids and Southern δ-Aquariids.

Recent work, carried out by Neslušan et al. (2013) investigated potential streams related to 96P, assuming an initial meteoroid ejection time 4000 years ago. They concluded that 96P may indeed produce eight different showers, though they were skeptical about the detectability of all of them. Instead, they argued that due to the proximity of four of the intersection points with the Earth's orbit, only six showers are expected to be identified. Although the authors recognized the $\sim$ 8200 years circulation cycle of the longitude of the ascending node and the argument of perihelion of 96P's orbit, they considered only half of that period in their investigation. Moreover, the authors did not compare the characteristics of the modeled meteoroid streams in detail with available observations.

Several recent works have suggested that the Marsden group of comets are the immediate parents of the daytime Arietids and the Northern and Southern δ-Aquariids (Ohtsuka et al., 2003; Sekanina and Chodas, 2005; Jenniskens, 2006). Ohtsuka et al. (2003) noted the similarity in the orbital evolution of 96P, the Marsden and Kracht group of sunskirting comets and the daytime Arietids, assuming their evolutionary cycles were shifted by a few hundred years. The authors suggested that the Arietids are related to the Marsden group but hinted that all bodies may be genetically related. Sekanina and Chodas (2005) performed numerical simulations to investigate the origin of the Marsden and Kracht group of comets. Based on the tendency of these comets to arrive at perihelion in pairs, the authors developed a detailed model and suggested that the sunskirting group of comets, along with the Arietids and southern δ-Aquariids, originated from a single comet break up, prior to 950 AD. However, these authors and earlier works have not attempted to constrain formation models of the 96P complex using detailed observations of the associated meteor showers.

1.6.2 96P/Machholz complex showers

The Quadrantids

The Quadrantids are unusual, being among the strongest of the annual showers with an extremely compact central portion, with a Full Width of Half Maximum (FWHM) of only ≈17 hours, encountered every year between January 3-4. This alone is a strong evidence that the core of the stream is young. Due to the presently large difference in the longitude of the ascending nodes of the stream and 96P/Machholz, the comet was not recognized as the immediate parent of the stream. Jenniskens et al. (1997) questioned the association of the Quadrantids and 96P and instead suggested that the parent may be an asteroid-like object, hidden in a high inclination orbit. With the discovery of asteroid 2003 EH_1, Jenniskens (2004) noted a striking similarity with the orbit of the Quadrantids and suggested a child-parent relationship. Wiegert and Brown (2005) performed a nodal regression analysis of the orbits of 2003 EH_1 and the Quadrantids, arguing that the core of the stream is only 200 years old. However, recent radar observations of the Quadrantids revealed that there is an older component of the stream, lasting from mid-November to mid-January (Brown et al., 2010). Using seven high-precision photographic Quadrantids, augmented with radar observations by the *Canadian Meteor Orbit Radar* (CMOR), we demonstrated using several independent lines of evidence that the core of the stream is related to asteroid 2003 EH_1 and most likely formed circa 1800 AD (Abedin et al., 2015). This study also found that the older component is associated with comet 96P and is several millenia old. For a thorough review of past works on the Quadrantids, the reader is referred to e.g., Jenniskens (2006); Neslušan et al. (2013); Abedin et al. (2015).

The Daytime Arietids

The shower is observed annually between mid-May and late June with a broad plateau of peak activity near solar longitude $\lambda_\odot = 80.5°$ (Bruzzone et al., 2015). The shower characteristics have mostly been constrained by radar observations, owing to the proximity of the radiant position to the Sun, with some recent observations by optical detections. Recently, we addressed the question as to the association of the stream with the Marsden group of comets or comet 96P (as discussed above). We performed detailed numerical simulations of meteoroids, ejected from 96P and the most notable member of the Marsden group of comets - P/1999 J6. The resulting streams from both comets were analyzed with respect to which could reproduce the main characteristics of the daytime Arietids. As observational constraints for the shower, we used data from the 12 year radar survey of the daytime Arietids by CMOR (Bruzzone et al., 2015), along with 14 TV observations by SonotaCo (2009) and 31 video events recorded by the

Cameras for All-sky Meteor Surveillance (CAMS) (Jenniskens et al., 2016). Our simulations indicated that the Marsden group of comets can not alone reproduce the observed characteristics of the shower and thus can not be the sole parents of the stream. Instead, we concluded that the broader activity of the daytime Arietids are associated with comet 96P and have an age of ~10000 years, though we demonstrated that the Marsden group of comets may contribute to the peak of the shower. An outstanding question for this shower relates to the difference in the orbital elements of optical and radar sized particles, a discrepancy previously noted by Jenniskens et al. (2012). Radar surveys measure systematically lower meteoroid geocentric speeds, and thus lower orbital semi-major axis, as compared to optical surveys. Jenniskens et al. (2012) attributed these differences to insufficient correction for deceleration of radar sized (a few hundreds of microns) meteoroids in the Earth's atmosphere. These are normally subject to a greater atmospheric drag than larger meteoroids. These differences, if they are real, imply that the daytime Arietids may be older than a few tens of millenia. The observed discrepancy remains unresolved.

Southern and Northern δ-Aquariids

The Southern δ-Aquariids are observed every year between late May to early July with a peak activity at solar longitude $\lambda_\odot = 126°$ (Brown et al., 2010). Though much weaker, the northern branch is active between late July to late August with a maximum activity occurring at $\lambda_\odot = 139°$. Although the showers stand well above the sporadic background and have been well measured, their origin has received less attention and is mostly limited to the works by Babadzhanov and Obrubov (1992); Sekanina and Chodas (2005); Jenniskens (2006) and Neslušan et al. (2013).

κ-Velids, α-Cetids, Carinids and Ursids

- The predicted κ-Velids have only recently been established as an annual shower (Pokorny et al. 2016), based on systematic radar observations by the *Southern Argentina Agile Meteor Radar* (SAAMER) (Janches et al., 2013, 2015). In contrast, there is no obvious shower listed in the IAU Meteor Data Center (IAU MDC) (`http://www.ta3.sk/IAUC22DB/MDC2007/`), corresponding to the radiant, speed and timing characteristics predicted by Babadzhanov and Obrubov (1992) for α-Cetids, though there are 19 different showers that are listed as Cetids. Likewise, there are 4 different showers listed as Carinids, though only θ-Carinids are well measured (Pokorny et al. 2016). Finally, the association of the Ursids with 96P is doubtful, as the stream has already been confirmed to be related to comet 8P/Tuttle (e.g., Jenniskens, 2006), which indicates that the stream had been either misidentified by Babadzhanov and Obrubov

(1992) or it overlaps with another nearby stronger meteor shower and hence can not be detected as individual, as previously suggested by Neslušan et al. (2013).

In this work, we aim to obtain a broader picture of the origin and past evolution of the complex of interplanetary bodies, associated with comet 96P. We approach that problem by simultaneously fitting the observed shower characteristics and attempt to answer the following questions:

1. What is the most dominant parent of the 96P meteoroid complex associated, comet 96P/Machholz or the Marsden group of comets?

2. What is the age and likely parent (comet 96P/Machholz or the Marsden group of comets) of the Southern and Northern δ-Aquariids and the recently established $\kappa-$Velids and θ-Carinids?

3. Do the Carinids, $\alpha-$Cetids and Ursids exist or they have been misidentified? If they exist, what is their likely age and parent?

4. Can we obtain a self-consistent scenario as to the epoch when comet 96P has been captured in a short period orbit and its past fragmentation history?

Bibliography

Abedin, A., Spurný, P., Wiegert, P., Pokorný, P., Borovička, J., Brown, P., 2015. On the age and formation mechanism of the core of the Quadrantid meteoroid stream. Icarus 261, 100–117. `1508.02418`.

A'Hearn, M.F., Millis, R.C., Schleicher, D.O., Osip, D.J., Birch, P.V., 1995. The ensemble properties of comets: Results from narrowband photometry of 85 comets, 1976-1992. Icarus 118, 223–270.

Amelin, Y., Krot, A.N., Hutcheon, I.D., Ulyanov, A.A., 2002. Lead Isotopic Ages of Chondrules and Calcium-Aluminum-Rich Inclusions. Science 297, 1678–1683.

Asher, D.J., 1991. The Taurid Meteoroid Complex. Ph.D. thesis.

Babadzhanov, P.B., Obrubov, I.V., 1992. Comet Machholz 1986 VIII and the Quadrantid meteroid shower - Orbital evolution and relationship. Astronomicheskii Vestnik 26, 70–78.

Bailey, M.E., Chambers, J.E., Hahn, G., 1992. Origin of sungrazers - A frequent cometary end-state. A&A 257, 315–322.

Beech, M., Brown, P., Jones, J., 1995. The Potential Danger to Space Platforms from Meteor Storm Activity. Quart. Journal of the Royal Astr. Soc 36, 127.

Beech, M., Steel, D., 1995. On the Definition of the Term Meteoroid. Quart. Journal of the Royal Astr. Soc 36, 281.

Ben-Menahem, A., 1975. Source parameters of the siberian explosion of June 30, 1908, from analysis and synthesis of seismic signals at four stations. Physics of the Earth and Planetary Interiors 11, 1–35.

Benz, W., Asphaug, E., 1999. Catastrophic Disruptions Revisited. Icarus 142, 5–20. `astro-ph/9907117`.

Bizzarro, M., Baker, J.A., Haack, H., 2004. Mg isotope evidence for contemporaneous formation of chondrules and refractory inclusions 431, 275–278.

Bottke, W.F., Nesvorný, D., Grimm, R.E., Morbidelli, A., O'Brien, D.P., 2006a. Iron meteorites as remnants of planetesimals formed in the terrestrial planet region. Nature 439, 821–824.

Bottke, W.F., Nolan, M.C., Greenberg, R., Kolvoord, R.A., 1994. Velocity distributions among colliding asteroids. Icarus 107, 255–268.

Bottke, Jr., W.F., Rubincam, D.P., Burns, J.A., 2000. Dynamical Evolution of Main Belt Meteoroids: Numerical Simulations Incorporating Planetary Perturbations and Yarkovsky Thermal Forces. Icarus 145, 301–331.

Bottke, Jr., W.F., Vokrouhlický, D., Rubincam, D.P., Broz, M., 2002. The Effect of Yarkovsky Thermal Forces on the Dynamical Evolution of Asteroids and Meteoroids. Asteroids III , 395–408.

Bottke, Jr., W.F., Vokrouhlický, D., Rubincam, D.P., Nesvorný, D., 2006b. The Yarkovsky and Yorp Effects: Implications for Asteroid Dynamics. Annual Review of Earth and Planetary Sciences 34, 157–191.

Bouvier, A., Wadhwa, M., 2010. The age of the Solar System redefined by the oldest Pb-Pb age of a meteoritic inclusion. Nature Geoscience 3, 637–641.

Brown, P., Wong, D.K., Weryk, R.J., Wiegert, P., 2010. A meteoroid stream survey using the Canadian Meteor Orbit Radar. II: Identification of minor showers using a 3D wavelet transform. Icarus 207, 66–81.

Brown, P.G., Assink, J.D., Astiz, L., Blaauw, R., Boslough, M.B., Borovička, J., Brachet, N., 2013. A 500-kiloton airburst over Chelyabinsk and an enhanced hazard from small impactors. Nature 503, 238–241.

Bruzzone, J.S., Brown, P., Weryk, R.J., Campbell-Brown, M.D., 2015. A decadal survey of the Daytime Arietid meteor shower using the Canadian Meteor Orbit Radar. MNRAS 446, 1625–1640.

Burns, J.A., Lamy, P.L., Soter, S., 1979. Radiation forces on small particles in the solar system. Icarus 40, 1–48.

Capaccioni, F., Coradini, A., Filacchione, G., Erard, S., Arnold, G., Drossart, P., 2015. The organic-rich surface of comet 67P/Churyumov-Gerasimenko as seen by VIRTIS/Rosetta. Science 347, aaa0628.

Ceplecha, Z., 1987. Geometric, dynamic, orbital and photometric data on meteoroids from photographic fireball networks. Bulletin of the Astronomical Institutes of Czechoslovakia 38, 222–234.

Ceplecha, Z., Borovička, J., Elford, W.G., Revelle, D.O., Hawkes, R.L., Porubčan, V., Šimek, M., 1998. Meteor Phenomena and Bodies. Space Sci. Reviews 84, 327–471.

Chesley, S.R., Ostro, S.J., Vokrouhlický, D., Čapek, D., Giorgini, J.D., Nolan, M.C., Margot, J.L., Hine, A.A., Benner, L.A.M., Chamberlin, A.B., 2003. Direct Detection of the Yarkovsky Effect by Radar Ranging to Asteroid 6489 Golevka. Science 302, 1739–1742.

Crida, A., 2009. Solar System Formation, in: Röser, S. (Ed.), Reviews in Modern Astronomy, pp. 215–227. `0903.3008`.

Davis, A.M., Richter, F.M., 2005. Condensation and Evaporation of Solar System Materials. Elsevier B. p. 407.

Delsemme, A.H., 1982. Chemical composition of cometary nuclei, in: Wilkening, L.L. (Ed.), IAU Colloq. 61: Comet Discoveries, Statistics, and Observational Selection, pp. 85–130.

Duncan, M.J., 2008. Dynamical Origin of Comets and Their Reservoirs. Space Sci. Reviews 138, 109–126.

Edgeworth, K.E., 1949. The origin and evolution of the Solar System. MNRAS 109, 600–609.

Fernández, J.A., 1997. The Formation of the Oort Cloud and the Primitive Galactic Environment. Icarus 129, 106–119.

Fernández, Y.R., Jewitt, D.C., Sheppard, S.S., 2001. Low Albedos Among Extinct Comet Candidates 553, L197–L200. `astro-ph/0104478`.

Gladman, B., Michel, P., Froeschlé, C., 2000. The Near-Earth Object Population. Icarus 146, 176–189.

Greenberg, J.M., 1998. Making a comet nucleus. A&A 330, 375–380.

Gronchi, G.F., Milani, A., 1999. Averaging on Earth-Crossing Orbits. Celestial Mechanics and Dynamical Astronomy 71, 109–136.

Gustafson, B.A.S., 1989a. Comet ejection and dynamics of nonspherical dust particles and meteoroids. ApJ 337, 945–949.

Gustafson, B.A.S., 1989b. Geminid meteoroids traced to cometary activity on Phaethon. A&A 225, 533–540.

Harris, A.W., 1996. The Rotation Rates of Very Small Asteroids: Evidence for 'Rubble Pile' Structure, in: Lunar and Planetary Science Conference.

Hawkes, R.L., 1993. Television meteors (Invited), in: Stohl, J., Williams, I.P. (Eds.), Meteoroids and their Parent Bodies, p. 227.

Hughes, D.W., 2000. On the velocity of large cometary dust particles. Planet. and Space Sci. 48, 1–7.

Janches, D., Close, S., Hormaechea, J.L., Swarnalingam, N., Murphy, A., O'Connor, D., Vandepeer, B., Fuller, B., Fritts, D.C., Brunini, C., 2015. The Southern Argentina Agile MEteor Radar Orbital System (SAAMER-OS): An Initial Sporadic Meteoroid Orbital Survey in the Southern Sky. ApJ 809, 36.

Janches, D., Hormaechea, J.L., Brunini, C., Hocking, W., Fritts, D.C., 2013. An initial meteoroid stream survey in the southern hemisphere using the Southern Argentina Agile Meteor Radar (SAAMER). Icarus 223, 677–683.

Jenniskens, P., 2004. 2003 EH_1 Is the Quadrantid Shower Parent Comet. Astron. Journ. 127, 3018–3022.

Jenniskens, P., 2006. Meteor Showers and their Parent Comets.

Jenniskens, P., Betlem, H., de Lignie, M., Langbroek, M., van Vliet, M., 1997. Meteor stream activity. V. The Quadrantids, a very young stream. A&A 327, 1242–1252.

Jenniskens, P., Duckworth, H., Grigsby, B., 2012. Daytime Arietids and Marsden Sunskirters (ARI, IAU #171). WGN, Journal of the International Meteor Organization 40, 98–100.

Jenniskens, P., Nénon, Q., Albers, J., Gural, P.S., Haberman, B., Holman, D., Morales, R., Grigsby, B.J., Samuels, D., Johannink, C., 2016. The established meteor showers as observed by CAMS. Icarus 266, 331–354.

Jewitt, D., Weaver, H., Agarwal, J., Mutchler, M., Drahus, M., 2010. A recent disruption of the main-belt asteroid P/2010A2. Nature 467, 817–819.

Jones, J., 1995. The ejection of meteoroids from comets. MNRAS 275, 773–780.

Jones, J., Jones, W., 1993. Comet Machholz and the Quadrantid meteor stream. MNRAS 261, 605–611.

Jopek, T.J., Valsecchi, G.B., Froeschlé, C., 2002. Asteroid Meteoroid Streams. pp. 645–652.

Kinoshita, H., Nakai, H., 1999. Analytical Solution of the Kozai Resonance and its Application. Celestial Mechanics and Dynamical Astronomy 75, 125–147.

Kozai, Y., 1962. Secular perturbations of asteroids with high inclination and eccentricity. Astron. Journ. 67, 591.

Kresak, L., 1976. Orbital evolution of the dust streams released from comets 27, 35–46.

Kresak, L., 1978. The Tunguska object - A fragment of Comet Encke 29, 129–134.

Levison, H.F., Duncan, M.J., 1997. From the Kuiper Belt to Jupiter-Family Comets: The Spatial Distribution of Ecliptic Comets. Icarus 127, 13–32.

Levison, H.F., Morbidelli, A., Van Laerhoven, C., Gomes, R., Tsiganis, K., 2008. Origin of the structure of the Kuiper belt during a dynamical instability in the orbits of Uranus and Neptune. Icarus 196, 258–273.

Lidov, M.L., 1962. The evolution of orbits of artificial satellites of planets under the action of gravitational perturbations of external bodies. Planet. and Space Sci. 9, 719–759.

Lowry, S.C., Fitzsimmons, A., Pravec, P., Vokrouhlický, D., Boehnhardt, H., Taylor, P.A., Margot, J.L., Galád, A., Irwin, M., Irwin, J., Kusnirák, P., 2007. Direct Detection of the Asteroidal YORP Effect. Science 316, 272–.

Martins, Z., Price, M.C., Goldman, N., Sephton, M.A., Burchell, M.J., 2013. Shock synthesis of amino acids from impacting cometary and icy planet surface analogues. Nature Geoscience 6, 1045–1049.

McCrosky, R.E., Boeschenstein, Jr., H., 1965. The Prairie Meteorite Network. SAO Special Report 173.

McIntosh, B.A., 1990. Comet P/Machholtz and the Quadrantid meteor stream. Icarus 86, 299–304.

Michel, P., Benz, W., Tanga, P., Richardson, D.C., 2001. Collisions and Gravitational Reaccumulation: Forming Asteroid Families and Satellites. Science 294, 1696–1700.

Millman, P.M., 1961. Meteor News. Journ. of Royal Astron. Soc. of Canada 55, 265.

Morbidelli, A., Bottke, Jr., W.F., Froeschlé, C., Michel, P., 2002. Origin and Evolution of Near-Earth Objects. Asteroids III , 409–422.

Morbidelli, A., Levison, H.F., Tsiganis, K., Gomes, R., 2005. Chaotic capture of Jupiter's Trojan asteroids in the early Solar System. Nature 435, 462–465.

Murray, C.D., Dermott, S.F., 2000. Solar System Dynamics.

Neslušan, L., Hajduková, M., Jakubík, M., 2013. Meteor-shower complex of asteroid 2003 EH1 compared with that of comet 96P/Machholz. A&A 560, A47.

Oberst, J., Molau, S., Heinlein, D., Gritzner, C., Schindler, M., Spurny, P., Ceplecha, Z., Rendtel, J., Betlem, H., 1998. The "European Fireball Network": Current status and future prospects. Meteoritics and Planetary Science 33, 49–56.

Ohtsuka, K., Nakano, S., Yoshikawa, M., 2003. On the Association among Periodic Comet 96P/Machholz, Arietids, the Marsden Comet Group, and the Kracht Comet Group. Publ. Astr. Soc. Japan 55, 321–324.

Oort, J.H., 1950. The structure of the cloud of comets surrounding the Solar System and a hypothesis concerning its origin. Bull. Astron. Inst. Netherlands 11, 91–110.

Petit, J.M., Morbidelli, A., Chambers, J., 2001. The Primordial Excitation and Clearing of the Asteroid Belt. Icarus 153, 338–347.

Pitjeva, E.V., 2005. High-Precision Ephemerides of Planets and Determination of Some Astronomical Constants. Solar System Research 39, 176–186.

Plavec, M., 1950. The Geminid Meteor Shower. Nature 165, 362–363.

Popova, O.P., Jenniskens, P., Emel'yanenko, V., Kartashova, A., Biryukov, E., Khaibrakhmanov, S., Shuvalov, V., Rybnov, Y., Dudorov, A., Grokhovsky, V.I., Badyukov, D.D., Yin, Q.Z., Gural, P.S., Albers, J., Granvik, M., Evers, L.G., Kuiper, J., Kharlamov, V., Solovyov, A., Rusakov, Y.S., Korotkiy, S., Serdyuk, I., Korochantsev, A.V., Larionov, M.Y., Glazachev, D., Mayer, A.E., Gisler, G., Gladkovsky, S.V., Wimpenny, J., Sanborn, M.E., Yamakawa, A., Verosub, K.L., Rowland, D.J., Roeske, S., Botto, N.W., Friedrich, J.M., Zolensky, M.E., Le, L., Ross, D., Ziegler, K., Nakamura, T., Ahn, I., Lee, J.I., Zhou, Q., Li, X.H., Li, Q.L., Liu, Y., Tang, G.Q., Hiroi, T., Sears, D., Weinstein, I.A., Vokhmintsev, A.S., Ishchenko, A.V., Schmitt-Kopplin, P., Hertkorn, N., Nagao, K., Haba, M.K., Komatsu, M.,

Mikouchi, T., aff34, 2013. Chelyabinsk Airburst, Damage Assessment, Meteorite Recovery, and Characterization. Science 342, 1069–1073.

Porubčan, V., Williams, I.P., Kornoš, L., 2004. Associations Between Asteroids and Meteoroid Streams. Earth Moon and Planets 95, 697–712.

Pravec, P., Harris, A.W., Michalowski, T., 2002. Asteroid Rotations. pp. 113–122.

Renne, P.R., Deino, A.L., Hilgen, F.J., Kuiper, K.F., Mark, D.F., Mitchell, W.S., Morgan, L.E., Mundil, R., Smit, J., 2013. Time Scales of Critical Events Around the Cretaceous-Paleogene Boundary. Science 339, 684–687.

Rickman, H., Fernandez, J.A., Gustafson, B.A.S., 1990. Formation of stable dust mantles on short-period comet nuclei. A&A 237, 524–535.

Rubin, A.E., Grossman, J.N., 2010. Meteorite and meteoroid: New comprehensive definitions. Meteoritics and Planetary Science 45, 114–122.

Rubincam, D.P., 2000. Radiative Spin-up and Spin-down of Small Asteroids. Icarus 148, 2–11.

Russell, C.T., Raymond, C.A., Coradini, A., McSween, H.Y., Zuber, M.T., Nathues, A., De Sanctis, M.C., Jaumann, R., Konopliv, A.S., Preusker, F., Asmar, S.W., Park, R.S., Gaskell, R., Keller, H.U., Mottola, S., Roatsch, T., Scully, J.E.C., Smith, D.E., Tricarico, P., Toplis, M.J., Christensen, U.R., Feldman, W.C., Lawrence, D.J., McCoy, T.J., Prettyman, T.H., Reedy, R.C., Sykes, M.E., Titus, T.N., 2012. Dawn at Vesta: Testing the Protoplanetary Paradigm. Science 336, 684.

Ryabova, G.O., 2016. A preliminary numerical model of the Geminid meteoroid stream. MN-RAS 456, 78–84.

Sagdeev, R.Z., Elyasberg, P.E., Moroz, V.I., 1988. Is the nucleus of Comet Halley a low density body? Nature 331, 240–242.

Schleicher, D.G., 2008. The Extremely Anomalous Molecular Abundances of Comet 96p/Machholz 1 from Narrowband Photometry. Astron. Journ. 136, 2204–2213.

Schulte, P., Alegret, L., Arenillas, I., Arz, J.A., Barton, P.J., Bown, P.R., Bralower, T.J., Christeson, G.L., Claeys, P., Cockell, C.S., Collins, G.S., Deutsch, A., Goldin, T.J., Goto, K., Grajales-Nishimura, J.M., Grieve, R.A.F., Gulick, S.P.S., Johnson, K.R., Kiessling, W., Koeberl, C., Kring, D.A., MacLeod, K.G., Matsui, T., Melosh, J., Montanari, A., Morgan, J.V., Neal, C.R., Nichols, D.J., Norris, R.D., Pierazzo, E., Ravizza, G., Rebolledo-Vieyra, M.,

Reimold, W.U., Robin, E., Salge, T., Speijer, R.P., Sweet, A.R., Urrutia-Fucugauchi, J., Vajda, V., Whalen, M.T., Willumsen, P.S., 2010. The Chicxulub Asteroid Impact and Mass Extinction at the Cretaceous-Paleogene Boundary. Science 327, 1214.

Sekanina, Z., Chodas, P.W., 2005. Origin of the Marsden and Kracht Groups of Sunskirting Comets. I. Association with Comet 96P/Machholz and Its Interplanetary Complex 161, 551–586.

Silber, E.A., ReVelle, D.O., Brown, P.G., Edwards, W.N., 2009. An estimate of the terrestrial influx of large meteoroids from infrasonic measurements. Journal of Geophysical Research (Planets) 114, E08006.

SonotaCo, 2009. A meteor shower catalog based on video observations in 2007-2008. WGN, Journal of the International Meteor Organization 37, 55–62.

Steel, D.I., 1995. The Association of Earth-Crossing Asteroids with Meteoroid Streams. Earth Moon and Planets 68, 13–30.

Stern, S.A., Colwell, J.E., 1997. Collisional Erosion in the Primordial Edgeworth-Kuiper Belt and the Generation of the 30-50 AU Kuiper Gap. ApJ 490, 879–882.

Vasilyev, N.V., 1998. The Tunguska Meteorite problem today. Planet. and Space Sci. 46, 129–150.

Vaubaillon, J., Colas, F., Jorda, L., 2005. A new method to predict meteor showers. I. Description of the model. A&A 439, 751–760.

Vokrouhlický, D., Farinella, P., 2000. Efficient delivery of meteorites to the Earth from a wide range of asteroid parent bodies. Nature 407, 606–608.

Walsh, K.J., Richardson, D.C., Michel, P., 2008. Rotational breakup as the origin of small binary asteroids. Nature 454, 188–191.

Weissman, P.R., 1980. Physical loss of long-period comets. A&A 85, 191–196.

Weissman, P.R., A'Hearn, M.F., Rickman, H., McFadden, L.A., 1989. Evolution of comets into asteroids, in: Binzel, R.P., Gehrels, T., Matthews, M.S. (Eds.), Asteroids II, pp. 880–920.

Weryk, R.J., Brown, P.G., 2012. Simultaneous radar and video meteors-I: Metric comparisons. Planet. and Space Sci. 62, 132–152.

Whipple, F.L., 1950. A comet model. I. The acceleration of Comet Encke. ApJ 111, 375–394.

Whipple, F.L., 1951. A Comet Model. II. Physical Relations for Comets and Meteors. ApJ 113, 464.

Whitman, K., Morbidelli, A., Jedicke, R., 2006. The size frequency distribution of dormant Jupiter family comets. Icarus 183, 101–114. `astro-ph/0603106`.

Wiegert, P., Brown, P., 2005. The Quadrantid meteoroid complex. Icarus 179, 139–157.

Williams, I.P., 1992. The Dynamics of Meteoroid Streams (lecture), in: Ferraz-Mello, S. (Ed.), Chaos, Resonance, and Collective Dynamical Phenomena in the Solar System, p. 299.

Williams, I.P., Wu, Z., 1993. The Geminid meteor stream and asteroid 3200 Phaethon. MN-RAS 262, 231–248.

Wyatt, S.P., Whipple, F.L., 1950. The Poynting-Robertson effect on meteor orbits. ApJ 111, 134–141.

Chapter 2

Age and Formation Mechanism of the Core of the Quadrantid Meteoroid Stream

A version of this chapter has been published as:

2.1   Introduction

The Quadrantids are among the most active meteor showers, reaching a peak activity of Zenithal Hourly Rate (ZHR) ~ 110 - 130 on 3-4 January each year (Shelton, 1965; Hindley, 1970; Hughes and Taylor, 1977), as determined by photographic, visual, video and radar techniques. The stream has recently been linked with asteroid 2003 EH$_1$ (Jenniskens, 2004).

The Quadrantid shower is unusual among meteoroid streams presently visible at the Earth for several reasons. Firstly, the Quadrantid meteor shower has a short duration of maximum activity, which we will call the 'core' or the "narrow structure" of the stream. The Full-Width at Half-Maximum (FWHM) of the core activity is $\approx$ 0.6 days (Shelton, 1965; Hughes and Taylor, 1977; Brower, 2006) for visual-sized particles, implying that this central portion is very young, while the shower as a whole has an overall duration of significant length ~ 4 days. Secondly, it has only become active recently, being first noted circa 1835 (Quetelet, 1839; Fisher, 1930). Moreover, the activity of the shower has changed dramatically over the last 150 years, from a very weak shower to among the strongest visible at the Earth (Jenniskens, 2006). Finally, recent radar observations (Brown et al., 2010b) suggest low level activity of the shower persisting for

a few months (November to mid January), suggesting the stream has an older component as well.

Presently, the presumed parent body of the core of the Quadrantids is the *Near Earth Object* (NEO) 2003 EH$_1$. Throughout this paper we will refer to it as asteroid 2003 EH$_1$. The object has been classified as an Amor type asteroid, although its nature is arguable based on dynamical criteria. Asteroid 2003 EH$_1$ has a short-period comet-like orbit, with a Tisserand parameter with respect to Jupiter of $T_J \approx 2.0$ (see Appendix D), but currently shows no evidence of cometary activity, suggesting that it is a strong candidate for either a recently dormant or extinct comet (Koten et al., 2006).

Prior to the discovery of 2003 EH$_1$, a few other objects with less similar orbits had been connected to the Quadrantid meteoroid stream, most notably comet 96P/Machholz (Jones and Jones, 1993; McIntosh, 1990; Babadzhanov and Obrubov, 1992) and comet C/1490 Y1 (Hasegawa, 1979; Lee et al., 2009; Williams and Wu, 1993; Williams and Collander-Brown, 1998). However, the relationship of these bodies to the Quadrantids remains unclear.

The earliest attempt to tackle the age of the Quadrantid meteoroids stream can be attributed to Hamid and Youssef (1963). The authors carried out a numerical secular perturbation analysis on the orbit of six doubly photographed Quadrantids and discovered large variations in the perihelion distance and the inclination of the stream orbit, with a period of 4000 years. Based on the backward secular solutions, the authors argued that the orbital elements of the six meteors were similar around 3000 years ago.

Williams et al. (1979) calculated the secular variations of the orbital elements of the mean Quadrantid stream and concluded that the Quadrantid meteoroid stream may have resulted from two major comet break-ups about 1690 and 1300 years in the past, where the resulting meteoroids converged into their present orbit around 200 - 150 years ago, explaining the recent appearance of the stream. Similar work was also performed by Hughes et al. (1979).

Hasegawa (1979), was the first to propose a potential parent body for the Quadrantids, noticing a similarity between the orbits of the mean Quadrantid stream and comet 1491 I (= C/1490 Y1), recorded in ancient Chinese observations. However, only a parabolic solution was assumed for the orbit of comet 1491 I, due to the low observational accuracy in the position of the comet. Based on the arguable similarity between the orbits of 1491 I and the Quadrantids, the authors concluded that 1491 I had been a periodic Jupiter-family comet, which suffered a very close encounter with Jupiter and was perturbed into a longer period orbit, where the orbital association with its meteoroid stream was lost.

Assuming that 1491 I was the actual parent of the Quadrantids using the calculated orbital elements of the comet, Williams and Wu (1993) concluded that the stream was created ~ 5000 years ago. Based on the hypothesis of a very shallow close encounter between comet 1491 I

and Jupiter, Williams and Wu (1993) demonstrated that prior to the encounter with Jupiter, the eccentricity of the orbit of the comet must had been $e \approx 0.77$. The newly derived value for the eccentricity was used for backwards integration of the orbit of the comet to about 5000 years. Then, that epoch was used for the meteoroids ejection whose orbits were integrated forward until the present. The authors argued that the observed mean orbital elements of the stream is consistent with dust particle ejection $\sim$ 5000 years ago. However, the lack of precise orbital elements for 1491 I, along with a hypothesized close encounter with Jupiter, renders the later conclusion uncertain. For a similar work, see also Lee et al. (2009).

Another possible parent of the Quadrantids is the comet 96P/Machholz (formerly P/1986 VIII). McIntosh (1990) calculated the secular precession of the orbital elements for the Quadrantids and comet 96P/Machholz and found that the long-term evolution of both orbits is strikingly similar, except for their precession cycles being shifted by a period of 2000 years. The author suggested that the stream was quite old and the phase shift in the precession cycles is due to the differential precession of the orbits of the stream and the comet. Moreover, the author argued that the Quadrantids may be a part of a larger complex of meteoroid streams, belonging to comet 96P/Machholz.

Babadzhanov and Obrubov (1992) integrated the orbits of three test particles similar to that of comet 96P/Machholz for 8000 years back in time. Then 20 test particles were ejected from the nucleus of 96P at the epoch of 4500 B.C and integrated forward until 3000 AD. For that period of 7500 years, the authors argued that meteoroids released by 96P can produce eight meteor showers on Earth within one precession cycle of the argument of perihelion ω of the meteoroids. Six of these showers have been identified as: the Quadrantids, the Ursids, Southern δ - Aquarids, daytime Arietids, Carinids and α - Cetids. That led the authors to conclude that 96P/Machholz is the parent of the Quadrantid meteoroid stream. For additional and more extensive work, see also Jones and Jones (1993) and Kańuchová and Neslušan (2007).

Jenniskens et al. (1997) used $\sim$ 35 doubly-photographed Quadrantids taken in 1995 by the *Dutch Meteor Society* (*DMS*) (Betlem et al., 1995), to argue that the age of the central portion of the Quadrantid stream is only $\sim$ 500 years old and the parent may be hidden on a *Near Earth Object* (*NEO*) - like orbit. With the discovery of 2003 EH$_1$ in 2003 (Jenniskens and Marsden, 2003; McClusky et al., 2003), Jenniskens (2004) noted the striking similarity between the current orbit of the Quadrantids and the orbit of 2003 EH$_1$ and proposed a sibling relationship.

Wiegert and Brown (2005) estimated an approximate age of 200 years for the core of the Quadrantids, based on the nodal regression rate of the stream and forward integration of meteoroids, released by 2003 EH$_1$ circa 1800 AD. The authors concluded that meteoroids released prior to 1800 AD appear on the sky at much earlier times than the first reported appearance

around 1835.

The main goal of this work is to estimate the most probable age of the central portion of the Quadrantid meteoroid stream and its mode of formation (e.g. cometary sublimation vs. asteroidal disruption). We seek to first constrain the approximate formation age assuming 2003EH$_1$ is the parent by first performing backward integrations of high precision Quadrantid meteoroids to compare the orbital similarity between the meteoroids and 2003 EH$_1$. Having established an approximate age from backward integrations we then attempt to simulate the formation of the core of the stream forward in time using the formation epoch found from backward integration and compare with the characteristics of the stream. However, our intention is not to provide a complete and detailed picture of all physical characteristics of the stream, rather we aim to demonstrate whether the observed overall characteristics of the core of the stream can be explained by assuming a relatively recent (a few hundred years) formation age derived from backward integrations of individual meteoroids.

As a test of reliability of our backward integration estimate of the age and formation mode of the stream, we compare the following theoretical and observed characteristics of the stream:

1. The timing of the appearance of the stream on the sky (around 1835 AD).
2. The mean position and spread of the geocentric radiant of the stream.
3. The position of the peak of the activity profile of the core.
4. The width of the activity profile of the core (FWHM $\approx$ 0.6 days).

Throughout this work, we use an approach similar to that of Gustafson (1989). That author integrated backward in time the orbits of 20 high precision Geminids, along with the parent 3200 Phaethon, and compared the epochs at which the orbits of the Geminids and that of Phaethon intersected. Moreover, he calculated the probable meteoroid ejection speed and location on the orbit of the parent, and concluded that the Geminids are consistent with cometary sublimation that might have taken place on Phaethon around 600 -2000 years ago. For an exhaustive description of the method see also Adolfsson (1996).

2.2   Asteroid 2003 EH$_1$ and the Quadrantids meteoroid streams

Asteroid 196256 (2003 EH$_1$) was discovered in March 2003 by the *Lowell Observatory Near-Earth Object Search* (LONEOS) and has been designated as a NEO Amor type asteroid. Currently, 2003 EH$_1$ moves on a highly inclined cometary-like orbit with a Tisserand parameter with respect to Jupiter of T_J=2.06 (see Appendix D) but shows no evidence of a cometary activity.

Recent photometric observations of the asteroid 2003 EH$_1$ give an absolute visual magnitude H = 16.2 mag, given by the NASA's JPL Small Body Database Browser (`http:`

//ssd.jpl.nasa.gov/sbdb.cgi). The diameter can be found using the expression given by Chesley et al. (2002):

$$D(km) = 1329A^{-0.5} \times 10^{-0.2H}, \tag{2.1}$$

where A is the geometric albedo and H is the absolute visual magnitude of the asteroid, respectively. A typical albedo value for asteroids (depending on the spectral class of the asteroid) is $0.04 < A < 0.4$ (Harris, 1989), which using Eq. 2.1 yields a diameter of 1.2 km $< D < 3.8$ km.

The present orbit of the asteroid 2003 EH$_1$ is presented in Fig. 2.1, along with the orbits of the Earth, Mars and Jupiter and the mean Quadrantid orbit. The orbital elements of 2003 EH$_1$ and the mean orbit of the Quadrantids are given in Table 4.1, along with other previously suggested parents, C/1490 Y1 and 96P/Machholz. The orbital elements of the mean Quadrantid stream are taken from Jenniskens et al. (1997).

The observed visual activity profile of the Quadrantid meteor shower is presented in Fig. 2.2. It is a composite (average) of activity profiles, as deduced from visual observations of Quadrantids, in the years of 1986, 1987, 1989, 1990 and 1992 (Rendtel et al., 1993). The core of the activity profile is easily seen to be less than a day wide, with a FWHM ≈ 0.5 days.

Fig. 2.3 shows the average radar activity profile of the Quadrantids (milligram size particles), as observed by the *Canadian Meteor Orbit Radar* "CMOR" (see Section 4.2 for details). The peak of the activity, located at $\lambda_\odot = 283.1°$ for equinox of J2000.0, occurs slightly before the visual meteors peak, but is in agreement within uncertainty of the two (averaged) profiles. The FWHM corresponds to approximately 0.8 days, slightly wider than the visual activity profile (see Fig. 2.2).

As shown in Fig. 2.1, the stream of particles producing the Quadrantids intersect the orbit of the Earth at their descending node, whereas the ascending node is located near the orbit of Jupiter. We emphasize that the mean Quadrantid orbit, as observed from the Earth, does not necessarily represent the orbit of the entire physical stream, but rather only that part that intersects the Earth. Meteoroid streams are usually dispersed and not all members intersect the Earth, so it is not possible to know the orbits of that portion of the stream that does not physically intersect the Earth's path. Therefore we refer to the mean Quadrantid stream as the mean of that portion that interacts with the Earth's atmosphere.

It is also evident that present orbit of the Quadrantid meteoroid stream and that of asteroid 2003 EH$_1$ are strikingly similar. However, the proximity of the parent and stream orbits is not a sufficient, nor necessary condition for a relation between the two. For example, initially close orbits (e.g. stream and parent) may follow dramatically different dynamical evolution due to the differential gravitational perturbations and solar radiation forces. Conversely, two
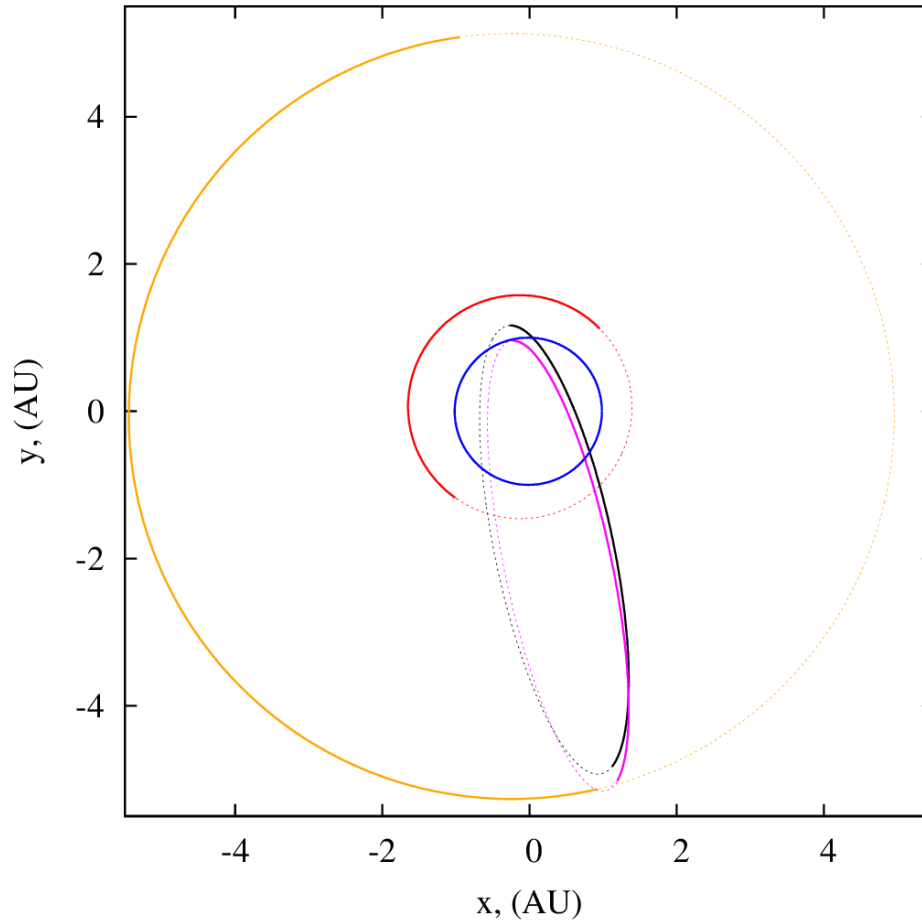
Figure 2.1: Orbits of asteroid 2003 EH$_1$ (black line) and the mean Quadrantid stream (Jenniskens et al., 1997) (magenta line), viewed from above the ecliptic plane. The orbit of Earth is indicated with blue, Mars with red and Jupiter with orange colors, respectively. The portions of the orbits, below the ecliptic are denoted with a dashed line. The ascending nodes of the orbits of both, the mean Quadrantids and 2003 EH$_1$ are located close to the Jupiter's orbit.

Object	Epoch (UT) (UT)	a (AU)	e	q (AU)	Q (AU)	i (deg)	ω (deg)	Ω (deg)
2003 EH$_1$	04 Nov. 2013	3.122	0.619	1.189	5.054	70.876	171.354	282.962
96P/Machholz	06 Sep. 2013	3.034	0.959	0.124	5.944	58.312	14.757	94.323
1490 Y1	26 Dec. 1490	—	1	0.737	—	51.65	129.84	295.89
Quadrantids	—	3.14	0.688	0.98	5.3	71.5	171.2	283.3

Table 2.1: The osculating orbital elements of asteroid 2003 EH$_1$, comet 96P/Machholz, comet 1490 Y1 and the mean Quadrantid orbit (J2000.0), as given in the NASA's JPL Horizons System (`http://ssd.jpl.nasa.gov/sbdb.cgi`). The orbital elements of the mean stream are taken from Jenniskens et al. (1997). Q and q in the table stand for the aphelion and perihelion distances respectively.
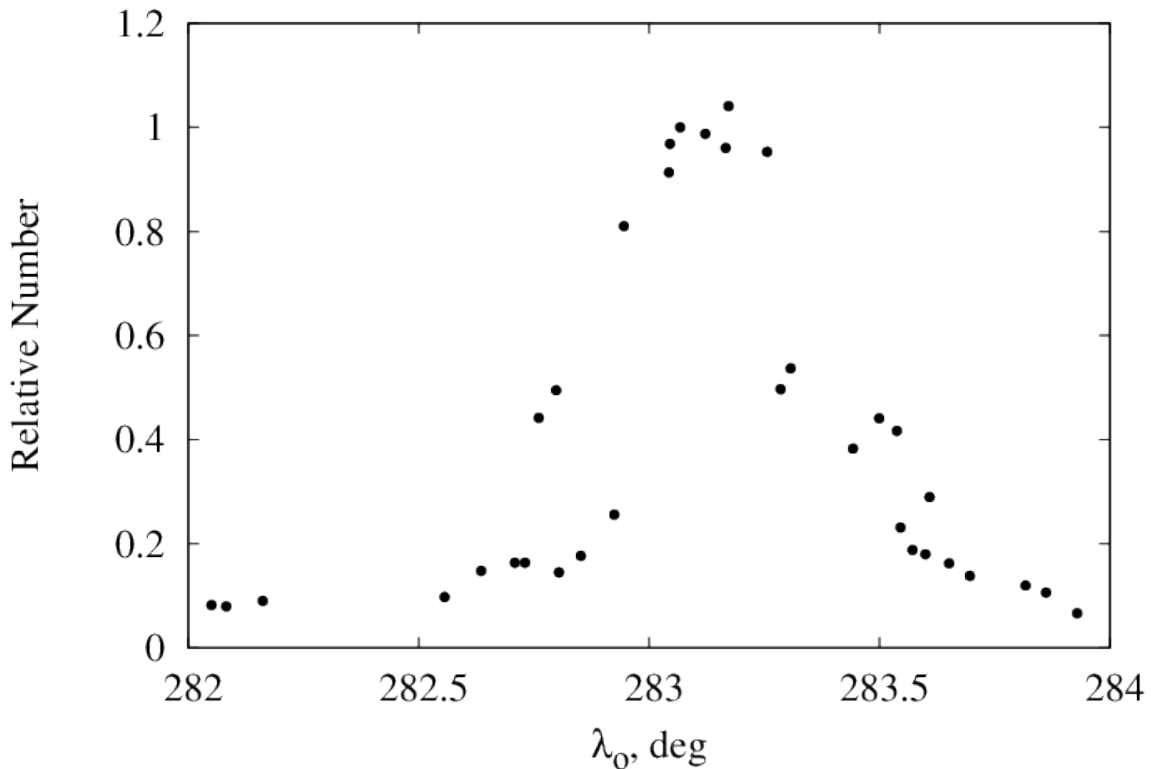
Figure 2.2: The average visual activity profile of the Quadrantid meteor shower. The profile is a stack of a few favorable observations between 1986 - 1992 (Rendtel et al., 1993). The peak of the activity is centered around $\lambda_\odot$ = 283.2° for equinox of J2000.0.

completely different orbits may end up into similar ones due to the aforementioned effect and result in a "false" sibling relationship between the two orbits. Thus, robust models of dynamical evolution of streams must be employed.

Jenniskens (2004) were the first to notice the similarity between 2003 EH$_1$ and the Quadrantids and proposed the former as the parent of the stream. However, the lack of cometary activity on 2003 EH$_1$ and the nature of its orbit make it a strong candidate for a recently dormant or defunct comet. The real nature, whether cometary or asteroidal, is unknown due to the lack of favorable returns and observations, rendering the formation mechanism of the Quadrantids uncertain.

The nature of 2003 EH$_1$ will determine the underlying mechanism by which it produced the Quadrantids. While cometary activity is driven by the sublimation of water ice, asteroids may also shed material by other processes. For example, Jewitt (2012) argued that the mass loss mechanism from the surface of 3200 Phaethon, another seemingly dormant or extinct comet, producing the Geminids meteor shower, is due to solar radiation pressure sweeping.
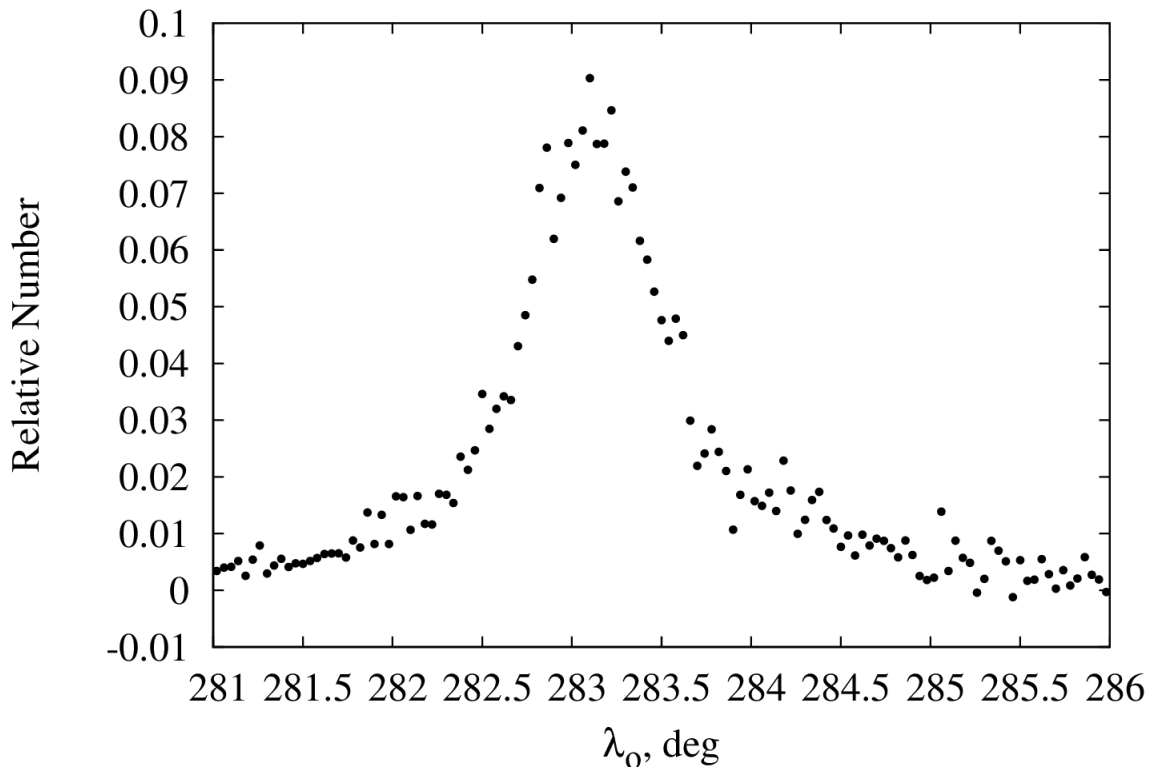
Figure 2.3: The average radar activity profile of the Quadrantid meteor shower as deduced by the *Canadian Meteor Orbit Radar* "CMOR". The profile is an average profile of all good quality observations between 2002 - 2014.

The inactivity of 2003 EH$_1$ points perhaps to an asteroidal nature. However, recent spectroscopic and double-station observations of 51 Quadrantids, revealed that unlike the Geminids the Quadrantids are not depleted in volatiles (Koten et al., 2006). In fact, the authors argued that the Quadrantids fall in a category between meteoroids of cometary and asteroid origin, and concluded that the parent 2003 EH$_1$ must be a dormant comet. Given 2003 EH$_1$'s comet-like orbit, we will here assume that material is released from it by traditional cometary activity in our forward modeling.

2.3 Meteoroid ejection model

Besides meteoroid ejection due to cometary sublimation, there are a few other potential mechanism of mass shedding from the surface of small bodies (e.g., Jewitt, 2012) such as impact ejection, rotational instability, electrostatic forces, thermal fracture and radiation pressure sweeping. However, in this work we limit ourselves to cometary sublimation as the most likely

mechanisms of formation of the narrow core of the Quadrantids.

2.3.1   Cometary sublimation

Presently, the meteoroid production mechanism due to cometary volatiles sublimation is relatively well understood, see e.g. (Whipple, 1951; Jones, 1995; Crifo and Rodionov, 1997; Ma et al., 2002; Hughes, 2000). All meteoroid ejection models to a great extent share the same physical concepts although with slight modifications.

Perhaps the very first meteoroid ejection model came with the pioneering work done by Fred Whipple (Whipple, 1951), when he proposed his "icy-conglomerate" ("dirty snowball") comet nucleus model. In his model, the comet nucleus consists of frozen volatiles - ices with solid refractory particles embedded within the ice. Once the comet nucleus is close enough to the Sun, e.g 3 AU (Delsemme, 1982), the cometary ices begin to sublimate, releasing and dragging along the embedded dust particles. In Whipple's model, the meteoroids leave the surface of the comet with speeds:

$$V_{\text{ej}} = 25.4\ r^{-1.125}\rho^{-1/3}R_c^{1/2}m^{-1/6}\ \text{(m/s)} \qquad (2.2)$$

where the r is the heliocentric distance in AU, ρ is the density of the meteoroid in kg/m^3, m is the mass of the meteoroid in kg and R_c is the radius of the comet in km. However, one major disadvantage of Whipple's model, later improved by Jones (1995), is the assumption of blackbody limited temperature of the comet nucleus. Moreover, Jones (1995) considered an adiabatic expansion of the escaping gas, i.e the sublimation of the ices results in cooling of the comet's surface. The terminal speed of the particles, leaving the surface of the comet, according to Jones (1995) is:

$$V_{ej} = 29.1\ r^{-1.038}\rho^{-1/3}R_c^{1/2}m^{-1/6}\ \text{(m/s)} \qquad (2.3)$$

where the variables and the units are the same as in Eq.2.2.

One major shortcoming of Jones' model is the assumption that the entire nucleus is active. Direct imaging of the nucleus of comet 1P/Halley, by *Giotto* and *Vega* comet probes, showed that the sublimation of the nucleus is confined to a small fraction of the cometary surface. Nonetheless, a close inspection of Eq. 2.3 shows that the latter expression is very similar to that derived by Whipple. This indicates that accounting for the adiabatic expansion of the escaping gases and eliminating the blackbody nucleus limitation yields little difference in the final result for the terminal velocity of the ejected meteoroids.

More recently, in their work of modeling the dynamical evolution of the Perseid meteoroid stream, Brown and Jones (1998) used a slightly modified version of the Jones (1995) ejection

speed as a function of the heliocentric distance. Moreover, the probability of particles having ejection speed $P(V - V_{ej})$ was assumed to be a parabolic distribution, where the meteoroid ejection directions are distributed isotropically on the sunlit hemisphere. Regarding the meteoroid production, we follow Kresak (1976), where the production rate is uniform in true anomaly (v). According to Brown and Jones (1998), the terminal speed at which the meteoroids leave the surface of the comet is given by:

$$V_{ej} = 10.2 \, r^{-0.5} \rho^{-1/3} R_c^{1/2} m^{-1/6} \; \text{(m/s)} \tag{2.4}$$

with ejection probability distribution:

$$P(V - V_{ej}) = 1 - \left(\frac{V}{V_{ej}} - 1 \right)^2 \; \text{with } 0 < V < 2V_{ej} \text{ and 0 outside} \tag{2.5}$$

where $P(V - V_{ej})$ is the probability of finding a meteoroid with ejection speed V.

In the beginning of 21st century, several interesting works appeared in which authors attempted to infer the ejection speeds of meteoroids causing a meteor outburst at the Earth. Observations of the profile of the shower, given the meteoroids were released at a certain perihelion passage of the parent, can be used to analytically solve for the ejection conditions from the parent. The method has extensively been applied to the 1999 Leonid outburst (e.g., Göckel and Jehn, 2000; Ma and Williams, 2001; Müller et al., 2001)). This approach, however, has its limitations i.e the meteoroids producing the outburst must be large (mm - cm) and originate from relatively young meteoroid trails e.g., a few orbital periods (Asher, 2008). The ejection conditions for much older meteoroids are more difficult (almost impossible) to be deduced as planetary perturbations, over several orbital periods, become significant thus rendering the recovery of ejection conditions impossible. This method, however, is not suitable for our simulations for a few reasons: first the most probable age of the Quadrantids, based on our backward integrations, (200-300 years $\approx$ 35-55 orbital revolutions of 2003 EH$_1$) renders it impossible to apply the above method. Secondly, we do not have a priori knowledge on the physical properties of the nucleus, as the cometary activity may vary significantly from comet to comet. This method, however, is worth future investigation.

Throughout this work, for our forward modeling, we choose to use the above (Eq 2.4 and Eq 2.5) ejection model by Brown and Jones (1998). We assume that 2003 EH$_1$ has a mean density of ρ_c = 800 kg/m^3 - a typical value for a comet nucleus (Weissman et al., 2004), while for the radius of the parent body we use an average value of R_c = 1 km, see Section 2.2. The meteoroids, on the other hand, are modeled as spherical grains of density ρ = 1900 kg/m^3 (Babadzhanov, 2002), where only the radius of the particles is allowed to vary (Section 2.5.3). Due to the present lack of cometary activity on 2003 EH$_1$, we assume it to be relatively depleted

of volatiles such as: CO, CO_2, CH_4, NH_3 etc. and thus comprising mostly of water ice (if any) and embedded refractory material (meteoroids). The water ice begins to sublimate at a heliocentric distance of roughly $r = 3$ AU (Delsemme, 1982), thus the meteoroids, in our simulations, will be released from 2003 EH_1 on an arc of the orbit within 3 AU from the Sun, centered at the perihelion of 2003 EH_1. For example, assuming an orbit similar to that of 2003 EH_1, see Tab 2.2, and meteoroid ejection model that of Brown and Jones (1998), the magnitude of the ejection speed of a meteoroid, with bulk density of $\rho = 1900$ kg.m^{-3} and mass $m = 7.6 \times 10^{-9}$kg (corresponding to a radius of 1 mm), will be $V_{ej} \sim 18$ m/s at $r= 1$ AU, $V_{ej} \sim 8.8$ m/s at $r= 2$ AU and $V_{ej} \sim 5.8$ m/s at $r= 3$ AU.

Model	ρ_c (kg.m^{-3})	R_c (m)	ρ_m (kg.m^{-3})
BJ98-1	800	600	2000
BJ98-2	800	1900	2000
BJ98-3	800	600	1500
BJ98-4	800	1900	1500
BJ98-5	800	1000	1500

Table 2.2: Five different variations of the "BJ98" (Brown and Jones, 1998) model. The bulk density of 2003 EH_1 is assumed to be 800 kg/m^3 while varying the bulk density of the meteoroids and the radius of the parent.

2.4 Observational Data

In our study, we use the orbital data of eight high-precision Quadrantids, photographed from multiple stations by the Czech part of the *European Fireball Network* ("EN"), (Spurný, 1994; Spurný et al., 2007). In addition to these bright photographic Quadrantids, we also use five core radar Quadrantids observed by the *Canadian Meteor Orbit Radar* (CMOR) (Jones et al., 2005), which sample the smaller members of the stream (milligram size). These Quadrantids were backward integrated and their orbit compared with that of 2003 EH_1 to search for epochs of close encounters which might indicate when the material forming the young core of the stream was released.

2.4.1 Photographic Quadrantids

Five out of the eight photographic Quadrantids pertain directly to the narrow portion of the stream, as they have been observed within a degree from the peak ($\lambda_\odot = 283.2°$), which we refer to as "core Quadrantids". The remaining three lie slightly outside of the core of the stream with two extreme cases being Dec. 31 ($\approx 3°$ from the peak) and Jan. 8 ($\approx 4.2°$) (see Table 2.3).

Meteors observed a few degrees away from the peak of the Quadrantid shower are referred to as "non-core Quadrantids".

These bright meteors are of an exceptional importance in our simulations, as their photometric mass (gram-kilogram) implies that the effect of the solar radiation pressure on these meteors, given the timescale of our simulations of a few hundred years, would be negligible. However, the mass of each individual photographic meteoroid can be uncertain by a factor of 3 due to our poor knowledge of the value of the *luminous efficiency* τ, used for the estimation of the ablated mass. Thus, in order to ensure that the effect of the solar radiation pressure has properly been taken into, we consider a wide range in the β - parameter, where $\beta = F_R/F_G$ is the ratio of the solar radiation pressure to the solar gravity (Section 2.5). The assumed values for the β - parameter are: $0, 10^{-3}, 10^{-4}, 10^{-5}$. The aim is to encompass the entire possible range in β, because of the a priori uncertainty in the mass of the meteoroids. The magnitude of β can be expressed as:

$$
\begin{aligned}
\beta &= \frac{F_R}{F_G} \approx 3.54 \times 10^{-5} \frac{Q_{pr}}{m_o^{1/3} \rho^{2/3}}, \quad \text{("cgs" units)} \\
\beta &= \frac{F_R}{F_G} \approx 3.54 \times 10^{-4} \frac{Q_{pr}}{m_o^{1/3} \rho^{2/3}}, \quad \text{("SI" units)}
\end{aligned}
\tag{2.6}
$$

where, for instance, a spherical meteoroid of mass 1 gram and bulk density of $\rho = 1.9$ g/cm^3 has $\beta \approx 2.3 \times 10^{-5}$. It is evident that the larger meteoroids are less susceptible to the solar radiation pressure and in fact, for bolides (kilogram size) β can safely be assumed to be zero.

Except the photometric mass, the quality of the data for each individual photographic Quadrantid is exceptionally good, with the uncertainty in the speed (before the atmospheric entry) ranging between ≈ 0.05-0.5 %, whereas the radiant position is known to $\approx 0.02°$. Unlike other authors who use the mean orbital elements of the Quadrantids as the starting point for integrations, we use these high precision observable and measurable quantities i.e the geographic coordinates and speed of a point on the meteor trajectory and the radiant coordinates. These quantities can directly be translated into geocentric state vectors for each observed Quadrantid providing a high precision initial osculating orbital elements used in our backward simulations.

2.4.2 Radar Quadrantids

Radar observations of the Quadrantid meteor shower have been reported by several authors since 1947 (Hawkins and Almond, 1952); with some major studies carried out by e.g. Hawkins and Almond (1952); Millman and McKinley (1953); Poole et al. (1972). Radar observations can be conducted even during daytime and overcast weather, and can detect meteoroids of much

Meteor Number	Date (UT)	λ (°)	φ (°)	h (km)	m∞ (g)	R.A (°) (J2000.0)	Dec. (°) (J2000.0)	V∞ (km/s)	a (AU)	e	i (°)	ω (°)	Ω (°)
Core Quadrantids													
EN030109	2009-Jan-3 18:19:14.461	11.1406 ±0.0003	48.95368 ±0.00005	93.29 ±0.02	1200	227.38 ±0.04	52.03 ±0.01	42.57 ±0.02	2.86 ±0.01	0.656 ±0.002	72.18 ±0.03	176.66 ±0.06	283.3930
EN040180	1980-Jan-4 17:07:34	16.05305 ±0.00004	50.12508 ±0.00001	93.30 ±0.01	1.9	232.28 ±0.02	50.40 ±0.01	41.92 ±0.10	2.79 ±0.05	0.650 ±0.005	70.98 ±0.08	168.51 ±0.08	283.7938
EN030189	1989-Jan-3 4:27:10	14.9824 ±0.0001	48.6881 ±0.0001	93.53 ±0.01	2.3	235.90 ±0.07	49.67 ±0.03	40.3 ±0.3	2.82 ±0.15	0.656 ±0.02	66.6 ±0.3	164.6 ±0.3	283.7938
EN040192	1992-Jan-4 2:48:30	15.98771 ±0.00002	49.92328 ±0.00001	91.33 ±0.01	80	227.38 ±0.02	49.96 ±0.01	42.54 ±0.07	2.71 ±0.03	0.637 ±0.004	71.87 ±0.08	174.45 ±0.04	283.1019
EN040111	2011-Jan-4 3:19:43	15.98771 ±0.00002	49.92328 ±0.00001	91.33 ±0.01	70	232.53 ±0.03	49.67 ±0.01	41.1 ±0.3	2.21 ±0.14	0.642 ±0.018	68.7 ±0.3	167.7 ±0.2	283.2498
Non-core Quadrantids													
EN311210	2011-Dec-31 3:21:49.71	14.39278 ±0.00040	47.37932 ±0.00023	93.71 ±0.03	650	226.77 ±0.14	51.11 ±0.02	42.32 ±0.17	2.88 ±0.09	0.659 ±0.011	70.0 ±0.2	173.10 ±0.18	279.1733
EN060111	2011-Jan-6 4:36:52.65	16.51110 ±0.00035	48.29288 ±0.00025	80.18 ±0.05	30	227.02 ±0.08	49.86 ±0.08	42.6 ±0.3	2.47 ±0.12	0.602 ±0.019	71.9 ±0.3	178.72 ±0.18	285.3437
EN080179	1979-Jan-8 3:43:55	15.61535 ±0.00007	48.96701 ±0.00005	98.02 ±0.02	60	233.53 ±0.08	48.55 ±0.08	43.21 ±0.3	3.73 ±0.12	0.738 ±0.019	71.61 ±0.18	170.41 ±0.10	287.5665

Table 2.3: Data for eight high precision Quadrantids, photographed from multiple stations by the Czech part of the *European Meteor Network*. The table is divided into two parts, *core Quadrantids* - observed within a day of the peak of the shower and *non-core Quadrantids* - observed within a few days of the peak. The first column is the meteor identification number. The second column is the date and time of observation in (UT). The third, fourth and fifth columns are the the geographic position of a point on the meteor trajectory (geographic longitude λ, geographic latitude φ and altitude h with respect to the sea level). The mass of the meteoroid is given in the sixth column. The seventh and eighth columns are the geocentric radiant position for (J2000.0) - Right Ascension α and Declination δ, followed up by the pre-atmospheric speed V∞ of the meteoroid (ninth column). The last five columns correspond to the heliocentric orbital elements (J2000.0) - semi-major axis (a), eccentricity (e), inclination (i), argument of perihelion (ω), and longitude of ascending node (Ω). All uncertainties are one σ.

smaller sizes (milligram size) than those responsible for the visual meteors (gram-kilogram). Radar observations of the Quadrantids complement visual measurements as the shower peaks in early January when weather conditions are often poor in the northern hemisphere.

CMOR is a triple-frequency multi-station meteor radar system (17.45, 29.85, 38.15 MHz), with the main station located near Tavistock, Ontario, Canada (43.264 N, 80.772 W), and five other remote sites, recording $\sim$ 4000 orbits per day. Using the time delay for common echoes between stations and echo directions of the received signal at the stations, a meteor's speed and atmospheric trajectory can be determined. While single station operation registers echoes (where only echo direction and ranges from the main site are measured) and provides some physical information about the meteoroid, a multi-station detection allows for the determination of a meteoroid's heliocentric orbit (e.g., Webster et al., 2004; Jones et al., 2005; Weryk and Brown, 2013).

During the 2013 campaign, CMOR measured $\approx$ 1440 radar Quadrantids orbits (with masses of the order 10^{-3} - 10^{-4} grams). Out of that list, we have selected 31 Quadrantids with heights above 100 km, to minimize atmospheric deceleration, and fractional error in the semi-major axis $da/a < 0.1$. Of the 31 preliminary selected Quadrantids, we extracted only 5 with highest signal-to-noise ratio echoes, as well as the least uncertainty in the atmospheric velocity $\approx$ 1% where all uncertainties were found using a Monte Carlo routine approach (Weryk and Brown, 2012). Table 2.4 lists the observed geocentric quantities and radiants for these high-quality radar orbits.

While the velocity is known to $\approx$ 1% in our data set, the mass estimate of the meteoroid is more uncertain. The ablated mass is a function of the speed of the meteoroid V in the atmosphere and the *electron line density q* (Verniani, 1973) created by collisions of the evaporated meteoric atoms with atmospheric molecules. The major uncertainty in the mass arises from the uncertainty in the electron line density q, which translates into an error in the mass of a factor of 3 (Weryk and Brown, 2012). For a bulk density of a meteor of ρ =1.9 g/cm^3 (Babadzhanov, 2002) and mean value for the mass of radar Quadrantids $m \approx 3 \times 10^{-3}$ grams, see Table 2.4, this yields for a typical β - parameter for a radar meteor $\beta \approx 1.6 \times 10^{-4}$, if we use for the *scattering efficiency* $Q_{pr} = 1$. Even if the mass for a radar Quadrantid was uncertain by a factor of 3, that would translate in error for the β - parameter $\beta \approx 2 \times 10^{-4}$ and $\beta \approx \times 10^{-4}$ for an under and overestimated mass, respectively. These last results confirm that we can safely use values for $10^{-5} < \beta < 10^{-3}$, in order to encompass the entire possible mass range of the radar Quadrantids.

Date	Time (UT)	λ (°)	ϕ (°)	h (km)	$m_\circ$ $\times 10^{-3}$ (g)	$\lambda_\odot$ (°)	α (°)	δ (°)	V_∞ (km/s)	a (AU)	e (°)	i (°)	ω (°)
								(J2000.0)					
20130103	09:11:22	-82.23	43.22	100.863	1.1	282.98	224.2	46.9	42.2 ±0.7	1.81 ±0.07	0.466 ±0.023	74.44 ±0.41	173.4 ±1.7
20130103	20:08:57	-79.47	43.55	101.482	1.7	283.44	230.5	48.4	40.2 ±0.8	2.01 ±0.04	0.512 ±0.011	69.84 ±0.15	168.1 ±0.5
20130103	20:26:56	-80.47	42.83	100.678	0.6	283.45	230.1	48.7	40.9 ±0.1	2.22 ±0.06	0.559 ±0.012	70.56 ±0.2	169.8 ±0.3
20130103	20:50:27	-78.52	44.25	103.118	5.5	283.47	224.1	46.8	41.5 ±0.1	1.87 ±0.11	0.476 ±0.031	73.43 ±0.59	171.6 ±2.1
20130104	06:16:11	-80.95	42.91	103.046	5.7	283.87	235.1	53.6	39.7 ± 0.3	1.91 ±0.07	0.488 ±0.021	68.23 ±0.37	171.2 ±0.4

Table 2.4: Data for five high quality radar Quadrantids, belonging to the narrow core of the stream, observed by CMOR during 2013. The columns represent the date of observation, time, geographic longitude λ, latitude ϕ and height h above the ground of point on the meteor trajectory, mass $m_\circ$ of the meteoroid, the solar longitude at the time of observation $\lambda_\odot$, geocentric right ascension α and geocentric declination δ of the radiant position and the speed V_∞ of the meteoroid above the Earth's atmosphere. The last four columns are the computed heliocentric orbital elements of the meteoroid, semi-major axis a, eccentricity e, inclination i and argument of perihelion ω. The average uncertainty in the radiant position is ± 0.2°.

2.5   Numerical Simulations

We explicitly assume that the parent body of the Quadrantids is the asteroid 2003 EH$_1$. For each individual Quadrantid, (see Table 2.3 and 2.4), we create 10^4 hypothetical clones with orbits similar to each individual Quadrantid (see Section 2.5.1). We then numerically integrate the equations of motion of all clones, along with the parent, backwards in time (Phase 1). Once the most probable formation epoch has been established, via these back integrations, then that time window is used for meteoroid ejection and forward in time integration of test particle orbits until the present (Phase 2).

2.5.1   The "clones"

The key point is to integrate the equations of motion of a large number of hypothetical meteoroids (clones) of a Quadrantid observed in the present epoch, along with the presumed parent body, backwards in time and to statistically attempt to determine the epoch of minimum distance between their orbits. This approach is more reliable rather than trying to locate the nearest epoch, back in time, when the parent and the meteoroid actually physically intersect. The latter event is very unlikely to occur, due to the inherent uncertainties in the position and velocity of the bodies, as well as computational errors (truncation and round-off) throughout numerical integrations. Even though the two bodies are seen to intersect in the simulations, that does not necessarily imply that we have identified the epoch of meteoroid release, due to the reasons mentioned above. A simple example can be used to demonstrate that even if one has calculated the semi-major axis a of a meteoroid orbit with an uncertainty of e.g $a \pm da = 2.855 \pm 0.013$ AU (as in the case of meteor EN030109 Table 2.3), over several revolutions of the meteoroid about the Sun, the uncertainty in its position will dramatically increase. Using and differentiating Kepler's third law, it can be demonstrated that;

$$dT = \frac{3a^{1/2}da}{2\sqrt{1-\beta}}, \tag{2.7}$$

where dT is the absolute uncertainty of the period of an orbit around the Sun. This yields a relative uncertainty of $dT/T \approx 7 \times 10^{-3}$ even for $\beta = 0$, corresponding to $dT \approx 12$ days per period or one orbit within ≈ 700 years, comparable to the time scales considered here. It is noteworthy that absolute uncertainty in dT increases for finite values of β. Thus, the data is not precise enough to determine when the meteoroid and the parent actually intersect: such studies will have to await even higher quality measurements. Nonetheless, we can use the intersection of the meteoroid and parent orbits to examine when such ejection could have occurred, as this is a necessary condition for meteoroid stream production.

For our study, for each observed Quadrantid we create 10^4 hypothetical clones, randomly selected from a six-dimensional Gaussian distribution of the six directly observed and measured quantities: geocentric radiant coordinates (α, δ), the geographic longitude, latitude and altitude (λ, ϕ and h) and the observed velocity at a point on the meteor trajectory (V_{obs}). These values can be translated directly into the initial heliocentric state vectors $\{V_{ix}, V_{iy}, V_{iz}\}$ and $\{X_i, Y_i, Z_i\}$ of each clone and are used as initial conditions for our backwards numerical integrations of the equations of motion. Each dimension of the six-dimensional Gaussian, is centered around the nominal values with one standard deviation 1 σ being equal to the magnitudes of the uncertainties of the initial variables (see Table 2.3). However, at the time of our simulations, we do not have information about the covariance between the errors in our initial condition quantities, thus we assume that the errors are uncorrelated, which may not be the case.

2.5.2   Phase 1: Backward integrations

The equations of motion of each clone along with the parent are then integrated backwards in time for 1000 years. The length of the backward integrations of 1000 years is chosen on the basis of the assumption of relatively young age of the central portion of the Quadrantid meteoroid stream (Jenniskens et al., 1997; Wiegert and Brown, 2005) and because we found that similar Quadrantid orbits in the current epoch integrated back in time, do not start to significantly disperse until $\approx$ 1300 AD. In addition, we aimed to check whether the age of the core of the Quadrantids could be as old as 500 - 1000 years as previously argued by some authors e.g. (Jenniskens et al., 1997; Williams and Wu, 1993). We note that integration for 1000 years back in time is beyond the Lyapunov time, however the mean orbital elements of the clones of 2003 EH$_1$, at the epochs of 1000 AD and 1500 AD, are used for forward integrations in order to compare the theoretical characteristics of core of the Quadrantid stream against the observed ones. Effectively, we explore whether the observed characteristics of the core of the Quadrantids can be explained by meteoroid ejections from 2003 EH$_1$ circa 1000 AD or 1500 AD. However, the results from forward integrations should be treated with caution, in particular when the initial orbital elements of the parent have been selected from backward integration beyond the Lyapunov time. Therefore, the results must be treated from a statistical point of view.

Throughout the integrations, we consider the perturbations on the meteoroids and 2003 EH$_1$ from each planet and also account for the planets' mutual interaction. We used JPL's "DE405" version of the planetary ephemeris for generating the initial positions of planets. The mutual interactions among the meteoroids and 2003 EH$_1$ are neglected, i.e they are considered

as test particles. Throughout the integrations we use Everhart's RADAU algorithm (Everhart, 1985). During the first 30 days of the integration of the orbits of the clones, i.e. when the meteoroid is in the Earth's vicinity (several Hill radii, where the Hill radius of the Earth ≈ 0.01 AU), we use a fixed time step of 1 minute, with the gravitational influence of the Moon being separately taken into account. When the meteoroid is sufficiently far away from the Earth, we then increase the time step from 1 minute to 1 day (from -30 days to -1000 years) in order to speed up the integrations. The orbital elements for each hypothetical clone and 2003 EH_1 are output at every 10 years. Furthermore, for all meteoroids, except for EN30109 (the largest at ≈ 1.2 kg.), we examine four different values for the ratio of the solar radiation pressure to the solar gravity "β - parameter", $\beta = 0, \beta = 10^{-3}, \beta = 10^{-4}$ and $\beta = 10^{-5}$.

Throughout the backward integrations, we numerically compute the minimum distance between the orbits (MOID) (see Appendix D) of each clone and the parent 2003 EH_1. The aim is to statistically determine the epoch when the MOID between each observed Quadrantid and asteroid 2003 EH_1 was at a minimum. We assume that the spreading time in the mean anomaly e.g., ≈ 100 years for JFCs and NEOs (e.g., Tancredi, 1998) is much shorter than the spreading time in the other orbital elements. Backwards integrations within a few Lyapunov times can reliably provide information on the minimum distance between the orbit of the parent and each Quadrantid, though longer ones may not. Our numerically calculated Lyapunov time for asteroid 2003 EH_1 is ≈ 80 years which is consistent with the values for JFC and NEOs found by Tancredi (1998)).

In addition to the computation of the MOID between the parent and each Quadrantid, we also used the standard orbital similarity functions D_{SH} (Southworth and Hawkins, 1963) and D' (Drummond, 1981), between the orbits of the parent and each clone as a check on our MOID results and found similar behavior. In an attempt to identify a probable formation mode of the core of the Quadrantid stream, we also compute the true anomaly θ at the MOID of the orbit of 2003 EH_1 and each clone. Meteoroid ejection due to cometary ice sublimation must be confined within an arc of the orbit when the parent is sufficiently close to the Sun, i.e within $r = 3$ AU. The backwards integrations of the equations of motion for the parent, 2003 EH_1, indicate that its orbital elements do not vary dramatically over 200 years from their present values. If the narrow portion of the Quadrantids was created through cometary meteoroid ejection around 1800 AD, that must had happened within an arc of $\theta \approx \pm 130°$ from perihelion which is roughly equivalent to a heliocentric distance of $r \approx 3$ AU.

In order to further constrain the meteoroid release mode, we also compute the relative velocity between the parent and each clone at the MOID. The aim is to compare whether the ejection velocities within the arc of water ice sublimation are consistent with cometary dust ejection speeds (see Section 2.3). Although, all meteoroid ejection models yield slightly

different ejection velocities (a few tens to few hundred m/s), nonetheless they all agree that the latter are unlikely to exceed ~ 1 km/s. Thus, if the relative velocity between the parent, 2003 EH_1, and each observed Quadrantid is within few-hundreds m/s, we may argue for cometary origin of the core of the Quadrantid stream.

2.5.3   Phase 2: Forward integrations

Using the results of the backward integrations to provide a time window for the likely formation epoch of the core of the Quadrantid meteoroid stream, we next use ejection models (described below) to generate a hypothetical meteoroid stream and integrate the equations of motion of the meteoroids forward in time.

Based on the results of Phase 1, we assume that meteoroid ejections took place between 1700 AD and 1900 AD, and we use this time window to eject meteoroids from the parent 2003 EH_1 between 1700 - 1900 AD. We explicitly assume that parent, 2003 EH_1, was an active comet prior to 1900 AD, supplying meteoroids to the Quadrantid meteoroid stream, and that activity ceased after the beginning of 20th century. The latter assumption will be motivated by our backwards integrations as described later. Thus, we effectively test the hypothesis whether meteoroids ejected during between 1700 - 1900 AD could reproduce the presently observed narrow structure of the Quadrantid stream (see Section 4.4 for details).

We first test what is the most likely epoch at which meteoroids have to be released from 2003 EH_1, so the resulting meteoroids start intersecting the Earth's orbit around 1835 AD i.e when the stream was first noticed. For this purpose, we eject 10^4 meteoroids, of both radar ($100\mu m$ - 1 mm) and visual sizes (1 mm - 1 cm), at various epochs as a single outburst from the parent and propagated their equations of motion forward in time. The ejection model that we used for the single outburst meteoroid ejection is the one by Brown and Jones (1998), described in Section 2.3. We note here that the epochs at which radar and visual size meteoroids are released from the parent so they can reach the Earth around 1835 AD are slightly different. This is due to the different orbital evolution of micron and centimeter sized meteoroids, for which the the magnitude of the solar radiation pressure force is different. Once the "correct" time window of meteoroid release has been identified (i.e the resulting meteoroids reach the Earth around 1835 AD), we then use that time window as a starting point for continues meteoroid ejection over multiple perihelion returns of 2003 EH_1. In the case of visual size particles this time window is between 1780 - 1786 AD, whereas for radar size meteoroids it is between 1790 - 1796 AD (see Section 4.4).

In the case of meteoroid ejections over multiple perihelion returns of the 2003 EH_1, 10^4 meteoroids are released at each perihelion passage of the parent (within an arc of 3 AU, cen-

tered at the perihelion of 2003 EH_1), both at radar and at visual sizes, to compare with both observation techniques. The meteoroid ejection speeds considered are described in Section 2.3. The number of particles, in a given size bin, were chosen uniformly in the logarithm of the size. During the integrations, the orbital elements, the resultant radiant position and geocentric velocity for the meteoroids are computed for each day. That allows us to closely examine the activity profile of the resultant stream as a function of the meteoroid size, i.e radar and visual meteors, and compare it with the observed activity profile, radiant position and dispersion and geocentric speed.

We would like to note, that we also performed sample simulations assuming the extreme values for the radius of 2003 EH_1, i.e R_c =2 km (see Section 2.2) as well as the density of the meteoroids within 0.8 g/cm^3 < ρ < 3 g/cm^3. However, the variation of the radius of the parent, did not show a noticeable difference in the final results. Furthermore, we also repeated the simulations with all variables as above, i.e parent's radius and density of meteoroids, number of meteoroids ejected per perihelion return of 2003 EH_1, meteoroid masses and β-values etc., thus replacing only the ejection speed model with the one resulting from hydrodynamical study of the cometary circum-nucleus coma by (Crifo et al., 1995; Crifo and Rodionov, 1997). The latter model is generally known to yield slightly lower meteoroid ejection speeds, as compared to e.g Whipple (1951); Brown and Jones (1998). Effectively, this allowed us to test the significance of the magnitude of the ejection speeds on our final results, keeping all other parameters same as above. However, the overall results did not show a modest difference, thus implying that the considered ejection model has negligible effect on the final results, over the time scale of integrations we are concerned with. We thus, did not see any strong reason to further investigate which ejection model e.g. Brown and Jones (1998) should be considered over another e.g. Crifo et al. (1995); Crifo and Rodionov (1997). Therefore, in this work we only present the results from the simulation, carried out assuming meteoroid ejection speeds modeled by (Brown and Jones, 1998).

2.6 Results

2.6.1 Phase 1: Meteoroid release epoch

In Phase 1, we integrated 10^4 hypothetical clones backwards for each observed Quadrantid (eight photographic and five radar). For brevity we show the results, from backward integrations, for only three core and two non-core Quadrantids. Moreover, we show the results for only $\beta = 0$, as the other instances of β yielded similar outcomes. The simulations are thus almost insensitive to the meteoroids' mass range, given the time scale of our simulations. De-

spite solar radiation pressure force being non-negligible for micrometer and millimeter sized particles, we do not find that modestly larger beta values noticeably change the final results.

Fig. 2.4 shows the evolution of the MOID (left panels) and the relative velocity at the MOID (right panels), between the orbits of 2003 EH$_1$ and 10^4 clones, for three core Quadrantids. The y - dimension of each pixel in Fig. 2.4 is equal to ∼ 0.005 AU in the left panels and ∼ 0.01 km/s in the right panels, whereas the x-dimension is 10 years. It is clearly seen, from Fig. 2.4, that the MOIDs between the clones of each integrated core-Quadrantid and 2003 EH$_1$ show a deep minimum ≈ 200 - 300 years before the present (≈ 1700 - 1800 AD), with little dispersion in the MOID at that particular epoch. The same general tendency of the MOID, with a minimum between 1700 AD -1800 AD, was observed even for particles with extreme values of $\beta = 10^{-3}$.

Similarly, Fig. 2.6 shows the evolution of the MOID (left panel) and relative velocity at the MOID (right panel), as above, for "non-core" (observed outside the narrow peak of the stream) meteoroids. Unlike core-Quadrantids, their non-core counterparts did not show an obvious minimum of the MOID. The exception was non-core meteor number EN060111 which did show a weak minimum in the MOID around 1650 AD but with a relatively high dispersion. We suggest that the non-core Quadrantids are much older, though the Lyapunov times are such that longer backwards integrations to confirm this hypothesis are problematic.

As an additional test as to the age of the core of the Quadrantid stream, we also computed the standard similarity functions D_{SH} (Southworth and Hawkins, 1963) and D' (Drummond, 1981), between the orbits of the clones of each individually observed core-Quadrantids and 2003 EH$_1$ Fig. 2.5. However, here we present the results for only 3 bolides, EN030109, EN040180 and EN040192. The results for the rest of the core-Quadrantids yielded similar results. The size of each pixel in the left panels is $\delta x = 10$ years, $\delta y = 0.01$, whereas in the right panels (D' criterion) $\delta x = 10$ years, $\delta y = 0.005$. Both similarity criteria yielded an unambiguous deep minimum between 1700 - 1800 AD, similar to the MOID criterion, for the core-Quadrantids. However, in the case of non-core Quadrantids there was not a clear minimum of the similarity function, the results which we have omitted here.

The effect of varying the β - parameter had little effect, that is the evolution of both, D_{SH} and D' criteria, yielded a minimum between 1700 - 1800 AD. The latter result is not surprising, given the time scale of our simulations and in particular the time of interest (200 - 300 years), i.e a few Lyapunov times.

We present the results for only one radar core-Quadrantid, since all other cases yielded similar results. From Fig. 2.7 it can be seen that, as in the case of the photographic core-Quadrantids, the minimum value of the MOID between the orbits of the parent and the fictitious clones of meteor 20130103-20:26:56 is reached around 1700 - 1800 AD. The simulations for different β - values also yield similar results. Fig. 2.8 shows the evolution of the orbital
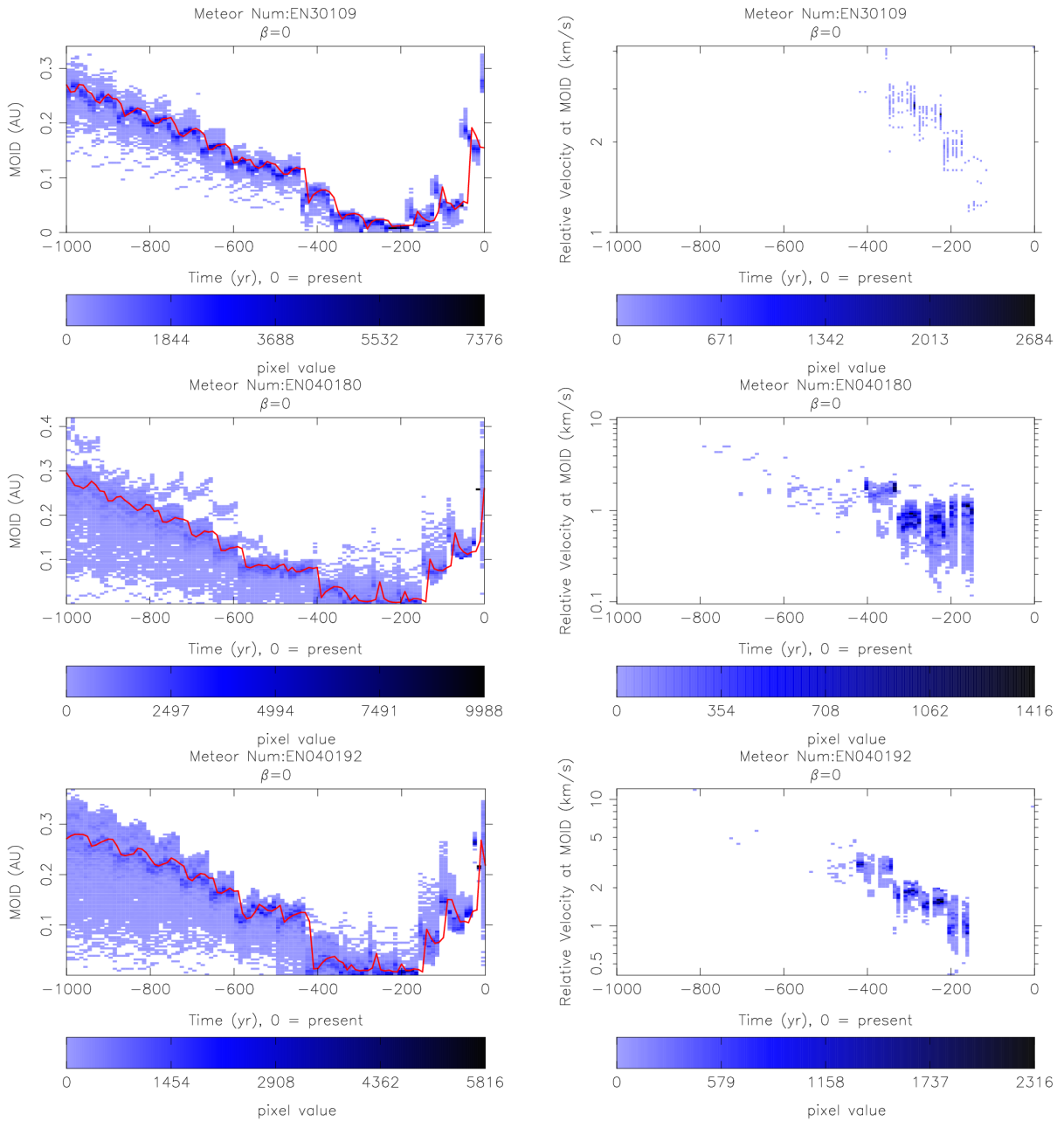
Figure 2.4: The Minimum Intersection Distance (MOID) (left panels) and the relative velocity at the MOID (right panels) between the orbits of asteroid 2003 EH$_1$ and 10^4 clones for each the three photographic meteors, belonging directly to the core of the Quadrantid meteoroid stream. The pixels in the figure are color coded in the hue of the blue color, with a darker blue corresponding to a greater number of clones. The red curve in the right panels corresponds to the median value of the MOID at the given epoch. The relative velocity at the MOID is presented in a logarithmic scale in the panels on the right hand side of the figures. Clones with MOID > 0.01 AU are not plotted in the right hand panels.
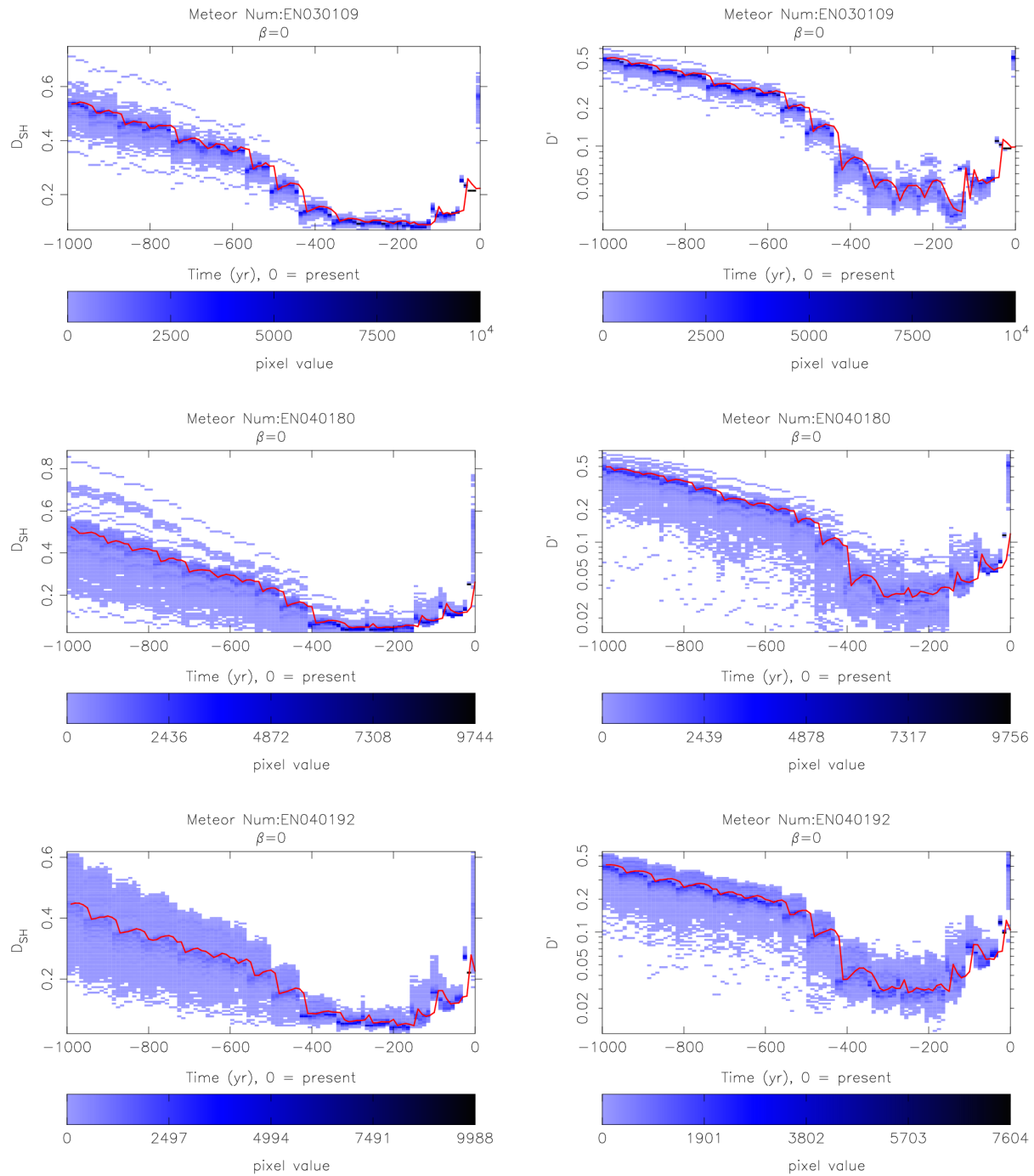
Figure 2.5: The evolution of the similarity criteria, D_{SH} (Southworth and Hawkins, 1963) (left panel) and D' (Drummond, 1981) (right panel), for 10^4 clones of each Quadrantid as a function of time. The red curve corresponds to the median value of the similarity functions, D_{SH} and D', respectively.
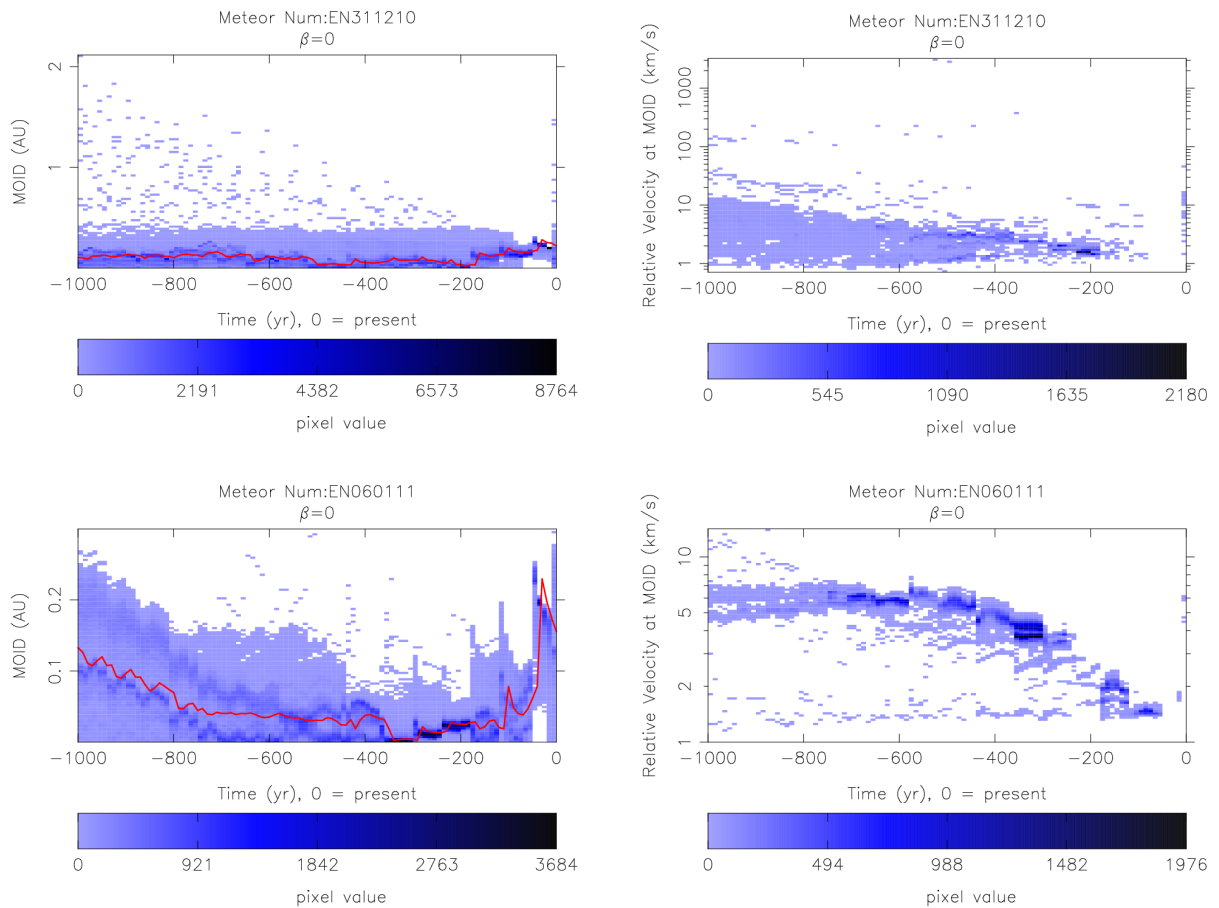
Figure 2.6: The Minimum Intersection Distance (MOID) (left panels) and the relative velocity at the MOID (right panels) between the orbits of asteroid 2003 EH_1 and 10^4 clones for two photographic meteors, not belonging directly to the narrow core of the Quadrantids. Clones with MOID > 0.01 AU are not plotted in the right hand panels.
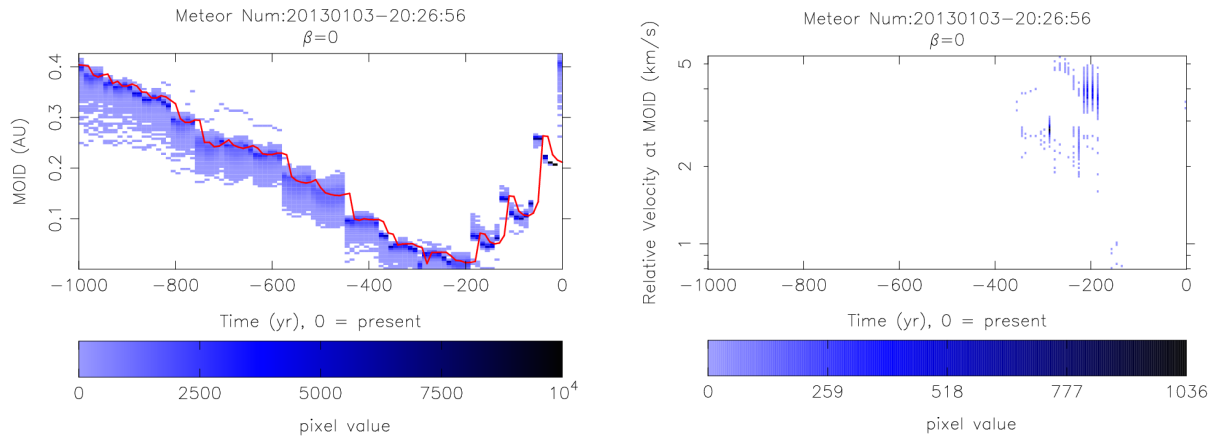
Figure 2.7: Evolution of the Minimum Orbit Intersection Distance (MOID), between the orbit of 2003 EH$_1$ and 10^4 fictitious clones of the radar meteor - 20130103-20:26:56 over a period of one-thousand years. This radar meteor belongs to the core of the Quadrantids. The red curve represents the median value of the MOID at a given epoch. Clones with MOIDs > 0.01 AU are not plotted in the right hand panels.

similarity functions, D_{SH} and D', between 10^4 clones of the radar core Quadrantid 20130103-20:26:56 and 2003 EH$_1$. In this case, the minimum of the similarity criteria was somewhat less obvious but still around 1800 AD. We note that radar orbital measurements are of lower precision compared to photographic or video observations. Nevertheless, the minima of the similarity functions, occurring after 1700 AD supports the hypothesized young age of the core of the Quadrantids.

As was the case with the photographic core Quadrantids, variation of the ratio of the solar radiation pressure to the solar gravity β did not change the overall results for radar meteoroids as to the position of the minima of both similarity functions. The latter result seems to be reasonable, given the time window we are interested in (200-300 years).

All lines of evidence from the backward integrations in Phase 1 point strongly to an origin in the past 200-300 years for the core Quadrantids.

2.6.2   Phase 1: Formation mechanism of the Quadrantid meteoroid stream

Another goal of this work is to constrain the formation mode of the core of the Quadrantid meteoroid stream. More precisely, we aim to test if it is consistent with the hypothesis of cometary origin.

We recall that existing dust ejection models from comet nuclei suggest that the ejection velocities are much smaller (few tens-hundreds m/s) than the orbital speed of the comet (few tens of km/s at perihelion), with extreme ejection velocities not exceeding 1 km/s (see e.g., (Whipple, 1950, 1951; Jones, 1995; Crifo et al., 1995; Crifo and Rodionov, 1997)).
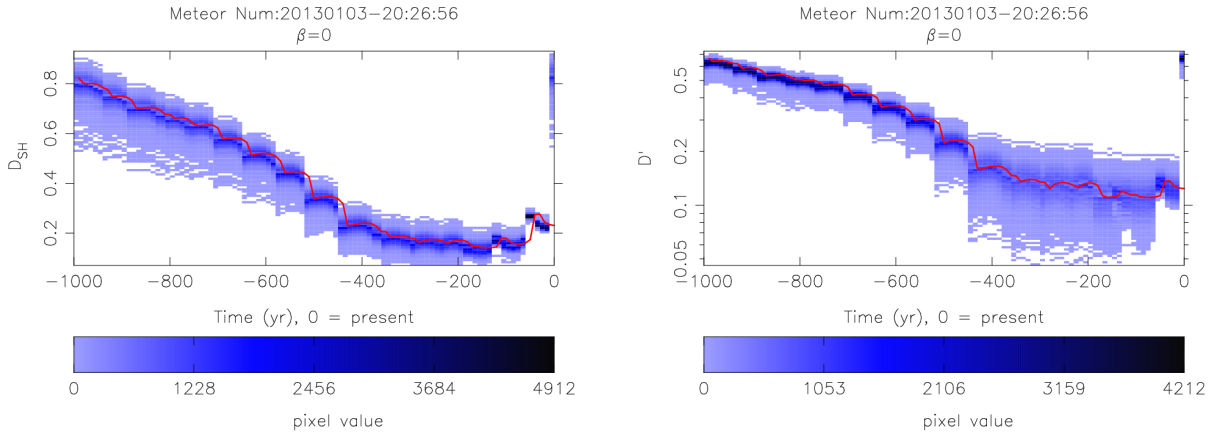
Figure 2.8: Evolution of the orbital similarity criteria, D_{SH} and D', between the orbit of 2003 EH$_1$ and ten-thousand fictitious clones of the radar meteor - 20130103-20:26:56 over a period of one-thousand years. This radar meteor belongs to the core of the Quadrantids. The red curve represents the median value of the similarity functions.

In order to test if the Quadrantid meteoroid stream may have resulted from a cometary activity on 2003 EH$_1$ we follow an approach similar to Gustafson (1989) and Adolfsson (1996), comparing the relative velocity at the MOID between 10^4 clones of each photographic and radar core-Quadrantid and 2003 EH$_1$. It has to be noted, though, that this approach has its limitations and should be used carefully. The uncertainties in all measurements e.g. position of the meteoroids and velocities are finite which over time will tend to increase. Therefore we emphasize that, we utilize this method assuming the age of the ejected meteoroids is less that a few Lyapunov spreading times of the meteoroids along their orbits. Secondly, there are uncertainties in the calculations of the meteoroids' initial (pre-atmospheric) masses, where the latter come into the equations of motion primarily by their β- values. Thus, the results from the simulations must be treated from a statistical point of view. Nevertheless, assuming that the core of the Quadrantid meteoroid stream is relatively young compared to the Lyapunov spreading time, we should be able to approximately constrain its age, treating the results from the backward and forward integrations in a statistical sense.

The results for the relative velocity between 2003 EH$_1$ and 10^4 clones of each photographic Quadrantid is presented in Fig. 2.4 (right panels) and radar Quadrantids in Fig. 2.7 (right panels). The epoch of interest is the one centered between -200 and - 300 years from the present. Relative velocities are computed only for clones with MOIDs less than 0.01 AU from the orbit of 2003 EH$_1$.

During the minimum of the MOID (left panel), the relative velocity at the MOID between the clones of each core Quadrantid and the parent 2003 EH$_1$ range from about 0.1 to 2 km/s. These values are on the high side for cometary ejection processes, as the ejection speeds of meteoroids leaving the surface of 2003 EH$_1$, given the perihelion distance, even for microm-

eter meteoroids are unlikely to exceed 200 m/s. However, the process of generating clones within the uncertainties necessarily generates many incorrect orbits: only one clone within the ensemble is the real particle. Thus, the existence of even one clone with a relative speed at the MOID suggests a possible cometary origin.

The lowest relative velocities within the clones of the core Quadrantids and 2003 EH_1, range from 200 m/s - 800 m/s, with the majority of the clones having relative velocities exceeding 1 km/s. Only 2 clones of bolide EN040180 attained a very low relative speed of $\approx$ 80 m/s while most had speeds as great as a few km/s. We conclude that these results are marginally consistent with cometary ejection processes but can not be used as definitive proof for a cometary sublimation origin for the core of the stream.

Similar results are found for the radar core Quadrantids (Fig. 2.7). Here we see even larger dispersion in the ejection speed from the parent, ranging from 0.8 km/s to $\sim$ 5 km/s, around 1800 AD. However, only between 1 - 4 particles demonstrated relative speeds of 0.8 km/s, while the majority had speeds above 1 - 3 km/s. This result is poorly consistent with the expected meteoroid ejection speed from comets, i.e it is unlikely that meteoroids would leave the surface of the parent with speeds of 800 m/s at a heliocentric distance of 1 AU under cometary sublimation alone. We recall, however, that the errors in the initial values of the position and speed of the radar meteoroids in the Earth's atmosphere are larger than those obtained by photographic observations.

As an additional constraint as to the more likely formation mechanism of the core of the Quadrantids, we also calculated the true anomaly at the MOID, of the orbit of 2003 EH_1, for 10^4 clones of each Quadrantid (see Section 2.5.2). Sublimation of cometary ices must take place closer to the Sun (within $\sim$ 3 AU for 2003 EH_1, assuming sublimation of water ice only).
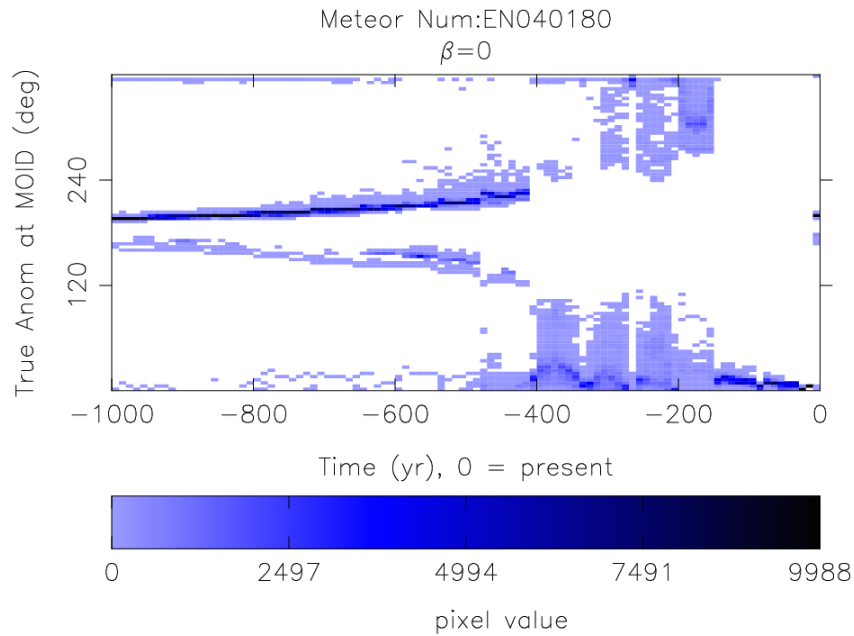
Figure 2.9: The true anomaly of 2003 EH$_1$ at the MOID of 10^4 fictitious meteoroids (clones) of the core-Quadrantid photographic meteor - EN040180 for a time span of 1000 years.
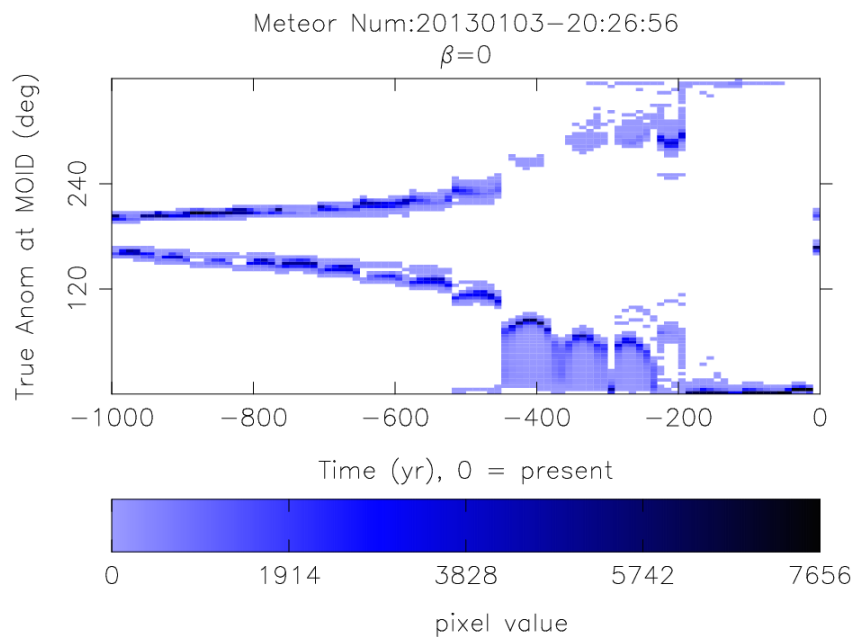
Figure 2.10: The true anomaly of 2003 EH$_1$ at the MOID of 10^4 fictitious meteoroids (clones) of the radar meteor - 20130103-20:26:56, for a time span of 1000 years.

Fig. 2.9 and 2.10 shows the true anomaly at the MOID for ten-thousand clones as a function of time of the photographic meteoroid EN040180 (1.9 g) and radar event 20130103-20:26:56,

both of which are core-Quadrantids. It can be seen that, for the epoch 1800 AD, there is a greater probability that the true anomaly at the MOID, on the orbit of 2003 EH$_1$, was between $v \approx \pm 60°$ from perihelion (translating to a heliocentric distance $r \approx$ 1.3 AU), which is consistent with cometary activity, resulting in meteoroids ejection from 2003 EH$_1$.

Examination of the results for the rest of the photographic and radar meteors in our sample were similar to those in Fig. 2.9 and 2.10, with some showing lower or higher dispersion in true anomaly at the MOID at the epoch of interest (1700 - 1900 AD). The effect of varying the β - value had little effect on the final outcome. The highest median value of the true anomaly at the MOID was $v \approx \pm 120°$ from perihelion (roughly corresponding to a heliocentric distance $r \approx 2.4$ AU). Nonetheless, all results showed a higher probability that the true anomaly at the MOID on 2003 EH$_1$ occurred close to perihelion, consistent with meteoroid ejection due to sublimation of ices.

The location of the MOIDs are certainly consistent with cometary ejection processes, while the relative velocities are low enough in some cases, but not all. Since, it is not possible to know the "true" backward evolution of any of the observed Quadrantid meteoroids, due to the inherent uncertainties in their position and speed, thus if even one clone has relative speed consistent with cometary ejection, it may point to origin consistent with cometary sublimation. We conclude here that cometary ejection processes may be a likely source of the core Quadrantids, or at least that we have sufficient grounds to proceed with forward modeling of the stream under this assumption.

2.6.3   Phase 2: Meteoroid ejection

In order to test the results obtained by backwards integrations, we employ the "direct approach" by ejection of a large number of hypothetical meteoroids from the parent, and integrate them forward in time. By the "direct approach" we test if the observed average physical characteristics of the Quadrantid stream, described in Section 2.1 and 2.2, are consistent with cometary ejection from 2003 EH$_1$ around 1700 - 1900 AD.

We briefly recall the constraints that we are attempting to match by the forward integrations.

1. The timing of the appearance of the stream on the sky (around 1835 AD) (Quetelet, 1839).

2. The mean position and spread of the geocentric radiant of the stream (e.g. (Jenniskens et al., 1997)).

3. The position of the peak of the activity profile of the core (e.g. (Rendtel et al., 1993)).

4. The width of the activity profile of the core (FWHM ≈ 0.6 days) (Hughes and Taylor, 1977; Rendtel et al., 1993; Jenniskens, 2006).

We first show the results for 10^4 meteoroids, ejected from 2003 EH$_1$, at different epochs in a single outburst (at a single point on the orbit). The aim is to obtain a time window as to when meteoroids must be ejected so they can reach the Earth's orbit around 1835 (see Section 2.5.3). Thus, meteoroids ejected prior to that time window will reach the Earth before 1835, i.e when the shower was first observed. Furthermore, we have to identify the epoch of ejection when meteoroids cease reaching the Earth. We then use these time windows for meteoroid ejection, at every perihelion passage in order to closely inspect the characteristics of these synthetic meteor showers.

Fig. 2.11 (upper panels) shows the evolution of the descending nodes of visual size meteoroids ejected from 2003 EH$_1$, in a single perihelion passage, in 1780 and 1786, respectively. Also, Fig. 2.11 (lower panels) show the mean radiant position of the simulated meteoroids, in sun-centered ecliptic longitude $\lambda - \lambda_\odot$ and latitude β. In the figures, only meteoroids having their descending node within 0.01 AU, from the orbit of the Earth are plotted so we can sample only those particle which may intersect the Earth. It is evident that meteoroids ejected prior to 1780 arrive near the Earth's orbit somewhat before 1835 (see Fig. 2.11-a), which is inconsistent with the timing of the shower's appearance (circa 1835 AD). However, it is difficult to argue when exactly meteoroids must had been released from the parent in order to arrive at the Earth at the right time (circa 1835). This is partly due to the unrealistically low number of the simulated particles considered in our simulations, as well as the lack of exact conditions during meteoroid ejection. In fact, in Fig. 2.11-a, although meteoroids ejected in 1780 arrive at the Earth a few decades before the shower's first appearance in the sky (1835), the activity level could had been much lower and the shower could had easily gone undetected. Therefore, we choose to use as initial ejection epoch the year 1780 instead of 1786.

The theoretical radiant position of the meteoroids (Fig. 2.11) is plotted along with the mean observed positions and dispersions of the Quadrantids as obtained by photographic and video meteor surveys. The Southern Ontario Meteor Network (SOMN) Quadrantids were selected as being potential Quadrantids if their radiant was within 5 degrees of the nominal Quadrantid radiant and if their speed was within 10% of nominal Quadrantid speed. Similarly, Fig. 2.11-b shows that meteoroids ejected around 1786 appear at the Earth just slightly after 1835 AD. The slight timing inconsistency is perhaps due to small number statistics. In fact, out of 10^4 particles ejected, only about 30 reach the Earth. Nevertheless, within the statistics considered in our simulations, the time of ejection and first appearance of the stream on the sky is in a good agreement with the minimum of the MOID in the backward integrations (Section 2.5.2). The theoretical radiant position seems to be in a reasonable agreement with the observations by SOMN, although there is slight discrepancy with the DMS photographic and video data (Fig. 2.11-a, b lower panel). Thus particles ejected from the parent in 1786 by cometary pro-

cesses produce a reasonable match with the observed shower properties. However, the descending nodes of meteoroids ejected after 1882 AD start to gradually move outward from the Earth's orbit, and eventually stop intersecting the Earth. The reason for that is the secular precession of the orbital elements, causing the heliocentric distance of the descending nodes of the meteoroids to recede slowly from the orbit of the Earth. Thus the current visual activity of the core of the Quadrantids shower can be explained by cometary activity of 2003 EH$_1$ between the years 1786 and 1882. The parent cannot have been active earlier because the Quadrantids shower would have become active earlier than is recorded in historical records. Whether the parent may have been active after 1882 remains unconstrained, except by the fact that dust production must have eventually diminished to the currently observed inactive state.

Source	$\lambda - \lambda_\odot$ (deg)	β (deg)	$\sigma (\lambda - \lambda_\odot)$ (deg)	$\sigma \beta$ (deg)
Photographic				
—DMS	277.8	63.5	2.4	1.1
Video				
—DMS	278.7	63.6	3.5	0.9
—SOMN	275.8	63.6	6.2	1.7
Radar				
—CMOR	277.2	63.2	6.8	3.1

Table 2.5: Radiant position and dispersion of the Quadrantid meteor shower obtained by photographic, video and radar techniques. The coordinates of the average radiant are given in the sun-centered ecliptic frame - ecliptic longitude $(\lambda - \lambda_\odot)$ and ecliptic latitude β.

Similarly, Fig. 2.12 shows the evolution of the descending nodes of radar size (100 μm - 1 mm) meteoroids, ejected from 2003 EH$_1$ in 1790 AD and 1796 AD. Meteoroids, ejected prior to 1796, appear at the Earth as early as 1800 AD. However, we do not really know when radar size particles first reached the Earth, as the earliest Quadrantid meteor radar observations date back only about six decades. The radiant position Fig. 2.12-a (lower panel) seems to fit well the observed mean Quadrantid radiant as measured by the CMOR. Thus 1796 AD seems to be in a good agreement with the minimum of the MOID, between the orbits of radar meteoroids and that of 2003 EH$_1$ (Section 2.5.2). Meteoroids ejected after 1886 AD, from 2003 EH$_1$, do not presently intersect the Earth's orbit due to, as in the case of visual meteoroids, secular precession of the orbital elements of the meteoroids.

We next present the results of meteoroids ejected over multiple perihelion returns of 2003 EH$_1$ for both, visual and radar size particles. According to our analysis from meteoroid ejections at a single point on the orbit of the parent, we obtained that visual size meteoroids appear and intersect the Earth if ejected roughly between 1780 - 1882 AD, whereas for radar size
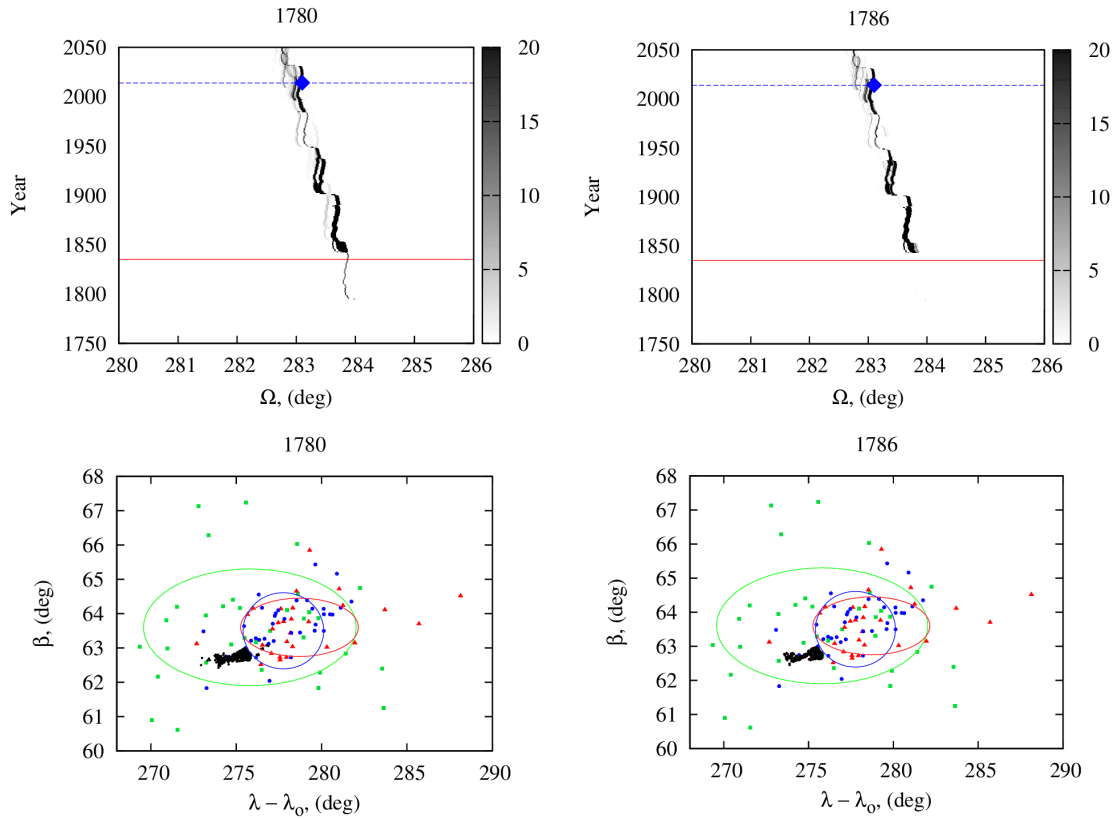
Figure 2.11: Evolution of the descending nodes of meteoroids (upper panels) ejected from 2003 EH$_1$ in 1780 and 1786. The red line marks the year of 1835 AD, i.e the first reported appearance of the Quadrantids (Quetelet, 1839). The blue line marks the year 2014, whereas the blue diamond corresponds to the solar longitude of the peak of the shower. Only meteoroids with nodes within 0.01 AU of the Earth's orbit are plotted.

The lower panels show the theoretical geocentric radiant position of meteoroids (black dots), ejected from 2003 EH$_1$ at the given ejection epoch, superimposed over the observed mean radiant positions measured by video and photographic observations. The red triangles are individual Quadrantid radiant positions from the *Dutch Meteor Society* DMS - video data (Betlem, 1995), the blue circles from the DMS - photographic data and the green squares are the Quadrantid radiants as detected by the *Southern Ontario Meteor Network* (SOMN) all-sky video systems (Brown et al., 2010a). The corresponding ellipses are centered at the mean values of the individual data sets, whereas the ellipses denote the dispersions of the corresponding techniques (see Table 2.5).

Figure 2.12: Evolution of the descending nodes of radar size meteoroids (upper panels), ejected from 2003 EH$_1$ in 1790 and 1796, until the present time. The red line marks the year of 1835 AD. The blue line marks the year of 2014, whereas the blue diamond corresponds to the solar longitude of the peak of the radar shower.

The lower panels show the simulated radiant positions (black dots). The green ellipse is centered at the mean radiant position as deduced from radar observations (CMOR) (see Table 2.5. Here the CMOR radiant is that deduced from a 3D wavelet transform isolating the location of the peak average radiant between 2012 - 2014 using the same technique as described in Brown et al. (2010b). In both figures, only simulated meteoroids approaching the Earth's orbit within 0.01 AU are plotted.

meteoroids this time window is 1796 - 1886. In this context, approximately 10^4 meteoroids were ejected per perihelion passage of the parent, within an arc of 3 AU from the Sun. In the case of the visual size particles, the meteoroids were ejected over ~ 18 perihelion passages of 2003 EH$_1$ with total number of ejected particles $\approx 1.8{\times}10^5$, whereas in the case of radar size meteoroids the the equivalent orbital revolutions of 2003 EH$_1$ are 16, totaling in $1.6{\times}10^5$ ejected meteoroids.

The stacked theoretical activity profile (blue boxes) of the visual Quadrantids ejected between 1780 and 1882 AD, is presented in Fig 2.13. It can be seen that the location of the peak activity of our simulated Quadrantid stream, as well as the FWHM of the core activity, match fairly well with the observations. The wider portion of the observed activity profile though is not well reproduced; we suspect these wings are likely much older than the timescales (of order a few hundred years) that we are concerned with in this work. The theoretical radiant of meteoroids, ejected between 1780 and 1882 AD, shows a fairly good match with the observed mean position and dispersion of individual visual Quadrantids (Fig. 2.14).
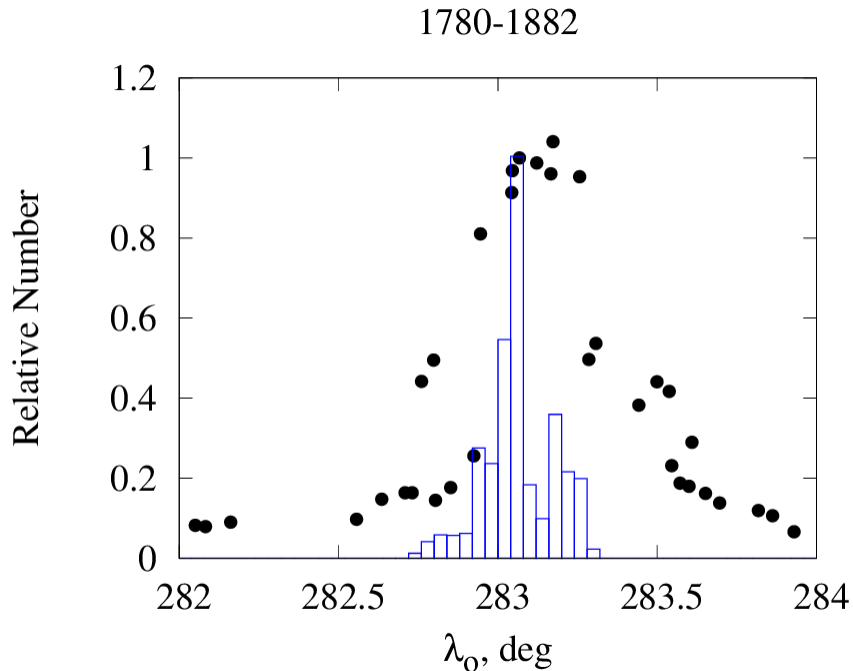
Figure 2.13: The simulated visual activity profile (blue boxes), superimposed over the observed activity profile (black dots) of the Quadrantid shower. Meteoroids not approaching the Earth's orbit within 0.01 AU are not plotted. The theoretical profile is a stack of 17 perihelion passages of 2003 EH$_1$, corresponding to meteoroid ejections from 1780 - 1882 AD. The observed activity profile is an average activity profile of a few years between 1986 - 1992 (J2000) (Rendtel et al., 1993).
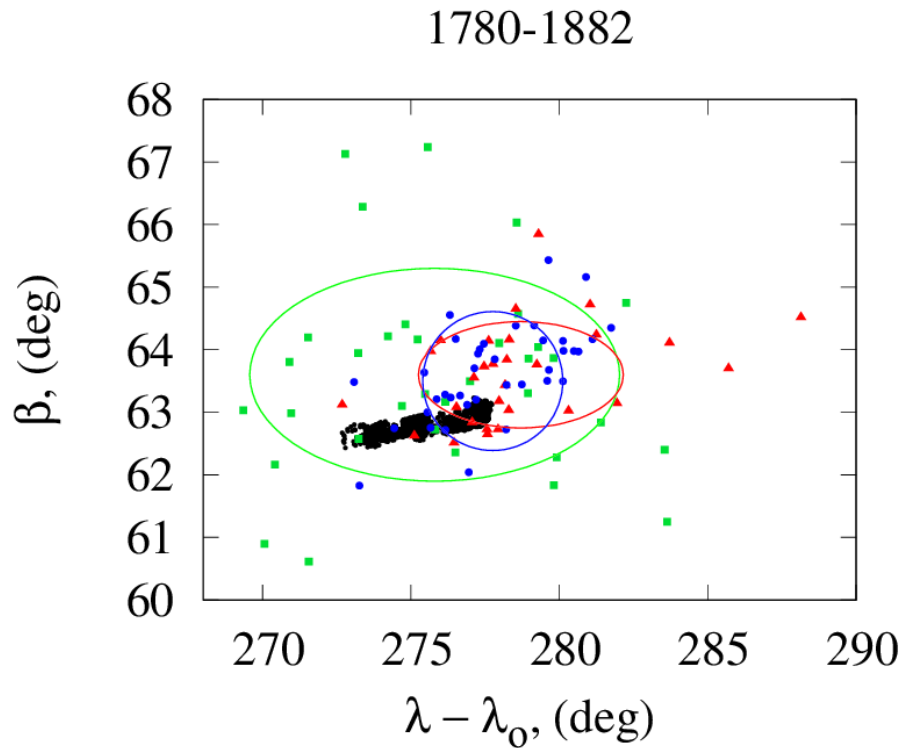
Figure 2.14: The simulated radiant positions of the visual Quadrantids (black dots), along with the observed mean radiant positions and dispersions. The average radiant position is a stack of 17 perihelion passages of 2003 EH_1, corresponding to meteoroid ejections from 1780 - 1882 AD. Meteoroids which do not approach the Earth's orbit within 0.01 AU are not plotted. The observed individual radiants and colors are the same as in Fig. 2.11.

Fig. 2.15 shows the stacked theoretical and observed radar activity profiles. The theoretical width of the core is narrower than the observed one, suggesting that there may be an older envelope of meteoroids encompassing the young core. That is, while the central portion appears to be relatively young, the wings are not.
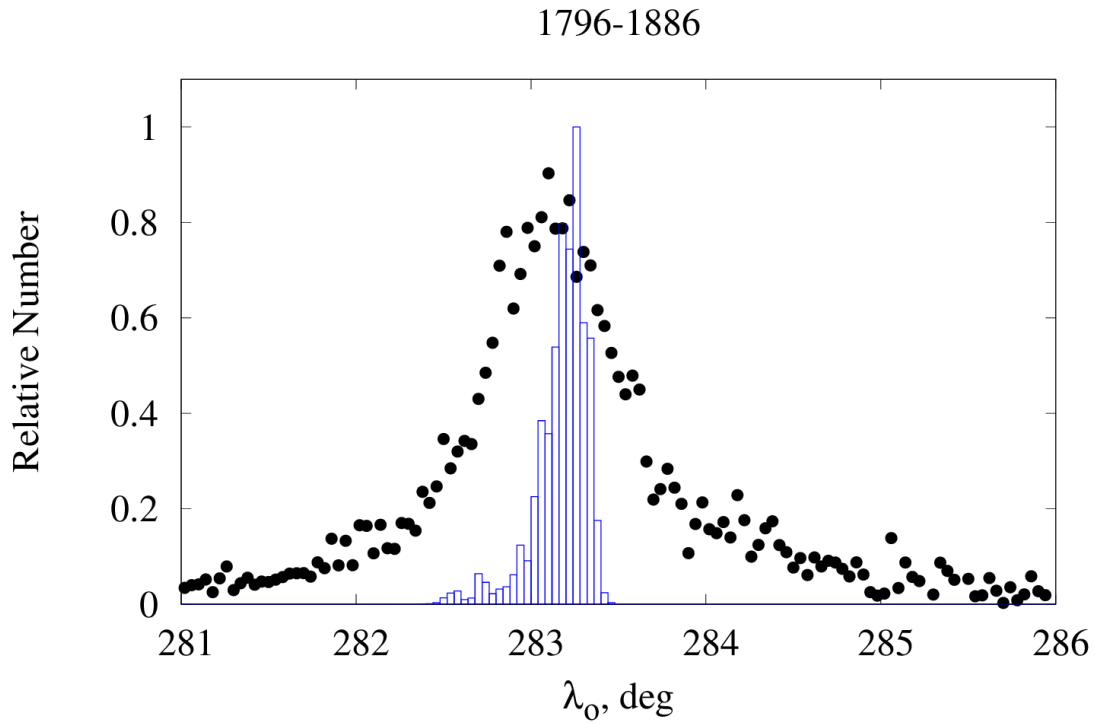
Figure 2.15: The simulated radar activity profile (blue boxes), superimposed over the observed CMOR - measured activity profile (black dots) from single-station echo observations following the same procedure described in (Ye et al., 2014) and (Brown and Jones, 1995). The theoretical profile is a stack of 15 perihelion passages of 2003 EH$_1$, corresponding to meteoroid ejections from 1796 - 1886 AD. Only meteoroids approaching the Earth's orbit within 0.01 AU are plotted. The observed activity profile is the average radar activity profile of the years 2002 to 2014.

Fig. 2.16 shows the simulated distribution of radar size Quadrantids ejected between 1796 and 1886. In this case, the theoretical radiants yield an even better match to the observed one than the visual Quadrantids (Fig. 2.14). However, meteors detected by radar techniques usually have a greater radiants scatter than photographic and video techniques. Thus, the better radiant match may simply be a result of a larger observed radiant dispersion.

1796-1886
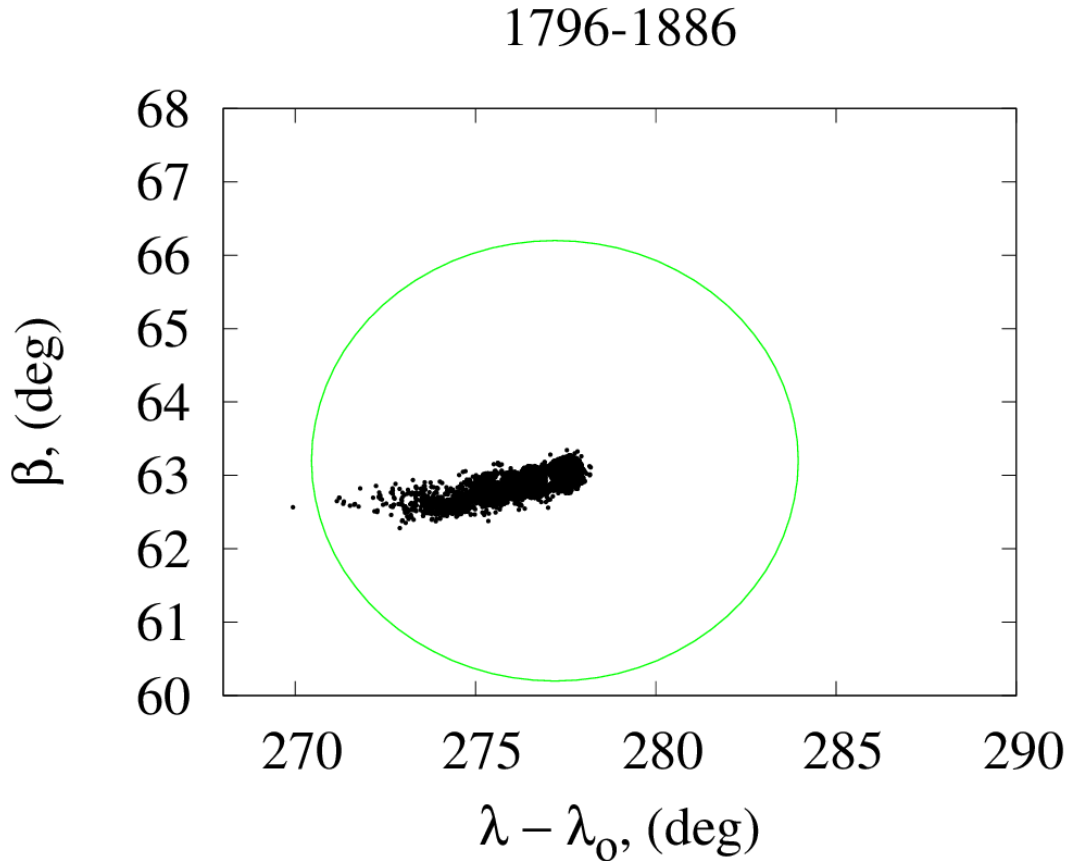
Figure 2.16: The simulated radiants position of the radar Quadrantids (black dots), along with the observed (CMOR) mean radiant position and dispersion. The simulated radiants are from ≈ 15 perihelion passages of 2003 EH_1, corresponding to meteoroid ejections from 1796 - 1886 AD. Only meteoroids approaching the Earth's orbit within 0.01 AU are plotted.

Some authors have argued for a much older age (older than 1000 years) of the Quadrantid meteoroid stream (Williams et al., 1979; Hughes et al., 1979; Williams and Wu, 1993). Therefore we decided to test the hypothesis whether the core of the Quadrantid meteor shower can be reproduced by meteoroid ejections around 1000 AD and 1500 AD.

Fig. 2.17 and 2.18 (upper panels) show the evolution of the descending nodes of meteoroids producing visual meteoroids, ejected from 2003 EH_1 in 1000 AD and 1500 AD respectively. In this scenario we ejected 10^4 particles in a single perihelion passage of 2003 EH_1 in either 1000 AD and 1500 AD.

Meteoroids ejected in 1000 AD and 1500 AD, show a better fit to the observed radiants positions (Fig. 2.17 and 2.18 lower panels) than ejection circa 1800 AD. However, in both cases the Quadrantid shower seems to first appear on the sky around 1650 AD - too early to be consistent with first report of the shower around 1835. Furthermore, the same procedure

was applied to radar sized particles which also appeared as early as 1650 AD. We also cannot uniquely distinguish which of the observed Quadrantids may be associated with the core and which are related to the activity wings which overlap in time.
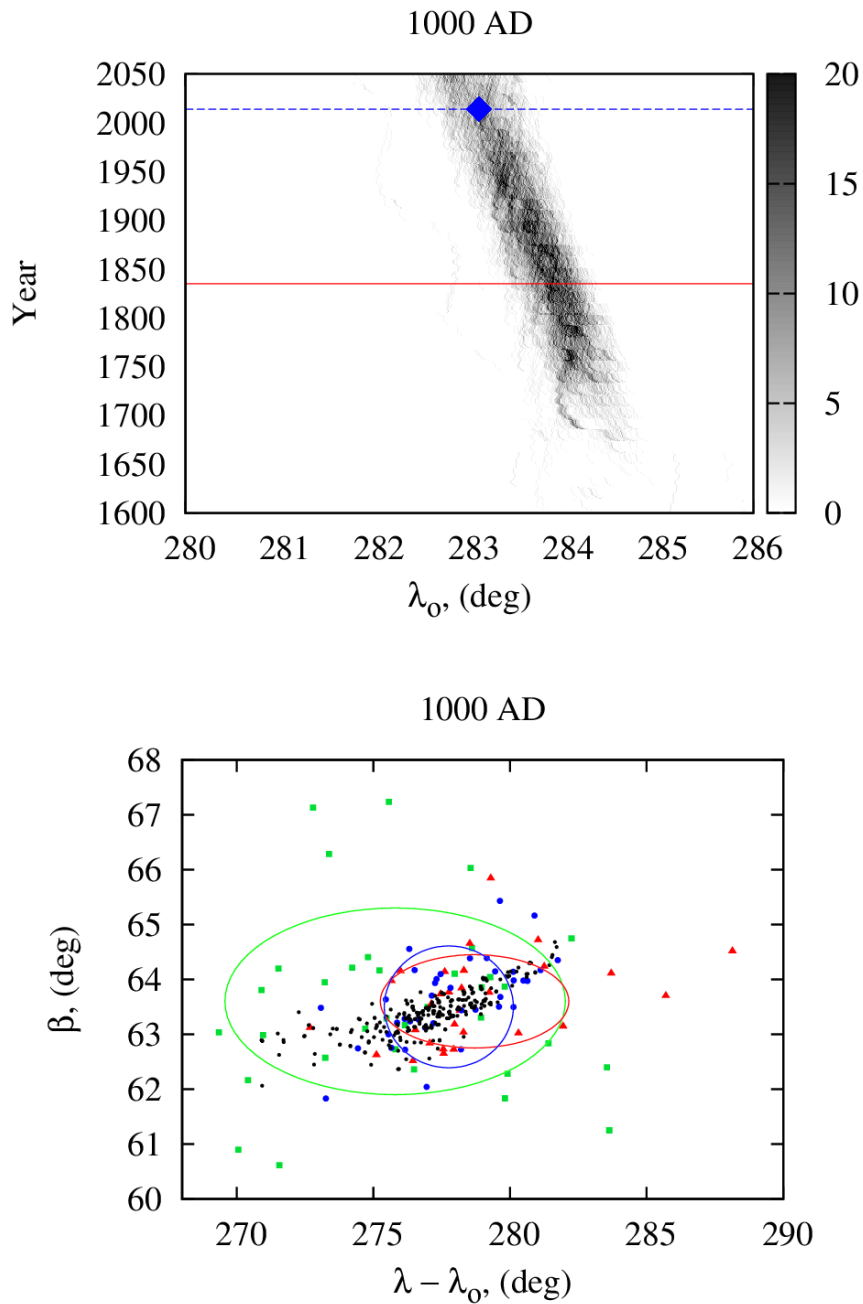
Figure 2.17: Evolution of the descending nodes of visual size meteoroids (upper panels), ejected from 2003 EH$_1$ in 1000 AD until the present time. The red line marks the year of 1835 AD. The blue line marks the year of 2014, whereas the blue diamond corresponds to the solar longitude ($\lambda = 283.2°$) of the peak of the radar shower. The lower panels show the simulated radiant position of meteoroids (black dots) superimposed over the observed mean radiant position, as measured by video and photographic techniques (see Fig. 2.11). In both figures, only simulated meteoroids approaching the Earth's orbit within 0.01 AU are plotted.
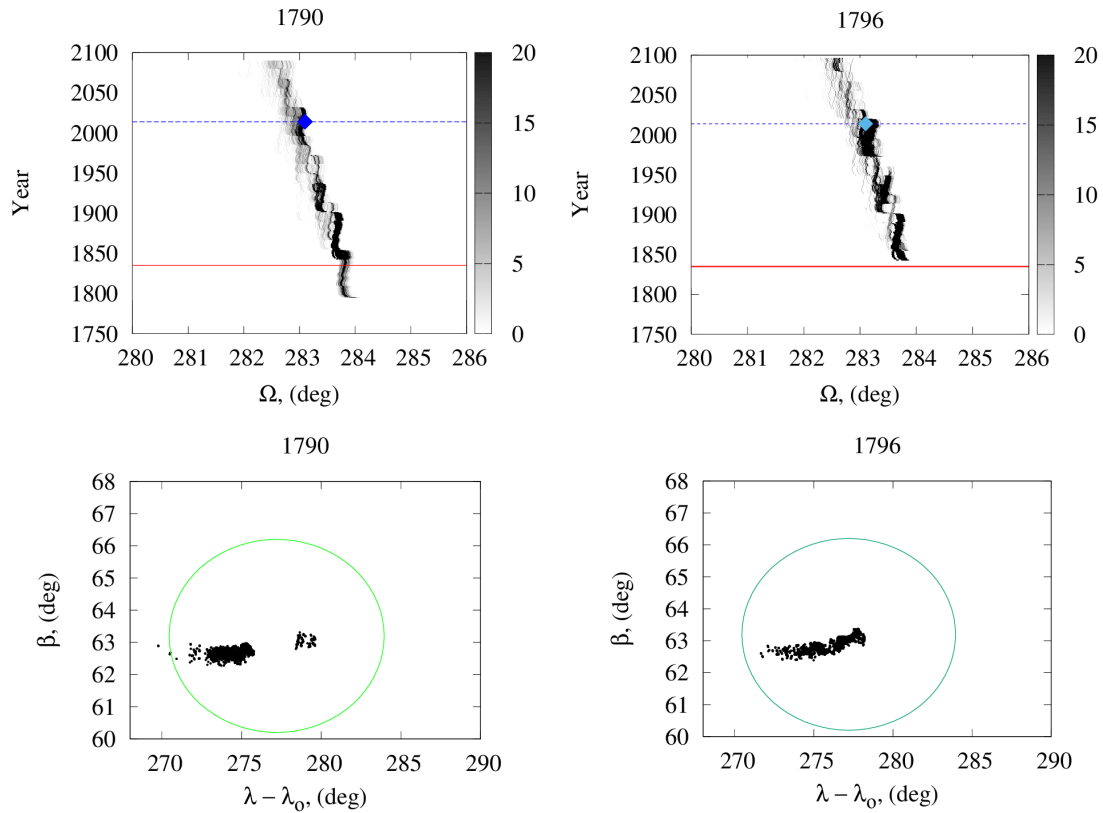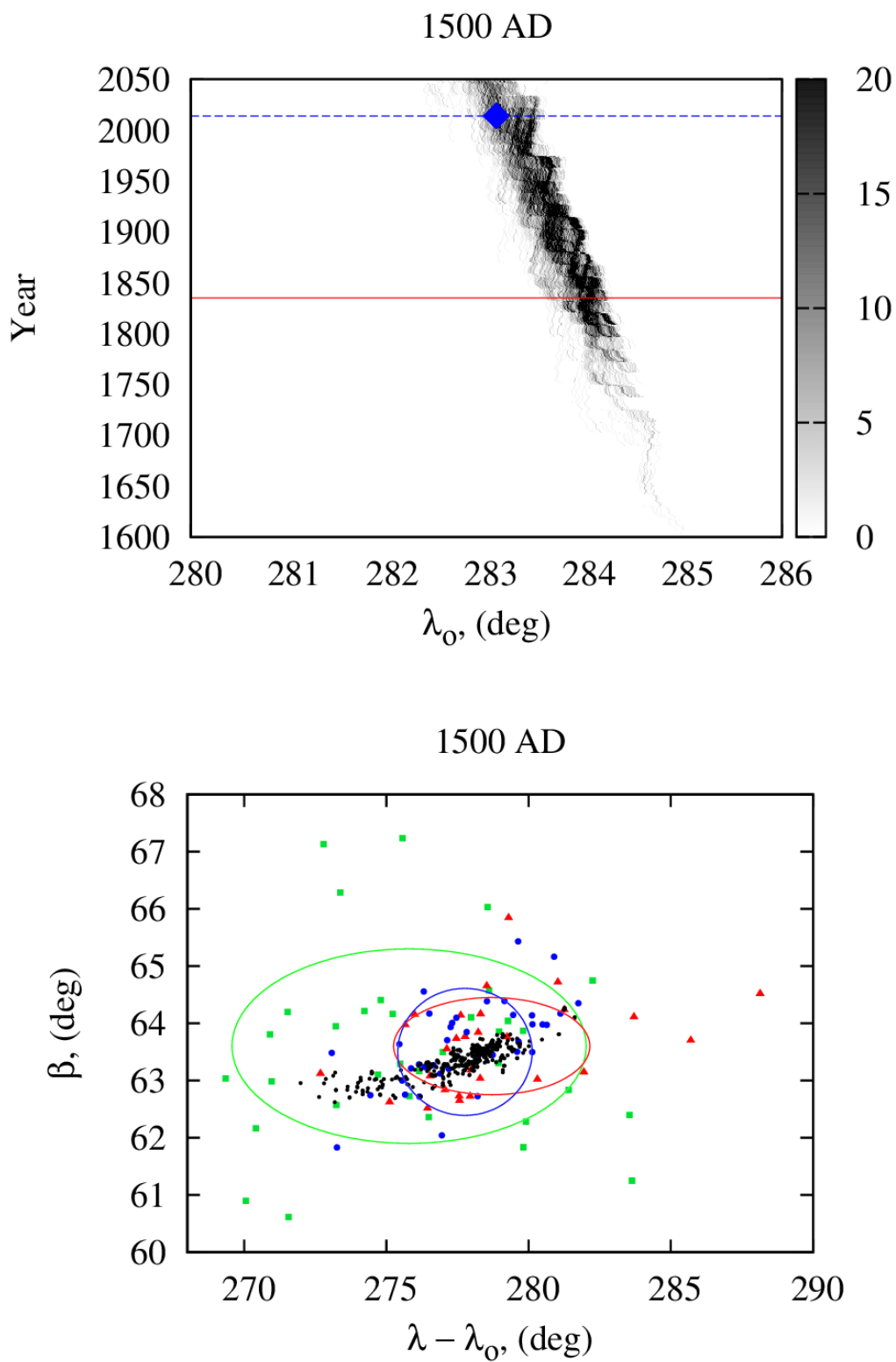
Figure 2.18: Evolution of the descending nodes of visual size meteoroids (upper panels), ejected from 2003 EH$_1$ in 1500 AD, until the present time. The red line marks the year of 1835 AD. The blue line marks the year of 2014, whereas the blue diamond corresponds to the solar longitude of the peak of the radar shower.
The lower panels show the simulated radiant positions (black dots) superimposed over the observed mean radiant position, as measured by video and photographic techniques (see Fig. 2.11). In both figures, only simulated meteoroids approaching the Earth's orbit within 0.01 AU are plotted.

2.7 Discussion and Conclusions

We have used eight high-precision photographic Quadrantid orbits and integrated their orbits backward in time, along with the assumed parent 2003 EH$_1$, in order to constrain the most likely age of the core of the Quadrantid meteoroid stream. Out of the eight Quadrantids, five belong directly to the core of the stream having been observed within a day of the peak of the shower. In addition, five of the best quality radar Quadrantids detected by CMOR in 2013 were used as a complementary data set, in order to compare backward integrations of core radar-sized particles results with the visual counterpart of the stream.

The most likely age of the core of the Quadrantid meteoroid stream, is $\approx$ 200 - 300 years, based on the backward integrations. This epoch was then used as a formation time window to test if the present observed characteristics of the radar and visual-sized particles in the 'core' of the stream could be explained by gas-drag ejection of meteoroids from 2003 EH$_1$ from this epoch.

During the backward integrations, different values (0,10^{-5}, 10^{-4}, 10^{-3}) for β (solar radiation pressure to solar gravity) were considered in order to properly reflect the uncertainty in the mass of each individually observed Quadrantid. Our results did not show a noticeable difference as a function of different β values, which is not surprising given the timescale (200-300 years) in our simulations.

Our forward simulations indicate that an onset of cometary activity in 2003 EH$_1$ circa 1790 - 1796 provides a good match to all the observed constraints for the stream. In particular, the onset time of the shower in these forward simulations is near 1830, consistent with historical data. Moreover, the location of the activity peak and the width of the core of the simulated activity profile are well reproduced in both photographic and radar simulations assuming ejection from this epoch. The broader (several day duration) weak activity surrounding the shower peak is not reproduced in our simulations, leading us to conclude that while the core of the shower appears to be young, the wings are not. The simulated radiants of the radar and visual showers also match observations well. We note that the simulated visual radiant is displaced approximately 1 degree from the mean observed radiant, but this is still reasonable as it lies within the broader scatter of the overall Quadrantid radiant (Jenniskens et al., 1997).

In our forward modeling, for the magnitude of the meteoroid ejection speeds we used the model by Brown and Jones (1998). However, in order to check the robustness of our final results against different meteoroid ejection models, we repeated our forward simulations using the meteoroid ejection model resulting from Crifo's distributed coma model (Crifo et al., 1995; Crifo and Rodionov, 1997), which generally yields slightly lower meteoroid ejection speeds compared to other models. In spite of the latter model being more sophisticated, the differences

in the final results were too small to change our conclusions. This perhaps should not be surprising given the time scales in our forward integrations (200-300 years). However, perhaps the difference in the final outcomes would be significant for relatively young meteoroid trails (as young as a few orbital periods of the parent) which requires certain meteoroid ejection conditions to be fulfilled in order for the trail to intersect the Earth's orbit.

In a summary, our forward integrations are able to reproduce the main features of the currently visible core portion of the Quadrantid stream using the formation epoch suggested from backward simulations ($\approx$ 1800 AD years). The wider portions of the shower (lasting a few days) and the recently discovered (Brown et al., 2010b) much longer radar activity (suggested as being a few months) are likely much older.

At this time, it is difficult to disentangle the real nature of 2003 EH_1, i.e a dormant comet or an asteroid. Could 2003 EH_1 have been active around 1700 - 1900 AD and gone undetected? It seems quite possible. Knowing the absolute asteroidal magnitude of 2003 EH_1 (H=16.2, `http://ssd.jpl.nasa.gov/sbdb.cgi`) we calculated its visibility from Earth throughout the 19th century. Though 2003 EH_1 reached almost 15th magnitude for a few brief periods in the 1800's, it could easily have escaped detection, as its average apparent magnitude was above 22. Of course, substantial cometary activity would have increased its brightness. According to Kronk (Cometography volume 2, p ix, 2003), in the 1800's, small refractors (15-20 cm) were the most commonly used for comet observations. Larger ones were built towards the end of the century, with the 102 cm Yerkes telescope becoming active in the late century, with "...the result was that early in the century comets were usually lost after having faded to magnitude 11 or 12, while at the end of the century comets were being followed until near magnitude 16..." (Kronk, 2003). So it is plausible that even several magnitudes of brightening could have gone unnoticed at this time. Given the current inactive state of 2003 EH_1 it is entirely possible it was simply too faint, even if weakly active, to be detected as a comet.

What might have triggered activity in a dormant parent? The orbit itself is stable in the century preceding our proposed start time, so it was not a dramatic orbital shift. Also, during the last few hundred years the perihelion distance of 2003 EH_1 has been consistently increasing, making it implausible that increasing solar heating triggered fresh activity. The ascending node of 2003 EH_1 was near Jupiter in the 1700-1800's, which makes collision with a main-belt asteroid unlikely, though a collision with a Jupiter Trojan remains a possibility. The descending node at the same time was near the Earth's orbit, though no close approaches between any clones and Earth were recorded in our simulations. Thus a tidal encounter with Earth is not a likely cause either.

We note that there was a relatively close approach between many of the clones of 2003 EH_1 and Jupiter in 1794, where the minimum distance reached 0.83 Hill radii. This was the closest

approach to the giant planet since 1663 when it reached 0.69 Hill radii. Thus, a reasonable explanation is that either tidal effects from the encounter with Jupiter or a collision with a Trojan asteroid activated the parent for a time, with the activity subsequently declining again to zero. However, the mechanisms of cometary activation and dormancy remain unclear and our proposed explanation is certainly not the only possibility.

Bibliography

Adolfsson, L.G., 1996. Meteoroid Stream Sources from Probabilistic Trajectory Analysis. Ph.D. thesis. University of Florida.

Asher, D.J., 2008. Meteor Outburst Profiles and Cometary Ejection Models. Earth Moon and Planets 102, 27–33.

Babadzhanov, P.B., 2002. Fragmentation and densities of meteoroids. A&A 384, 317–321.

Babadzhanov, P.B., Obrubov, I.V., 1992. Comet Machholz 1986 VIII and the Quadrantid meteroid shower - Orbital evolution and relationship. Astronomicheskii Vestnik 26, 70–78.

Betlem, H., 1995. DMS Photographic meteor database .

Betlem, H., Ter Kuile, C., Johannink, C., Jobse, K., 1995. Boötiden 1995: een legendarische aktie!! Radiant, Journal of the Dutch Meteor Society 17, 16–29.

Brower, J.L., 2006. Global forward scatter observations of the 2006 Quadrantid maxima. WGN, Journal of the International Meteor Organization 34, 25–29.

Brown, P., Jones, J., 1995. A Determination of the Strengths of the Sporadic Radio-Meteor Sources. Earth Moon and Planets 68, 223–245.

Brown, P., Jones, J., 1998. Simulation of the Formation and Evolution of the Perseid Meteoroid Stream. Icarus 133, 36–68.

Brown, P., Weryk, R.J., Kohut, S., Edwards, W.N., Krzeminski, Z., 2010a. Development of an All-Sky Video Meteor Network in Southern Ontario, Canada The ASGARD System. WGN, Journal of the International Meteor Organization 38, 25–30.

Brown, P., Wong, D.K., Weryk, R.J., Wiegert, P., 2010b. A meteoroid stream survey using the Canadian Meteor Orbit Radar. II: Identification of minor showers using a 3D wavelet transform. Icarus 207, 66–81.

Chesley, S.R., Chodas, P.W., Milani, A., Valsecchi, G.B., Yeomans, D.K., 2002. Quantifying the Risk Posed by Potential Earth Impacts. Icarus 159, 423–432.

Crifo, J.F., Itkin, A.L., Rodionov, A.V., 1995. The Near-Nucleus Coma Formed by Interacting Dusty Gas Jets Effusing from a Cometary Nucleus: I. Icarus 116, 77–112.

Crifo, J.F., Rodionov, A.V., 1997. The Dependence of the Circumnuclear Coma Structure on the Properties of the Nucleus. Icarus 129, 72–93.

Delsemme, A.H., 1982. Chemical composition of cometary nuclei, in: Wilkening, L.L. (Ed.), IAU Colloq. 61: Comet Discoveries, Statistics, and Observational Selection, pp. 85–130.

Drummond, J.D., 1981. A test of comet and meteor shower associations. Icarus 45, 545–553.

Everhart, E., 1985. An efficient integrator that uses Gauss-Radau spacings, in: Carusi, A., Valsecchi, G.B. (Eds.), Dynamics of Comets: Their Origin and Evolution, Proceedings of IAU Colloq. 83, held in Rome, Italy, June 11-15, 1984. Edited by Andrea Carusi and Giovanni B. Valsecchi. Dordrecht: Reidel, Astrophysics and Space Science Library. Volume 115, 1985, p.185, p. 185.

Fisher, W.J., 1930. The Quadrantid Meteors - History to 1927. Harvard College Observatory Circular 346, 1–11.

Göckel, C., Jehn, R., 2000. Testing cometary ejection models to fit the 1999 Leonids and to predict future showers. MNRAS 317, L1–L5.

Gustafson, B.A.S., 1989. Geminid meteoroids traced to cometary activity on Phaethon. A&A 225, 533–540.

Hamid, S.E., Youssef, M.N., 1963. A short note on the origin and age of the Quadrantids. Smithsonian Contributions to Astrophysics 7, 309.

Harris, A.W., 1989. The H-G Asteroid Magnitude System: Mean Slope Parameters, in: Lunar and Planetary Institute Science Conference Abstracts, p. 375.

Hasegawa, I., 1979. Orbits of Ancient and Medieval Comets. Publ. Astr. Soc. Japan 31, 257–270.

Hawkins, G.S., Almond, M., 1952. Radio echo observation of the major night-time meteor streams. MNRAS 112, 219.

Hindley, K.B., 1970. The Quadrantid meteor stream in 1970. Journal of the British Astronomical Association 80, 479–486.

Hughes, D.W., 2000. On the velocity of large cometary dust particles. Planet. and Space Sci. 48, 1–7.

Hughes, D.W., Taylor, I.W., 1977. Observations of overdense Quadrantid radio meteors and the variation of the position of stream maxima with meteor magnitude. MNRAS 181, 517–526.

Hughes, D.W., Williams, I.P., Murray, C.D., 1979. The orbital evolution of the Quadrantid meteor stream between AD 1830 and 2030. MNRAS 189, 493–500.

Jenniskens, P., 2004. 2003 EH$_1$ Is the Quadrantid Shower Parent Comet. Astron. Journ. 127, 3018–3022.

Jenniskens, P., 2006. Meteor Showers and their Parent Comets.

Jenniskens, P., Betlem, H., de Lignie, M., Langbroek, M., van Vliet, M., 1997. Meteor stream activity. V. The Quadrantids, a very young stream. A&A 327, 1242–1252.

Jenniskens, P., Marsden, B.G., 2003. 2003 EH_1 and the Quadrantids. IAU Circular 8252, 2.

Jewitt, D., 2012. The Active Asteroids. Astron. Journ. 143, 66. `1112.5220`.

Jones, J., 1995. The ejection of meteoroids from comets. MNRAS 275, 773–780.

Jones, J., Brown, P., Ellis, K.J., Webster, A.R., Campbell-Brown, M., Krzemenski, Z., Weryk, R.J., 2005. The Canadian Meteor Orbit Radar: system overview and preliminary results. Planet. and Space Sci. 53, 413–421.

Jones, J., Jones, W., 1993. Comet Machholz and the Quadrantid meteor stream. MNRAS 261, 605–611.

Kańuchová, Z., Neslušan, L., 2007. The parent bodies of the Quadrantid meteoroid stream. A&A 470, 1123–1136.

Koten, P., Borovička, J., Spurný, P., Evans, S., Štork, R., Elliott, A., 2006. Double station and spectroscopic observations of the Quadrantid meteor shower and the implications for its parent body. MNRAS 366, 1367–1372.

Kresak, L., 1976. Orbital evolution of the dust streams released from comets. Bulletin of the Astronomical Institutes of Czechoslovakia 27, 35–46.

Kronk, G.W., 2003. Cometography.

Lee, K.W., Yang, H.J., Park, M.G., 2009. Orbital elements of comet C/1490 Y1 and the Quadrantid shower. MNRAS 400, 1389–1393. `0908.2547`.

Ma, Y., Williams, I.P., 2001. The ejection velocity of meteoroids from cometary nuclei deduced from observations of meteor shower outbursts. MNRAS 325, 379–384.

Ma, Y., Williams, I.P., Chen, W., 2002. On the ejection velocity of meteoroids from comets. MNRAS 337, 1081–1086.

McClusky, J., Trentman, R., Glaze, M., Skiff, B.A., Shelus, P.J., Holvorcem, P.R., Schwartz, M., Marsden, B.G., 2003. 2003 EH1. Minor Planet Electronic Circulars , 27.

McIntosh, B.A., 1990. Comet P/Machholtz and the Quadrantid meteor stream. Icarus 86, 299–304.

Millman, P.M., McKinley, D.W.R., 1953. The Quadrantid Meteor Shower. Journ. of Royal Astron. Soc. of Canada 47, 237.

Müller, M., Green, S.F., McBride, N., 2001. Constraining cometary ejection models from meteor storm observations, in: Warmbein, B. (Ed.), Meteoroids 2001 Conference, pp. 47–54.

Poole, L.M.G., Hughes, D.W., Kaiser, T.R., 1972. Radio-echo observationsof the MA .or night-time meteor streams-III. Quadrantids. MNRAS 156, 223.

Quetelet, L.A.J., 1839. Catalogue des principles apparitions d'etoiles filantes.

Rendtel, J., Koschack, R., Arlt, R., 1993. The 1992 Quadrantid meteor shower. WGN, Journal of the International Meteor Organization 21, 97–109.

Shelton, J.W., 1965. Photographic Quadrantid meteors. Astron. Journ. 70, 337.

Southworth, R.B., Hawkins, G.S., 1963. Statistics of meteor streams. Smithsonian Contributions to Astrophysics 7, 261.

Spurný, P., 1994. Recent fireballs photographed in central Europe. planss 42, 157–162.

Spurný, P., Borovička, J., Shrbený, L., 2007. Automation of the Czech part of the European fireball network: equipment, methods and first results, in: Valsecchi, G.B., Vokrouhlický, D., Milani, A. (Eds.), IAU Symposium, pp. 121–130.

Tancredi, G., 1998. Chaotic dynamics of planet-encountering bodies. Celestial Mechanics and Dynamical Astronomy 70, 181–200.

Verniani, F., 1973. An Analysis of the Physical Parameters of 5759 Faint Radio Meteors. J. Geophys. Res. 78, 8429–8462.

Webster, A.R., Brown, P.G., Jones, J., Ellis, K.J., Campbell-Brown, M., 2004. Canadian Meteor Orbit Radar (CMOR). Atmospheric Chemistry & Physics 4, 679–684.

Weissman, P.R., Asphaug, E., Lowry, S.C., 2004. Structure and density of cometary nuclei. pp. 337–357.

Weryk, R.J., Brown, P.G., 2012. Simultaneous radar and video meteors-I: Metric comparisons. Planet. and Space Sci. 62, 132–152.

Weryk, R.J., Brown, P.G., 2013. Simultaneous radar and video meteors-II: Photometry and ionisation. Planet. and Space Sci. 81, 32–47.

Whipple, F.L., 1950. A comet model. I. The acceleration of Comet Encke. ApJ 111, 375–394.

Whipple, F.L., 1951. A Comet Model. II. Physical Relations for Comets and Meteors. ApJ 113, 464.

Wiegert, P., Brown, P., 2005. The Quadrantid meteoroid complex. Icarus 179, 139–157.

Williams, I.P., Collander-Brown, S.J., 1998. The parent of the Quadrantid meteoroid stream. MNRAS 294, 127.

Williams, I.P., Murray, C.D., Hughes, D.W., 1979. The long-term orbital evolution of the Quadrantid meteor stream. MNRAS 189, 483–492.

Williams, I.P., Wu, Z.D., 1993. The Quadrantid Meteoroid Stream and Comet 1491I. MNRAS 264, 659.

Ye, Q., Wiegert, P.A., Brown, P.G., Campbell-Brown, M.D., Weryk, R.J., 2014. The unexpected 2012 Draconid meteor storm. MNRAS 437, 3812–3823. 1311.1733.

Chapter 3

The age and the probable parent body of the daytime Arietid meteor shower

A version of this chapter has been published as:

3.1   Introduction

The daytime Arietids meteor shower is amongst the strongest annual showers, comparable in activity and duration to the major night-time meteor showers such as the Perseids and Geminids (Aspinall and Hawkins, 1951; Campbell-Brown, 2004). Despite its prominence, the shower has only recently begun to be characterized, as the radiant is close to the Sun and hence the shower is mainly accessible via radar techniques. A daytime shower is defined by the International Astronomical Union (IAU) as having a radiant position within 30° from the Sun at maximum activity, thus limiting video observations to one hour before sunrise or one hour after sunset. The daytime Arietids are observed annually from mid-May to late June where the core of the activity profile is located between solar longitudes $73.5° < \lambda_\odot < 84.5°$, with a broad 4-day maximum centered at $\lambda_\odot = 80.5°$ (Bruzzone et al., 2015). The duration and the broad maximum of the core of the stream implies an old age, perhaps of order of a few millenia. Despite the proximity of the radiant to Sun, its detectability is not strictly limited to radar techniques. There have been a handful of Arietids detected by TV techniques in the hours before dawn (Jenniskens et al., 2016; SonotaCo, 2009; Fujiwara et al., 2004).

The parent of the Arietids remains uncertain, although the stream has previously been

linked to comet 96P/Machholz (McIntosh, 1990; Babadzhanov and Obrubov, 1992; Jones and Jones, 1993) and more recently to the Marsden group of sun-skirting comets (Ohtsuka et al., 2003; Sekanina and Chodas, 2005; Jenniskens et al., 2012). Interestingly, there are significant discrepancies in the semi-major axis and eccentricity of Arietid meteors as measured by radar and video techniques. Radar measures systematically lower values for the semi-major axis, with values as low as 1.6 AU, while optical semi-major axis values typically lie between 2-3.5 AU. If these differences are real, this suggests a strong mass-dependent semi-major axis sorting of the stream, a feature which formation models must explain.

Generally, radar observations of meteors are less precise than those accomplished by video techniques (McKinley, 1961; Hawkes, 1993, 2002). The largest uncertainty is typically in the geocentric velocity of the meteoroids, which translates into an uncertainty in the semi-major axis of the orbit. Although modern meteor radar detections have significantly improved in precision over the past few decades, (see e.g., Baggaley et al., 1994; Jones et al., 2005), the puzzle of the large difference in the semi-major axis of the Arietids, measured by different techniques, namely radar and TV, remains unsolved. Jenniskens et al. (2012) suggested that the discrepancy in the semi-major axes, obtained by radar measurements may be due to the improper correction for the deceleration of the meteors in the Earth's atmosphere.

In the period 2002 and 2013, the Canadian Meteor Orbit Radar (CMOR) carried out an extensive survey of the daytime Arietids, where more than 2×10^4 meteor orbits with representative masses of 8×10^{-8} kg and sizes $\sim 400~\mu$m, were measured (Bruzzone et al., 2015). This allowed for the observed characteristics of the Arietids to be relatively well constrained. In particular, that study focused on attempting to provide a best estimate of the speeds of the Arietids. Despite their work, the result remains that CMOR radar-derived speeds are noticeably lower than optical measurements, consistent with lower speeds measured in earlier radar surveys (Bruzzone et al., 2015).

Based on that decadal survey, the Arietids were found to move on orbits with a mean perihelion distance in the order of 15 solar radii (~ 0.075 AU). Optical techniques yield slightly lower perihelion distance ($q \sim 13~R_\odot$). The orbit of the often cited parent comet 96P has a current perihelion distance of 0.12 AU $\sim 25~R_\odot$ but undergoes a Kozai type oscillation (Bailey et al., 1992), where the perihelion distance q of the comet swings between the extremely low value of ~ 0.05 AU to about 1 AU, with a period of ~ 4500 years.

The similar evolutionary behavior of the orbits of the Arietids led McIntosh (1990) to suggest a sibling relationship between the daytime Arietids, comet 96P/Machholz and the Southern Delta Aquariids based on the similar secular evolution of their orbits. Although the present perihelion distance of the orbit of 96P is much greater than that of the Arietids, both the lines of apses of the Arietids and 96P have similar orientation in the space of the ecliptic longitude

and latitude (L_π, B_π), suggesting that they may be related but are in a different phase of the the Kozai cycle. Babadzhanov and Obrubov (1992, 1993) showed that comet 96P, in addition to the daytime Arietids, can produce 8 meteor showers in total (among them the Quadrantids, Ursids, Carinids, α-Cetids, κ-Velids, Northern and Southern δ-Aquariids) within one precession cycle of the comet. Jones and Jones (1993) carried out numerical simulations to study the formation of the Quadrantid meteoroid stream and confirmed the results from previous studies that meteoroids ejected from 96P/Machholz can produce the daytime Arietids, as well as some of the streams proposed by Babadzhanov and Obrubov (1992, 1993). They argued that 96P/Machholz was captured into a 2:1 mean motion resonance with Jupiter some 2200 years ago, and predicted that some of the resulting meteoroid streams must exhibit a bimodal activity distribution due to the resonance.

Comet 96P/Machholz has been classified as a Jupiter Family Comet (JFC)(`http://ssd.jpl.nasa.gov/sbdb.cg`), although its Tisserand's parameter with respect to Jupiter is $T_j = 1.942$ (see Appendix D), a value typical for a Halley Family Comets (HFC) (see e.g., Carusi et al., 1987). Thus, 96P/Machholz has the shortest period among the HFCs. Another interesting feature of 96P is the reported unusual chemistry of the comet (Langland-Shula and Smith, 2007; Schleicher, 2008). During post-perihelion photometric and spectroscopic observations of 96P, it was noted that the comet exhibits anomalously low C_2, C_3 and CN production, relative to NH, an observation confirmed for only a few other comets (A'Hearn et al., 1995). Schleicher (2008) argued that may be an indicator for an extrasolar origin of 96P, or abnormal thermal alteration of its chemistry via unclear processes. This feature of 96P/Machholz render the origin of the daytime Arietids extremely interesting, if the latter originated from 96P.

The extremely low perihelion distance of the mean orbit of the daytime Arietids, led Sekanina and Chodas (2005) to suggested that the stream is perhaps more closely related to the Marsden and Kracht's group of sunskirting comets, rather than to comet 96P/Machholz (see also Ohtsuka et al., 2003; Jenniskens et al., 2012). The tendency of most sun-skirting (Marsden and Kracht) and sun-grazing (Meyer and Kreutz) groups of comets to arrive at perihelion as doublets and triplets suggests that the Mayer and Kreutz sunskirters, along with P/1999 J6 and 96P/Machholz, may have originated from a fragmentation of a single large body, prior to 950 AD (Sekanina and Chodas, 2005). The authors referred to that large parent as the first generation fragment, and deduced a few likely break-up epochs - 150 AD, 350 AD, 500 AD, 700 AD and 950 AD.

In the process of testing the parent-child relationship of a meteoroid stream and a comet or an asteroid, it is customary to assume a given parent body, and then to model the resulting meteoroid stream numerically. However, the assumption that the Arietids are related to the Marsden group of comets renders it impractical to test child-parent relationships with each

individual member of the group. Instead we will consider the most notable member, among the ~ 35 comets in the group, namely comet P/1999 J6 (Sekanina and Chodas, 2005), and test it as a potential parent of the Arietids. The choice of P/1999 J6 as a potential parent of the Arietids is further motivated by the fact that P/1999 J6 is the brightest and has better constrained orbit than any other member of the Marsden group and was suggested as the immediate parent of the Arietids by Sekanina and Chodas (2005).

In summary, previous authors have suggested that either comet 96P/Machholz or the Marsden group of sunskirters are the most probable parents of the daytime Arietid meteor shower, but there has not yet been a detailed dynamical study dedicated to understanding the formation and evolution of the daytime Arietid meteoroid stream. Such a study must match and explain the observed characteristics of the stream, particularly the orbital characteristics, activity profile and radiant. This work is a first attempt to fill this gap. The goal of this study is to understand the "child-parent" relationship between the daytime Arietids and comet 96P/Machholz and/or P/1999 J6, based on the observed (radar and video) characteristics of the shower and to provide a best estimate for the age of the stream.

3.2 Observations

The earliest radar detections of the Arietids were made by Clegg et al. (1947), who reported increased meteor activity from a radiant near η-Aquarii, in 1946. It was not until 1949 when Aspinall et al. (1949) correctly determined the radiant position. Davies and Greenhow (1951) were the first to use radar to measure the in-atmosphere speeds of the Arietids. They found a value of 38.5 km.s^{-1} based on observations from 1949 and 37.6 km.s^{-1} using observations from 1950, leading to the determination of the first set of orbital elements for the stream (Almond, 1951). For an extensive historical overview of radar observations of the Arietids, the reader is referred to Bruzzone et al. (2015).

Contemporary radar observations of meteor showers, e.g. (AMOR Baggaley et al., 1994) Advanced Meteor Orbit Radar and Canadian Meteor Orbit Radar (CMOR Jones et al., 2005) have significantly improved the number and quality of the measured meteoroid stream orbits. The daytime Arietids have been extensively studied by CMOR, where in the period 2002 - 2013 more than 2×10^4 Arietids, with representative masses of 8×10^{-8} kg, were recorded (Bruzzone et al., 2015). It is notable that meteors at these sizes are difficult to observe optically, due to their small masses. However, a handful of optical observations of larger Arietids do exist (see e.g., Fujiwara et al., 2004; SonotaCo, 2009; Jenniskens et al., 2016) despite the proximity of the radiant position to the Sun. Our modeling of the Arietids will mainly use the radiant and activity profile of the stream reported in the decadal survey of the shower by CMOR

(Bruzzone et al., 2015). We augment these data with 14 TV Arietids recorded by the SonotaCo network (SonotaCo, 2009) and 31 video events by the Cameras for All-sky Meteor Surveillance (CAMS), detected between 2011 and 2012 (Jenniskens et al., 2016).

It is widely accepted that individually measured photographic and TV meteoroid orbits yield more accurate pre-atmospheric speed (and hence orbital elements) than radar techniques, (e.g., Hawkes, 1993, 2002). However, the large number of individually recorded Arietid orbits by CMOR provide a solid statistical constraint of the observed characteristics of the Arietids in the hundreds of μm size range, particularly radiant location and activity profile.

In the literature, there are large differences in the pre-atmospheric speeds of individual Arietids reported by radar as compared to optical techniques (see e.g., Jenniskens et al., 2011, 2016; Bruzzone et al., 2015). In particular, the radar measurements yield systematically lower pre-atmospheric speeds for the stream, as compared to optical observations. This difference reaches values as high as 2 km/s (see Table 1 and Table 2 of Bruzzone et al. (2015)), resulting in a difference in the calculated semi-major axes of the meteoroids of more than 1 AU (see Fig. 18 of Bruzzone et al. (2015)). Figure 4.2 shows the orbits of the mean Arietids stream as measured by CMOR and CAMS, along with the orbits of the potential parents, considered in this work.

It is not clear whether this difference in the speeds as measured by optical and radar techniques implies a mass segregation of the meteoroids or to systematic technique-specific errors. The best estimate after careful comparison to ablation modeling of the mean pre-atmospheric geocentric speed of the Arietids by CMOR (Bruzzone et al., 2015) yields, $V_g = 38.9 \pm 0.7$ km.s^{-1}, where the same quantity obtained from TV observations of 14 Arietids is $V_g = 40.55 \pm 0.47$ km.s^{-1} (SonotaCo, 2009) and $V_g = 40.70 \pm 1.59$ km.s^{-1}, based on 31 video events (Jenniskens et al., 2012). The resulting semi-major axis of the mean Arietids with corresponding one standard deviation, based on the CMOR is $a = 1.7 \pm 0.2$ AU (Bruzzone et al., 2015), $a = 2.34 \pm 0.6$ AU based on 14 TV Arietids (SonotaCo, 2009) and $a = 2.768 \pm 0.812$ AU according to Jenniskens et al. (2016) as measured by CAMS (for details and comparison between the other orbital elements, see Table 2 of Bruzzone et al. (2015)). This difference in the speeds and semi-major axis is comparable to the scatter of the different measurement techniques. That logically leads to the question whether these differences can be associated to the modeled deceleration of the meteoroids in the Earth's atmosphere or are artificial due to the large scatter in the optical surveys. Smaller meteoroids (hundreds of μm) are subject to greater deceleration in the Earth's atmosphere, as compared to the millimeter or centimeter size particles that are detected optically. Jenniskens et al. (2012) attributed the differences in the pre-atmospheric speeds as measured by CMOR and optical techniques (e.g. CAMS) to an improper account for the deceleration of the Arietids, where the deceleration corrections employed are mean values
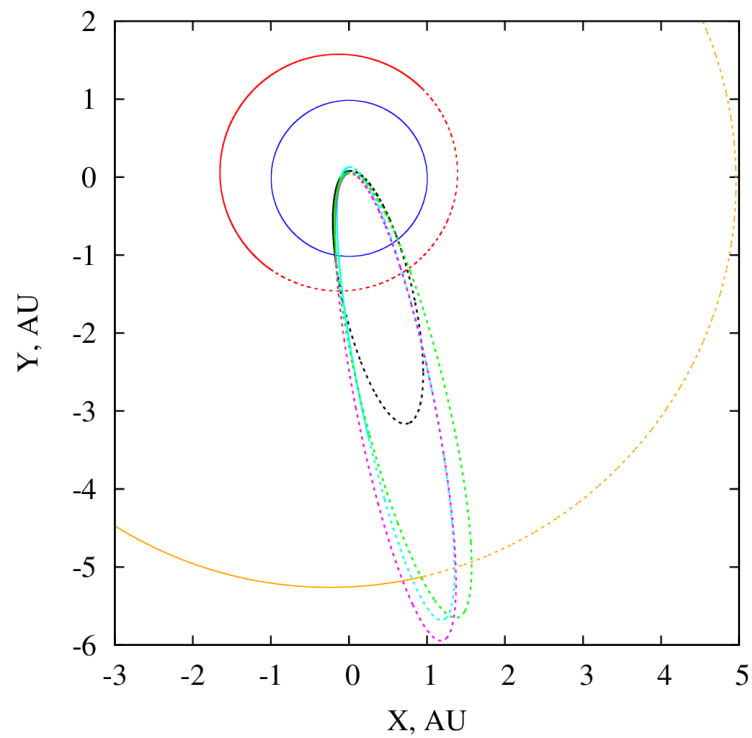
Figure 3.1: The orbits of 1999 J6 (magenta), 96P (cyan) and the mean of the daytime Arietids[1] (black) from CMOR and daytime Arietids[2] (green) from CAMS, as seen from above the ecliptic plane. The portion of the orbits below the ecliptic are presented with a dashed line. The orbits of the Earth (blue), Mars (red), and Jupiter (orange) are also shown.

[1]The mean orbital elements of the Arietids, based on radar survey, are taken from (Bruzzone et al., 2015).

[2]The mean orbital elements of the Arietids, based on optical survey, are taken from (Jenniskens et al., 2016).

from observations of other meteor showers with known speeds.

This difference may also be due to mass segregation of meteoroids along the mean orbit of the Arietids. In this case, the inconsistency in the speeds and orbital elements is one of appearance only. The size and mass of the meteoroids affect the dynamics mainly through the non-gravitational forces from the Sun, namely solar radiation pressure and Poynting-Robertson drag (see e.g., Burns et al., 1979), where these forces are more significant on smaller particles. While the solar radiation pressure acts to weaken the solar gravity, the Poynting-Robertson drag causes the angular momentum of the meteoroids to decrease, resulting in a decrease of their semi-major axis and eccentricity. Thus, it is expected that the semi-major axes of smaller meteoroids will decrease over time, resulting in a natural separation between small and large particles purely due to radiation effects.

In our simulations of the daytime Arietids, in addition to constraining the most likely parent and age of the stream, we attempt to address the question as to whether the observed differences in the orbital elements as deduced by radar and TV observations are real or an instrumental artifact.

3.3   Numerical Simulations

3.3.1   Stage I - Backward integrations of potential stream parent bodies

We first integrate the orbits of both proposed parents 96P/Machholz and P/1999 J6, backwards in time along with 10^4 clones for each parent. These integrations provide us with a starting point from which forward modelling of meteoroid stream production by the proposed parents can proceed. The clones are sampled from the six-dimensional orbital phase space using the covariance between the orbital elements given for the epoch of osculation. The orbital elements of a given clone y_i can be written in the form:

$$y_i = y_o + X_{ik}\Lambda_{kj}\xi_j, \tag{3.1}$$

where y_o is a 6×1 column vector of the nominal orbital elements of the comet, X_{ik} is 6×6 matrix with columns equal to the eigenvectors of the covariance matrix, Λ_{kj} is a 6×6 diagonal matrix with elements the corresponding eigenvalues of the eigenvectors, ξ_j is a column vector of random numbers, distributed normally around zero. The osculating orbital elements as well as the covariance matrix for the orbital elements of the comets were taken from the NASA's JPL Horizon system: `http://ssd.jpl.nasa.gov/sbdb.cgi`. During the backward integrations, we accounted for the gravitational perturbations from all the planets and also allowed for their mutual interactions, where the Earth and the Moon were taken together, i.e. their barycenter.

We used the JPL's DE 405 integrated planetary ephemeris file (`ftp://ssd.jpl.nasa.gov/pub/eph/planets/ascii/`) to generate the state vectors of the planets, for a given epoch for which the osculation elements of either of the comets are available.

The clones in our simulations were considered as test particles, i.e their mutual interaction and collisions were neglected. Considering the behavior of the clones and not solely the nominal orbit provides a measure of the confidence we can ascribe to the parent's past history. If many of the clones behave in a consistent way, we can assert that the parent did as well, while if the clones disperse, our own confidence in the past dynamical evolution of the parent disperses with them.

3.3.2   Parent candidate # 1: P/1999 J6

Numerical integrations of high-eccentricity orbits require careful choice of time step so that the motion around perihelion is well-sampled. Because of the extremely low perihelion distance of P/1999 J6 ($q \sim 10 R_\odot$), before the main backward integrations, we tested various integration time steps, ranging from 1 to 12 hours. We found that a time step of 4 hours is a good compromise between integration speed and accuracy: that time step was used throughout the backward integrations of P/1999 J6. In addition to Newtonian gravity, we also accounted for the primary general relativistic effects (through the post-Newtonian approximation), despite the fact that 1999 J6 spends only a short time in the vicinity of the Sun. The equations of motion of all planets (except Pluto), P/1999 J6, and its clones, were integrated backwards using the hybrid symplectic scheme (Chambers, 1999), which also allows for inspection of close encounters between the comet and the planets. The equations of motion were integrated backwards in time for 2000 years, until 0 AD. This time scale was chosen, in conformance with the conjecture that the P/1999 J6 broke up from a larger progenitor, between 100 AD and 950 AD (Sekanina and Chodas, 2005). We emphasize that, although P/1999 J6 arguably separated from a larger progenitor via fragmentation (thermal or tidal disruption), we assume here that the meteoroid ejection mechanism will be standard cometary sublimation. Sekanina (1977, 1978) showed that the separation velocities between fragments of split comets is of the order of a few m/s, a few order of magnitudes less than the ejection speeds of meteoroids from the surface of a low-perihelion comet. Thus, we do not expect that a possible splitting of P/1999 J6 would result in a broader stream than that due to the normal outgassing of a comet.

During the backward integrations, we found that the orbit of P/1999 J6 quickly becomes chaotic, over a time scale of approximately 500 years, which is evidenced by the dispersal in the orbital elements displayed in Fig 3.2. This stochastic behavior imposes limits as to how reliably one can know the past osculating orbital elements of P/1999 J6, which are used here for

meteoroid ejection and integration of their orbits forward in time. However, a careful selection of sets of orbital elements of P/1999 J6 (or clones), at a given epoch in the chaotic region, may still be used for meteoroid ejection. The key point is to select clones which are located close to the nominal orbit, and use them as the virtual meteoroid parent, when integrated forward in time. Because the scattering of the clones arises primarily in this case, from planetary encounters, parent-clones which are located far from the nominal orbit cannot match the timing, spread of the activity profile and radiant location of the current Arietids. Such an occurrence would require that all or nearly all of the meteoroids they eject suffer planetary encounters that place them on the present Arietid orbit, which cannot happen in practice due to the stochastic nature of planetary encounters. In this manner, we select clones which could with reasonable probability reproduce the daytime Arietids as we see them today. Though we can push a certain extent into the chaotic zone, we do not attempt to go further back than 2000 years.
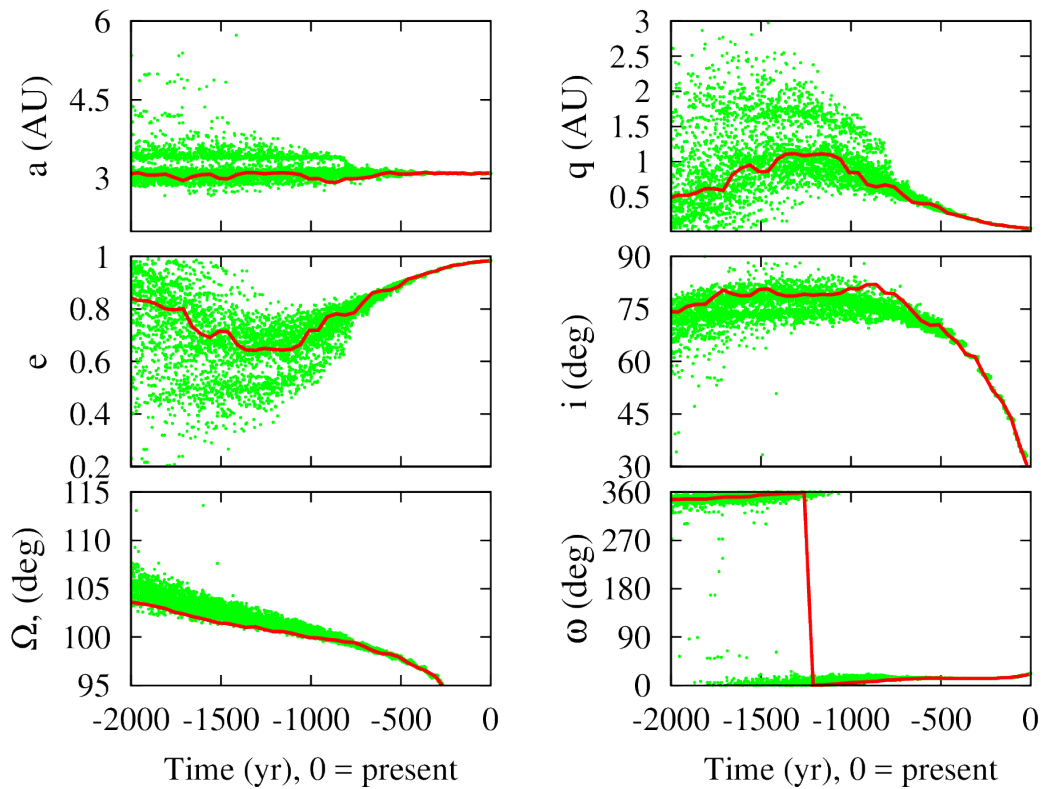
Figure 3.2: Backward evolution of the nominal orbital elements of comet P/1999 J6 (red), along with 10^4 clones (green), over 2000 years.
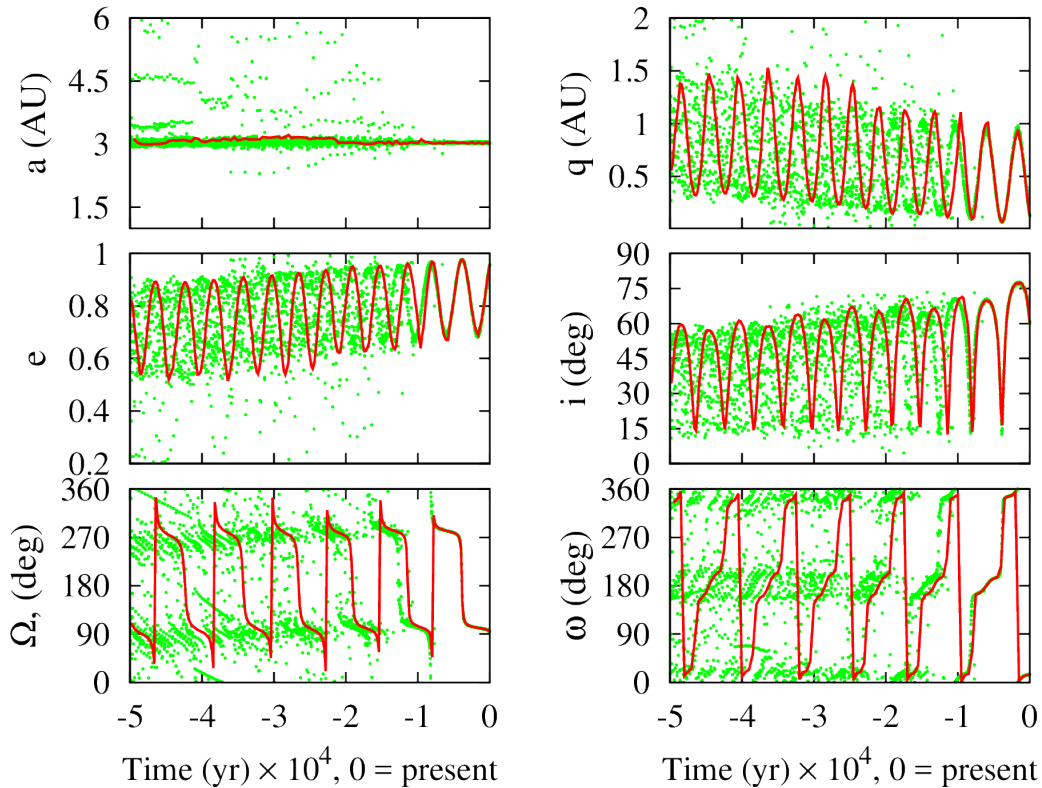
Figure 3.3: Backward evolution of the nominal orbital elements of comet 96P/Machholz (red), along with 10^4 clones (green), over 5×10^4 years.

3.3.3   Parent candidate # 2: 96P/Machholz

As a possible parent, the orbit of comet 96P was integrated backwards in time along with 10^4 clones until 50000 BC. The length of the integration was chosen somewhat arbitrarily, mainly because of a lack of a priori knowledge as to the age of Arietids and secondly we aimed to obtain a broader picture as to the backward evolution of the orbit of comet 96P which will be used as a starting points for forward modeling of the stream. Moreover, the long duration of the shower's activity (more than a month) indicates that it is likely old if it formed by standard cometary activity.

As with P/1999 J6, we used the hybrid symplectic integrator, the only difference being that a larger time step of 12 hours. Time steps between 2 - 24 hours were tested beforehand in order to determine an optimal value between the integration speed and accuracy. We chose to use a time step of 12 hours, because it yielded similar results over 50000 years when compared to simulations with shorter time steps. The same assumptions for the planets accounted for, non-gravitational effects etc., were used as those in the case of the backward integrations of P/1999 J6 (see Sec. 3.3.2).

The orbit of 96P is not chaotic currently and evolves smoothly over about 7500 years into the past before planetary encounters begin to disperse the clones (Fig. 3.3). Moreover, the evolution of the orbit of 96P is dominated by the Kozai oscillation (Kozai, 1962; Kinoshita and Nakai, 1999), which manifests itself in a distinct correlation between the eccentricity (e), inclination (i) and argument of perihelion (ω) of the orbit, a condition often seen in sun-grazing comets (Bailey et al., 1992).

3.3.4   Stage II - Meteoroid ejection and forward integrations

The formation of meteoroid streams is relatively well understood. In the classical meteoroid formation model (Whipple, 1950, 1951), meteoroids are released from the surface of the comet due to sublimating gas. Thus, meteoroids move with a slightly different velocity than the comet which results in, among other things, a small change in the orbital energy and semi-major axis of the particles. As this change in a also produces a change in the orbital period, meteoroids will tend to disperse along the orbit of the comet, resulting in a closed stream of meteoroids. Furthermore, the solar radiation pressure, acting on micrometer meteoroids, will counteract the gravitational pull by the Sun, effectively weakening the Solar gravity. This in turn will cause the semi-major axis of meteoroids to increase, resulting in a mass segregation along the orbit. The dynamical evolution of the stream will further be affected by planetary perturbations and eventually, if at some point in time the stream crosses the Earth's orbit, it may produce a meteor shower. In this section, we describe the meteoroid ejection model and the forward integrations of the resulting particles, with an aim to investigate the synthetic meteoroid streams of comets P/1999 J6 and 96P.

Meteoroid ejection modeling

In all simulations, we model the meteoroids as spherical particles of density 2.5×10^3 kg/m^3 with sizes randomly selected from a flat distribution in the logarithm of their radii, in the range $s = 100\,\mu$m to $s = 1$ mm. We emphasize that our knowledge of the actual particle distribution in the stream is highly biased towards hundred micron sizes, due to the daytime nature of the Arietids shower and detectability mostly by radar techniques. The size range chosen is not meant to reflect the expected size distribution, but rather allows us to efficiently explore the differential dynamical evolution of radar and visual meteoroids and to examine a possible mass segregation across the activity profile of the shower.

We assume that meteoroid ejection starts when the clones are within 3 AU from the Sun (i.e the heliocentric distance at which water ice begins to sublimate (Delsemme, 1982)). The meteoroid ejection, as a function of the heliocentric distance and ejection speed was modeled

according to (Brown and Jones, 1998), where the ejection speed is given by:

$$V_{ej} = 10.2 \, r^{-1.038} \rho^{-1/3} R_c^{1/2} m^{-1/6} \text{ (m/s)} \tag{3.2}$$

where r is the heliocentric distance in (AU), ρ is the bulk density of the meteoroid in (g cm^{-3}), R_c is the radius of the comet nucleus in (km) and m is the mass of the meteoroid in (grams). The meteoroids are ejected with speeds, distributed isotropically on the sunlit hemisphere, with dust production rate assumed to be uniform in true anomaly of the clones of the comet. Furthermore, the direction of meteoroid ejection is random over the sunlit hemisphere.

The equations of motion of the meteoroids along, with their parent clones, are integrated forward in time using Chamber's hybrid symplectic scheme (Chambers, 1999), until the present. The size of the meteoroids is considered in the dynamics via the standard β-parameter and the Poynting-Robertson drag, where $\beta = F_R/F_G$ is the ratio of the solar radiation pressure to the solar gravity. The magnitude of the β-parameter is given by Burns et al. (1979) as:

$$\beta = \frac{F_R}{F_G} \sim 5.7 \times 10^{-6} \frac{Q_{pr}}{\rho s}, \tag{3.3}$$

where ρ is the density of the meteoroid in kg/m^3, s is the meteoroid radius in meters and Q_{pr}, which we assume to be unity (= 1), is non-dimensional coefficient representing the scattering efficiency of meteoroids. Furthermore, due to the extreme amplitude of the perihelion distances of both comets, P/1999 J6 and 96P/Machholz, we also accounted for general relativistic effects, even though both comets spend a very short time in the vicinity of the Sun, compared to their orbital periods.

Meteoroid ejection from parent candidate #1: P/1999 J6

To test child-parent relationship between the daytime Arietids and P/1999 J6, we considered five different origin epochs of the shower from P/1999 J6. Case 1 - with meteoroid production onset in 150 AD, case 2 - for ejection in 350 AD, case 3 - for ejection in 500 AD, case 4 - for ejection in 700 AD and case 5 for meteoroid ejection in 950 AD, see Table 3.1. These meteoroid ejection epochs were chosen based on the work by Sekanina and Chodas (2005), who proposed that first precursors of comet P/1999 J6 and daytime Arietids may have separated from a common progenitor at these epochs. The ejected meteoroids as well as their ejection velocities were modeled as described in Sec. 3.3.4.

Due to the stochastic nature of the orbital evolution of P/1999 J6 once we go more than 500 years into the past (see Fig. 4.4) we chose to eject meteoroids from 9 different clones of the comet as well as the nominal orbit of P/1999 J6. The selected clones have orbits located near the nominal trajectory in the phase space of the orbital elements. This selection was made

Case №	Met. ejection onset	Num. of every fifth perihelion returns of P/1999 J6 N_p	Num. of met. ejected at every fifth perihelion N_e	Total number of simulated particles $N_{tot} = N_p \times N_e$
1	150 AD	70	250×10 clones	$\sim 1.8 \times 10^5$
2	350 AD	62	250×10 clones	$\sim 1.6 \times 10^5$
3	500 AD	52	250×10 clones	$\sim 1.3 \times 10^5$
4	700 AD	45	250×10 clones	$\sim 1.1 \times 10^5$
5	950 AD	37	250×10 clones	$\sim 9.2 \times 10^4$

Table 3.1: Various meteoroid ejection scenarios from P/1999 J6. For all cases, it is assumed a constant continuous cometary activity between the onset time and the present. The meteoroids are released from each individual clone at every fifth perihelion return until the present. Assuming, a period of $P = 5.3$ years for P/1999 J6, meteoroid release takes place every ~ 26.5 years.

on the basis that clones with orbital elements completely different from nominal orbit are less likely to return close to the present orbit of P/1999 J6. Starting at each of the initial epochs in Table 3.1, a set of 250 meteoroids are released from each of the 10 clones of P/1999 J6 resulting in 2500 meteoroids at every fifth perihelion return of the clones, or equivalently roughly every 30 years. For each case, the procedure is followed until the present with the number of meteoroids increasing by 2500 during each fifth perihelion return. We thus, effectively assume uniform cometary activity over the period of interest. This results in a synthetic meteoroid stream, at the present, consisting of a different number of particles $N_{tot} = N_p \times N_e$, as a function of the initial meteoroid ejection onset epoch (see Table 3.1).

Following the forward evolution of the orbits of the Arietid meteoroid stream, we imposed a perihelion distance limit, inside which the particles were considered "dead", and thus removed from the stream. The cut-off distance was chosen to be $q = 0.025$ AU (or ~ 5 $R_\odot$), based on the physical ability for a meteoroid to survive at such low perihelion distances without being completely evaporated by solar heating (Peterson, 1971). We do not, however, have a priori knowledge on the exact chemical composition and physical strength of the daytime Arietid meteoroids, primarily because of the limited number of optical observations. However, assuming a genetic relationship between the Arietids and Quadrantids (e.g., McIntosh, 1990; Ohtsuka et al., 2003; Wiegert and Brown, 2005), it seems reasonable to assume a similar composition. We note, however, that due to the lower perihelion distance of the Arietids as compared to the Quadrantids, it is expected that the former to be relatively depleted of volatiles and more compacted. Thus, a perihelion cut-off distance of ~ 5 $R_\odot$ seems reasonable, so we do not unintentionally remove potential Arietids from the stream. Furthermore, we did not model particle sublimation effects near the Sun, nor did we account for the Lorentz force in the equations of motion of the meteoroids.

Meteoroid ejection from parent candidate # 2: 96P/Machholz

To test the parent-child relationship between the daytime Arietids and comet 96P/Machholz, we followed an approach similar to the case of P/1999 J6. However, due to the lengthy backward integrations (see Fig. 4.3) and the onset of chaos approximately 7500 years into the past, it is difficult to obtain meaningful results well in the chaotic region. Therefore, we constrain ourselves to epochs later than 10000 BC and thus obtain a lower limit as to the age of the daytime Arietids. Furthermore, similar to the case with P/1999 J6, meteoroids were modeled as described in Sec. 3.3.4. The parameters of the simulations were otherwise the same as earlier, except for a time step of integrations being $\delta t = 12$ hours.

Here, we considered 9 different meteoroid ejection onset epochs. These epochs are divided into two groups: (1) epochs before the orbit of 96P becomes chaotic, based on the backward integrations and (2) epochs in the chaotic region. The reason for this division is that we use two different approaches in selecting representative clones of 96P, which will be used for forward modeling of meteoroid ejection.

The first group of ejection epochs were chosen as 1000 AD, 0 AD and 3000 BC respectively. We refer to these epochs as "case 1", "case 2" and "case 3" (see Table 3.2). In cases 1-3, the meteoroids were released from the nominal orbit of 96P/Machholz. The use of the nominal orbit seems plausible as in this time frame we do not see large dispersion in the orbital elements of the clones of comet (Fig. 4.3). Moreover, the median values of the orbital elements of the clones are a good representation of the nominal orbit, at any given epoch from the present back until 5500 BC. In cases 1-2, the meteoroids were released from the nominal orbit of 96P at every fifth perihelion return of the parent, whereas in cases 3 at every tenth perihelion return, maintaining uniform cometary activity of 96P/Machholz over these time intervals. That is, we double the number of meteoroids ejected per perihelion for case 3, in order to compensate for the greater interval between active perihelion returns, with all cases amounting in ~ 500 meteoroids per perihelion passage.

In cases 4, 5, 6, 7, 8 and 9 the meteoroids are released from 10 different clones of comet 96P/Machholz, instead of the nominal orbit, due to the chaos beyond 5500 AD. The clones are selected based on their Kozai evolution, so that they lie on or close to the nominal Kozai trajectory of 96P in $(e - \omega)$ space (see Fig. 3.4). The Kozai energy C is given by e.g., Kinoshita and Nakai (1999) as:

$$C = (2 + 3e^2)(3 \cos i^2 - 1) + 15e^2 \sin i^2 \cos 2\omega, \qquad (3.4)$$

where e is the eccentricity, i is the inclination and ω is argument of perihelion of the orbit respectively. Fig. 3.4 shows the theoretical Kozai cycle of comet 96P, in $(e - \omega)$ space, for

different value of the Kozai energy integral C (Eq. 4.4), with the actual trajectory of the comet and 10^3 clones superimposed over the calculated curves. It is to be noted that the evolution of 96P does not preserve the nominal Kozai energy precisely, as shown in Fig. 3.4. The reason for that may be due to close encounters with Jupiter or proximity of the orbit of 96P to a mean motion resonance with Jupiter, none of which are accounted for in the Kozai formalism. We have also indicated the sample of clones that we use for meteoroid ejection (red dots) and one "bad" clone (blue circle) which has been discarded in our simulations.

Similar to case 3, the meteoroids were released at every 10 perihelion returns, or roughly every 60 years, with 5000 particles equally distributed between the clones (see Table 3.2). In cases 4 and 6, we maintained an uniform meteoroid production rate, with (500 meteoroids/perihelion passage/clone × 10 clones = 5000 meteoroids per perihelion passage). However, cases 5 and 7 are somewhat different, assuming a variable dust production rate for the clones of 96P/Machholz (see Fig. 3.5). For cases 5 and 7, we investigate a simple model of decreasing cometary activity: 5000 meteoroids ejections per clone for the time interval 10000 BC – 6500 BC, 3000 meteoroids per clone between 6500 BC and 3000 BC and 1000 meteoroids per clone between 3000 BC and the present. The goal is to try to better match the much older "wings" of the activity profile of the Arietid shower. The motivation for this scenario does not seem unreasonable i.e. to expect that cometary activity to decrease over time, in particular over a time scale of a few thousand years, given the short period orbital nature of 96P. However, we emphasize that this scenario may break if there was fragmentation in the past evolution of 96P, which is generally accompanied with excessive dust production. The latter has been observed for several split comets, e.g. comet 73P/Schwassmann-Wachmann 3 which has begun to fall apart in 2006 and showed an increased brightness in the light curve, likely attributed to excess of gas and dust emission (e.g., Sekanina, 2005).

At the end of the simulations, these discrete meteoroid ejection epochs are weighted by the perihelion distance of the parent at the time of meteoroids' ejection. The reason for that weighting is to account for the higher dust production rate at stages of very low perihelion distances, due to the greater proximity to the Sun. The weighting parameter that we use was adopted from Jones (2003) and is given by:

$$w = \frac{\theta_c (1 - e)^2}{q^2 \sqrt{1 - e^2}}, \tag{3.5}$$

where θ_c is the true anomaly of the comet within which it becomes active, e is the eccentricity of the orbit and q is the perihelion distance of the comet, at the time of meteoroid ejection.

We emphasize that the variability of the activity of 96P/Machholz is not an unreasonable

assumption, as it is unlikely that the comet has maintained a constant activity since 10000 BC. There are various mechanisms, that lead to decrease in cometary activity over time, such as volatile depletion and formation of an inert crust on the surface of comets (e.g., Rickman et al., 1990). However, we do not know the exact function or rate at which the activity of 96P/Machholz has decreased over time, instead our approach provides grounds to test the hypothesis of decreasing activity over time.

Case 5 is similar to case 7, with the major difference being the initial meteoroid ejection onset time 6500 BC. Furthermore, in order to be consistent with case 7, we ejected 3000 particles per clone between 6500 BC and 3000 BC and 1000 particles per clone between 1000 BC and the present. In general, there are myriad of parameters that can be adjusted to reflect various meteoroid ejection scenarios, however the exact combination of these variables are not known. We thus, only investigate a few simple hypotheses.
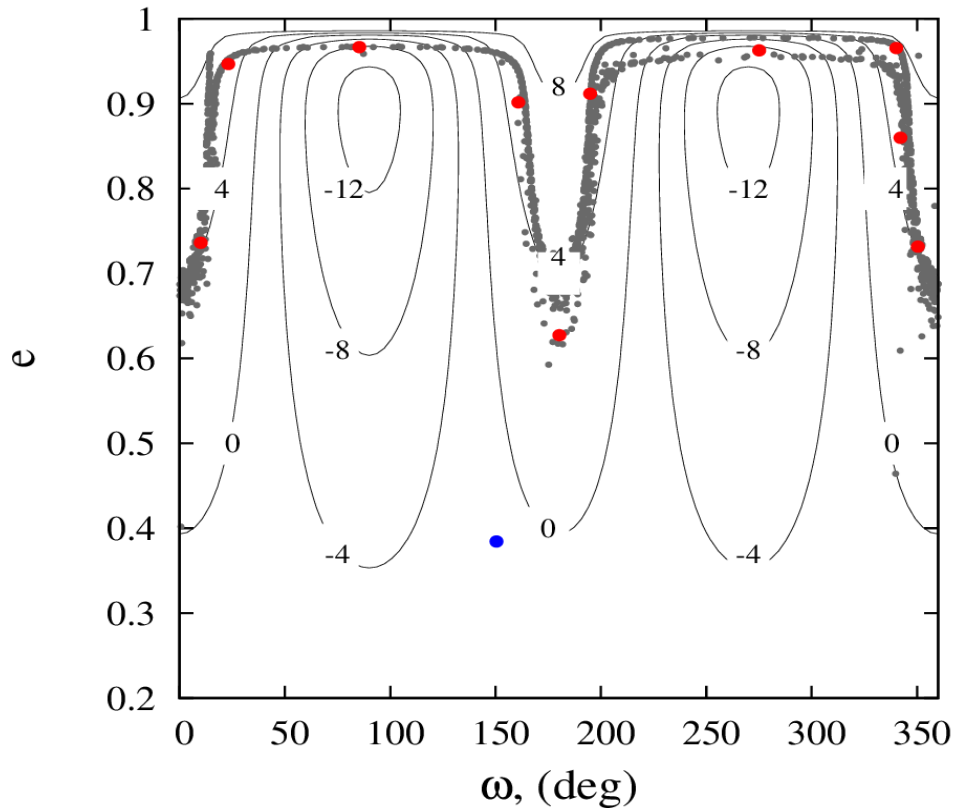
Figure 3.4: Past Kozai-type evolution of the orbit of 96P (black dots) for 20000 years, across the lines of different values for the energy C in the Kozai resonance (solid lines). The red dots indicate "good" clones selected for forward integration as meteoroid ejections. The blue dot represent a sample "bad" clone, which we do not use for meteoroid ejection.

Finally, cases 8 and 9 were designed to test whether the discrepancy between the orbital elements of the daytime Arietids, as derived from radar and optical surveys, can be attributed

Case №	Epoch of ejection	Ejection every N peri.	Number of active perihelion returns (N_p)	Number of meteoroids ejected over N_p (N_e)	Total number of ejected particles ($N_{tot} = N_p \times N_e$)
1	1000 AD	$N = 5$	38	2500	$\sim 9.5 \times 10^4$
2	0 AD	$N = 5$	76	2500	$\sim 1.9 \times 10^5$
3	3000 BC	$N = 10$	95	5000	$\sim 4.7 \times 10^5$
4	6500 BC	$N = 10$	160	5000 $\times$10 clones	$\sim 8 \times 10^6$
5	6500 BC	$N = 10$	160	Variable dust prod.	$\sim 2.9 \times 10^6$
6	10000 BC	$N = 10$	226	5000 $\times$10 clones	$\sim 1.1 \times 10^7$
7	10000 BC	$N = 10$	226	Variable dust prod.	$\sim 6.2 \times 10^6$
8	20000 BC	$N = 1$	1	$(5 \times 10^4) \times$ 10 clones	5×10^5
9	30000 BC	$N = 1$	1	$(5 \times 10^4) \times$ 10 clones	5×10^5

Table 3.2: The various cases used for meteoroid ejection throughout our forward simulations of 96P. Cases 1-3 correspond to meteoroid ejections before the chaotic region, whereas cases 4 through 9 (see Fig. 4.3) are well withing the chaotic zone. Cases 5 and 7 account for a variable dust production rate, of the clones of 96P/Machholz, as a function of time. In case 5, 3000 meteoroids per clone are ejected between 6500 BC and 3000 BC and 1000 meteoroids per clone between 3000 BC and the present. In case 7, 5000 meteoroids per clone are ejected between 10000 BC and 6500 BC, 3000 meteoroids per clone between 6500 BC and 3000 BC and 1000 meteoroids per clone between 3000 BC and the present. Cases 8 and 9 correspond to meteoroid ejection from 10 different clones of 96P/Machholz, at a single perihelion passage.
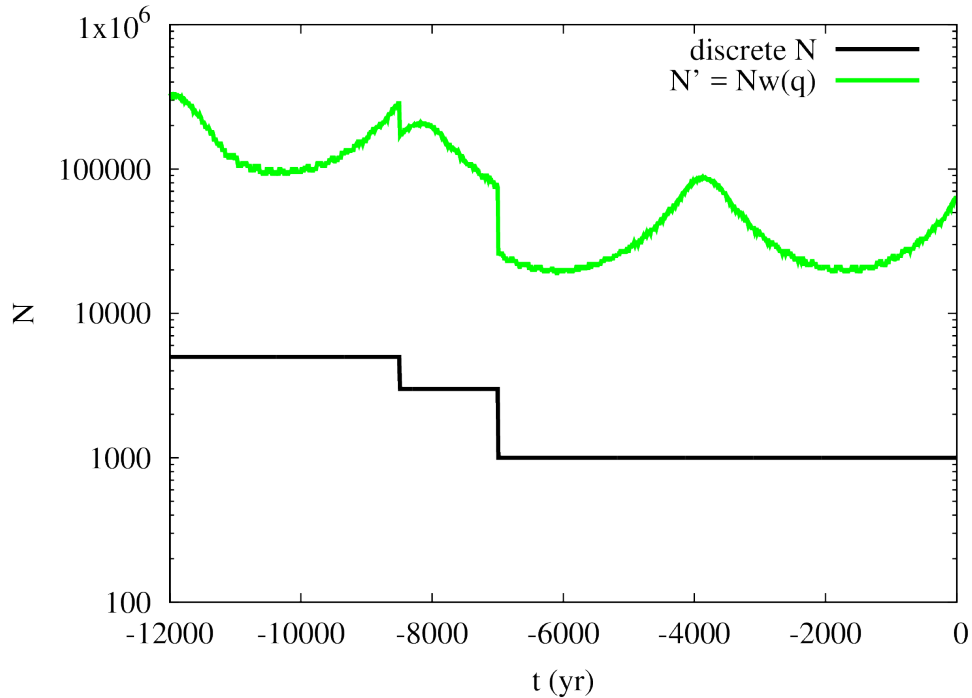
Figure 3.5: Assumed variability of the meteoroid production rate for cases 5 and 7 in Table 3.2, starting in 10000 BC and continuing until the present. The black line indicates discrete meteoroid ejections, with 5000 meteoroids per clone ejected between 10000 BC and 6500 BC, 3000 meteoroids ejected between 6500 BC and 3000 BC and 1000 meteoroids between 3000 BC and the present. The green curve is a weighting of the discrete ejection as a function of the perihelion distance of the parent. The weighting scheme is adopted from Jones (2003).

to the Poynting-Robertson drag (e.g., Robertson, 1937; Burns et al., 1979), given a sufficiently long period of time. The explicit change in the semi-major axis and eccentricity of the orbit due to the Poynting-Robertson drag can be found in (e.g., Klačka, 2004) which we omit here. Bruzzone et al. (2015) found that the values of semi-major axes and eccentricities for radar and optical size particles converged to similar values between 10^4 and 10^5 years, i.e. the discrepancy between radar and optical size particles can be removed if Poynting-Robertson drag has acted over time scales greater than 10000 years. In their work Bruzzone et al. (2015) do not consider the gravitational influence of the Sun and planets on the meteoroids, and merely consider that the particles are subjected to only radiation effects from the Sun.

In the cases 8 and 9, we considered only meteoroids with radii $s = 50\mu$m, with equivalent $\beta \sim 5 \times 10^{-3}$ being strongly affected by the solar radiation pressure. The density of the meteoroids and the ejection speeds were modeled as described in Sec. 3.3.4. In contrast to previous cases, 5×10^4 meteoroids were ejected at a single perihelion passage and epoch centered at 20000 BC and 30000 BC (see Table 3.2) from 10 different clones of 96P/Machholz. We note that, the aim of cases 8 and 9, is merely to test whether the discrepancy of the semi-major axis and eccentricity can be attributed to the Poynting-Robertson drag alone. That is, given

a sufficiently large time scale our goal is to investigate whether Poynting-Robertson drag can decrease the semi-major axis and eccentricity of $50\mu m$ size Arietids (an extreme lower limit for CMOR sizes) to their presently observed values.

The equations of motion were integrated forward in time, starting from each individual epoch 30000 BC and 20000 BC, until the present using the Chambers' symplectic scheme (Chambers, 1999). During the integrations we accounted for the gravitational influence of all eight planets, general relativistic effects due to the meteoroids' low perihelion distances as well as solar radiation pressure and Poynting-Robertson drag. However, we neglected the Lorentz force as well as the solar wind drag, as the latter forces are small (e.g., Leinert and Grun, 1990) compared to solar radiation pressure and Poynting-Robertson drag, for the particles of interest in this work.

3.4   Results

3.4.1   Parent candidate #1: P/1999 J6

In order to compare the observed and simulated characteristics of the daytime Arietids, we consider the simulated Arietids to be any meteoroids which have their orbital nodes within 0.01 AU from the Earth's orbit. In reality, only meteoroids that hit the much-smaller Earth may produce detectable meteors, though our sieve distance of 0.01 AU is a compromise to avoid low meteoroid number statistics. In addition, we only present results for six clones out of ten and compare the simulated and observed characteristics of the daytime Arietids only for case 1 in Table 3.1. The rest of the cases yielded similar results which we decided to omit here.

Fig. 3.6 presents the activity profiles for six different clones for meteoroid ejection in case 1. The combined profile is a stack of meteoroids of all sizes with radii between $s = 100\ \mu m$ and $s = 1$ mm, and we refer to that profile as the "unweighted" profile. In addition, superimposed is the observed activity profile of the Arietids by CMOR as an average from the years 2002-2013 (Bruzzone et al., 2015), including meteors to a limiting radio magnitude of +6.5. It is evident that the selection of different clones of P/1999 J6 has little effect on the final results. The resulting profiles are too narrow to be consistent with the observations by CMOR. However, these profiles do not realistically capture the meteoroid population in the stream, as they assume a dust production rate independent of the perihelion distance of the parent at the time of meteoroid ejection. Since they do not yet account for dust production variations with perihelion, it is not unreasonable to expect that an increased supply of dust would be produced at lower perihelion distances. In order to examine this, we first examine a plot of the solar longitude $\lambda_\odot$ of particles presently intersecting the Earth, as function of their time of ejection

and their perihelion distance at the time of ejection (Fig. 3.7). It is evident that since 1200 AD, most of the meteoroids are ejected from their parent at perihelia below 1 AU, with extreme values of ~ 0.1 AU for meteoroids released only about two hundred years ago. Thus, it is reasonable to expect that the dust released during these stages of very low perihelion distance, should contribute relatively more to the stream than particles ejected at larger q. Therefore, we apply a perihelion-based weighting to the activity profile in order to more realistically model the number of particles in the present activity profile. We hereafter refer to that profile as to the "weighted" profile. The weighting parameter that we use is given by Eq. 3.5
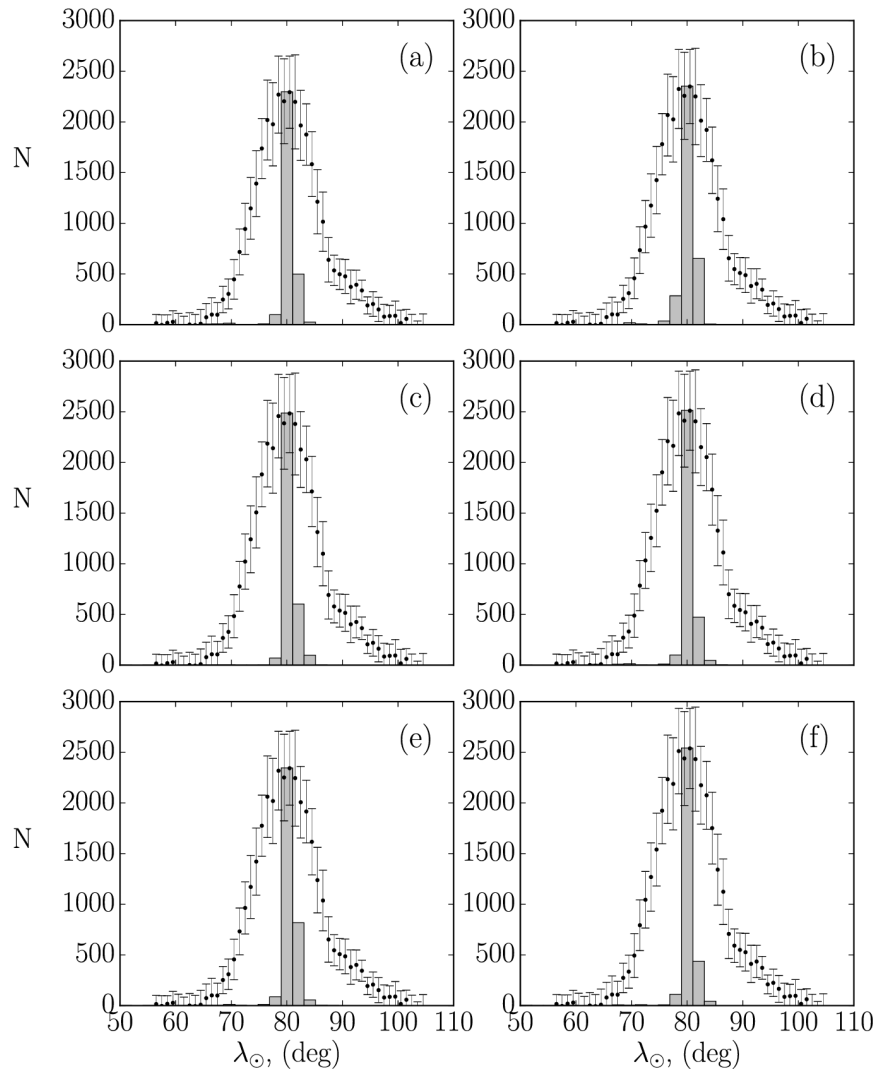
Figure 3.6: Simulated activity profile for the daytime Arietids, at the present, for meteoroid ejection for case 1 and for six different clones panel (a), (b), (c), (d), (e) and (f), superimposed over the normalized observed profile by the CMOR (black dot with error bars). The observed profile is a stack for the years of 2002-2013 and includes meteoroids, equivalent to radar meteors of radar magnitude +6.5. The error bars in the observed profile correspond to 1 σ from Bruzzone et al. (2015). For the theoretical profile, only meteoroids presently approaching the Earth's orbit within 0.01 AU have been considered.

Thus, the number of particles N_i' in the i−th bin of solar longitude $\lambda_{\odot i} + \Delta\lambda_\odot$, as a function of their perihelion distance at the time of ejection, is:

$$N_i' = \sum_{j=1}^{n} N_{ij} w_j(q_j), \tag{3.6}$$

where N_{ij} is the $j - th$ particle in the i−th bin with perihelion distance q_j at the ejection epoch, w_j is the wighting factor for a given perihelion distance q_j. The result of weighting of the activity profile is presented in Fig 3.8. In order to check whether there is a particular mass sorting along the profile, the weighted activity profile also provides information of particle size in each bin. However, our results did not show any particular mass segregation as a function of solar longitude $\lambda_\odot$.

Regardless of the initial meteoroid ejection onset epoch, the activity profile resulting from P/1999 J6 results in a sharp maximum and very weak broader activity, which is inconsistent with the overall activity profile. The reason can be gleaned from Fig. 3.7 where it can be seen that only particles ejected prior to 1000 AD contribute to the wings of the activity profile. However, these meteoroids were ejected at larger perihelion distances and thus according to our weighting scheme they contribute less than the particles released in the last 1000 years. The result for the rest of our cases and clones yielded similar results. Due to the greater concentration of meteoroids near the peak of the activity profile $\lambda_\odot = 80.5°$ (see Fig. 3.7), at any ejection epoch, the weighted activity profile will always result in a narrow sharp maximum, regardless of the perihelion distance weighting factor. In fact, the rest of the cases (cases 2-5) resulted in even narrower profiles due to the lack of particles to fill the wings. Thus, based on our simulations, comet P/1999 J6 alone can not explain the entire activity profile of the shower, though it may contribute to the core of the stream.

The simulated radiant position of the daytime-Arietids, from comet P/1999 J6, is presented in Fig. 3.9, along with the observed radiant containing 68 % and 95 % of the observed meteoroids as derived by CMOR from Bruzzone et al. (2015). The radiant positions are presented in a sun-centered reference frame $\lambda - \lambda_\odot$ and b, in order to account for the Earth's orbital motion. The four panels show the simulated radiant distribution for particles, according to their ejection epoch - panel (a), their geocentric speed V_g in panel-(b), the perihelion distance of the parent at the time of meteoroid ejection in panel (c) and meteoroid radiation pressure β-value in panel-(d). The simulated radiant produced a relatively good match with the observations, except for a few particles outside the 95% confidence region. There is a lack of any mass segregation along the width of the stream as is evident from Fig. 3.9, which is also reflected in Fig. 3.8.

Fig 3.10 shows the theoretical distribution of the orbital elements of the daytime Arietids assuming an origin from P/1999 J6 in 150 AD (case 1) for only one clone, as the rest yielded
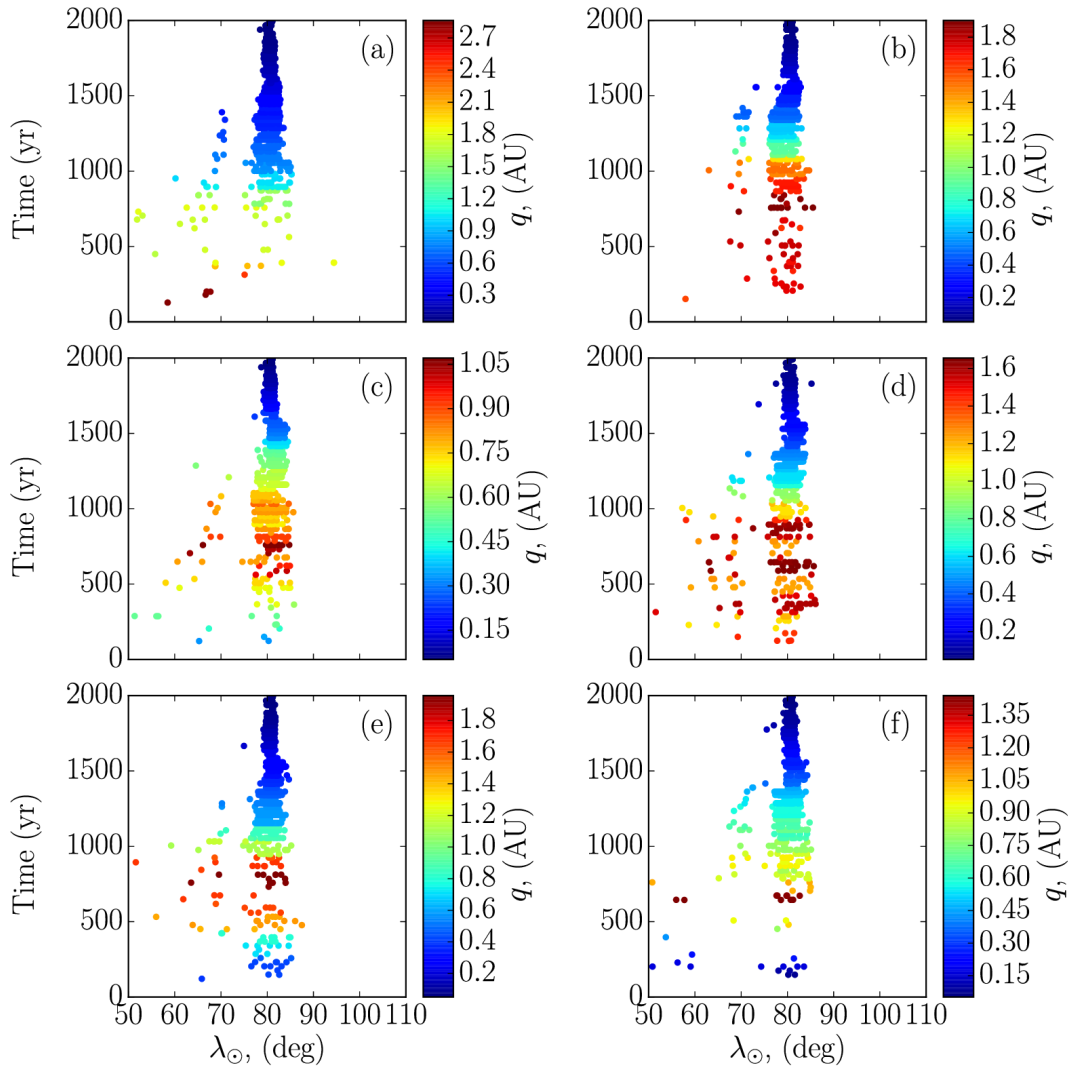
Figure 3.7: The present distribution of the solar longitude $\lambda_\odot$ of meteoroids, as a function of the ejection epoch in the common era. The color bar corresponds to the perihelion distance (q) of the meteoroids at the time of ejection. Only meteoroids approaching the Earth's orbit within 0.01 AU have been considered. Six different clones of P/1999 J6 are shown, following the naming in Fig. 3.6.

similar results. It is evident that, there is a poor match in the present a, e and Q, with radar observations by CMOR and other radar measurements as given in Bruzzone et al. (2015). In fact, the simulated orbital elements are more consistent with TV and video observations which predict systematically higher values for a and e and Q, as compared to radar surveys. Poynting-Robertson drag in our simulation did not change the semi-major axis of the meteoroids enough to bring them close to the predicted values by CMOR, over the the time scale of our simulations. In summary, the conjecture that the daytime Arietids are solely associated with Marsden group of sunskirting comets was not supported by our simulations, though our results indicate that comet P/1999 J6 could contribute to the peak of the shower.
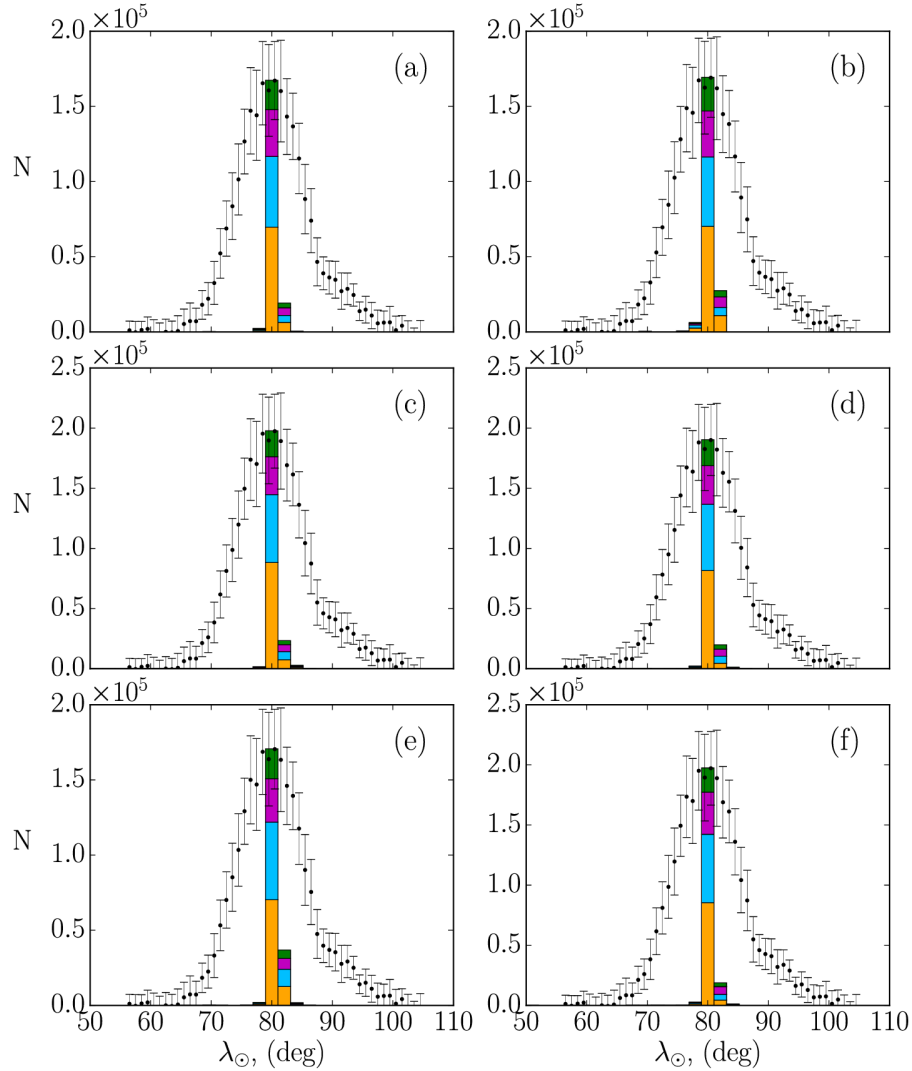
Figure 3.8: The weighted activity profile for the daytime Arietids, at the present, as a function of the perihelion distance of the parent during meteoroid ejection for case 1. The profiles are presented for six different clones - panels (a), (b), (c), (d), (e) and (f), superimposed over the observed profile by the CMOR (black dot with error bars) for meteors brighter than radio magnitude of +6.5. The error bars in the observed profile correspond to 1 σ. The four different colors in each stacked histogram denote particles of various size (expressed in terms of particles β−parameter). The "yellow" color corresponds to $\beta = (2 \times 10^{-4} - 6.5 \times 10^{-4})$, "blue" $\beta = (6.5 \times 10^{-4} - 1.1 \times 10^{-3})$, "magenta" $\beta = (1.1 \times 10^{-3} - 1.55 \times 10^{-3})$, and "green" $\beta = (1.55 \times 10^{-3} - 2 \times 10^{-3})$. Effectively, the "yellow" color corresponds to the smallest and the "green" color to the largest particles, respectively. For the theoretical profile, only meteoroids presently approaching the Earth's orbit within 0.01 AU have been considered.

3.4.2   96P/Machholz

In this section we examine the hypothesis that comet 96P/Machholz is the parent of the daytime Arietids and present the results from the forward numerical simulations of meteoroids released from the comet. Similar to the previous section, we show results for only six clones. We present a detailed discussion of the outcome of our simulations only for cases 5, 6 and 7 in
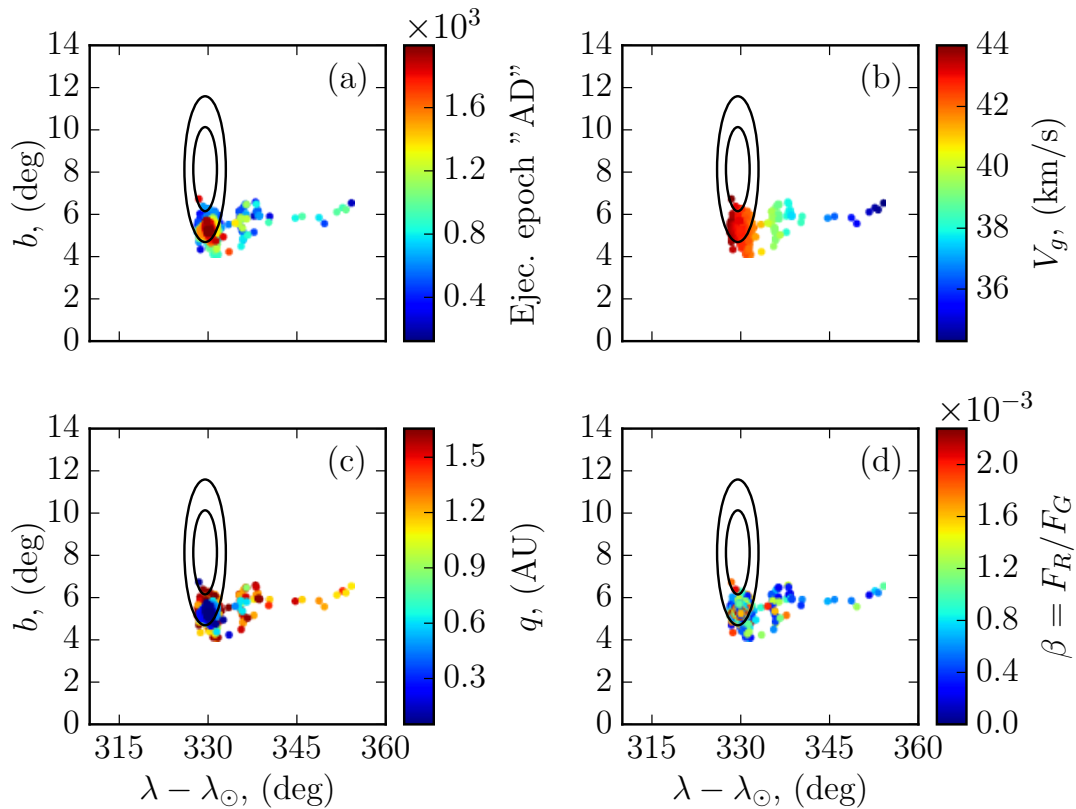
Figure 3.9: Radiant position of the simulated daytime Arietids (color dots) for case 1 in Table 3.2 and for clone (b) in Fig. 3.8, superimposed over the observed radiant position by CMOR (black circles). The radiant position is given in sun-centered reference frame with coordinates - the sun-centered longitude $\lambda - \lambda_\odot$ and ecliptic latitude b. The two circles correspond to 70% and 95% confidence region respectively. The observed radiant includes meteors to a limiting magnitude +6.5 and is adapted from Bruzzone et al. (2015). The the individual simulated radiants are color coded in terms of ejection epoch-panel (a), geocentric velocity V_g - panel (b), perihelion distance q at time of ejection - panel (c) and meteoroid β-value in panel (d). For the theoretical individual radiants, only meteoroids presently approaching the Earth's orbit within 0.01 AU have been considered.

Table 3.2 and provide a short discussion for the remaining cases which were similar in most respect.

Cases 6 and 7.

In case 6 we assumed a uniform cometary activity for 96P/Machholz. Figure 3.11 shows the individual theoretical "unweighted" activity profiles of the daytime Arietids, for meteoroid ejection onset in 10000 BC (case 6 in Table 3.2), for six individual clones of 96P. Superimposed is the observed normalized profile by CMOR, as a stack for the years of 2002-2013. The unweighted profiles combine simulated particles of all sizes, with radii between $s = 100 \ \mu m$ and $s = 1$ mm which span mass ranges for both radar and TV/Video meteors.
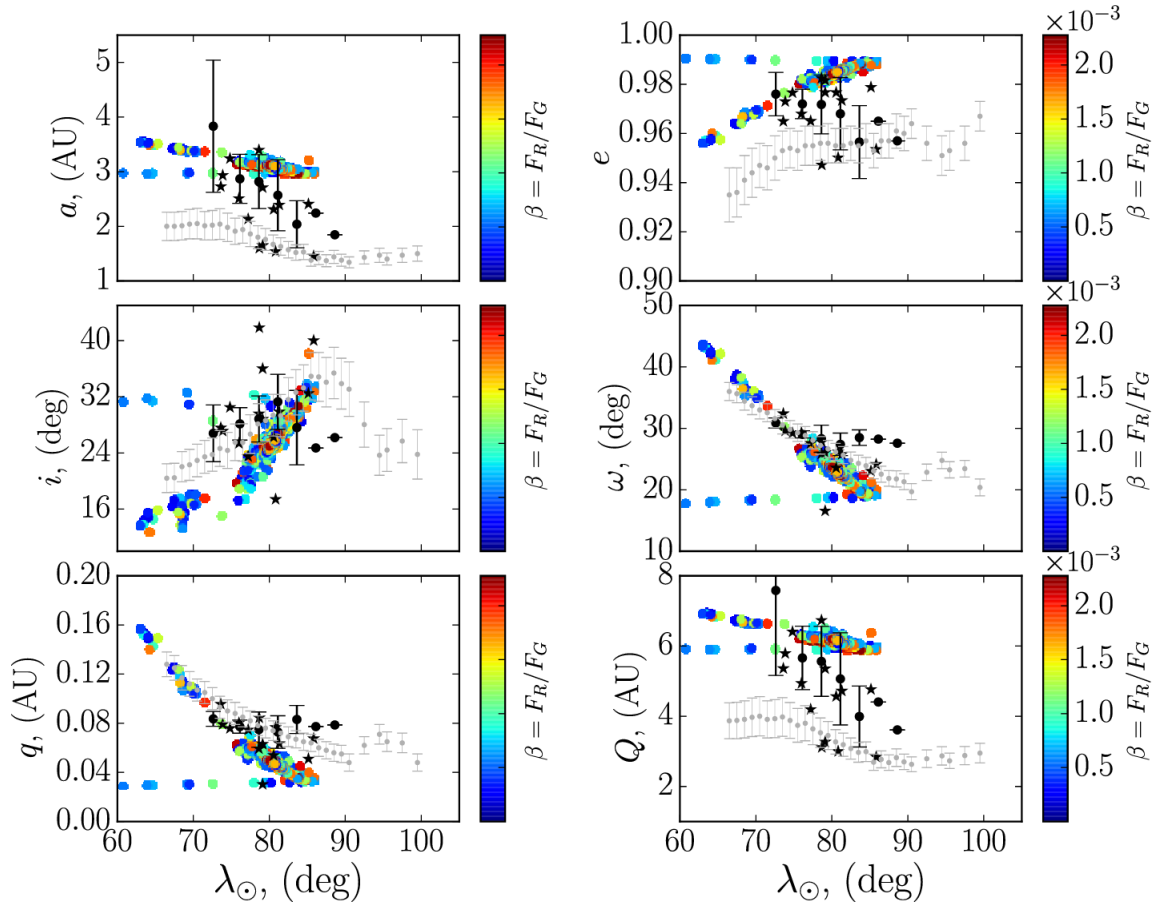
Figure 3.10: Distribution of the mean orbital elements, semi-major axis a, eccentricity e, inclination i, argument of perihelion ω, aphelion distance Q and perihelion distance q of the Daytime Arietids as a function of the solar longitude. Individual color dots correspond to individual simulated meteoroids, ejected from clones of P/1999 J6 starting in 150 AD (case 1), where the color coding is in terms of the meteoroids' β-values. The black dots with 1-σ error bars correspond to 31 video Arietids, detected between 2011-2012 and taken from the CAMS data from (Jenniskens et al., 2016). The grey dots with 1-σ error bars are derived from a decadal survey of the Arietids by CMOR (Bruzzone et al., 2015) and the black stars correspond to 14 individual TV events by (SonotaCo, 2009).

It is evident that that the peak of the activity profile is reproduced fairly well, while the resulting width of the profile is too narrow to be consistent with the observations. However, we have not yet weighted dust production by the parent's perihelion at the time of ejection. The resulting "weighted" profiles, for the six clones of 96P/Machholz, are presented in Fig. 3.12.

The weighted profile produces a good match, though the wings are still not reproduced well. For example, clone (a), produced the worst match in our sample, with sharp peak and a lower background activity exceeding the observed width of the shower's profile. Clone (b), on the other hand, yielded the best fit although not entirely filling the wings. The reason for the relatively poor match is the low number of particles away from the peak of the profile ($\sim 80.5°$). Figure 3.13 illustrates the situation by showing the time of ejection and the perihelion distance
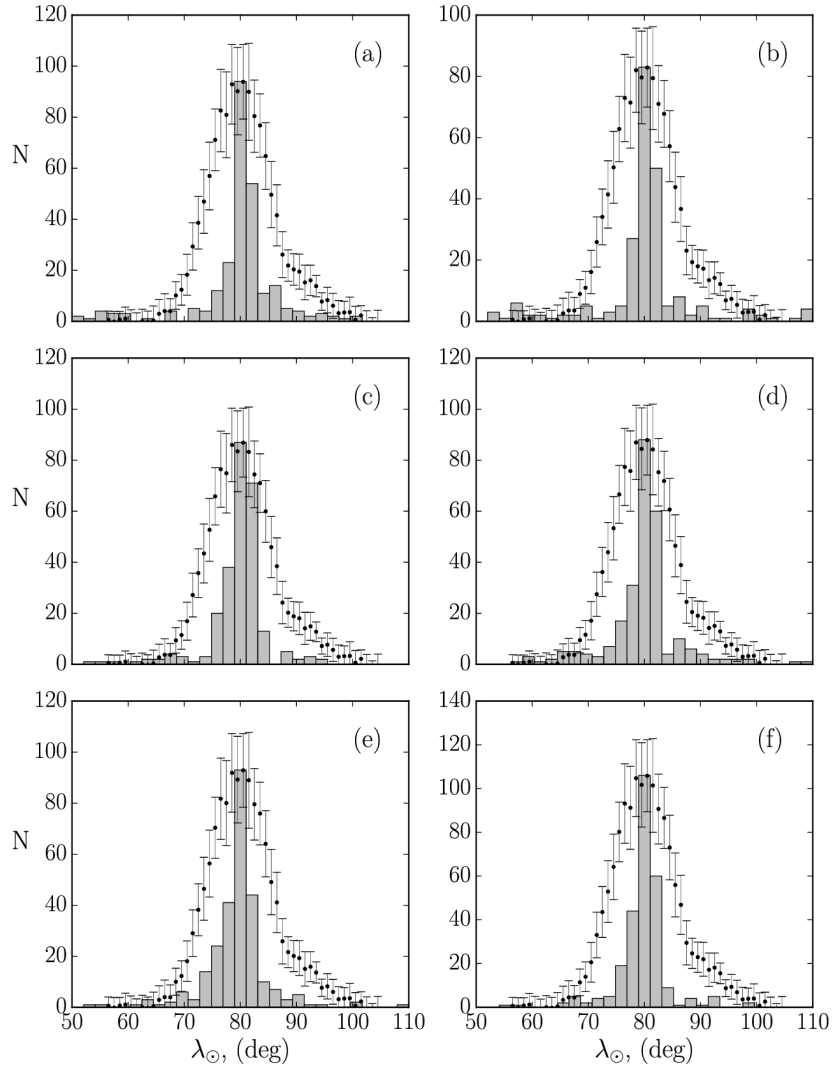
Figure 3.11: The simulated unweighted activity profile for the present daytime Arietids for meteoroid ejection in case 6, for six different clones - panels (a), (b), (c), (d), (e) and (f), superimposed over the observed profile by the CMOR (black dot with error bars), taken from Bruzzone et al. (2015).

of the parent at that time. The epochs of minimum perihelion distance are separated by ~ 4000 years (half the period of the Kozai cycle, see Sec. 3.3.3), so these particles ejected at these times are expected to contribute more to the activity profile of the Arietids. However, the particle distribution at epochs of low perihelion distance tend to be tightly concentrated contributing to a narrow peak. There are some older particles dispersed enough to fill the wings, but this would require the comet to have had higher dust production at early times, a scenario which we will investigate next.

Assuming that 96P/Machholz has been captured into a short period orbit circa 10000 BC, it is not unreasonable to expect that its activity level (dust and gas production rate) has changed over time, being more active in the past. In order to investigate that scenario, we modified case 6
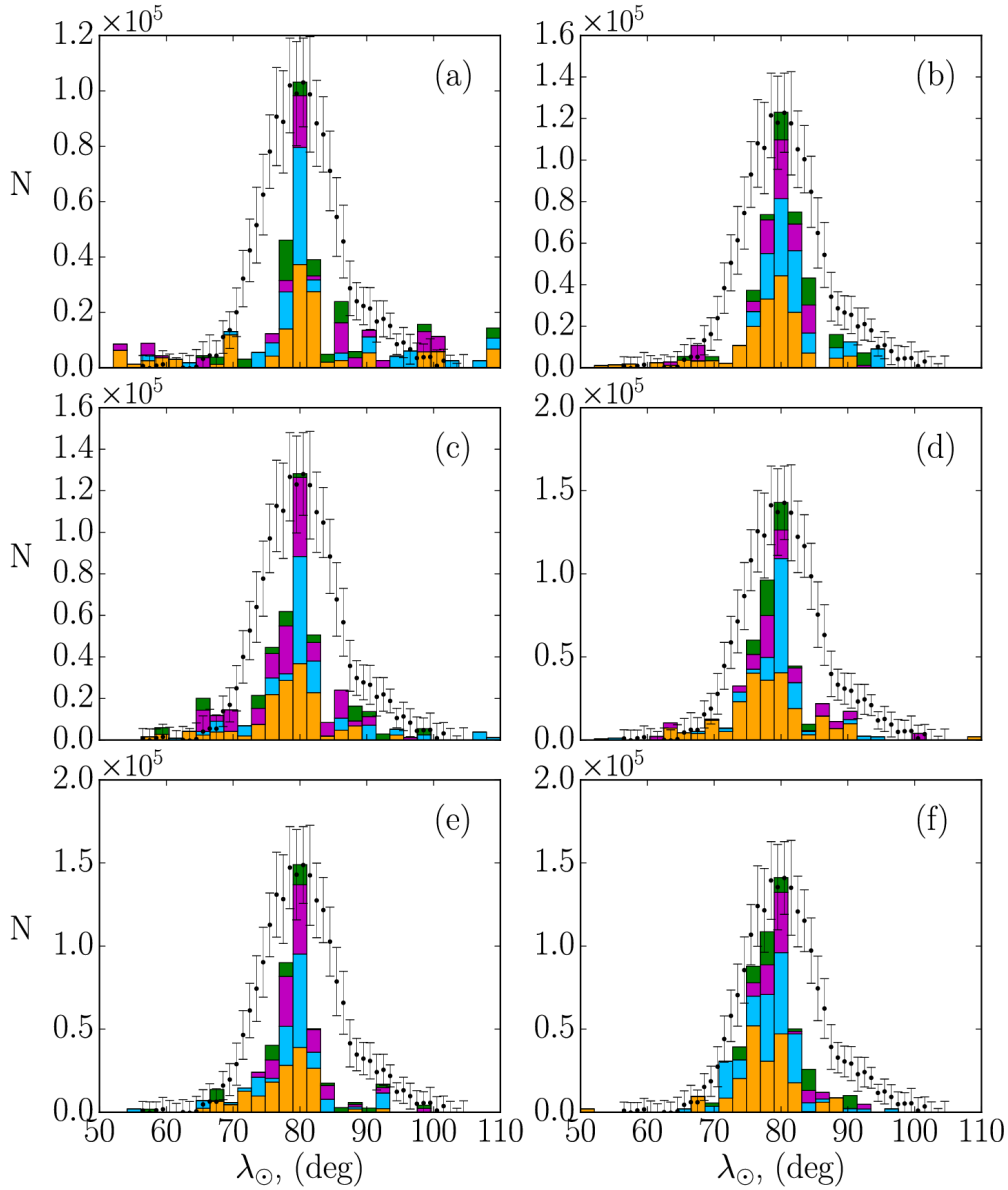
Figure 3.12: The weighted activity profile for the daytime Arietids, at the present for meteoroid ejection in case 6 in Table 3.2. The profiles are presented for six different clones - panels (a), (b), (c), (d), (e) and (f), superimposed over the observed profile by the CMOR (black dot with error bars) for meteors brighter than radio magnitude of +6.5. The error bars in the observed profile correspond to $1\,\sigma$. The four different colors in each stacked histogram denote particles of various size (expressed in terms of particles β−parameter). The "yellow" color corresponds to $\beta = (2 \times 10^{-4} - 6.5 \times 10^{-4})$, "blue" $\beta = (6.5 \times 10^{-4} - 1.1 \times 10^{-3})$, "magenta" $\beta = (1.1 \times 10^{-3} - 1.55 \times 10^{-3})$, and "green" $\beta = (1.55 \times 10^{-3} - 2 \times 10^{-3})$. Effectively, the "yellow" color corresponds to the smallest and the "green" color to the largest particles, respectively.
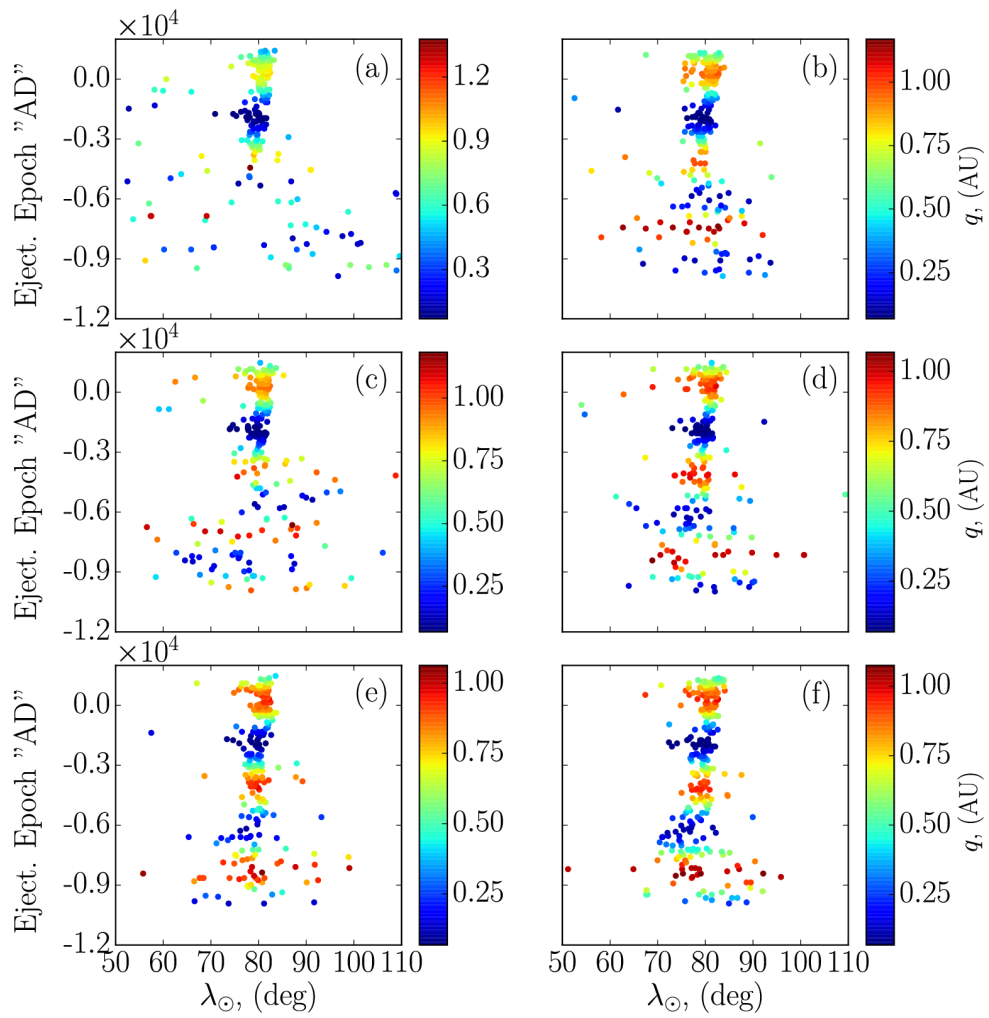
Figure 3.13: The present simulated distribution of the solar longitude $\lambda_\odot$ of meteoroids, for six clones of 96P/Machholz, as a function of the ejection epoch, for case 6 in Table 3.2. The color bar corresponds to the perihelion distance (q) of the meteoroids at the time of ejection.

(see Table 3.2 in Sec. 3.3.4), to reflect a decrease in the activity of 96P. We refer to this scenario as case 7. Figure 3.14 shows the unweighted activity profile of the daytime Arietids for case 7, and for six different clones. Relative to case 6, it produced a better fit to the observed profile by CMOR, matching the wings well. The worst match was observed for clone (a), producing a very sharp peak with wide lower background activity, whereas the rest of the clones reproduced the observed profile very well, with the best match being observed for clone (d). Similar to the previous case, however, this profile does not provide information about the particle size in each bin, nor does it capture the variability of the activity of 96P/Machholz. We therefore, apply the same weighting scheme, as in for case 6, to account for a higher dust production rate, expected during stages of lower perihelion distance. Fig. 3.15 shows the meteoroid distribution, presently approaching the Earth's orbit within 0.01 AU, as a function of their ejection epoch and perihelion distance at the time of ejection from six clones. The result of weighting the activity profile, as before, is presented in Fig. 3.16. It is evident that for some clones (b) and (e) the wings of the profile are reproduced fairly well, while for clone (a) the match was poor. The omitted clones also yielded relatively good matches typically consistent with the observed profile within the error bars.

The resulting simulated radiant position of the daytime Arietids for case 7 and clone (b) is shown in Fig. 3.17, superimposed over the observed mean radiant by CMOR. Different panels in the figure illustrate the individual radiants of the simulated meteoroids as a function of ejection epoch, geocentric speed V_g, perihelion distance at time of ejection and meteoroid β-values. The fit to the observations is exceptionally good with only a few particles being outside the 95% confidence region. It can be seen that the particles that are well outside the 95% confidence region hit the Earth with speeds below 38 km/s (panel (b) in Fig. 3.17), so that these meteoroids might not have been identified as Arietids by CMOR. Furthermore, we do not observe any mass segregation along the radiant (panel (d)), although there seems to be a slight correlation between the meteoroid ecliptic latitude b and the ejection epoch, where the latter differs by about 3° for youngest and oldest particles.

As was the case with the Marsden group comet P/1999 J6, simulations of 96P were not able to reproduce the distribution of all orbital elements of the daytime Arietids, as a function of the solar longitude $\lambda_\odot$ as observed by CMOR. Figure 3.18 shows the orbital elements according to our simulations superimposed over the observations by CMOR (Bruzzone et al., 2015), and 14 TV and 31 video daytime Arietids. Our simulations yielded systematically higher values for the semi-major axis a of the meteoroid, presently approaching the Earth's orbit within 0.01 AU, compared to CMOR measurements. A similar outcome was observed for the eccentricity e and the aphelion distance Q, while the inclination i, argument of perihelion ω and the perihelion distance yielded a good fit to the radar data. Our simulations are more consistent with the
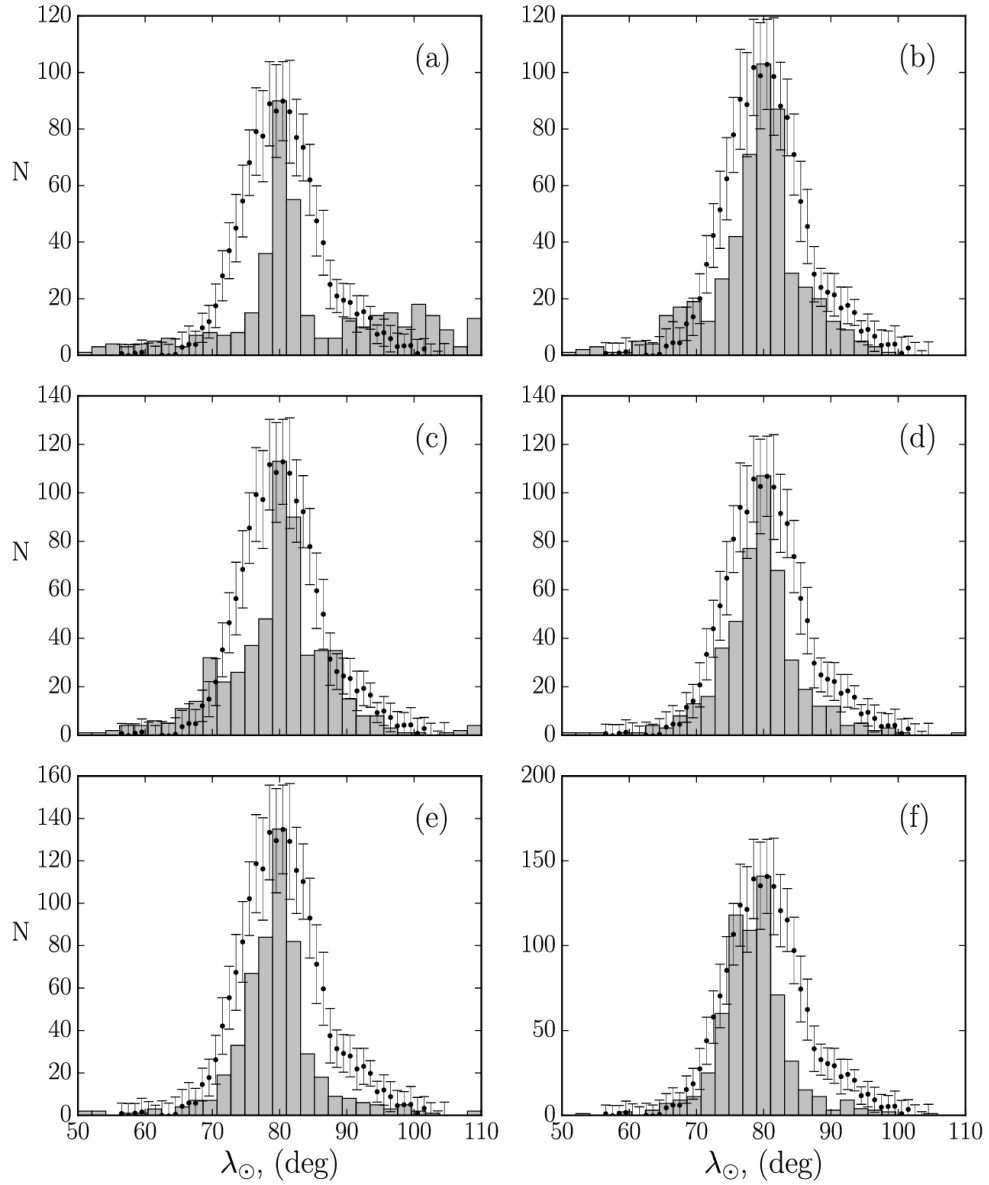
Figure 3.14: Simulated unweighted activity profile for the daytime Arietids, at the present, for meteoroid ejection for case 7 for six different clones panel (a), (b), (c), (d), (e) and (f), superimposed over the observed profile by the CMOR (black dot with error bars). The observed profile is a stack for the years of 2002-2013 and includes meteors to radar magnitude +6.5. The error bars in the observed profile correspond to 1 σ.
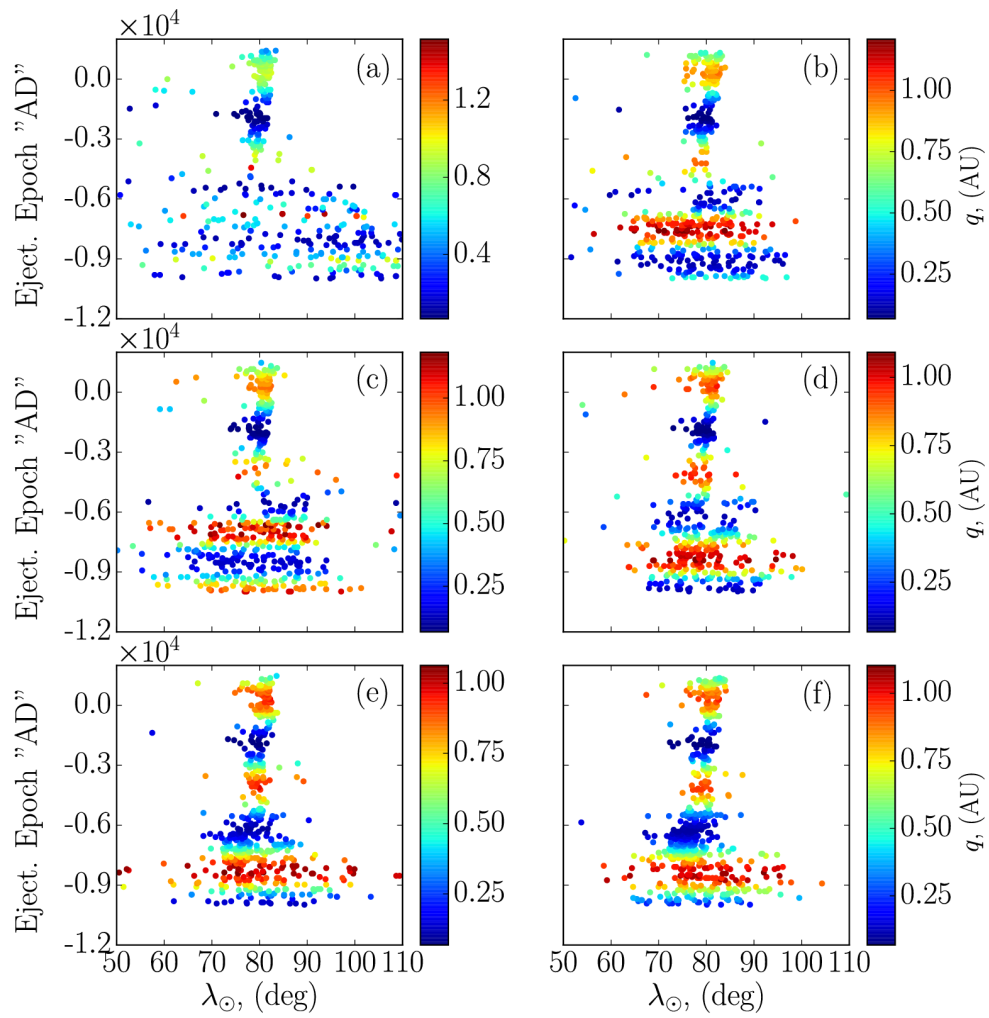
Figure 3.15: The present distribution of the solar longitude $\lambda_\odot$ of meteoroids, as a function of the ejection epoch for case 7 in Table 3.2. The color bar corresponds to the perihelion distance (q) of the meteoroids at the time of ejection.
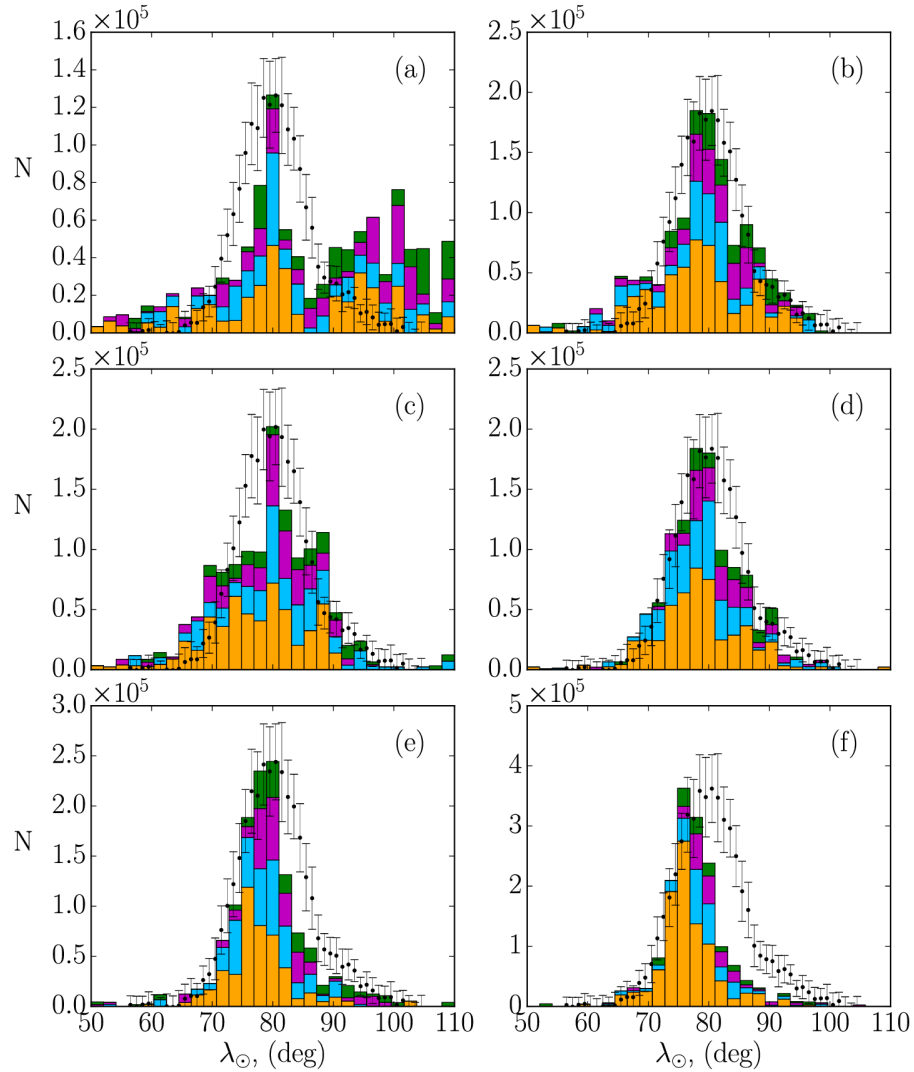
Figure 3.16: The weighted activity profile for the daytime Arietids, at the present for meteoroid ejection in case 7. The profiles are presented for six different clones - panels (a), (b), (c), (d), (e) and (f), superimposed over the observed profile by the CMOR (black dot with error bars) for meteors brighter than radio magnitude of +6.5. The error bars in the observed profile correspond to 1 σ. The four different colors in each stacked histogram denote particles of various size (expressed in terms of particles β−parameter). The "yellow" color corresponds to $\beta = (2 \times 10^{-4} - 6.5 \times 10^{-4})$, "blue" $\beta = (6.5 \times 10^{-4} - 1.1 \times 10^{-3})$, "magenta" $\beta = (1.1 \times 10^{-3} - 1.55 \times 10^{-3})$, and "green" $\beta = (1.55 \times 10^{-3} - 2 \times 10^{-3})$. Effectively, the "yellow" color corresponds to the smallest and the "green" color to the largest particles, respectively.

Figure 3.17: Radiant position of the simulated daytime Arietids (color dots) for case 7 in Table 3.2 for clone (b), superimposed over the observed mean radiant position by CMOR (black circles). The radiant position is given in sun-centered reference frame with coordinates - the sun-centered longitude $\lambda - \lambda_\odot$ and ecliptic latitude b. The two circles correspond to 70% and 95% confidence region respectively. The observed radiant includes meteors to a limiting magnitude +6.5 and is adapted from Bruzzone et al. (2015). The the individual simulated radiants are color coded in terms of ejection epoch-panel (a), geocentric velocity V_g - panel (b), perihelion distance q at time of ejection - panel (c) and meteoroid β-value in panel (d).

optical surveys. It is still not clear as to the origin of the discrepancies in *a*, *e* and *Q* between radar/optical and model values. We recall that Jenniskens et al. (2012) attributed the mismatch between the radar and optical surveys to an improper account for the deceleration profile for meteoroids detectable by radars which remains a possibility, despite the work of Bruzzone et al. (2015) which appeared to validate the observed radar speeds. Finally, all other clones which have been omitted here for convenience, resulted in very similar outcome, none being able to reproduce the observed distribution of the semi-major axis, eccentricity and the aphelion distance, with radar but resulting in a very good match with the optical surveys.
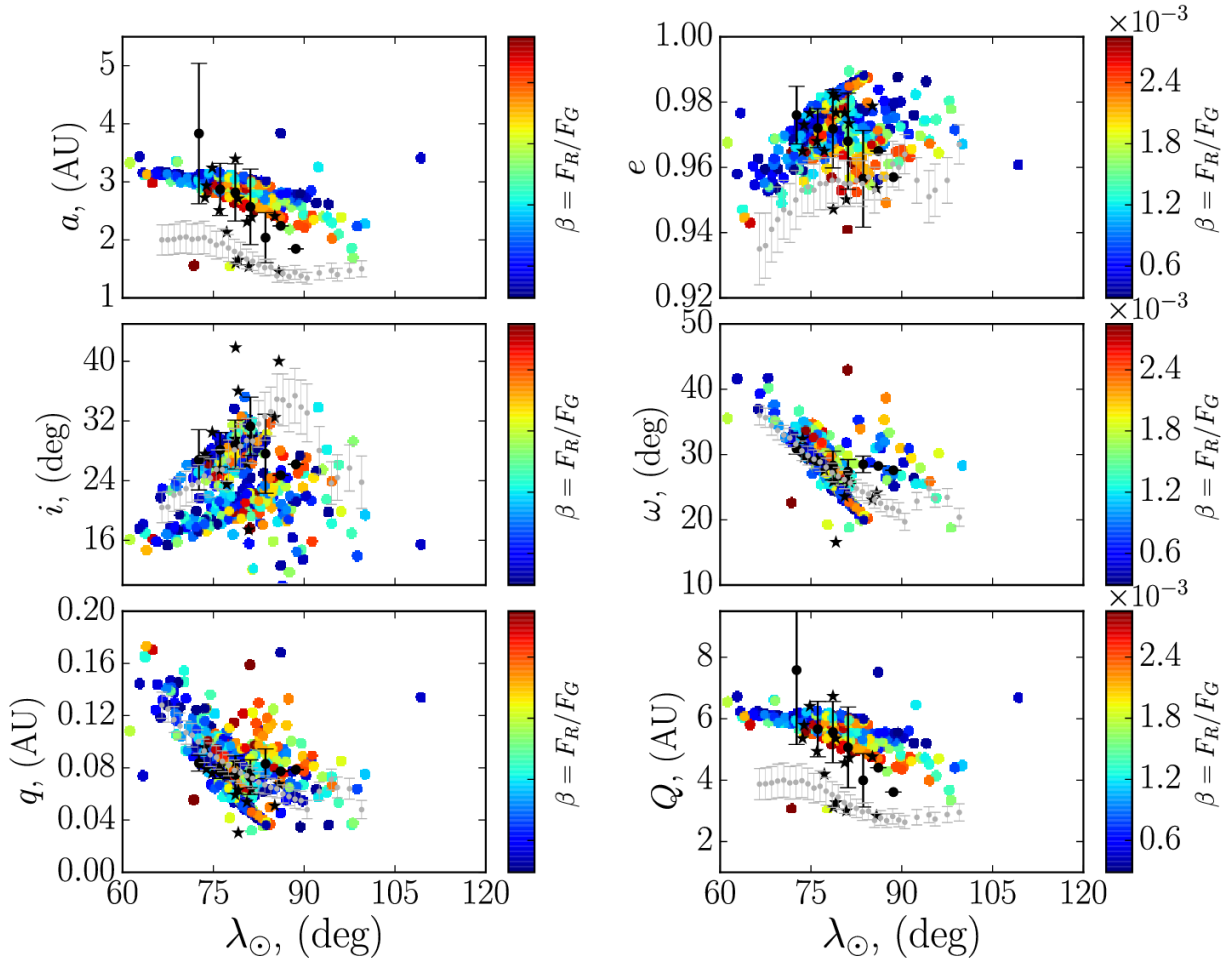
Figure 3.18: Distribution of the mean orbital elements, semi-major axis *a*, eccentricity *e*, inclination *i*, argument of perihelion *ω*, aphelion distance *Q* and perihelion distance *q* of the Daytime Arietids as a function of the solar longitude. Individual color dots correspond to individual simulated meteoroids, ejected from clones of 96P/Machholz starting in 10000 BC (case 7), where the color coding is in terms of the meteoroids' *β*-values. The black dots with 1-*σ* error bars correspond to 31 video Arietids, detected between 2011-2012 and taken from the CAMS data (Jenniskens et al., 2016). The grey dots with 1-*σ* error bars are derived from a decadal survey of the Arietids by CMOR (Bruzzone et al., 2015) and the black stars correspond to 14 individual TV events by (SonotaCo, 2009).

Case 5

In case 5, we use similar approach to case 7, assuming a variable dust production for 96P, with 3000 meteoroids per clone ejected between 6500 BC and 3000 BC and 1000 meteoroids per clone between 3000 BC and the present, see Table 3.2. Case 4, in our simulations, assumed a constant dust production rate over time and produced a narrow profile, inconsistent with the observed profile of the shower. The aim of case 5 is to check how well a variable dust production of 96P (similar to case 7) can reproduce the observed characteristics of the shower and to compare that to case 4. Fig. 3.19 shows the "unweighted" activity profile for six different clones in case 5. Moreover, this profile stacks particles of all size with radii between $100\mu m$ and 1 mm. It can be seen that the match is not as nearly good as in case 7, with all clones producing a relatively narrow peak and weak background activity. The reason for that can be inferred from Fig. 3.20, as the older particles are rather dispersed in nodal longitude, compared to particles ejected prior to 5000 BC. As a result, younger particles cause the peak to increase, whereas the dispersed older particles contribute only moderately to the wings.

In order to obtain a more realistic picture of the activity profile, we apply the same activity weighting as used in the cases 6 and 7, to account for the rate of dust production as a function of the perihelion distance. The result of this weighting is presented in Fig. 3.21 which also captures information about the particle size distribution in each bin of solar longitude $\lambda_\odot$. Regardless of the weighting, the match between the observations and our simulations was poorer compared to case 7, with the wings of the theoretical profiles being too narrow to match the observations by CMOR. Case 4, in our simulations produced a similar outcome, though with somewhat narrower wings, compared to case 5. In addition, we do not observe mass segregation along the activity profile, which could potentially explain the inconsistency in the distribution of the orbital elements as a function of the solar longitude, between the radar and optical surveys.

Fig 3.22 shows the simulated individual radiant positions of the daytime Arietids for case 5 and for clone (b). As in previous cases, the radiant position is given in sun-centered reference frame $(\lambda - \lambda_\odot)$ and (b), which aims to correct for the motion of the Earth on its orbit. Interestingly, the radiant produced produced a slightly better match as compared to case 7, though the width of the activity profile was inconsistent with the observations. The lack of mass sorting along the radiant is also evident from the figure (panel (d)), although obviously there is a strong correlation between the radiant position and the particles geocentric speed (panel (b)), and somewhat lower correlation as a function of the ejection epoch (panel (a)) and perihelion distance at the time of ejection (in panel (c)). However, it is not unreasonable to expect that small particles with speeds below 38 km/s are not associated with the stream in the CMOR study, so the particles outside the 95% confidence region may have been too sparse and slow
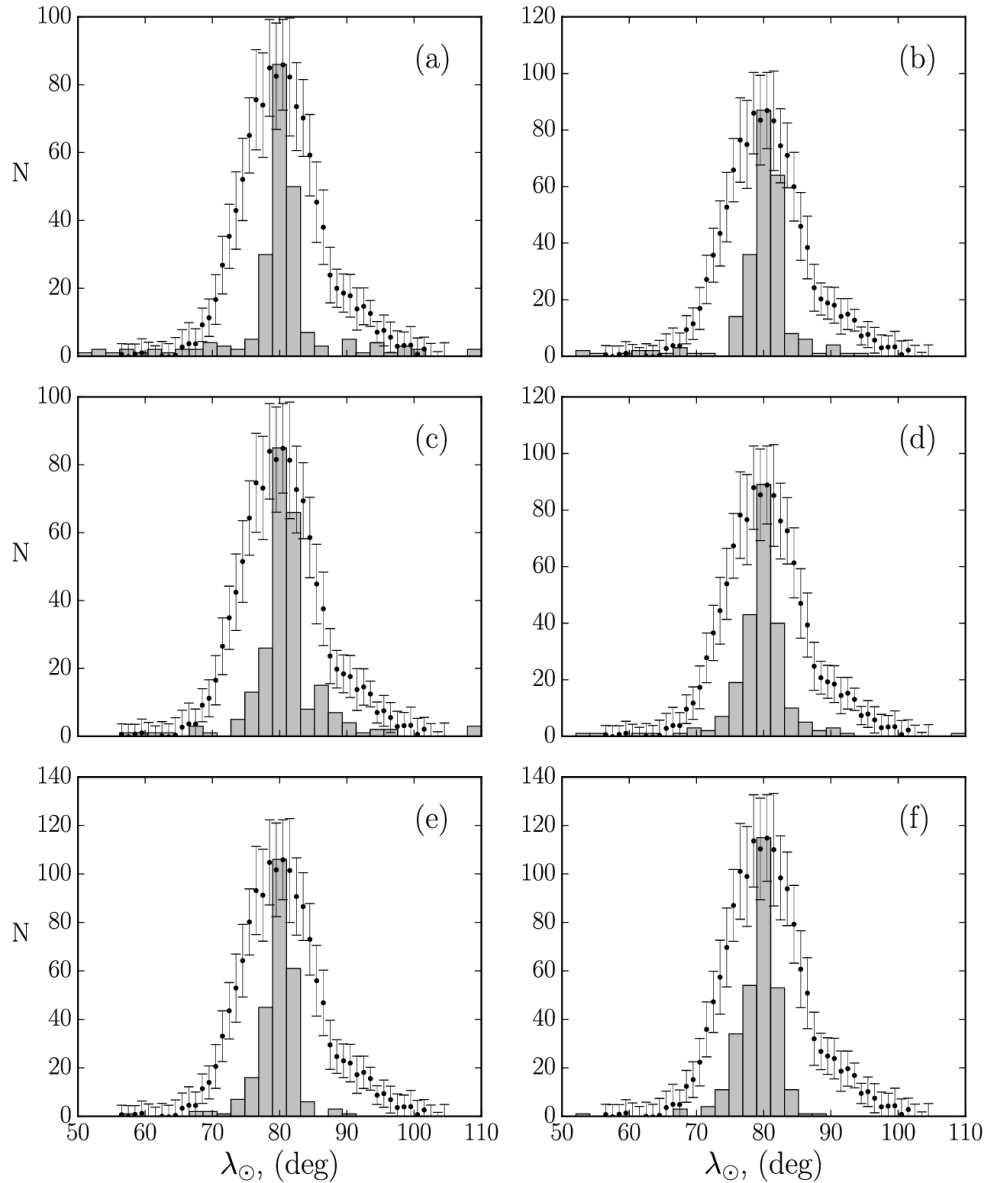
Figure 3.19: Simulated unweighted activity profile for the daytime Arietids, at the present, for meteoroid ejection for case 5 for six different clones panel (a), (b), (c), (d), (e) and (f), superimposed over the observed profile by the CMOR (black dot with error bars). The observed profile is a stack for the years of 2002-2013 and includes meteors to radar magnitude +6.5. The error bars in the observed profile correspond to 1 σ. For the theoretical profile, only meteoroids presently approaching the Earth's orbit within 0.01 AU have been considered.

to be registered by CMOR, as a part of the shower.

The distribution of the orbital elements, of meteoroids currently approaching the Earth's orbit within 0.01 AU, as a function of the solar longitude is presented in Fig. 3.23. These did not differ significantly from the previous cases. Some of the orbital elements, such as semi-major axis (a), eccentricity (e) and the aphelion distance (Q), of the simulated meteoroids, yielded systematically higher values, compared to the decadal radar survey of the Arietids by CMOR.
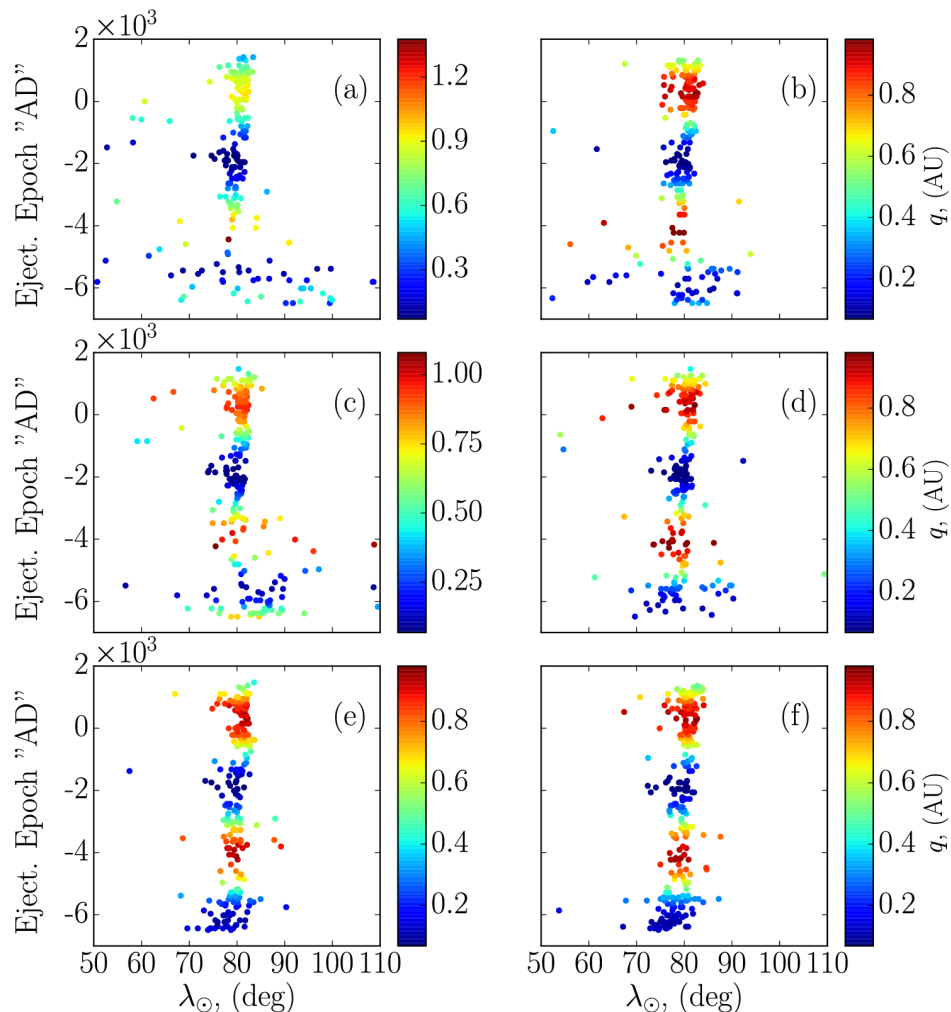
Figure 3.20: The present distribution of the solar longitude $\lambda_\odot$ of meteoroids, as a function of the ejection epoch for case 5 in Table 3.2. The color bar corresponds to the perihelion distance (q) of the meteoroids at the time of ejection. Only meteoroids approaching the Earth's orbit within 0.01 AU have been considered.

The effect of the Poynting-Robertson drag is too small to explain the orbit inconsistency between the radar and optical surveys, over these formation time periods. In fact, our simulated meteoroids matched better the 14 TV (SonotaCo, 2009) and the 31 CAMS (Jenniskens et al., 2016) events, although we observed a large dispersion among individual optically detected Arietids.

Assuming that the underlying mechanism of the formation of the daytime Arietids is due to a normal cometary outgassing, our results indicate that the origin of the stream is more consistent with comet 96P/Machholz, rather than the most prominent member of the Marsden group of sunskirting comets P/1999 J6. Moreover, our simulations indicate that age of the daytime Arietids is at least 12000 years, based on the comparison of our theoretical results compared to the decadal survey of the daytime Arietids meteor shower by CMOR, in particular
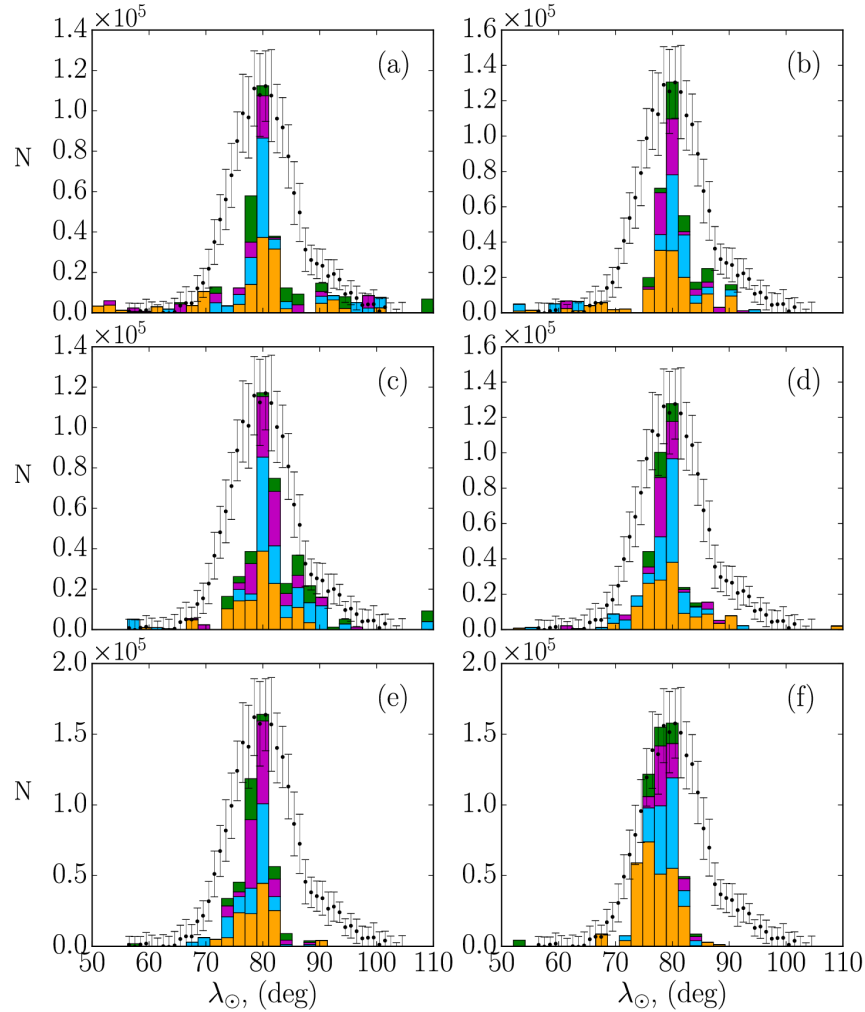
Figure 3.21: The weighted activity profile for the daytime Arietids, at the present for meteoroid ejection in case 5. The profiles are presented for six different clones - panels (a), (b), (c), (d), (e) and (f), superimposed over the observed profile by the CMOR (black dot with error bars) for meteors brighter than radio magnitude of +6.5. The error bars in the observed profile correspond to 1 σ. The four different colors in each stacked histogram denote particles of various size (expressed in terms of particles β−parameter). The "yellow" color corresponds to $\beta = (2 \times 10^{-4} - 6.5 \times 10^{-4})$, "blue" $\beta = (6.5 \times 10^{-4} - 1.1 \times 10^{-3})$, "magenta" $\beta = (1.1 \times 10^{-3} - 1.55 \times 10^{-3})$, and "green" $\beta = (1.55 \times 10^{-3} - 2 \times 10^{-3})$. Effectively, the "yellow" color corresponds to the smallest and the "green" color to the largest particles, respectively. For the theoretical profile, only meteoroids presently approaching the Earth's orbit within 0.01 AU have been considered.

the spread in nodal longitudes. Finally, our results indicate that P/1999 J6 and perhaps other members of the Marsden group of sunskirters may contribute to the peak of stream but are not able to explain the older "wings". Hence, these sunskirters alone are not responsible for the stream.
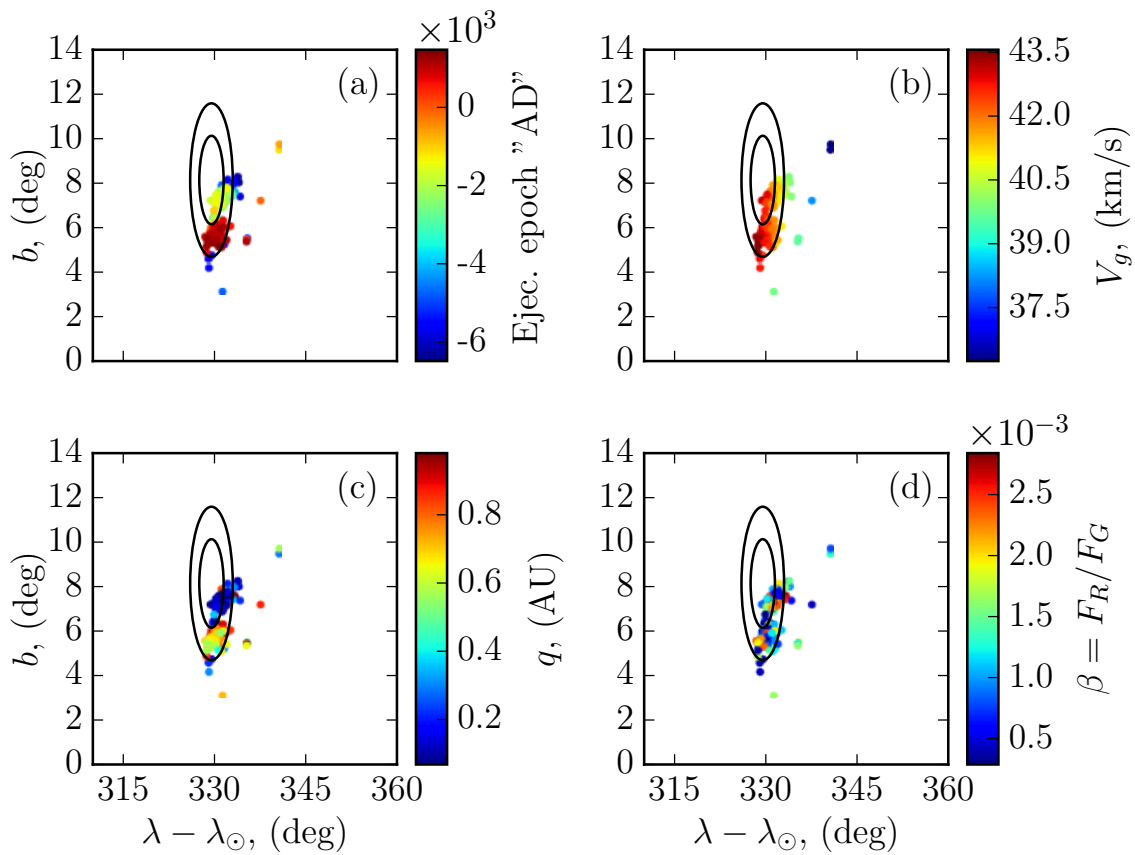
Figure 3.22: Radiant position of the simulated daytime Arietids (color dots) for case 5 in Table 3.2 for clone (b), superimposed over the observed mean radiant position by CMOR (black circles). The radiant position is given in sun-centered reference frame with coordinates - the sun-centered longitude $\lambda - \lambda_\odot$ and ecliptic latitude b. The two circles correspond to 70% and 95% confidence region respectively. The observed radiant includes meteors to a limiting magnitude +6.5 and is adapted from Bruzzone et al. (2015). The the individual simulated radiants are color coded in terms of ejection epoch-panel (a), geocentric velocity V_g - panel (b), perihelion distance q at time of ejection - panel (c) and meteoroid β-value in panel (d). The theoretical individual radiants include only meteoroids, that approach the Earth's orbit within 0.01 AU.
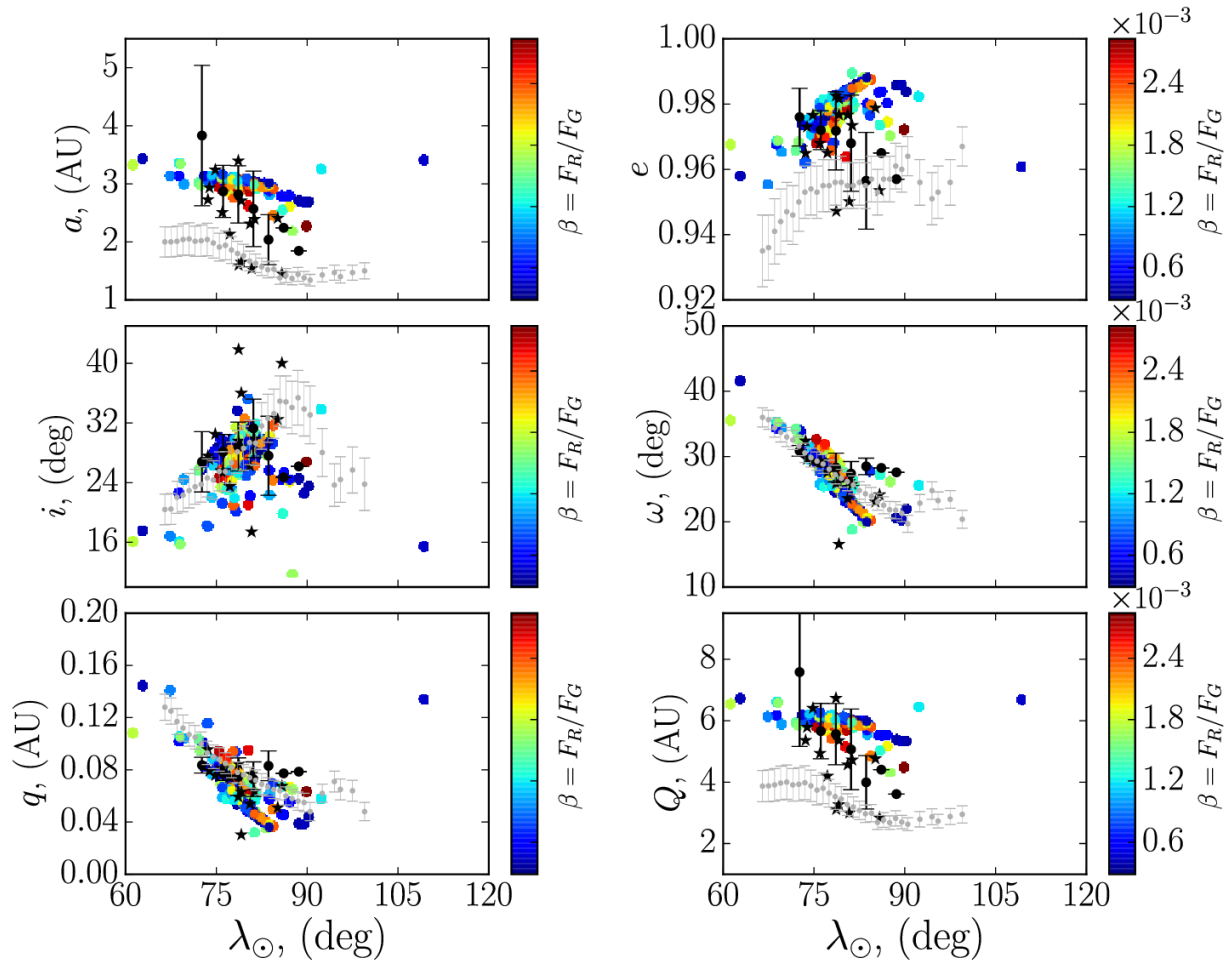
Figure 3.23: Distribution of the mean orbital elements, semi-major axis *a*, eccentricity *e*, inclination *i*, argument of perihelion ω, aphelion distance *Q* and perihelion distance *q* of the observed and simulated daytime Arietids as a function of the solar longitude. Individual color dots correspond to individual simulated meteoroids, ejected from clones of 96P/Machholz starting in 6500 BC (case 5), where the color coding is in terms of the meteoroids' β-values. The black dots with 1-σ error bars correspond to 31 video Arietids, detected between 2011-2012 and taken from the CAMS data (Jenniskens et al., 2016). The grey dots with 1-σ error bars are derived from a decadal survey of the Arietids by CMOR (Bruzzone et al., 2015) and the black stars correspond to 14 individual TV events by (SonotaCo, 2009).

Cases 8 and 9: Discrepancy between radar and optical Arietids surveys

In previous sections, we briefly discussed the observed discrepancy between some of the orbital elements of the Arietids as deduced from radar and optical surveys. To address this question more fully, we performed additional simulations (cases 8 and 9 in Table 3.2 in Sec. 3.3.4) in order to test whether the inconsistency between the orbital elements of 50 - 100 *μm* and millimeter size meteoroids can be attributed to the Poynting-Robertson drag, acting over a prolonged time scale. We first show the results for an assumed age of 30000 BC (case 9) and

we then compare these results to case 8.

Fig. 3.24 shows the simulated distribution of the orbital elements for the daytime Arietids, ejected from one particular clone of 96P/Machholz in 30000 BC (case 9). In addition, superimposed are the observed distributions of the mean orbital elements as derived from the decadal survey by CMOR (Bruzzone et al., 2015), 31 video observations by CAMS (Jenniskens et al., 2016) and 14 individual TV Arietids from (SonotaCo, 2009). It is evident from the figure that the action of Poynting-Robertson drag, over a time interval of 32000 years, is sufficient to decrease the semi-major axis of 100 μm size Arietids, to their presently observed values by CMOR, though the nodal timing for these meteoroids is inconsistent with the observations. That is, meteoroids with semi-major axis of the order of 1.5 AU and below, would peak a month later than the presently observed time of maximum activity, for our particular starting orbits. Moreover, it is also evident from Fig. 3.24 that the continuous action of the Poynting-Robertson drag, over 32000 years, decreases the eccentricity of meteoroids' orbits to values as low as e ~0.88, whereas CMOR yields values of the order of e ~0.96. An obvious discrepancy is also observed between the angular orbital elements (inclination and argument of perihelion), as well as the perihelion and aphelion distances, with other clones of 96P/Machholz yielding similar results. This is not surprising as we are using test orbits for the stream, much older than it is possible to know the true parent and hence the simulated particles end up in random phases of the Kozai cycle.

The simulated radiant positions of individual Arietids, ejected in 30000 BC (case 9) is presented in Fig. 3.25, along with 68% and 95% confidence regions as observed by CMOR (Bruzzone et al., 2015). Evidently, our simulations of the radiant position do not match the radar observations, with the simulated radiant positions yielding slightly higher values for the ecliptic latitude of the radiant with a significant scatter in the ecliptic longitude. Clearly, the action of the Poynting-Robertson drag over 32000 years leads to low values of the semi-major axis and in particular of the eccentricity, where the latter is even significantly lower than the predicted values by CMOR. Without knowing the actual parent orbit this far in the past, we can only say that it is possible that the differential Poynting-Robertson drag has produced the differences in the orbital elements between the radar and optical measurements and if so, the stream must be much older than $\sim$ 12000 years.

To test whether given a shorter action time scale of the Poynting-Robertson drag can reproduce the observed distribution of the orbital elements of radar Arietids, we ejected 5×10^4 meteoroids from 10 clones of 96P/Machholz in 20000 BC which is our case 8. We used values of 50 μm for radar sized Arietids, almost certainly a factor of several too small relative to CMOR values. Figure 3.26 shows the simulated distribution of the orbital elements of the meteoroids, presently approaching the Earth within 0.01 AU, compared with the radar and op-
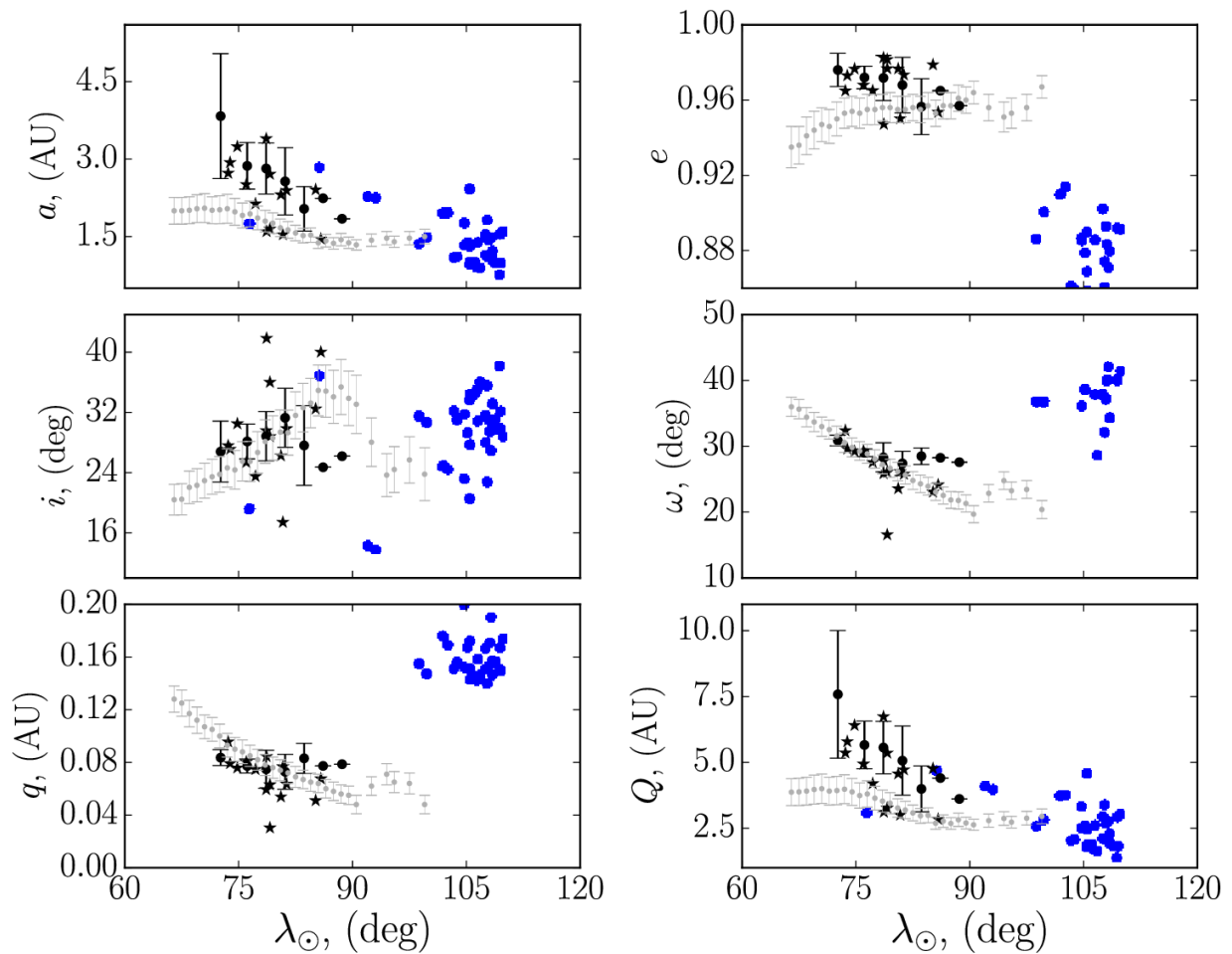
Figure 3.24: Distribution of the mean orbital elements of the simulated daytime Arietids as a function of the solar longitude, ejected in 30000 BC (case 9). The blue dots correspond to individual simulated meteoroids whereas the grey dots with 1-σ error bars correspond to the mean orbital elements of the Arietids, as detected by CMOR (Bruzzone et al., 2015). The black dots with 1-σ error bars are derived from video observations by CAMS (Jenniskens et al., 2012) and the black stars correspond to 14 TV events by (SonotaCo, 2009).

tical observations. Although the resulting values of the semi-major axis and eccentricity of the orbits were slightly higher compared to meteoroids ejected in 30000 BC, the position of the simulated peak activity was again shifted to higher values of solar longitude, predicting that the maximum activity would occur somewhat 30 days later than the presently observed location of the peak, a situation also observed in case 9. In addition, the angular orbital elements as well as the perihelion and aphelion distances did not fit the observations as expected, . Figure 3.27 shows the simulated individual radiant positions of the meteoroids for case 8, compared to the 68% and 95% confidence regions of the mean radiant position as observed by CMOR. Similar to case 9, the ecliptic latitude was inconsistent with the observations, though the dispersion in the ecliptic longitude was lower compared to meteoroids ejected in 30000 BC. The rest of

Figure 3.25: Individual radiant position distribution (blue dots) for meteoroids ejected in 30000 BC (case 9) from one particular clone of comet 96P/Machholz. The two superimposed circles correspond to 68% and 95% confidence regions of the mean radiant of the Arietids, as derived by CMOR (Bruzzone et al., 2015).

the clones yielded similar overall results, with some meteoroids attaining orbits with very low semi-major axis (even lower that the predicted values by CMOR) though the timing (location of the peak) is inconsistent with the observations.
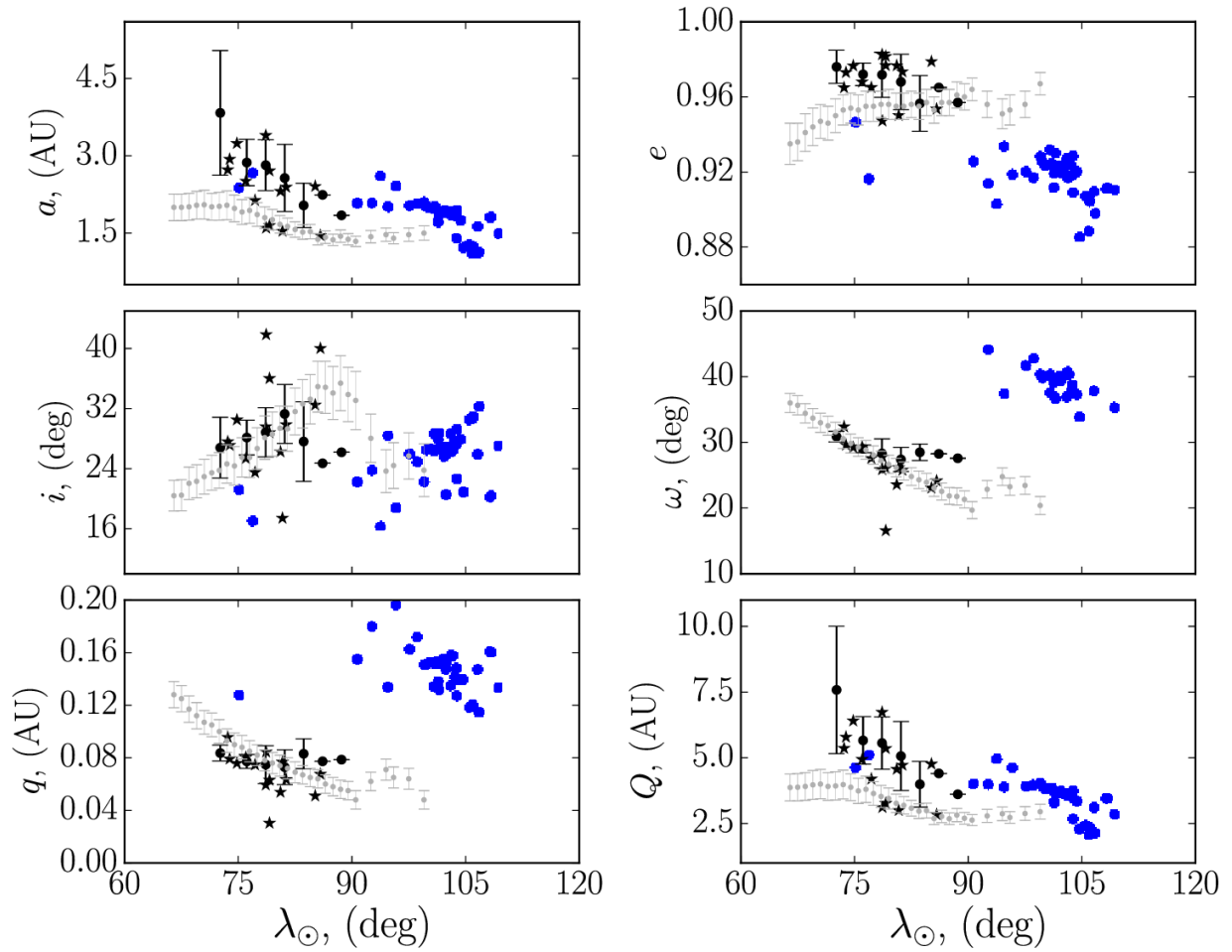
Figure 3.26: Distribution of the mean orbital elements of the daytime Arietids as a function of the solar longitude, ejected in 20000 BC (case 8). The blue dots correspond to individual simulated meteoroids whereas the grey dots with 1-σ error bars correspond to the mean orbital elements of the Arietids, as detected by CMOR (Bruzzone et al., 2015). The black dots with 1-σ error bars are derived from video observations by CAMS (Jenniskens et al., 2016) and the black stars correspond to 14 TV events by (SonotaCo, 2009).

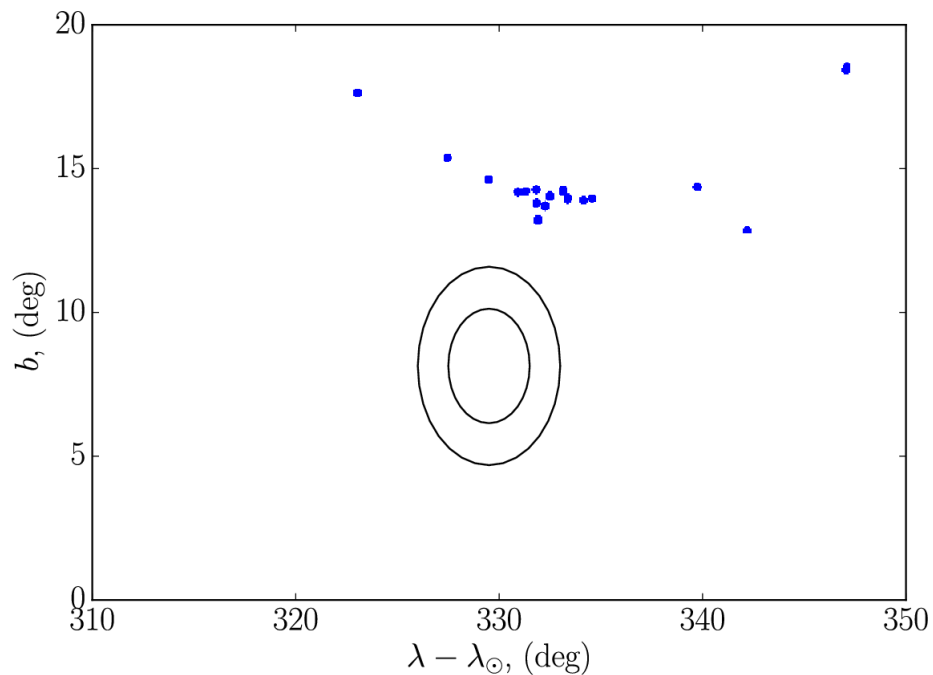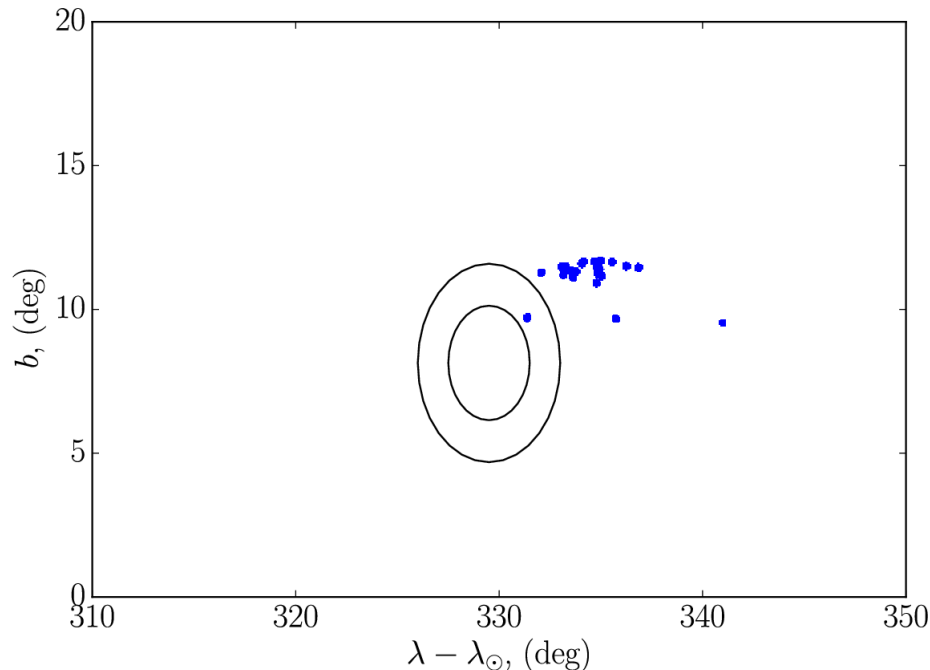Figure 3.27: Individual radiant position distribution (blue dots) for meteoroids ejected in 20000 BC (case 8) from one particular clone of comet 96P/Machholz. The two superimposed circles correspond to 68% and 95% confidence regions of the mean radiant of the Arietids, as derived by CMOR (Bruzzone et al., 2015).

Finally, our simulations suggest that if the daytime Arietids originated from 96P/Machholz, the secular action of Poynting-Robertson drag over a time scale of $(2 - 3) \times 10^4$ years can significantly decrease the orbits of particles with radius $s = 50\mu$m to values presently observed by radar surveys, though we do not know the true orbit of the parent this far back in the past. This renders it difficult draw any rigorous conclusions as to the orbit discrepancies between radar and optical daytime Arietid surveys. Furthermore, particles with radii $s = 50\mu$m, entering the Earth's atmosphere with geocentric speeds of $V_g \approx 40$ km/s are probably below the detectability threshold of CMOR, given the uncertainties in the mass scale (e.g., Weryk and Brown, 2013).

Unfortunately, we do not presently have sufficient information to argue conclusively as to whether the discrepancy in the orbital elements between radar and optical sized daytime Arietids is due to some systematic errors in radar surveys (e.g., inappropriate account for atmospheric deceleration) or systematic effects in the optical detection of the stream (e.g., all optical detections occur with very low local radiants) or some physical effect which mass separates them on orbits presently detected by radar systems.

3.5 Discussion and Conclusions

We have performed a numerical study to investigate the origin and formation of the daytime Arietids, in order to constrain its age and to investigate the child-parent relationship of the stream with the two proposed parents, comet 96P/Machholz and the Marsden group of sunskirting comets. Throughout, this work we examined various possible scenarios of the formation of the stream, considering various formation epochs but constraining ourselves to only formation of the stream via normal cometary activity.

We first investigated a possible origin of the daytime Arietids from the Marsden sunskirting group of comets. We considered the most prominent member, namely P/1999 J6 which has survived at least a few perihelion returns to the Sun on an orbit with extreme perihelion distance of ~10 $R_\odot$. Our selection of P/1999 J6 was motivated by the fact that most of the Marsden group of sunskirters are very faint and with poorly constrained orbits, while the orbit of P/1999 J6 is relatively reliable. We therefore, tested a possible origin of the stream from P/1999 J6, considering various meteoroid ejection onset epochs (cases 1 through 5) as suggested by Sekanina and Chodas (2005). The theoretical characteristics of the resulting stream were compared against the decadal survey of the daytime Arietids by CMOR (Bruzzone et al., 2015).

For case 1, we expected the widest profile, due to earlier ejection times, but case 1 along with all other cases resulted in a very sharp peak of both, the unweighted and weighted activity profiles, matching the observed location of the maximum activity, though producing a very narrow overall profile, inconsistent with the observations by CMOR. As a result, we conclude P/1999 J6 cannot have produced the entire Arietids stream though it may well contribute to its core. The theoretical distribution of many of the orbital elements such as, the semi-major axis a, eccentricity e and aphelion distance Q, as a function of the solar longitude $\lambda_\odot$, do match radar observations, with the numerical integrations yielding systematically higher values for a, e and Q, mostly consistent with optical surveys of the daytime Arietids by SonotaCo and CAMS.

For the second parent candidate, 96P/Machholz, we investigated seven different scenarios (cases 1 through 7) assuming various meteoroid ejection onset times and variable dust production rate for some cases. Similar to the case with P/1999 J6 (above), we utilized a weighting factor as a function of the parent body's perihelion distance at the time of ejection.

The best match between the observed and simulated characteristics of the daytime Arietids, assuming an origin from 96P/Machholz, was observed for case 7, with an onset 12000 years ago and a decreasing dust production over time through the present. For this simulation, the match in the activity profiles was very good, with the model being able to reproduce both the

location of the peak and the width of the observed activity profile. Other cases produced a good fit to the location of the peak, though the width of the profile was too narrow and thus inconsistent with the observations by CMOR. The radiant location was a good match for all cases with the bulk of the individual radiants being within the 95% confidence region of the mean radiant position as deduced by CMOR. Similar to the case with P/1999 J6, there was a correlation between the the individual radiant location and the particles' geocentric speed, with slower particles having radiant outside the 95% confidence region of the observed radiant, so those slow particles might not have been counted as Arietids by CMOR's software.

Despite the excellent match of the activity profile and radiant position for case 7, there was still a discrepancy between the observed radar and simulated distribution of orbital elements of the meteoroids as a function of the solar longitude. Our simulations yielded systematically higher values for the semi-major axis a, eccentricity e and the aphelion distance Q than the radar data, but consistent with optical surveys of the daytime Arietids by SonotaCo (SonotaCo, 2009) and CAMS Jenniskens et al. (2016).

Lastly, we have investigated whether the discrepancy in the orbital elements as deduced from radar and optical surveys can be attributed solely to the Poynting-Robertson drag, acting on radar size particles. We investigated two different cases with particles of radii s=50 μm released from 96P/Machholz at two different discrete eras, 20000 BC and 30000 BC. We conclude that the continuous action of Poynting-Robertson drag, over time scales of $(2\text{-}3)\times10^4$ years may decrease the semi-major axis to the presently observed values by radar surveys, though the location of the peak was inconsistent, being more than a month later than its present value. We mote the choice of particles with radii s=50 μm, hitting the Earth's atmosphere, are extreme lower limits to the detection of the daytime Arietids by CMOR, rendering the obtained values for the semi-major axis of the orbits only a lower limit.

In summary, we conclude that the daytime Arietid meteoroid stream is most likely associated with comet 96P/Machholz and has an age of at least 12000 years. However, a child-parent relationship between the Arietids and the Marsden group of sun-skirting comets can not be completely ruled out, and P/1999 J6 may contribute to the core of the stream. Unfortunately, we can not discern whether the discrepancy between the orbital elements, derived from radar and optical surveys, is real or an artifact. However, our simulations suggest that if the mass segregation is real, then the stream must be several tens of thousands of years old, in order for such a large difference between the orbital elements to exist.

Bibliography

A'Hearn, M.F., Millis, R.C., Schleicher, D.O., Osip, D.J., Birch, P.V., 1995. The ensemble properties of comets: Results from narrowband photometry of 85 comets, 1976-1992. Icarus 118, 223–270.

Almond, M., 1951. The summer daytime meteor streams of 1949 and 1950. III. Computation of the orbits. MNRAS 111, 37.

Aspinall, A., Clegg, J.A., Lovell, A.C.B., 1949. The Daytime Meteor Streams of 1948. Part I. Measurement of the Activity and Radiant Positions. MNRAS 109, 352.

Aspinall, A., Hawkins, G.S., 1951. The summer daytime meteor streams of 1949 and 1950. I. Measurement of the radiant positions and activity. MNRAS 111, 18.

Babadzhanov, P.B., Obrubov, Y.V., 1992. P/Machholz 1986 VIII and quadrantid meteoroid stream. Orbital evolution and relationship, in: Harris, A.W., Bowell, E. (Eds.), Asteroids, Comets, Meteors 1991, pp. 27–32.

Babadzhanov, P.B., Obrubov, Y.V., 1993. Dynamics and relationship between interplanetary bodies: Comet P/Machholz and its meteor showers, in: Stohl, J., Williams, I.P. (Eds.), Meteoroids and their Parent Bodies, p. 49.

Baggaley, W.J., Bennett, R.G.T., Steel, D.I., Taylor, A.D., 1994. The Advanced Meteor Orbit Radar Facility - AMOR. Quart. Journ. of the Royal Astron. Soc. 35, 293.

Bailey, M.E., Chambers, J.E., Hahn, G., 1992. Origin of sungrazers - A frequent cometary end-state. A&A 257, 315–322.

Brown, P., Jones, J., 1998. Simulation of the Formation and Evolution of the Perseid Meteoroid Stream. Icarus 133, 36–68.

Bruzzone, J.S., Brown, P., Weryk, R.J., Campbell-Brown, M.D., 2015. A decadal survey of the Daytime Arietid meteor shower using the Canadian Meteor Orbit Radar. MNRAS 446, 1625–1640.

Burns, J.A., Lamy, P.L., Soter, S., 1979. Radiation forces on small particles in the solar system. Icarus 40, 1–48.

Campbell-Brown, M.D., 2004. Radar observations of the Arietids. MNRAS 352, 1421–1425.

Carusi, A., Kresak, L., Perozzi, E., Valsecchi, G.B., 1987. High-Order Librations of Halley-Type Comets. A&A 187, 899.

Chambers, J.E., 1999. A hybrid symplectic integrator that permits close encounters between massive bodies 304, 793–799.

Clegg, J.A., Hughes, V.A., Lovell, A.C.B., 1947. The Daylight Meteor Streams of 1947 May-August. MNRAS 107, 369.

Davies, J.G., Greenhow, J.S., 1951. The summer daytime meteor streams of 1949 and 1950. II. Measurement of the velocities. MNRAS 111, 26.

Delsemme, A.H., 1982. Chemical composition of cometary nuclei, in: Wilkening, L.L. (Ed.), IAU Colloq. 61: Comet Discoveries, Statistics, and Observational Selection, pp. 85–130.

Fujiwara, Y., Ueda, M., Sugimoto, M., Sagayama, T., Abe, S., 2004. TV Observation of the Daytime Meteor Shower; The Arietids. Earth Moon and Planets 95, 595–600.

Hawkes, R.L., 1993. Television meteors (Invited), in: Stohl, J., Williams, I.P. (Eds.), Meteoroids and their Parent Bodies, p. 227.

Hawkes, R.L., 2002. Meteors in the Earth's Atmosphere. p. 97.

Jenniskens, P., Duckworth, H., Grigsby, B., 2012. Daytime Arietids and Marsden Sunskirters (ARI, IAU #171). WGN, Journal of the International Meteor Organization 40, 98–100.

Jenniskens, P., Gural, P.S., Dynneson, L., Grigsby, B.J., Newman, K.E., Borden, M., Koop, M., Holman, D., 2011. CAMS: Cameras for Allsky Meteor Surveillance to establish minor meteor showers. Icarus 216, 40–61.

Jenniskens, P., Nénon, Q., Albers, J., Gural, P.S., Haberman, B., Holman, D., Morales, R., Grigsby, B.J., Samuels, D., Johannink, C., 2016. The established meteor showers as observed by CAMS. Icarus 266, 331–354.

Jones, J., 2003. Modeling the sporadic meteoroid complex. Cooperative agreement NCC8-185 between University of Western Ontario and NASA , 1–51.

Jones, J., Brown, P., Ellis, K.J., Webster, A.R., Campbell-Brown, M., Krzemenski, Z., Weryk, R.J., 2005. The Canadian Meteor Orbit Radar: system overview and preliminary results. Planet. and Space Sci. 53, 413–421.

Jones, J., Jones, W., 1993. Comet Machholz and the Quadrantid meteor stream. MNRAS 261, 605–611.

Kinoshita, H., Nakai, H., 1999. Analytical Solution of the Kozai Resonance and its Application. Celestial Mechanics and Dynamical Astronomy 75, 125–147.

Klačka, J., 2004. Electromagnetic Radiation and Motion of a Particle. Celestial Mechanics and Dynamical Astronomy 89, 1–61. `astro-ph/0301138`.

Kozai, Y., 1962. Secular perturbations of asteroids with high inclination and eccentricity. Astron. Journ. 67, 591.

Langland-Shula, L.E., Smith, G.H., 2007. The Unusual Spectrum of Comet 96P/Machholz. ApJ 664, L119–L122. `0706.2022`.

Leinert, C., Grun, E., 1990. Interplanetary Dust. p. 207.

McIntosh, B.A., 1990. Comet P/Machholz and the Quadrantid meteor stream. Icarus 86, 299–304.

McKinley, D.W.R., 1961. Meteor science and engineering.

Ohtsuka, K., Nakano, S., Yoshikawa, M., 2003. On the Association among Periodic Comet 96P/Machholz, Arietids, the Marsden Comet Group, and the Kracht Comet Group. Publ. Astr. Soc. Japan 55, 321–324.

Peterson, A.W., 1971. A determination of the vaporization temperature of circumsolar dust at 4 R sun., in: Bulletin of the American Astronomical Society, p. 500.

Rickman, H., Fernandez, J.A., Gustafson, B.A.S., 1990. Formation of stable dust mantles on short-period comet nuclei. A&A 237, 524–535.

Robertson, H.P., 1937. Dynamical effects of radiation in the solar system. MNRAS 97, 423.

Schleicher, D.G., 2008. The Extremely Anomalous Molecular Abundances of Comet 96p/Machholz 1 from Narrowband Photometry. Astron. Journ. 136, 2204–2213.

Sekanina, Z., 1977. Relative motions of fragments of the split comets. I - A new approach. Icarus 30, 574–594.

Sekanina, Z., 1978. Relative motions of fragments of the split comets. II - Separation velocities and differential decelerations for extensively observed comets. Icarus 33, 173–185.

Sekanina, Z., 2005. Comet 73P/Schwassmann-Wachmann: Nucleus Fragmentation, Its Light-Curve Signature, and Close Approach to Earth in 2006. International Comet Quarterly 27, 225–240.

Sekanina, Z., Chodas, P.W., 2005. Origin of the Marsden and Kracht Groups of Sunskirting Comets. I. Association with Comet 96P/Machholz and Its Interplanetary Complex. ApJS 161, 551–586.

SonotaCo, 2009. A meteor shower catalog based on video observations in 2007-2008. WGN, Journal of the International Meteor Organization 37, 55–62.

Weryk, R.J., Brown, P.G., 2013. Simultaneous radar and video meteors II: Photometry and ionisation. Planet. and Space Sci. 81, 32–47.

Whipple, F.L., 1950. A comet model. I. The acceleration of Comet Encke. ApJ 111, 375–394.

Whipple, F.L., 1951. A Comet Model. II. Physical Relations for Comets and Meteors. ApJ 113, 464.

Wiegert, P., Brown, P., 2005. The Quadrantid meteoroid complex. Icarus 179, 139–157.

Chapter 4

Formation and past evolution of the showers of 96P/Machholz complex

Abedin, Abedin; Janches, Diego; Wiegert, Paul; Pokorný, Petr; Brown, Peter; Hormaechea, Jose Luis (2016): "Formation and past evolution of the showers of 96P/Machholz complex", *Icarus*, In Press.

4.1   Introduction

This work is a continuation of our series of studies with the aim of investigating the origin and past evolution of the meteoroid complex, related to comet 96P/Machholz (96P hereafter). In a previous work, we investigated the formation mechanism and the age of the Quadrantid meteoroid stream (Abedin et al., 2015) and more recently the origin of the daytime Arietids meteor shower (Abedin et al, in Press). Our goal is to develop a self-consistent scenario of the hierarchical fragmentation and subsequent evolution of the 96P complex, using detailed observational characteristics of the associated Machholz shower complex to constrain age and history of the comet breakup.

Comet 96P is unusual among the short-period comets. It has an extremely low perihelion distance, grazing the Sun at a distance of 0.123 AU or roughly $26.5R_{\odot}$, and has been associated with a number of other comets and objects of asteroid appearance. In particular, it is thought that 96P shares a genetic relationship with the *Marsden* and *Kracht* group of sunskirting comets and the *Kreutz* sungrazers (e.g., Sekanina and Chodas, 2005; Jenniskens, 2006). It is also associated with up to eight different meteor showers (e.g., Babadzhanov and Obrubov, 1992; Neslušan et al., 2013b). This ensemble of interplanetary bodies is referred to as the *Machholz interplanetary complex* and is believed to have originated from a single split of a larger progenitor prior to 950 AD (Sekanina and Chodas, 2005). Despite the association of 96P with the

aforementioned bodies, some of their present orbital elements differ noticeably, owing to the differential planetary perturbations (mainly due to Jupiter). Presently, the Marsden sunskirters approach the Sun within $8 - 11R_\odot$ and have mean orbital inclination of $\approx 26°$, whereas the Kracht group of comets have perihelia in the range $6.7 - 11.6R_\odot$ and inclination of $\approx 13°$. For comparison, the present inclination of 96P is $i \approx 58°$ and perihelion distance of 0.123 AU. Furthermore, 96P is interesting among other comets as it has anomalous molecular abundances (e.g., A'Hearn et al., 1995; Schleicher, 2008), being relatively depleted in CN, C_2, C_3 compared to the OH abundance. That indicates that 96P has either formed in a region of the early Solar system with unusual conditions or is interstellar in origin.

Comet 96P was mentioned for first time in the context of meteor astronomy by McIntosh (1990). The author noted the similar orbital evolution of 96P and the Quadrantid meteoroid stream, though their evolutionary cycles were offset by 4000 years. That led McIntosh (1990) to suggest a sibling rather than child-parent relationship.

Numerical simulations of the long-term evolution of the orbit of 96P were performed by Babadzhanov and Obrubov (1992). They were the first to suggested that within one circulation cycle of the longitude of the ascending node Ω and the argument of perihelion ω (≈ 8200 years), the comet may give rise to eight different meteor showers. The Earth intersects four of these showers at their descending nodes and four at their ascending nodes. The authors identified these showers as the Quadrantids, daytime Arietids, Southern and Northern δ-Aquariids, Ursids, κ-Velids, Carinids and the α-Cetids. The first four showers are well known and constrained. The existence of the rest of the other showers has remained uncertain, partly due to the lack of systematic meteor surveys from the Southern hemisphere.

Jones and Jones (1993) argued that if comet 96P had been captured by close approach with Jupiter, about 2200 years ago, there has been sufficient time for the comet to produce most of the observed characteristics of the Quadrantids, the daytime Arietids and Southern δ-Aquariids.

Recent work, carried out by Neslušan et al. (2013b) investigated potential streams related to 96P, assuming an initial meteoroid ejection time 4000 years ago. They concluded that 96P may indeed produce eight different showers, though they were skeptical about the detectability of all of them. Instead, they argued that due to the proximity of four of the intersection points with the Earth's orbit, only six showers are expected to be identified. Although the authors recognized the ~ 8200 years circulation cycle of the longitude of the ascending node and the argument of perihelion of the 96P's orbit, they considered only half of that period in their investigation. Moreover, the authors did not compare the characteristics of the modeled meteoroid streams in detail with available observations.

Several recent works have suggested that the Marsden group of comets are the immediate parents of the daytime Arietids and the Northern and Southern δ-Aquariids (Ohtsuka et al.,

2003; Sekanina and Chodas, 2005; Jenniskens, 2006; Jenniskens et al., 2012). Ohtsuka et al. (2003) noted the similarity in the orbital evolution of 96P, the Marsden and Kracht group of sunskirting comets and the daytime Arietids, assuming their evolutionary cycles were shifted by a few hundred years. The authors suggested that the Arietids are related to the Marsden group but hinted that all bodies may be genetically related. Sekanina and Chodas (2005) performed numerical simulations to investigate the origin of the Marsden, and Kracht group of comets. Based on the tendency of these comets to arrive at perihelion in pairs, the authors developed a detailed model and suggested that the sunskirting group of comets, along with the Arietids and southern δ-Aquariids, originated from a single comet break up, prior to 950 AD. However, these authors and earlier works have not attempted to constrain formation models of the 96P complex using detailed observations of the associated meteor showers.

4.1.1   96P/Machholz complex showers

Some of the individual showers belonging to 96P complex have already been studied by several authors, including our series of studies. Below, we provide a brief background in order of shower strength:

The Quadrantids

The Quadrantids are unusual, being among the strongest of the annual showers with an extremely compact central portion, with a Full Width of Half Maximum (FWHM) of only $\approx$17 hours, encountered every year between January 3-4. This alone is a strong evidence that the core of the stream is young. Due to the presently large difference in the longitude of the ascending nodes of the stream and 96P/Machholz, the comet was not recognized as the immediate parent of stream. Jenniskens et al. (1997) questioned the association of the Quadrantids and 96P and instead suggested that the parent may be an asteroid-like object, hidden in a high inclination orbit. With the discovery of asteroid 2003 EH_1, Jenniskens (2004) noted a striking similarity with the orbit of the Quadrantids and suggested a child-parent relationship. Wiegert and Brown (2005) performed a nodal regression analysis of the orbits of 2003 EH_1 and the Quadrantids, arguing that the core of the stream is only 200 years old. However, recent radar observations of the Quadrantids revealed that there is an older component of the stream, lasting from mid-November to mid-January (Brown et al., 2010). Using seven high-precision photographic Quadrantids, augmented with radar observations by the *Canadian Meteor Orbit Radar* (CMOR), we demonstrated using several independent lines of evidence that the core of the stream is related to asteroid 2003 EH_1 and most likely formed circa 1800 AD (Abedin et al., 2015). This study also found that the older component is associated with comet 96P and is

several millenia old. For a thorough review of past works on the Quadrantids, the reader is referred to (e.g., Jenniskens, 2006; Neslušan et al., 2013b; Abedin et al., 2015).

The Daytime Arietids

The shower is observed annually between mid-May and late June with a broad plateau of peak activity near solar longitude $\lambda_\odot = 80.5°$ (Bruzzone et al., 2015). The shower characteristics have mostly been constrained by radar observations, owing to the proximity of the radiant position to the Sun, with some recent observations by optical detections. Recently, we addressed the question as to the association of the stream with the Marsden group of comets or comet 96P (as discussed above). We performed detailed numerical simulations of meteoroids, ejected from 96P and the most notable member of the Marsden group of comets - P/1999 J6. The resulting streams from both comets were analyzed with respect to which could reproduce the main characteristics of the daytime Arietids. As observational constraints for the shower, we used data from the 12 year radar survey of the daytime Arietids by CMOR (Bruzzone et al., 2015), along with 14 TV observations by SonotaCo (2009) and 31 video events recorded by the *Cameras for All-sky Meteor Surveillance* (CAMS) (Jenniskens et al., 2015 In Press). Our simulations indicated that the Marsden group of comets can not alone reproduce the observed characteristics of the shower and thus can not be the sole parents of the stream. Instead, we concluded that the broader activity of the daytime Arietids are associated with comet 96P and have an age of ∼10000 years, though we demonstrated that the Marsden group of comets may contribute to the peak of the shower. An outstanding question for this shower relates to the difference in the orbital elements of optical and radar sized particles, a discrepancy previously noted by Jenniskens et al. (2012). Radar surveys measure systematically lower meteoroid geocentric speeds, and thus lower orbital semi-major axis, as compared to optical surveys. Jenniskens et al. (2012) attributed these differences to insufficient correction for deceleration of radar sized (a few hundreds of microns) meteoroids in the Earth's atmosphere. These are normally subject to a greater atmospheric drag than larger meteoroids. These differences, if they are real, imply that the daytime Arietids may be older than a few tens of millenia. The observed discrepancy remains unresolved.

Southern and Northern δ-Aquariids

The Southern δ-Aquariids are observed every year between late May to early July with a peak activity at solar longitude $\lambda_\odot = 126°$ (Brown et al., 2010). Though much weaker, the northern branch is active between late July to late August with a maximum activity occurring at $\lambda_\odot = 139°$. Although the showers stand well above the sporadic background and have been

well measured, their origin has received less attention and is mostly limited to the works by Babadzhanov and Obrubov (1992); Sekanina and Chodas (2005); Jenniskens (2006) and Nes-lušan et al. (2013b).

κ-Velids, α-Cetids, Carinids and Ursids

- The predicted κ-Velids have only recently been established as an annual shower (Pokorny et al. 2016), based on systematic radar observations by the *Southern Argentina Agile Meteor Radar* (SAAMER) (Janches et al., 2013, 2015). In contrast, there is no obvious shower listed in the IAU Meteor Data Center (IAU MDC) (`http://www.ta3.sk/IAUC22DB/MDC2007/`), corresponding to the radiant, speed and timing characteristics predicted by Babadzhanov and Obrubov (1992) for α-Cetids, though there are 19 different showers that are listed as Cetids. Likewise, there are 4 different showers listed as Carinids, though only θ-Carinids are well measured (Pokorny et al. 2016). Finally, the association of the Ursids with 96P is doubtful, as the stream has already been confirmed to be related to comet 8P/Tuttle (e.g., Jenniskens, 2006), which indicates that the stream had been either misidentified by Babadzhanov and Obrubov (1992) or it overlaps with another nearby stronger meteor shower and hence can not be detected as individual, as previously suggested by Neslušan et al. (2013b).

In this work, we aim to obtain a broader picture of the origin and past evolution of the complex of interplanetary bodies, associated with comet 96P. We approach that problem by simultaneously fitting the observed shower characteristics and attempt to answer the following questions:

1. What is the most dominant parent of the 96P meteoroid complex associated, comet 96P/Machholz or the Marsden group of comets?

2. What is the age and likely parent (comet 96P/Machholz or the Marsden group of comets) of the Southern and Northern δ-Aquariids and the recently established $\kappa-$Velids and θ-Carinids?

3. Do the Carinids, $\alpha-$Cetids and Ursids exist or they have been misidentified? If they exist, what is their likely age and parent?

4. Can we obtain a self-consistent scenario as to the epoch when comet 96P has been captured in a short period orbit and its past fragmentation history?

4.2   Observations

In this section we present the observational characteristics of the showers that we will aim to match and also provide some observational observational constraints on the parent bodies considered in this work.

Babadzhanov and Obrubov (1992) were the first to note that comet 96P may intersect the Earth's orbit at eight different locations, during one Kozai cycle ($\approx$ 8200 years) of its argument of perihelion. As a result, it could produce 8 meteor showers at Earth. Figure 4.1 shows the intersection points of the descending and ascending nodes with the Earth's orbit, after one full Kozai cycle. Some of these showers are well known - The Quadrantids, daytime Arietids, Southern and Northern δ-Aquariids and κ-Velids. Their observational characteristics have been constrained by both, radar and optical meteor surveys. However, the identification of some of the showers, which Babadzhanov and Obrubov (1992) have named the Carinids, α-Cetids and Ursids are uncertain. We note that there are no showers in the IAU MDC which match the characteristics of the Carinids and α-Cetids as given by Babadzhanov and Obrubov (1992). The shower designated as Ursids by Babadzhanov and Obrubov (1992) is not well documented in the literature and should not be mistaken with the 00015 (URS) Ursids in the IAU MDC, which is a different shower, unambiguously associated with 8P/Tuttle (Jenniskens et al., 2002). Therefore, as part of this work, we aim to examine the reality of these "misidentified" showers by fitting our simulated shower characteristics to the observations of the well constrained showers (QUA, ARI, SDA, NDA and KVE) and then performing a search for the predicted showers in radar and optical databases.

For the shower data required in this study, such as shower duration, orbits and radiants, we use the orbits measured by the Canadian Meteor Orbit Radar (CMOR) (Brown et al., 2010) and by the Southern Argentina Agile Meteor Radar (SAAMER) (Janches et al., 2013, 2015). The CMOR data gathered between 2002-2015 was stacked into an equivalent virtual year comprising 1.5×10^7 orbits. SAAMER data from 2012-2015 is stacked in the same manner to produce 10^6 orbits.

We took the simulation results which predict where shower radiants are expected, together with the expected speed and timing and performed a 3D wavelet search following the methodology described in Brown et al. (2010) and updated in Pokorny et al. (2016). For all predicted radiants we extended our search $\pm$ 10 degrees relative to the predicted radiant and ten degrees of solar longitude before and after the expected activity dates based on the simulations. Finally, we searched over a window of $\pm$ 10 km/s from the predicted speeds for each shower. Our wavelet transforms were computed in steps of 0.2 degrees (providing a lower bound to our radiant precision) and in steps of 0.5% in speed. We used fixed wavelet probe sizes of 4 degrees in angular coordinates and 12% probe size in speed, based on results from Campbell-Brown and Brown (2015) and Pokorny et al. (2016). From these wavelet computations, we identified local maxima, which we define as being excursions in the wavelet coefficient of 3σ above the median background based on the year of data outside the shower window that fell in our analysis windows. Based on the variance in daily radiant location and speed, we esti-
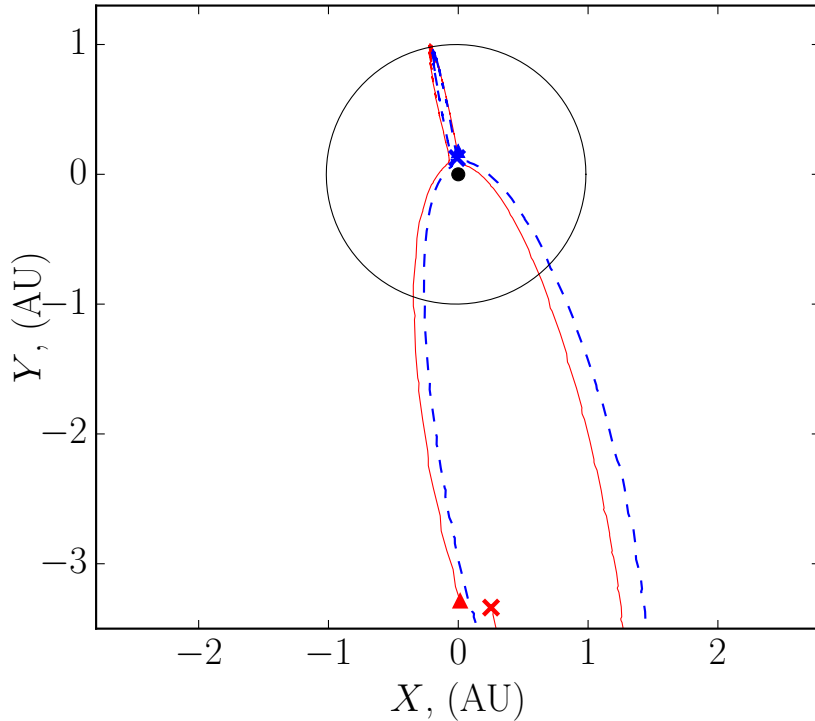
Figure 4.1: Backwards time evolution of the ascending (blue dash line) and descending (red solid line) nodes of the orbit of comet 96P/Machholz for one Kozai circulation cycle ($\sim$ 8200 years) of longitude of the ascending node (Ω) and argument of perihelion (ω). The "x" symbols indicate the starting position of the cycle (present) and the triangle denotes the end position.

mated our uncertainties to be 1 degree in radiant position and 5% in speed - these uncertainties are used for all subsequent estimates of error in daily mean shower orbital elements. Finally, we automatically link shower maxima together if individual maxima occur withing 2 degrees in solar longitude, have radiants less than two degrees in sun-centered radiant coordinates and are less than 10% different in speed. In general, each of our searches produced only one possible maximum each day and these we are able to associate with the probable 96P predicted showers - ie. there was no significant source confusion in our search windows. We also attempted to link each maxima point with pre-existing showers listed in the IAU MDC, assuming common radiants were within 3 degrees in angular coordinates and 10% in speed.

As a result of the search and our stream modelling, we have identified three observed showers as likely part of the 96P complex and roughly similar to the original predictions by Babadzhanov and Obrubov (1992). These are the "December α-Draconids" (IAU #00334, DAD) that partially overlaps with the "November ι-Draconids" (IAU #00392, NID), the "daytime λ-Taurids" (IAU #00325, DLT), "θ-Carinids" (IAU #00785, TCD). The DADs and the NIDs belong to the northern toroidal source and are the Ursids counterpart identified by Babadzhanov and Obrubov (1992). The DLTs are the southern branch of the daytime Ari-

etids and are likely the shower named α-Cetids by Babadzhanov and Obrubov (1992). Finally, the TCD belong to the southern toroidal source and have only recently been established as a separate meteor shower (Pokorny et al. 2016). Analyzing the observed CMOR shower characteristics of the DAD and NID, we found that the latter two showers are weak and partially overlap in time, which renders their identification as separate showers difficult. We note that these two showers have been identified as separate in the IAU MDC. Furthermore, towards the end of the activity of the DAD ($\lambda_{\odot end}$ = 271.5°), there is significant background activity that overlaps with the onset of the Quadrantids. Brown et al. (2010) argued that Quadrantids demonstrate a low background activity that last about two months. In light of our simulations and more sensitive shower search, we suggest that this extended activity is not in fact one long individual shower, but instead likely three similar showers of the 96P complex, sharing similar radiant and orbital characteristics but slightly offset in nodal times.

The observational characteristics of all these showers are presented in Tab 4.1, as derived from radar (CMOR and SAAMER) and optical (CAMS) surveys. Generally, radar and optical meteor detections sample different meteoroid sizes, with the former being capable of detecting particles of size of a few hundreds of microns, whereas the optical techniques detect larger meteoroids (millimeter and larger). Thus, combining radar and optical observations will allow us to fit our stream modelling to observed shower characteristics, equivalent to a few hundred micrometers and millimeter size meteoroids, as well as to investigate the past evolution of meteoroids of different sizes.

In Sec. 4.4 we provide detailed observational characteristics of the showers in Tab. 4.1 fitting them directly to our simulations. By simultaneous match of all eight showers, our goal is to explain the age estimates of the showers and put them into perspective in the context of the origin of the 96P complex.

4.2.1   Parent bodies

In this work, we consider two parent bodies for testing a child-parent relationship with the observed meteor showers. These bodies are the comet 96P/Machholz and the most prominent member of the Marsden group of comets, P/1999 J6. The latter was chosen as it has the best constrained orbit among other group members. It would be impractical to simulate the meteoroid streams originating from each individual member of the Marsden group of sunskirters.

Comet P/1999 J6 was discovered by the coronograph on-board of the *Solar and Heliospheric Observatory* (SOHO) and according to the NASA's JPL Horizon database has been classified as a Jupiter-Family Comet (JFC) (`http://ssd.jpl.nasa.gov/sbdb.cgi`), despite its low Tisserand parameter with respect to Jupiter (T_j = 1.942) (see Appendix D),

Shower	$\lambda_{\odot start}$	$\lambda_{\odot max}$	$\lambda_{\odot end}$	$\lambda - \lambda_{\odot}$	b	V_g	α_g	δ_g	a	q	e	i	ω
	(deg)	(deg)	(deg)	(deg)	(deg)	(kms^{-1})	(deg)	(deg)	(AU)	(AU)		(deg)	(deg)
QUA[a]	267.5	283.0	291.0	273.0	64.0	41.7	231.0	48.5	2.77	0.977	0.648	71.7	169.5
QUA[b]	270.0	283.0	296.4	277.5	63.7	40.7	230.2	49.5	2.82	0.979	0.657	71.2	171.4
QUA[d]	275.2	283.0	288.6	-	-	-	-	-	-	-	-	-	-
ARI[a]	62.0	80.5	95.0	348.3	7.4	39.1	44.9	25.5	1.71	0.074	0.957	30.6	26.4
ARI[b]	73.0	77.0	89.4	331.6	7.3	41.1	43.9	24.4	2.67	0.078	0.974	27.7	28.7
SDA[a]	114.5	123.5	163.5	210.9	-7.2	41.3	338.8	-16.7	2.23	0.058	0.974	31.5	155.7
SDA[b]	117.9	128.0	145.9	208.8	-7.2	41.3	341.3	-15.7	2.59	0.069	0.975	29.0	152.9
SDA[d]	109.8	124.5	144.4	–	–	–	–	–	–	–	–	–	–
NDA[a]	126	139	156	208.8	7.8	37.3	345.2	2.6	1.70	0.096	0.944	24.8	329.9
NDA[b]	120.9	141.0	207.5	208.4	6.8	38.4	347.6	2.1	1.97	0.090	0.955	22.3	330.7
NDA[d]	113.4	149.0	151.1	–	–	–	–	–	–	–	–	–	–
DLT[a]	71	86	98	331.2	-8.6	35.6	52.5	10.1	1.49	0.109	0.927	23.5	211.1
NID[a]	221.0	241.0	264.0	265.1	61.6	43.0	196.1	65.3	2.44	0.984	0.598	73.7	188.1
NID[b]	239.3	242.0	267.9	260.9	63.2	42.0	196.5	68.3	3.62	0.973	0.734	72.9	194.7
DAD[b]	248.8	256.0	262.6	272.0	62.8	40.8	210.8	58.6	2.48	0.983	0.603	71.8	177.4
TCD[c]	274.0	276.0	280.0	282.3	-60.3	41.7	156.8	-59.2	2.38	0.966	0.595	74.5	342.2
KVE[c]	272.0	276.0	286.0	257.8	-60.5	40.5	141.1	-51.0	2.08	0.965	0.560	72.9	19.1

Table 4.1: Geocentric characteristics of the meteor showers, possibly associated with the Machholz complex at their time of maximum activity. The columns denote: 1. The solar longitude of the start time of the activity profile, 2. The time of maximum activity, 3. The end time of the activity, 4. Sun-centered ecliptic longitude of the radiant, 5. Ecliptic latitude of the radiant, 6. Geocentric speed, 7. Geocentric equatorial right-ascension of radiant position in J2000.0. 8. Geocentric equatorial declination of the radiant in J2000.0. The remaining columns list the orbital elements at maximum activity. The superscript (a) indicates data obtained by CMOR, (b) corresponds to CAMS data, (c) observations derived by SAAMER and (d) corresponds to visual observations by IMO.

a value typical for Halley type comets. Generally, JFCs have typical Tisserand parameters with respect to Jupiter of $2 < T_j < 3$. The present period of the comet is $P = 5.46$ years and based on 267 observations it has orbital elements: $a = 3.100499137 \pm 0.000027986$ AU, $e = 0.984177313 \pm 0.000015813$, $i = 26.613141 \pm 0.020234$ deg, $\omega = 21.976803 \pm 0.080133$ deg and $\Omega = 81.613781 \pm 0.072701$ deg, taken from the NASA's JPL Horizon System `http://ssd.jpl.nasa.gov/sbdb.cgi`. Presently, P/1999 J6 approaches the Sun within $q \approx 0.049$ AU or roughly $10R_\odot$.

Comet 96P/Machholz was discovered on May 12, 1986 and has also been classified as a JFC ((`http://ssd.jpl.nasa.gov/sbdb.cgi`). According to the NASA's JPL Horizon database it has an orbital period of $P \sim 5.3$ years, with a Tisserand parameter with respect to Jupiter of $T_j = 1.942$ (`http://ssd.jpl.nasa.gov/sbdb.cgi`). Similar to P/1999 J6, this value is low and typical for Halley type comets. The present orbital elements of 96P are: $a = 3.033939724939583 \pm 0.000000024505$ AU, $e = 0.95921182874981 \pm 0.000000046985$, $i = 58.312214235 \pm 0.000044922$ deg, $\omega = 14.757748401 \pm 0.000020956$ deg and $\Omega = 94.323236311 \pm 0.000011819$ deg. Presently, the perihelion distance of 96P is $q \approx 0.124$ AU or roughly $25R_\odot$.
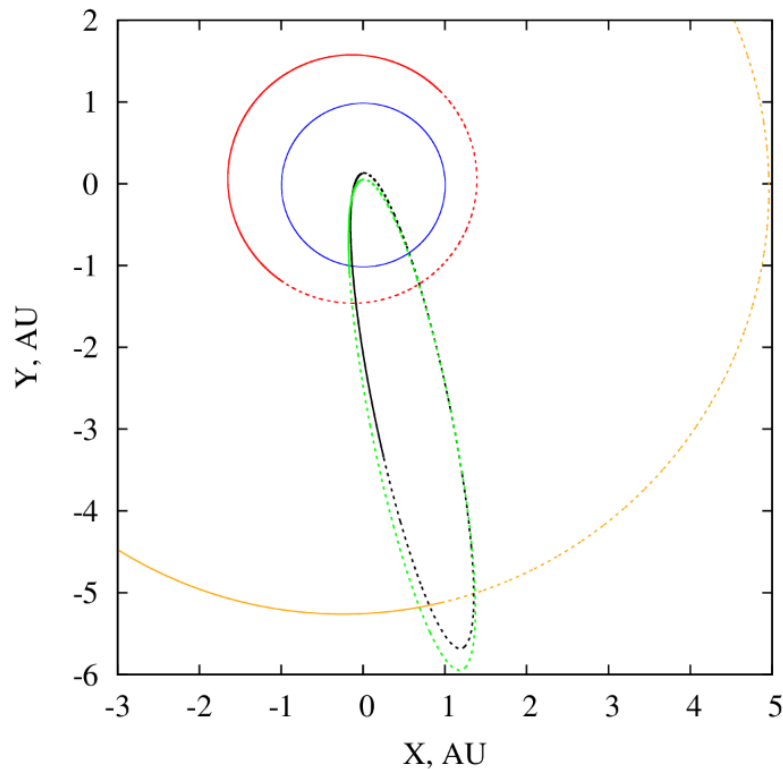

Figure 4.2: The orbits of comet 96P/Machholz (black line) and comet P/1999 J6 (green line) viewed from above the ecliptic plane. The solid lines indicate the portion of the orbits above the ecliptic whereas the dotted lines denote the portions below the ecliptic.

The present orbits of the two hypothetical parents, comets 96P and and P/1999 J6, are presented in Fig. 4.2. It is evident that the two orbits are strikingly similar, indicating a possible genetic relationship. Currently, the ascending node of the orbit of 96P is located near the Sun, whereas the descending node is between the orbits of Mars and Jupiter. In contrast, while the ascending node of P/1999 J6 is also close to the Sun, the descending node is close to the Earth's orbit and most likely supplies "young" meteoroids that are presently encountered by the Earth.

4.3 Numerical Simulations

4.3.1 Solar System model and numerical integrator

In our simulations, we model the Solar system as comprising the Sun and all planets. Effectively, the parents and their synthetic meteoroid streams will move under the gravitational attraction from the Sun, where the planets will act as perturbing forces on their Keplerian motion. We account for the mutual interaction between the planets, though the parent clones and individual meteoroids will be considered as test particles. In addition to gravitational effects, the meteoroids will be also subjected to non-gravitational forces such as the solar radiation pressure force (e.g., Burns et al., 1979) and Poynting-Robertson (PR) drag (e.g., Burns et al., 1979; Klačka, 2004; Klačka and Kocifaj, 2008). The solar radiation pressure affects the dynamics of micron and millimeter sized particles and manifests itself as weakening of the solar gravitational attraction force F_G. Usually, the radiation force is considered via the standard β-parameter and is given by Burns et al. (1979) as:

$$\beta = \frac{F_R}{F_G} = 5.7 \times 10^4 \frac{Q_{pr}}{\rho s}, \tag{4.1}$$

where ρ is the meteoroid's bulk density in kg.m^{-3}, s is the radius of the meteoroids in meters and Q_{pr} is the light scattering efficiency, considered to be unity in our simulations. Similarly, the PR drag decreases particle's semi-major axis, due to anisotropic emission of the absorbed solar radiation, in the reference frame of the Sun, and causes them to slowly spiral towards the Sun. In this work do not account for the Lorentz force and solar wind drag as they are ∼ 1000 times smaller than the solar radiation pressure (e.g., Leinert and Grun, 1990) for 100 μm particles and their influence decrease for larger meteoroids.

The radiation forces are virtually zero for the considered parent bodies. The only significant non-gravitational force on comet nuclei is the "rocket" like acceleration induced by the sublimation of the cometary volatiles, which causes the trajectory of a comet to deviate from pure gravitational motion. However, we do not model these forces due to their stochastic na-

ture over the time scales considered in this work. Thus, the parent bodies will be subject to gravitational force only. Furthermore, the orbital evolution of both parents 96P and P/1999 J6 are in state of Kozai-type oscillation (Sec. 4.3.3). That leads to episodically decrease of their perihelia to distances of 0.025 AU or roughly 5 $R_\odot$. For this reason, despite the fact that a body would generally spend a very short time near perihelion, we decided to also include general relativistic effects.

The equations of motion of all bodies (planets, parent bodies and meteoroids) will be integrated using the Chambers' hybrid symplectic scheme (Chambers, 1999). During the backward integrations of the orbits of 96P and P/1999 J6, we take snapshots of the state vectors of the clones and the planets every year. These state vectors will be used as the basis for meteoroid ejections at any instant of time from suitably selected clones for both parents.

4.3.2   Meteoroid ejection

The meteoroids are modeled as spherical particles of density $\rho_m = 2500$ kg.m^{-3} with radii ranging from $s = 100$ μm, size appropriate for radar meteors (e.g., Weryk and Brown, 2013) to $s = 1$ mm, a typical value for optical or visual meteors. They were sampled from a uniform distribution of the logarithm of their radii. Although, this is not a realistic size distribution, we aimed to sample a wide size range in order to investigate the resulting shower for radar and optical size meteors. Later, we apply weighting to the number of meteoroids as a function of their size and perihelion distance at the time of ejection (Sec. 4.3.4 and Sec. 4.3.4)..

The meteoroids are ejected as a result of cometary outgassing, where the ejection speed is modeled according to Brown and Jones (1998) and is given by:

$$V_{ej} = 10.2r^{-1.038}\rho^{-1/3}R_c^{1/2}m^{-1/6} \text{ (m/s)} \tag{4.2}$$

where r is the heliocentric distance in (AU), ρ is the bulk density of the meteoroid in (g.cm^{-3}), R_c is the radius of the comet nucleus in (km) and m is the mass of the meteoroid in (grams). The meteoroids are ejected isotropically on the sunlit hemisphere, and dust production rate assumed to be uniform in true anomaly of the parent clones. For example, the mass of a meteoroid at the lower size range ($s = 100\mu m$), considered in our simulations, would have a mass of $m \approx 10^{-6}$ grams. The magnitude of the ejection speed for such a meteoroid, released from the nucleus of 96P/Machholz at a heliocentric distance of 1 AU would be $V_{ej} \approx 160$m s^{-1}, whereas meteoroid of radius $s = 1$mm would have a terminal speed of $V_{ej} \approx 50$m s^{-1}.

As mentioned earlier in the text, Sekanina and Chodas (2005) argued that the ARI, SDA and NDA originate from the Marsden group of comets between 100 - 950 AD. Since, the most prominent member of the Marsden group, P/1999 J6, is significantly smaller than 96P, it is not

unreasonable to expect that it will have a less dust production compared to 96P. However, here we will initially assume the same dust production rate for P/1999 J6, for two reasons:

1. Lack of information on the physical parameters of the P/1999 J6 nucleus, so that a relative to 96P dust production rate can be determined.

2. We need to eject a relatively large number of particles from both parents, so we have a good particle number statistics.

This seems a reasonable assumption, since our goal is to test the streams of which parent body will produce a better match to the observed width of the activity profiles, which is to a first order a proxy as to the age of the shower. The amount of dust production is not expected to affect the width of the profiles but only the relative number of particles in each bin of the solar longitude. The size of the cross-section of a stream, and thus the width of the activity profile, will depend on the differential planetary perturbations and non-gravitational forces over time.

Selecting "clones" for backward integrations

The first step in meteoroid stream modelling is to integrate the orbit of a hypothetical parent back in time to an epoch of interest that will be used for meteoroid ejection and forward integrations. Despite the good quality of the contemporary small Solar system body observations, their "true" orbits are not exactly known but instead come with a confidence region. Therefore, we sample the uncertainty region of the phase space of their orbital elements aiming to consider all orbits consistent with the "true" orbit. Each set of the sampled orbital elements is referred to as "clone". Assuming that we have a set of six orbital elements $y_i = (a, e, i, \omega, \Omega, M)$, and they are correlated, the orbital elements for each clone, can therefore be written in the form:

$$y_i = y_0 + X_{ik}\Lambda_{kj}\xi_j, \tag{4.3}$$

where y_0 is 6×1 column vector of of the nominal orbital elements of the body, X_{ik} is 6×6 matrix, with columns equal to the eigen-vectors of the covariance matrix of the orbital elements, Λ_{kj} is a diagonal matrix with elements corresponding to the eigen-values of the covariance matrix and ξ_j is a random number sampled from a normal distribution with mean $\mu = 0$ and standard deviation $\sigma = 1$. Using that approach, we create 1000 clones for each assumed parent body, 96P and P/1999 J6, that will be integrated back in time, until an epoch for interest.

4.3.3　Phase 1: Backward integrations of parent body candidates

Parent candidate #1 96P/Machholz

We model 96P as spherical nucleus of radius $R = 5$ km and bulk density of $\rho = 700$ kg.m^{-3}. We note that there is no way to know actual size of the comet about 20000 years ago. Recent studies of the nucleus brightness suggest a radius between $R = 2 - 2.5$ km (e.g., Green et al., 1990; Sekanina, 1990; Licandro et al., 2000) and more recently $R = 3.2$ km (Lamy et al., 2004). We chose to use a value of $R = 5$ km as compromise, accounting for a possible nucleus erosion over time.

The equations of motion of comet 96P and each clone are integrated back in time, until 50000BC, using a force model as described in Sec. 4.3.1. The lengthy backward integration (5×10^4 years) was chosen with the aim of encompassing at least a few circulation cycles of the longitude of the ascending node (Ω), allowing us to study the resulting meteoroid streams over a long time period. However, we emphasize that even though our backward integrations go back to 50000 BC, we only consider meteoroid ejection epochs since 20000 BC. The reason for that is that the time window of 50 millenia is comparable to the dynamical and physical lifetimes of JFC (e.g., Levison and Duncan, 1994, 1997). The aim of the backward integrations until 50000 BC was merely to illustrate the past evolution of the orbit of 96P.

We used a fixed integration time step of Δt=12 hours. Prior to the main integrations, we performed sample simulations in order to determine an optimal time step for both parents, 96P and P/1999 J6 where the method is described in details in Abedin et al. (2016). For the parent candidate 96P, we found an optimal integration time step of Δt =12 hours. In order to reduce the accumulation of numerical error during the backward integration we take a snapshot of the state vectors of the parent clones and the planets every year. These state vectors will be used for forward modelling of meteoroid ejection at an epoch of interest.

During the backward integrations, we imposed a perihelion cut-off distance of 5 $R_{\odot}$. Any clone or the parent body that approached the Sun below that limit was considered "dead" and removed from the simulations. Comets are unlikely to survive at such short distances from the Sun, which is also evidenced by the continuous disruption of sungrazing comets e.g., *Marsden* and *Kreutz* groups of comets (Sekanina and Chodas, 2005). In fact, the sun grazing stage of the evolution of comets is considered a frequent end state of most comets (e.g., Bailey et al., 1992).

The evolution of the orbital elements of the 1000 clones and the nominal orbit of 96P are presented in Fig. 4.3. The orbit is stable over a time scale of $\sim$ 7500 years and evolves smoothly, where beyond that time the dispersal of the clones becomes significant. Furthermore, the orbit of 96P/Machholz is in state of Kozai type oscillation, which manifests itself in a
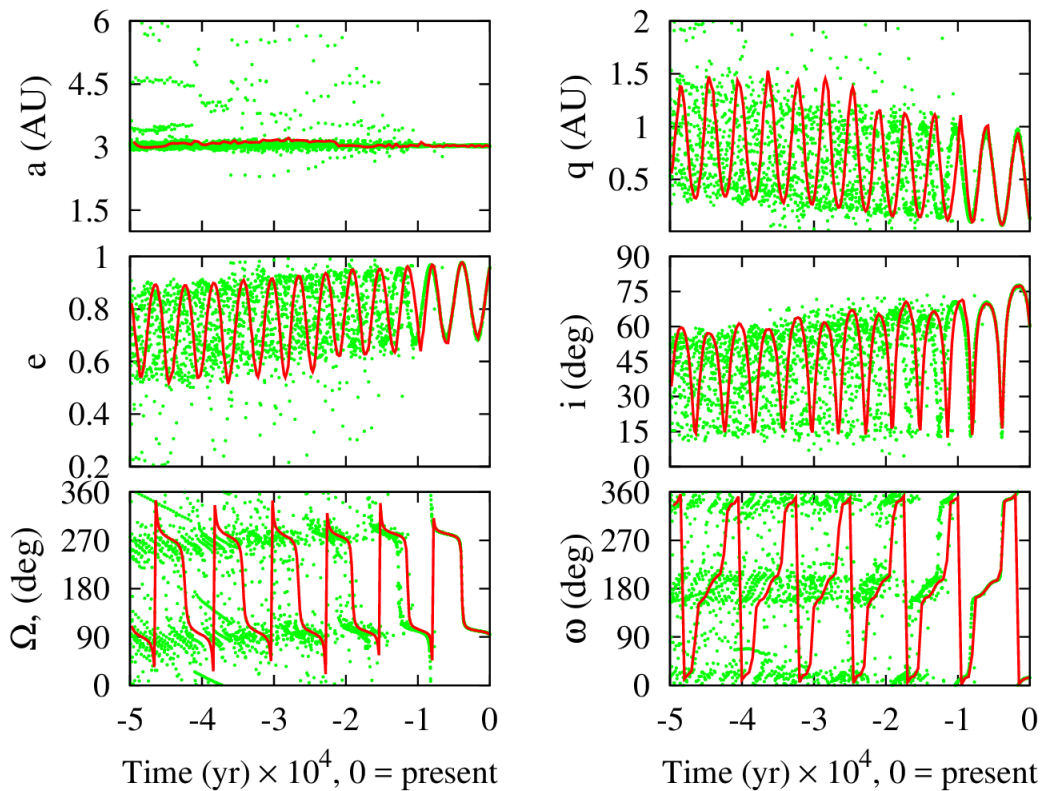
Figure 4.3: Backward evolution of the nominal orbital elements of comet 96P/Machholz (red line), along with 10^3 clones (green dots), over $5×10^4$ years.

distinct correlation in the variation of some of the orbital elements. In the Kozai-type orbital evolution, the semi-major axis of the orbit is approximately conserved, while there is out-of-phase oscillation of the perihelion distance, eccentricity and inclination of the orbit. That is, when the orbital inclination is at its maximum value $i ≈ 80°$, the orbital eccentricity reaches a minimum $e ≈ 0.7$, while the perihelion distance is also at its maximum value $q ≈ 1$ AU. Conversely, when the inclination is at minimum $i ≈ 15°$, the eccentricity is at its maximum ($e ≈ 0.99$) while the perihelion distance reaches a minimum value of $q ≈ 0.05$ AU. This oscillation in (e, i, q) for 96P occurs with at a period of $≈ 4100$ years, whereas the longitude of the ascending node ($Ω$) and the argument of perihelion ($ω$) circulate from 0° to 360°, with a period of $≈ 8200$ years (see Fig. 4.3). The fact the orbit of 96P is in a state of Kozai-type oscillation will be used for selecting clones for meteoroid ejection in Sec 4.3.4.

Parent candidate #2 P/1999 J6

Without a priori knowledge of the physical parameters of the nucleus of comet P/1999 we assume a radius of $R = 0.5$ km and bulk density of $ρ =700$ kg.m^{-3}. Generally, the faintest

sungrazing comets are estimated to be larger than 5 meters (e.g., Sekanina, 2002). Since P/1999 J6 has the best constrained orbit among the sunskirting comets and presumably has survived at least several perihelion returns (Sekanina and Chodas, 2005), that implies the comet must be relatively large compared to other members of the group.

Using the approach outlined in Sec. 4.3.2, we created 1000 clones, sampled from the 6-dimensional phase space of the nominal orbital elements of P/1999 J6. Then the orbits of the clones were integrated backwards in time until 0 AD. This time span was motivated by the hypothesis that the Marsden group of comets, ARI, SDA and NDA may have formed between 100-950 AD (Sekanina and Chodas, 2005). The epoch of 100 AD will be used for meteoroid ejection onset time from P/1999 J6 and forward integrations of their orbits.

During the integrations we used a fixed time step of $\Delta t = 4$ hours, utilizing the force model as described in Sec. 4.3.1. We note the shorter integration time step used for the orbit of P/1999 J6, compared to $\Delta t = 12$ hours for 96P. The reason for that is that P/1999 J6 has a lower perihelion distance and a time step of $\Delta t = 4$ hours provides a smooth sampling of its motion in the Sun's vicinity. Furthermore, similar to the case of 96P (Sec. 4.3.3), for the sake of reducing numerical errors, snapshots of the state vectors of the parent clones and planets were taken every year.

The result from the backward integrations are presented in Fig. 4.4. The orbit of P/1999 J6 quickly becomes chaotic, after only 500 years, owing to frequent close encounters with Jupiter. Presently, the perihelion distance of the comet reaches its minimum distance of $q \approx 0.05$ AU, while the eccentricity is almost at its maximum value of $e \approx 0.98$ (see Fig. 4.4). The present value of the inclination is $i \approx 26.6°$ but only 1.5 millenia ago it was about $i \approx 75°$, where the perihelion distance was at its maximum value of $q \approx 1$ AU. Despite, the chaotic behavior of the orbital elements, a careful selection of clones using the past evolution of P/1999 J6, could still provide meaningful results from the forward simulations. Due to the quick dispersal of the clones of P/1999 J6, it becomes difficult to know the true orbit of the comets prior to 100 AD.

4.3.4   Phase2: Forward integration

Selection of "clones" for meteoroid ejection from parent candidate #1 96P/Machholz

We use the fact that the orbit of 96P is in state of Kozai oscillation in order to select clones for meteoroid ejection and forward integrations. This type of secular evolution approximately conserves the Kozai energy (e.g., Kozai, 1962; Kinoshita and Nakai, 1999) which can be expressed as.

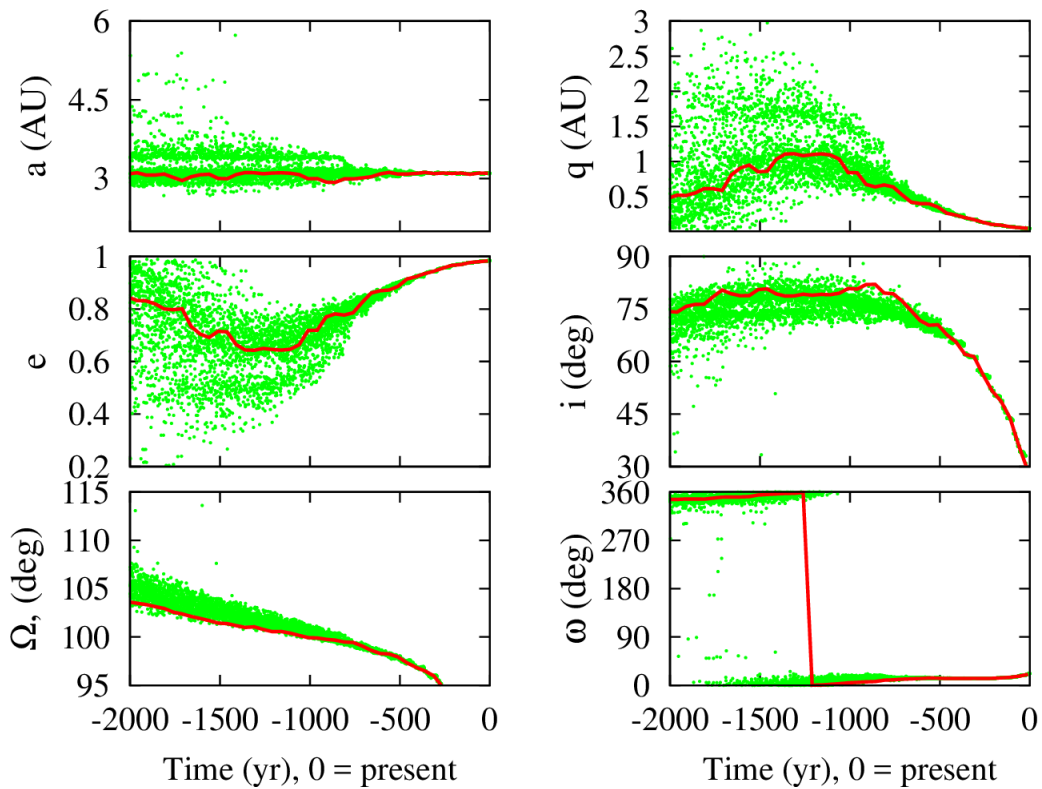$$C = (2 + 3e^2)(3 \cos i^2 - 1) + 15e^2 \sin i^2 \cos 2\omega, \qquad (4.4)$$

Figure 4.4: Backward evolution of the nominal orbital elements of comet P/1999 J6 (red line), along with 10^3 clones (green dots), over 2000 years.

where e is the eccentricity, i is the inclination and ω is argument of perihelion of the orbit respectively. Over the period of interest here (22000 years in the past) the argument of perihelion (ω) would have completed roughly 3 precession cycles, indicating that the 96P's osculating value of (ω) can take any value between $0°$ and $360°$, where as the eccentricity of the orbit would lie between $e \sim 0.7 - 0.97$. However, due to the correlation between e and ω, the actual values that the orbit of 96P can take are constrained to a curve called the *Kozai trajectory* for a given value of the Kozai energy C. Figure 4.5 shows the Kozai trajectories for the nominal orbit of 96P/Machholz, in the ($e - \omega$) space, for different values of the Kozai energy C. In addition, the orbital elements of all clones of 96P, for the epoch of 20000 BC are mapped.

It is evident from Fig. 4.5 that the Kozai energy for 96P/Machholz is not strictly conserved, owing to the fact that close approaches to Jupiter and planetary perturbations are not considered in the Kozai formalism. Nevertheless, using the information of an approximate conservation of C provides a vital information about the appropriate selection of clones for forward simulations.
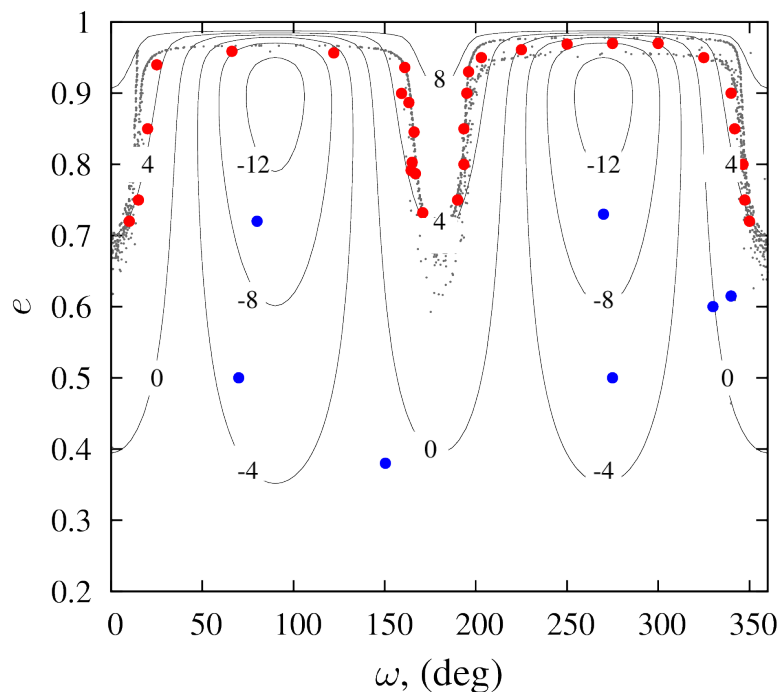
Figure 4.5: Snapshot of the Kozai evolution of the orbit of 96P/Machholz in 20000 BC, for different values of the Kozai energy *C*. The grey dots denote all the clones, superimposed over the trajectories of constant *C*, where the red dots indicate "good" clones, that we select for meteoroid ejection and forward integrations. Examples of "bad" clones, that are discarded in our simulations, are denoted with blue dots.

During the secular evolution of the orbit of 96P, we expect that the true orbit must lie on or near a Kozai trajectory for $C = 4$. We sample our clones for forward integrations along that trajectory (see Fig. 4.5 for details). Ideally, one would select as many clones as possible, covering the entire range of argument of perihelion (ω) and eccentricity (e). However, here we sample only 10 clones due to the lengthy integrations times. The sampled clones are equally spaced in the range of $\omega = 0° - 360°$, while covering the interval $e = 0.7 - 0.97$.

Selection of "clones" for meteoroid ejection from parent candidate #2: P/1999 J6

Assuming that the primary reason for the dispersal of the clones is due to close planetary encounters, we chose to select clones that were situated close to the nominal orbit of the comet. The reason for that is that clones that lie far from the the orbit could not produce the observed characteristics of the resulting meteoroid stream i,e., location of peak activity and spread, radiant location, geocentric speed etc. Such an occurrence would require that all or nearly all of the meteoroids that clones eject, suffer planetary encounters that place them on the present orbits of the observable streams, which cannot happen in practice due to the stochastic nature of planetary encounters.

Using the above argument, we select 10 clones near the nominal orbit of P/1999 J6. Clones

"near" the nominal orbit are considered as those with orbital elements differing by no more than 1% of the orbital elements of P/1999 J6. That should ensure that meteoroids ejected from these clones, would end up in or close to the phase space of orbital elements of those meteoroids, presently intersecting the Earth.

Orbit integration of meteoroids ejected from parent candidate #1 96P/Machholz

Using that approach outlined in Sec. 4.3.2 3000 meteoroids are ejected at every 10 perihelion passages (or roughly every 55 years) from ten suitable clones, over an arc, assuming the comet activity turns on at a heliocentric distance of $r \leq 3$ AU. That distance roughly corresponds to the threshold at which the water ice begins to sublimate (Delsemme, 1982). Assuming the orbital period of 96P (roughly 5 years) does not vary dramatically, and the meteoroid ejection onset is ~20000 BC. That roughly corresponds to meteoroid ejection over ~ 400 perihelion returns, until the present. This amounts in ~ 1.2×10^6 particles per clone, in the size range of $s = 100 \mu m - 1$ mm.

Similar to the backward integrations, the equations of motion of the ejected meteoroids are integrated forward in time with a fixed time step of Δt=12 hours, until the present. During the forward integrations we imposed a perihelion cut-off distance of 0.025 AU or $5R_\odot$, within which the meteoroids were considered "dead" and thus removed from the simulations. Meteoroids capable of producing a shower, at the Earth, were considered those having their nodes within 0.01 AU from the Earth's orbit. In reality, only meteoroids actually hitting the Earth can be observed as meteors, however due to the unrealistically low number of the simulated meteoroids, a nodal distance of 0.01 AU seems a good compromise.

Orbit integration of meteoroids ejected from parent candidate #1 P/1999 J6

Due to the shorter time-scales of integrations here (2000 years), compared 20000 years for 96P, in order to maintain approximately the same dust production (~ 1.2×10^6 particles per clone), 3000 meteoroids are ejected from 10 clones of P/1999 J6 every fifth perihelion return (or approximately every 25 years), compared to every tenth in the case of 96P. That results in 80 active perihelion returns of each clone. Finally, only remaining difference here is that we use a shorter integration time step of 4 hours (as for the backward simulations), due to the extreme perihelion distance of P/1999 J6. All other parameters such as comet activity turn-on distance, perihelion cut-off distance and meteoroid sieve distance are the same as described in Sec. 4.3.4.

Weighting of meteoroids by their perihelion distance at time of ejection

The comet sublimation rate increases with the heliocentric distance (e.g., Sekanina, 1988, 1992) and is a non-linear process. As a comet approaches the Sun, sublimation becomes more violent which increases in dust production rate (Schulz, 2006) and higher meteoroid ejection speeds (Whipple, 1950, 1951; Brown and Jones, 1998). Thus, the number of meteoroids will be dependent on the perihelion distance of the parent at the time of ejection. We use a weighting scheme suggested by Jones (2002), given as:

$$W_s = \frac{\theta_c \, (1 - e)^2}{q^2 \, \sqrt{1 - e^2}} \qquad\qquad (4.5)$$

where

$$\theta_c = \arccos\left(\frac{q(1 + e) - r_0}{r_0 e}\right) \qquad\qquad (4.6)$$

is the true anomaly at which the comet-Sun distance is r_0 in AU, e is the eccentricity of the orbit and q is the perihelion distance in AU. In our simulations $r_0 = 3$ AU, which roughly corresponds to the heliocentric distance at which the water ice begins to sublimate (e.g., Delsemme, 1982). It is well known that more volatile components such as, CO and CO_2 begin to sublimate at much larger heliocentric distances e.g., as large as $r_0 \approx 5$ AU (see Sekanina, 1988), but it is unlikely that the gas pressure can lift hundreds of microns size particles off the comet's surface.

Using the above weighting scheme each particle is assigned a weight depending on the perihelion distance of the parent, at the time the meteoroid was ejected. For example, a meteoroid ejected from a parent with perihelion distance of 1 AU and the eccentricity of $e = 0.96$, assuming $r_0 = 3$ AU will be weighted by $W_s \approx 6$, where as a particle released from a parent with a perihelion distance of $q = 0.1$ AU and same eccentricity (orbit size and shape similar to 96P/Machholz) will be weighted by $W_s \approx 340$. Thus, during the analysis of particles, from our simulations we use their perihelion distance at time of ejection and calculate the above weighting to correct for the meteoroids' number distribution.

Weighting by meteoroid size

In Sec. 4.3.2 we mentioned that the ejected meteoroids, in our simulations, are sampled from a size distribution which is flat in the logarithm of particles' size, in the range 100μm - 1 mm, equivalent to radar and optical meteors respectively. However, this size distribution is not realistic. Generally, more particles are released at smaller sizes, compared to larger ones which is

evidenced from meteor observations. Following Wiegert et al. (2009), this flat size distribution can be calibrated to a differential size distribution, as $dN/dr = r^\alpha$. Thus, the weighting that needs to be applied to account for differential size distribution is just $W_r = r^{\alpha+1}$.

The observed sized distribution of meteors can roughly be approximated with a power-law as $dN(m) \propto m^{-s}dm$, where $s \sim 2.34$ (see Whipple, 1967; Grun et al., 1985) is referred to as *mass index* of the distribution. Since $m \propto r^3$, then $dN(r) \propto r^{-3s+2}dr \approx r^{-5}dr$. Thus, the needed weighting to correct for the meteors' size distribution is $W_r \approx r^{-3s+3} \approx r^{-4}$. Finally, the total weighting that is needed to be applied to the meteors, in order to account for a realistic meteor number distribution, will be the product of particles' perihelion distance at time of ejection and particle size distribution, namely $W_{tot} = W_s W_r$.

4.4 Results

In this section we present the results of the simulated meteoroid streams of both parent candidates, 96P and P/1999 J6, and provide a detailed comparison of their resulting showers with the observations by radar (CMOR and SAAMER), optical (CAMS) and visual (IMO) surveys. We first examine the simulation-observation fits for each individual meteor showers, produced by each individual parent candidate and then provide a qualitative comparison of their combined contribution to the common showers.

For the sake of brevity, we present results for only one clone for each parent body, that produces the best fit in our simulations. Moreover, we show the results of one single initial meteoroid ejection onset time which yields a best match. Snapshots of the fits of the simulated shower widths to the observations between 20000 BC and the present with a time step of 1000 years, is presented in the Supplementary Material in Appendix A. All of our results are presented for only meteoroids that approach the Earth's orbit within 0.01 AU.

The width of the activity profile is a rough proxy of the age a shower. We will be using that information and attempt to simultaneously fit the observed characteristics of all resulting showers, from each parent body, in order to obtain a self-consistent scenario of the age and formation mechanism of the meteoroid complex of 96P.

Finally, we omit the results for the Arietids which were investigated in a previous work (Abedin et al., 2016). However, in the conclusions part we provide a brief discussion as to how the results of that work fit in the context of the formation of the 96P complex.

4.4.1   The simulated meteor showers of parent candidate - 96P/Machholz

Assuming a meteoroid ejection onset epoch 20000 BC, the longitude of the ascending node and argument of perihelion, of the orbit of 96P, will complete approximately 2.5 Kozai circulation cycles, causing the ejected meteoroids to intersect the Earth's orbit at 8 different locations (cf. Fig. 4.1 in Sec. 4.2) and thus resulting in 8 different meteor showers, as originally suggested by Babadzhanov and Obrubov (1992). Figure 4.6 shows the simulated shower radiants with meteoroid ejection onset time in 20000 BC. Four of these showers, QUA, ARI, SDA and NDA were identified by Babadzhanov and Obrubov (1992) and are well known. The remaining four showers, which we call "filaments", have relatively recently been identified as showers. The Quadrantids and filament 1 are part of the northern toroidal source (Brown et al., 2010; Jenniskens et al., 2016), whereas filament 2 is the southern branch of the ARI and contributes to the hellion sporadic source (Brown et al., 2008). The SDA and NDA are part of the anti-hellion sporadic source (e.g., Brown et al., 2010; Jenniskens et al., 2016), while filaments 3 and 4 are found in the southern toroidal source (Pokorny et al., 2016).

An interesting feature is the clear correlation between the perihelion distance and the showers' radiants (Fig. 4.6). The toroidal showers have perihelion close to 1 AU, and the intersection with the Earth's orbit occurs close to that point. The ecliptic showers, on the other hand, are in a sunskirting state approaching the Sun as close as 0.025 AU or slightly farther than $5R_\odot$. Figure 4.6 shows that there is no strong correlation between the showers' radiants and the meteoroid ejection epoch, though it is evident that cores of some of the showers are dominated by younger particles.

The Quadrantids (QUA)

In Abedin et al. (2015) we investigated the Quadrantid meteoroid stream. We demonstrated that the age of the central part of the stream is only 200 years old and is associated with asteroid 2003 EH_1. We also showed that the wings of the activity profile must be much older and are associated with comet 96P. These results had been suggested by several previous studies (e.g., Jenniskens, 2004; Wiegert and Brown, 2005; Neslušan et al., 2013a). However, in the current work we will mainly concern ourselves with the broader (long-lasting) component of the QUA, associated with 96P.

Fig. 4.7 shows the simulated weighted activity profile of the QUA, assuming meteoroid ejection from comet 96P with initial onset epoch in 10000 BC. The location of the peak of the activity profile produced a good match with the CMOR and IMO visual observations, though the simulated *Full Width of Half Maximum* FWHM≈ 6 days was significantly wider. Figure 4.8 shows the simulated distribution of meteoroids, presently reaching the Earth, as a function of
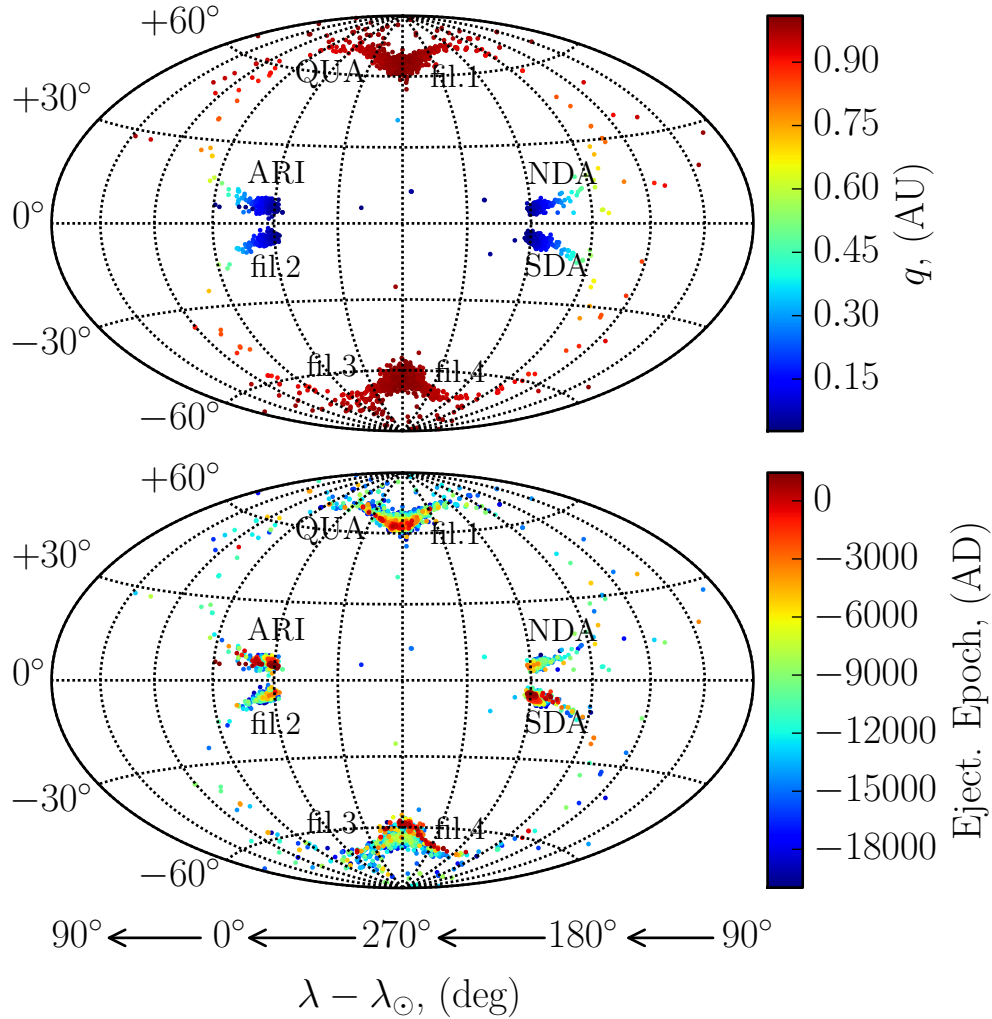
Figure 4.6: Resulting radiant distribution of meteoroids ejected from a single clone of comet 96P with meteoroid ejection onset time 20000 BC. The radiants in top panel are color coded in terms of meteoroids' present perihelion distance, and as a function of meteoroid ejection epoch (lower panel).

their ejection epoch and perihelion distance at that epoch. The perihelion distance of 96P was very low between 7000 BC and 5000 BC, so meteoroids released within that time frame are weighted more, which is the reason for the presently wider FWHM. The poor match between the simulated and observed peak of the QUA is not surprising, as the contribution of asteroid 2003 EH$_1$ is not considered here, whose ejecta were shown to has dominated the core of the stream (Abedin et al., 2015). That results in a very narrow peak activity consisting of relatively large meteoroids, while the extended moderate activity is associated with 96P.

Our interest here is in the wings of the activity profile which produce a relatively good match to the CMOR observations. Brown et al. (2010) argued that QUA show a significant low level activity in the range $232° < \lambda_\odot < 270°$, which was also predicted by simulations.

However, we found that the long-lived activity identified by Brown et al. (2010), as part of the QUA, is a results from two weak nearby showers that peak in the range $232° < \lambda_\odot < 260°$ and partially overlap with the wings of the QUA (see Sec. 4.4.1).
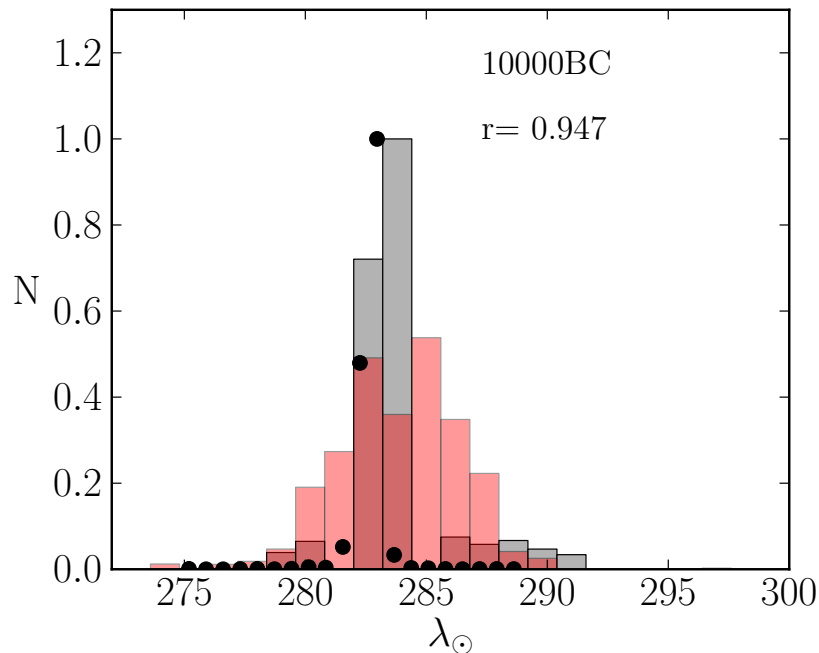
Figure 4.7: Simulated, weighted and normalized activity profile (red histogram) of the QUA, originating from 96P/Machholz with meteoroid ejection onset in 10000 BC. Superimposed are the observed normalized relative activity profiles by CMOR (grey histogram) and IMO visual observations (black circles). The quantity r denotes the sum of the residuals of the fit between the theoretical and CMOR profile.

The simulated radiant drift of the QUA is presented in Fig. 4.9, superimposed over the measurements by CMOR. The simulated mean radiant position at the peak activity $\lambda_\odot = 283.5°$ was $\lambda - \lambda_\odot = 276.4° \pm 3.9°$ and $b = 63.8° \pm 0.9°$, which translates in a mean difference with the CMOR radiant of approximately 0.8 degrees. Our simulations indicate that the QUA stream seems to be mainly dominated by relatively old ejecta (prior to 3000 BC) (see Fig. 4.8) and mostly comprised of small β meteoroids. The reason for that may be the 2:1 MMR with Jupiter (see Appendix D) (e.g., **?**Froeschle and Scholl, 1986; Gonczi et al., 1992; Wiegert and Brown, 2005), which has perhaps scattered away most of the smaller component of the stream, preferentially leaving larger meteoroids. We note that the mean semi-major axis of the stream places it just outside of the 2:1 MMR (Froeschle and Scholl, 1986; Wiegert and Brown, 2005), however solar radiation pressure may have increased the size if the orbits of smaller meteoroids and bring them to Jupiter intersecting orbits, which may has resulted in a subsequent scattering.

Figure 4.10 shows the distribution of the orbital elements of the QUA, assuming meteoroid ejection onset circa 10000 BC from comet 96P, as a function of the solar longitude $\lambda_\odot$. The simulated orbital elements yielded a good match to the measurements by CMOR and CAMS,
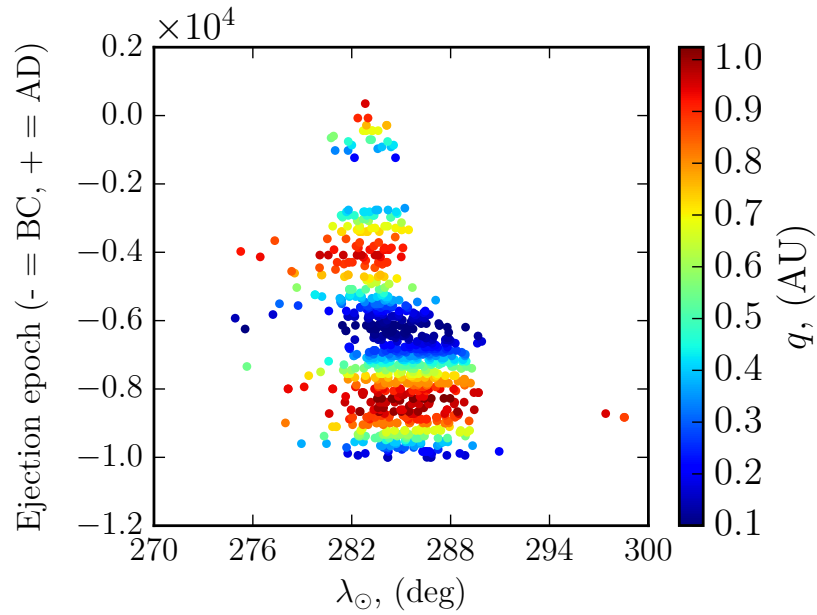
Figure 4.8: Solar longitude distribution of QUAs as a function of meteoroid ejection epoch, from comet 96P/Machholz. Individual meteoroids are color coded in terms of their perihelion distance at time of ejection.

even though the contribution of asteroid 2003 EH$_1$ has been omitted here. The fit of our simulations to the observations, suggest that the wings of the QUA can be explained by a continuous cometary activity of 96P over the last 12000 years, which renders the current age estimate significantly higher than previous estimates of 2200 - 8000 years (Gonczi et al., 1992; Jones and Jones, 1993; Williams and Wu, 1993; Neslušan et al., 2013b).
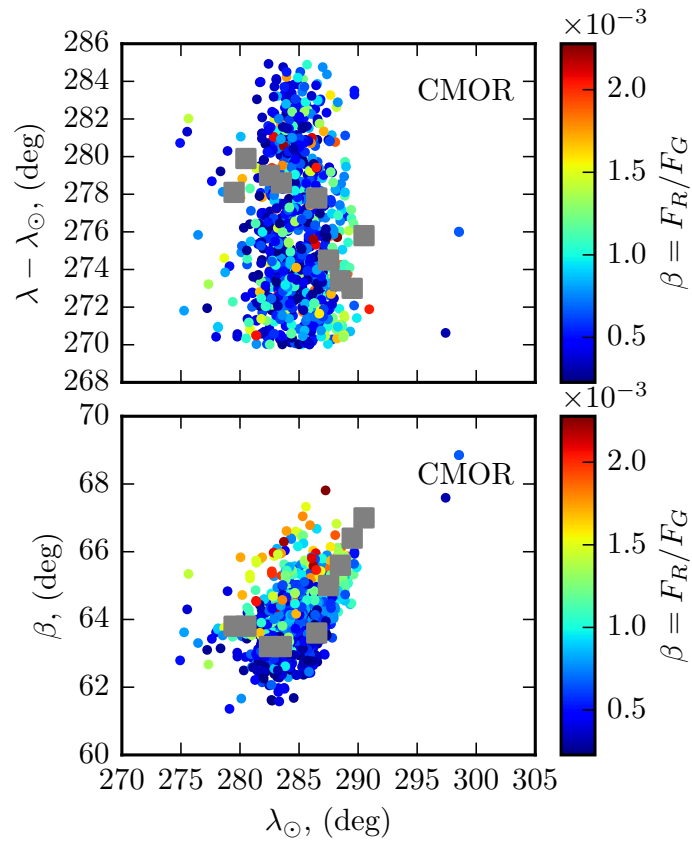
Figure 4.9: Simulated sun-centered radiant drift of QUA, with assumed meteoroid ejection onset in 10000 BC from comet 96P. The color coding is in terms of meteoroid size. Superimposed is the observed radiant drift by CMOR (grey squares).
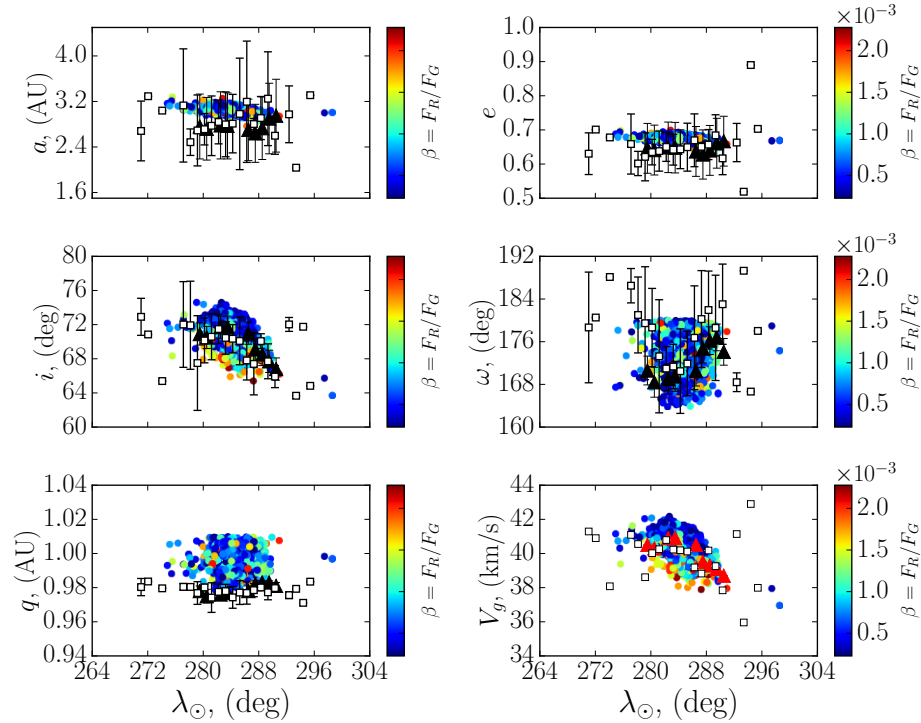
Figure 4.10: Simulated distribution of the orbital elements of the QUA (color dots) for assumed meteoroid ejection onset epoch in 10000 BC from comet 96P. The color coding is in terms of meteoroids' β-parameter (or equivalent to meteoroid size). Superimposed are the observed distributions by CAMS (open squares) and CMOR (grey triangles).

The Southern δ-Aquariids (SDA)

The simulated activity profile of the SDAs originating from 96P and assuming a meteoroid ejection onset time in 17000 BC, is presented in Fig. 4.11 and compared to the observed activity profiles by CMOR and IMO. We recall that we show the simulated resulting shower characteristics only for meteoroid ejection epoch, that produces the best match (see Sec.4.4). Older or earlier ejecta produce poorer fits to the observations. Figure 4.12 shows the nodal longitude of meteoroids, presently approaching the Earth's orbit within 0.01 AU, as a function of their ejection epoch and perihelion distance at the time of ejection. It is evident that meteoroids, primarily contributing to the peak of the profile are those ejected circa 2000 BC and 6000 BC. Particles, older than 10000 BC contribute mainly to the wings of the profile.

Overall, the peak location and the width of the wings of the activity profile yielded a good match to the observation. The FWHM is somewhat narrower than observed but significantly improves when the contribution of comet P/1999 J6 is added (Sec. 4.4.2). The sum of the residuals begin to deteriorate for particles released after 17000 BC, resulting in a too narrow profile, inconsistent with the observations. Conversely, ejections older than 17000 BC produce

activity of longer duration than found from observations.
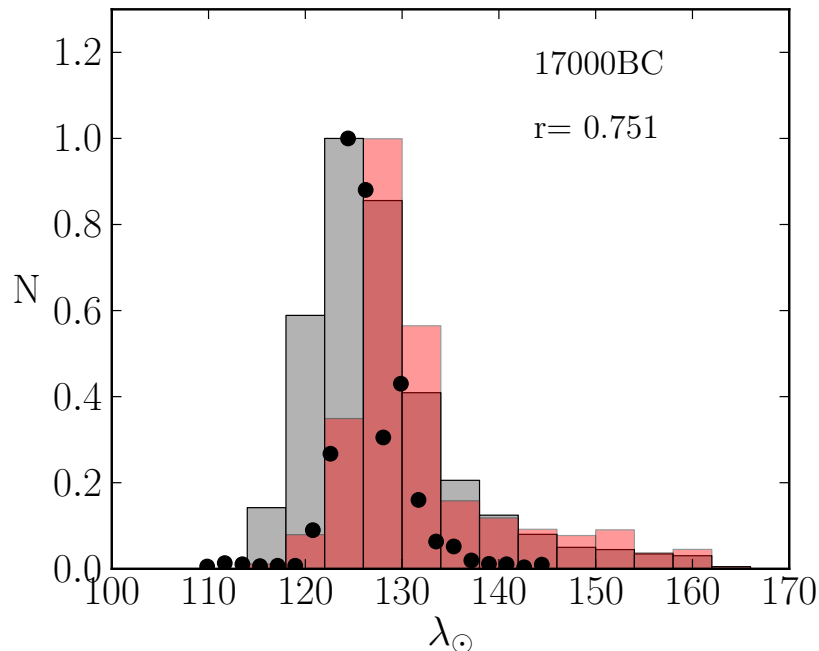
Figure 4.11: Simulated, weighted and normalized activity profile (red histogram) of the SDA, originating from 96P/Machholz with meteoroid ejection onset in 17000 BC. Superimposed are the observed normalized relative activity profiles by CMOR (grey histogram) and IMO visual observations (black circles). Details similar to Fig. 4.7.

The predicted mean radiant position of the SDA at the simulated peak activity $\lambda_\odot = 125°$ was $\lambda - \lambda_\odot = 208.8° \pm 0.5°$ and $b = -6.9° \pm 0.6°$. That results in a mean radiant difference of 1.2 degrees compared to CMOR observations. It is worth noting that the CMOR observed radiant has a significant spread as well (of order 2-3 degrees) due to measurement uncertainties.

The simulated radiant drift is presented in Fig. 4.13. It shows a significant spread of $\Delta(\lambda - \lambda_\odot) \approx 15°$, along the ecliptic, but only a moderate dispersal in ecliptic latitude b. In contrast, the CMOR observations measure a nearly constant β for $140° < \lambda_\odot < 165°$, which was not reproduced by our simulations. A possible reason for that may be that there is another body (or bodies) that may be contributing to the SDAs that has not been accounted for in the current study. In fact, beside comet 96P and P/1999 J6, Neslušan et al. (2013a) showed that asteroid 2003 EH$_1$ also contributes to the SDAs. Nevertheless, meteoroid ejections from 96P, circa, 17000 BC produce a good match to the observed characteristics of the SDAs, in particular the duration of the shower activity.
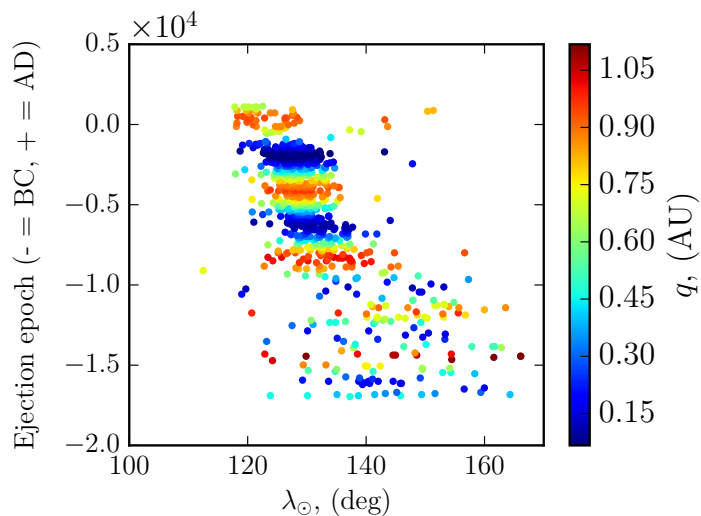
Figure 4.12: Solar longitude distribution of SDA as a function of meteoroid ejection epoch, from comet 96P/Machholz. Individual meteoroids are color coded in terms of their perihelion distance at time of ejection.
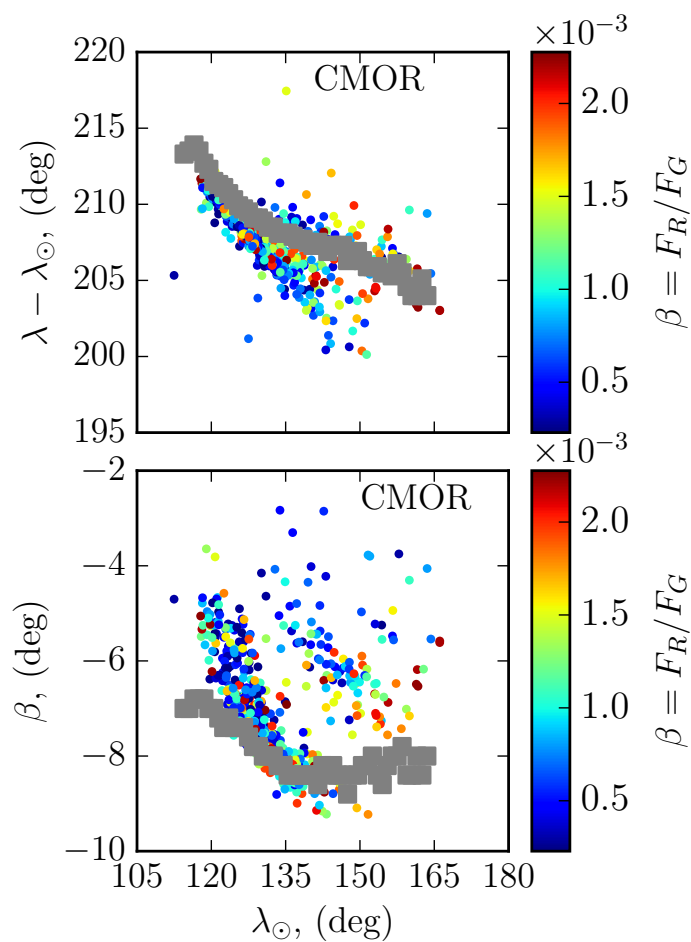

Figure 4.13: Simulated sun-centered radiant drift of SDA, with assumed meteoroid ejection onset in 17000 BC from comet 96P. The color coding is in terms of meteoroid size. Superimposed is the observed radiant drift by CMOR (grey squares).

Figure 4.14 shows the simulated distribution of the orbital elements of the SDAs as a function of solar longitude, for meteoroid ejection onset in 17000 BC. The theoretical values are compared against the observations by the CMOR and CAMS meteor surveys. There has been a long-standing discrepancy of the meteoroids' calculated orbital semi-major axis and geocentric speeds derived from optical and radar surveys (Jenniskens et al., 2012). It is evident that the meteoroids' semi-major axes deduced from radar measurements are systematically lower than the optical measurements. Sometimes, these differences are larger than the scatter of individual meteoroids. Jenniskens et al. (2012) suggested that the discrepancy is likely due to improper account for atmospheric deceleration of radar size particles. Apart from these discrepancies, the rest of the simulated orbital elements produced a relatively good match to both radar and optical measurements.
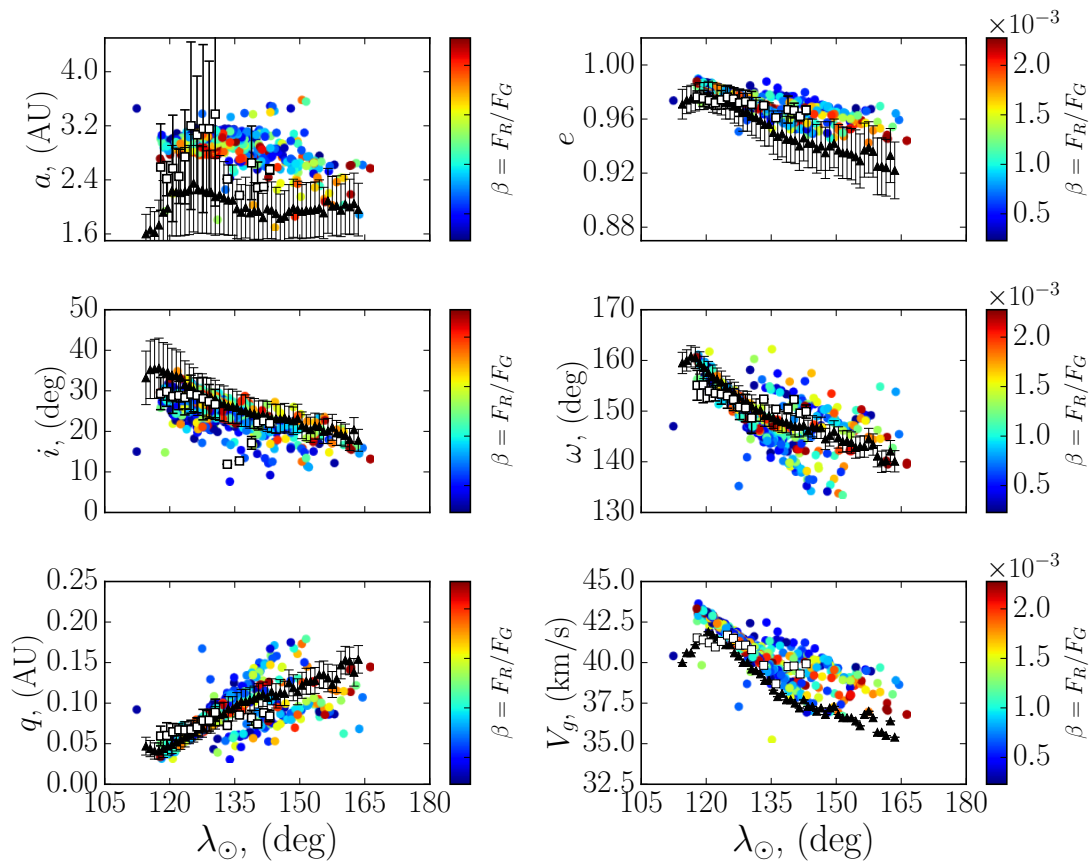
Figure 4.14: Simulated distribution of the orbital elements of the SDAs (color dots) for assumed meteoroid ejection onset epoch in 17000 BC, from comet 96P. The color coding is in terms of meteoroids' β-parameter (or equivalent to meteoroid size). Superimposed are the observed mean values of the orbital elements in each bin, respectively by CAMS (open squares) and CMOR (grey triangles). The error bars correspond to 1σ uncertainty.

The Northern δ-Aquariids (NDA)

The NDAs are the northern branch of the SDAs and are also found in the anti-hellion sporadic source. The simulated activity profile of the NDAs is presented in Fig. 4.15 for meteoroid ejection onset time in 16000 BC, and compared to observed ones by CMOR and IMO. Figure 4.16 shows which particles have been ejected at lower perihelion distances and at what epoch, so those meteoroids will receive a larger weights (Sec 4.3.4 and Sec. 4.3.4). Our simulations show that the bulk of the meteoroids contributing to the NDAs have been released prior to 10000 BC and the resulting FWHM of the activity profile is wider, compared to the SDAs for example, mainly due to the ejections between 10000 BC and 14000 BC.

Figure 4.15 shows that the IMO visual observations are rather scattered, without a clear peak. That is mainly due to the weak nature of the NDAs and preferential detection of only the larger meteoroids by visual observations. In contrast, the radar measurements yielded a better defined overall profile, though also without a clearly distinct peak. Instead, the CMOR profile shows an almost constant activity in the range $130° < \lambda_\odot < 145°$ with a local maximum around $\lambda_\odot=137°$. In comparison, our simulated profile yielded a slightly better defined shape and peak, though the latter seems to occur near $\lambda_\odot=140°$. Overall, the simulated width of the activity profile produced a good fit to the CMOR data. There may be other bodies (not included in this study) also contributing to the NDAs. Nonetheless, our analysis of the fit between the theoretical and observed activity profiles suggest that the shower is much older than the 2000 years previously suggested by Sekanina and Chodas (2005).
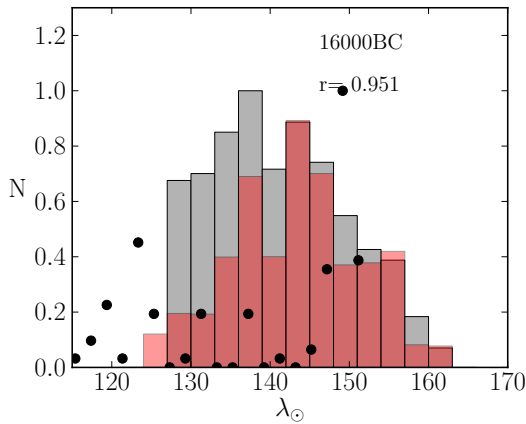

Figure 4.15: Simulated, weighted and normalized activity profile (red histogram) of the NDA, originating from 96P/Machholz with meteoroid ejection onset in 16000 BC. Superimposed are the observed normalized relative activity profiles by CMOR (grey histogram) and IMO visual observations (black circles). Details similar to Fig. 4.7.
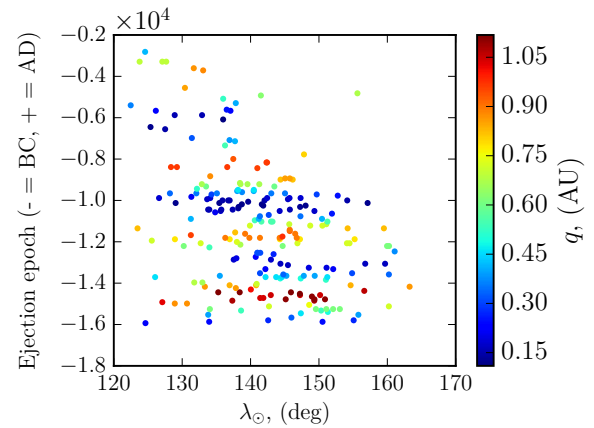
Figure 4.16: Solar longitude distribution of NDA as a function of meteoroid ejection epoch, from comet 96P/Machholz. Individual meteoroids are color coded in terms of their perihelion distance at time of ejection.

The simulated mean radiant location at $\lambda_\odot = 140°$ is $\lambda - \lambda_\odot = 206.0° \pm 1.4°$ and $b =$

6.7° ± 0.4°, with a difference of 2.5 degrees from the CMOR measured mean radiant (see Tab. 4.1 in Sec. 4.2 for details). The simulated radiant drift is presented in Fig. 4.17 and is compared to the CMOR observations. The simulation yielded satisfactory results, given the uncertainties and the assumptions used in the radiant computation. CMOR measures a substantial drift of almost $\Delta(\lambda - \lambda_\odot) = 10°$ along the ecliptic but almost none along the ecliptic latitude b. Our simulations produced a less good fit to the drift along b (see Fig. 4.17).
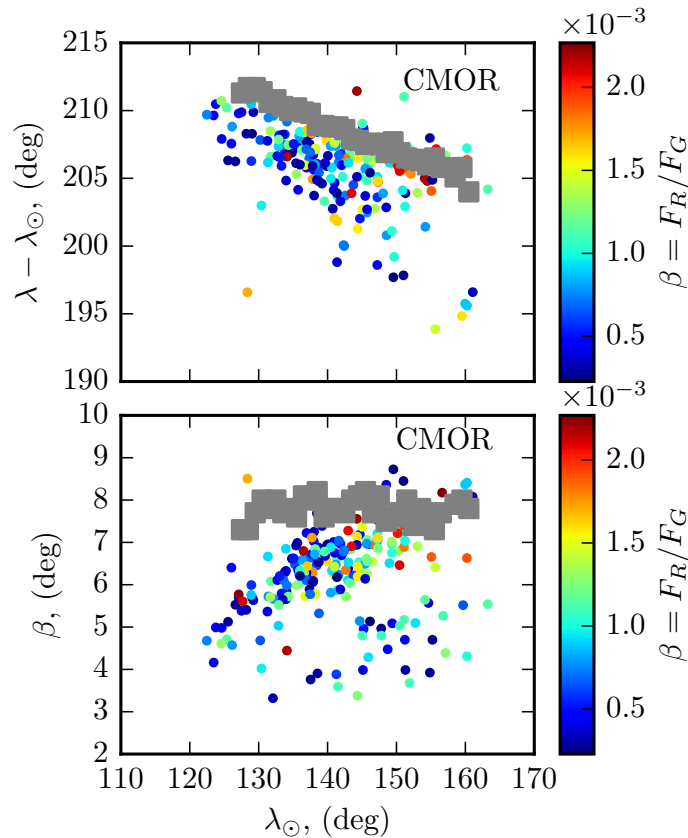
Figure 4.17: Simulated sun-centered radiant drift of NDA, with assumed meteoroid ejection onset in 16000 BC from comet 96P. The color coding is in terms of meteoroid size. Superimposed is the observed radiant drift by CMOR (grey squares).

The simulated distribution of the orbital elements of the meteoroids, approaching the Earth within 0.01 AU, is presented in Fig. 4.18 and compared with optical and radar observations by CAMS and CMOR, respectively. Similar to previous cases, there is an obvious discrepancy between the simulated and measured semi-major axes and meteoroids' geocentric speeds. Our simulations predict a mean semi-major axis of $a \approx 3$ AU, whereas the radar and CAMS has measured a systematically lower values of $a \approx 1.8$ AU. For other showers that we have examined, the optical measurements show larger values for a, though in this case they seem to be in a good agreement with radar data. However, the semi-major axes measured by CAMS

show a significant scatter prior to the peak activity , a dispersion comparable to the error bars due to small number statistics. Furthermore, the CAMS measurements are consistent with the semi-major axes calculated by CMOR near and after the peak. We note that, similar to visual observations, video and TV observations are biased towards larger (millimeter) and faster meteoroids, though the sensitivity threshold is much higher than visual observations. In contrast, aside from the capability of detecting smaller and slower meteors, the radar detections are not limited by the weather conditions and daylight. Thus, it is not unreasonable to expected the CMOR data to be more uniform time wise than the CAMS data.
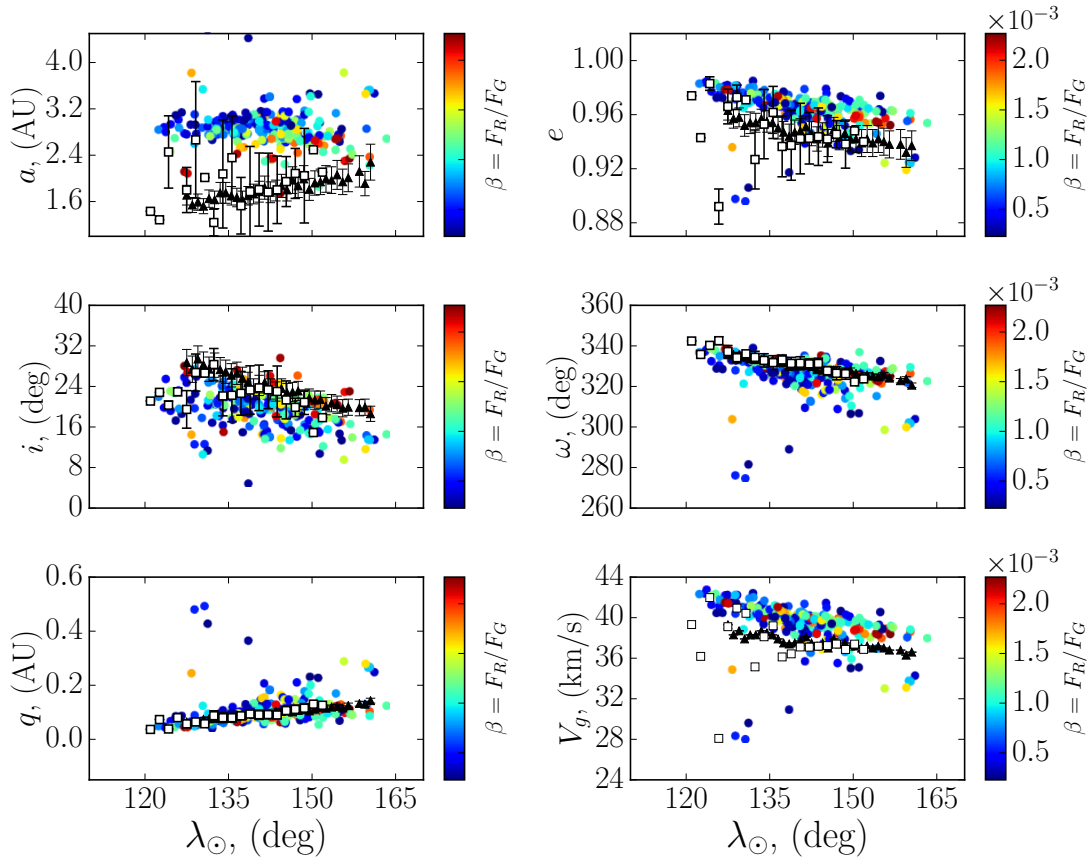
Figure 4.18: Simulated distribution of the orbital elements of the NDAs (color dots) for assumed meteoroid ejection onset epoch in 16000 BC, from comet 96P. The color coding is in terms of meteoroids' β-parameter (or equivalent to meteoroid size). Superimposed are the observed distributions by CAMS (open squares) and CMOR (black triangles).

Filament 1

Our numerical simulations from 96P predicted a meteor shower in the north toroidal source with radiant location between $210° < (\lambda - \lambda_\odot) < 270°$ and $55° < b < 70°$ with activity pe-

riod between $220° < \lambda_\odot < 270°$. Using a 3D-Wavelet search, described in Sec. 4.2 we have identified two weak showers in the CMOR data, that overlap in time (Fig. 4.6) and also simultaneously matched, within the uncertainty, the QUA shower. These showers are the November ι-Draconids (NID) and the December α-Draconids (DAD), being identified as separate in the IAU MDC. The simulated activity profile of this filament is presented in Fig. 4.19, and compared to the CMOR observations. Our simulations suggest that if this filament is considered as a single shower, then its activity steadily increases reaching a maximum activity near $\lambda_\odot = 260°$ and then suddenly decreases to the sporadic background activity and merges with QUAs. However, if the filament indeed consists of two weak nearby showers, their separation is not possible by the wavelet search, similar to the result reported by Neslušan et al. (2013b). According to Brown et al. (2010), the NIDs are active from $221° < \lambda_\odot < 267°$ with maximum activity near $\lambda_\odot = 241°$, whereas the CAMS data sets the activity period $239° < \lambda_\odot < 267°$ with a peak activity at $\lambda_\odot = 242°$ (Jenniskens et al., 2016). In contrast, the CAMS measured activity period of the DADs is $239° < \lambda_\odot < 262°$ with a maximum activity at $\lambda_\odot = 256°$ (Jenniskens et al., 2016). Evidently, the NID and DAD peak at the same time, both eventually merging with early QUA activity. We call these two showers - filament 1. The best match between the CMOR-derived activity profile of filament 1 and our simulations was obtained assuming meteoroid ejection onset time circa 18000 BC, from comet 96P. Earlier ejections resulted in a too narrow profile and low activity, inconsistent with the CMOR-derived profile. In fact the youngest particles that presently reach the Earth must have been released around 3000 BC (see Fig. 4.20).
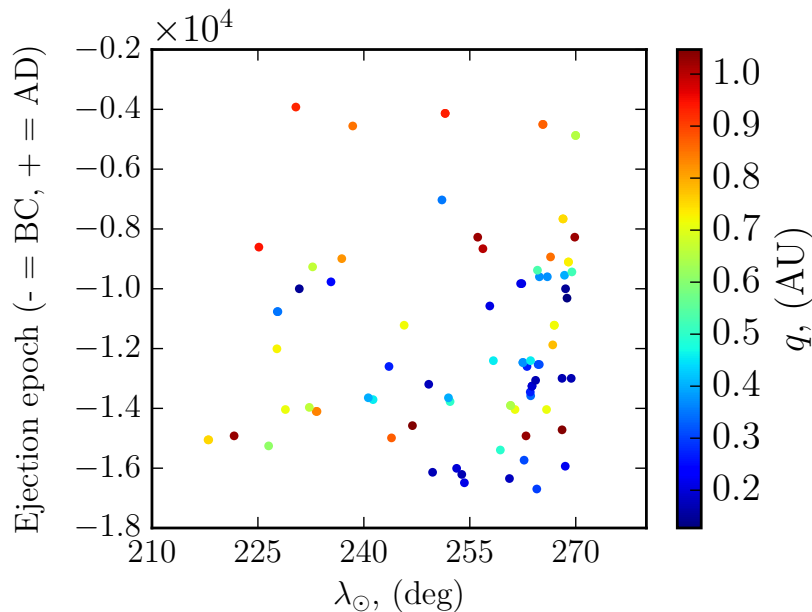

Figure 4.20: Solar longitude distribution of filament 1 as a function of meteoroid ejection epoch, from comet 96P/Machholz. Individual meteoroids are color coded in terms of their perihelion distance at time of ejection.
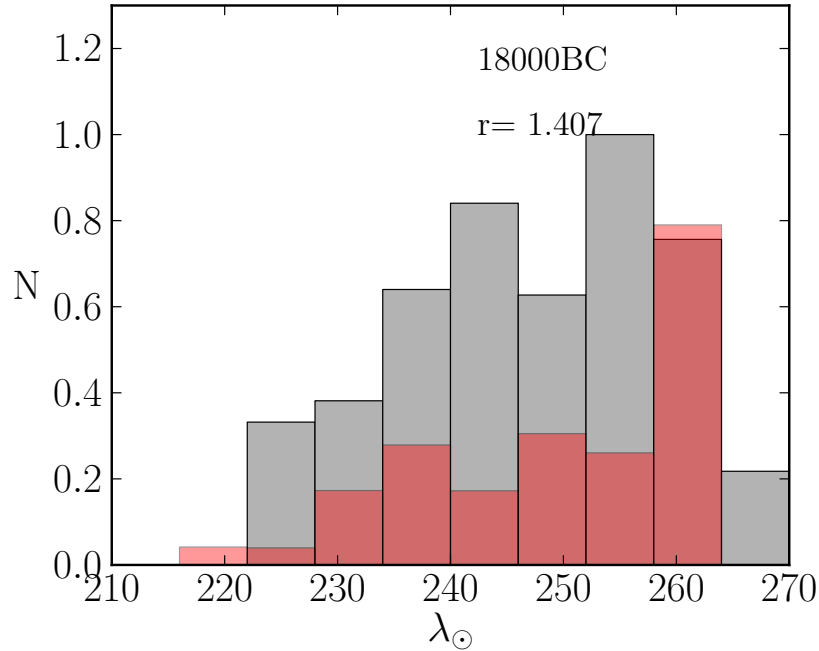
Figure 4.19: Simulated, weighted and normalized activity profile (red histogram) of filament 1, originating from 96P/Machholz with meteoroid ejection onset in 18000 BC. Superimposed are the observed normalized relative activity profiles by CMOR (grey histogram). See Fig. 4.7 for details.

Our calculated mean radiant location at the peak activity of $\lambda_\odot = 256°$ was $\lambda - \lambda_\odot = 259.2° \pm 18.9°$ and $b = 66.7° \pm 3.1°$. That peak location corresponds to the maximum activity time of the DAD (Jenniskens et al., 2016), and the comparison with the CAMS radiant results in a mean difference of about 11 degrees (Sec. 4.2, Tab. 4.1). That is clearly a poor match with the observations. However, if we calculate the radiant at the peak time of the NID ($\lambda_\odot = 242°$), then the resulting mean radiant is $\lambda - \lambda_\odot = 267.2° \pm 8.2°$ and $b = 64.1° \pm 0.3°$, with a mean difference with the CMOR-derived radiant of 2.6 degrees. The overall NID simulated radiant position yielded a better fit to the observations, while the DAD demonstrated a large radiant dispersion which results in a difference of almost 20 degrees with the mean CAMS radiant. However, given the simulation uncertainties and the observational resolution the NID and DAD appear as a single weak and diffuse shower. In fact, these radiants are quite diffuse in the radar measurements as well. However, we note that the 3D wavelet search applies a speed and radiant probe size, as well as an activity threshold (3σ above the median sporadic background), used to isolate the radiants. That, along with the weak nature are possible reasons of the inseparability of the two showers, or the NID and DAD are indeed a single continuous shower.

The simulated radiant drift match (Fig. 4.21) was also poor, where observations predict almost no drift while our simulations predicted a drift of almost $\Delta(\lambda - \lambda_\odot) \approx 80°$ and $\Delta b \approx 15°$. If our simulations represent the past evolution of the complex, its nature is even more complicated

than initially thought, where 96P maybe contributes to a few weak nearby showers as well, essentially rendering them as a continuous complex of meteoroids whose radiant separation is virtually impossible.
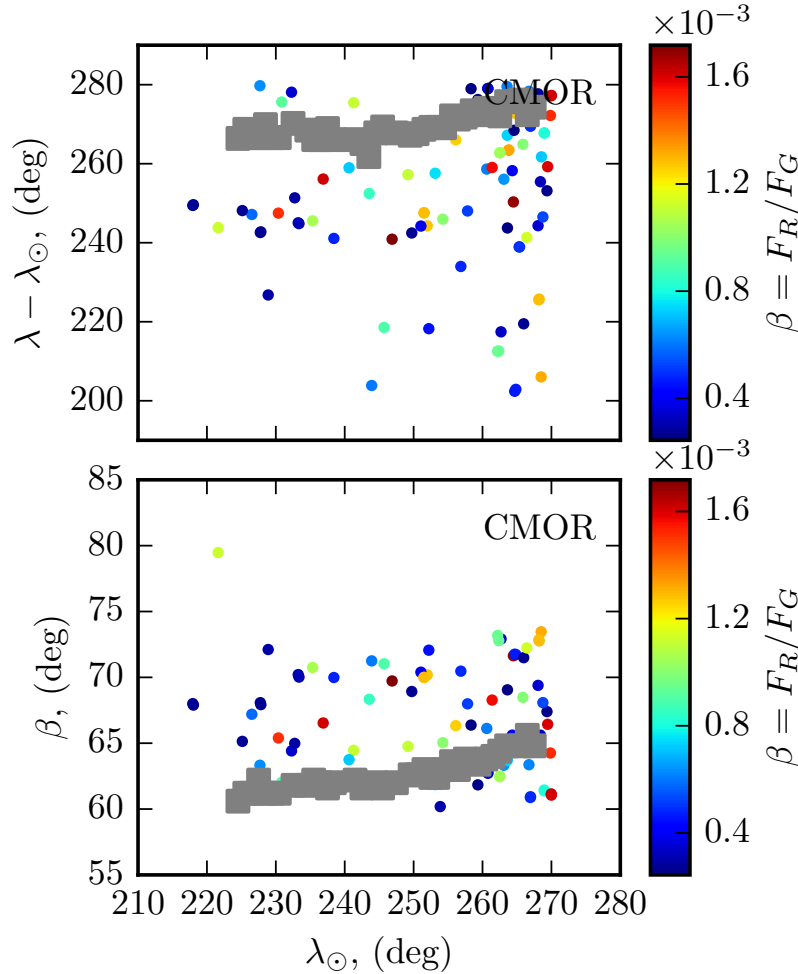

Figure 4.21: Simulated sun-centered radiant drift of filament 1, with assumed meteoroid ejection onset in 18000 BC from comet 96P. The color coding is in terms of meteoroid size. Superimposed is the observed radiant drift by CMOR (grey squares).

Figure 4.22 shows the simulated distribution of the orbital elements of meteoroids, presently reaching the Earth, as a function of the solar longitude. In addition to the recurring issue whereby CMOR measured speeds tend to produce smaller semi-major axis than the simulations predict, the overall fit to the measured orbital elements was poor. Our simulations predicted a greater scatter in the geocentric speeds and most of the orbital elements between individual meteoroids. The inclination and the argument of perihelion showed a dispersion of almost 20 and 15 degrees, respectively while the theoretical eccentricity was overestimated by approximately 0.15. The poor match of our simulations with the observations may be suggests that there is

another more dominant parent/parents contributing to filament 1 which was not considered in this work. Conversely, if our simulations represent the past evolution of the 96P complex, that may imply that 96P contributes to a few other meteor showers in the north toroidal source.
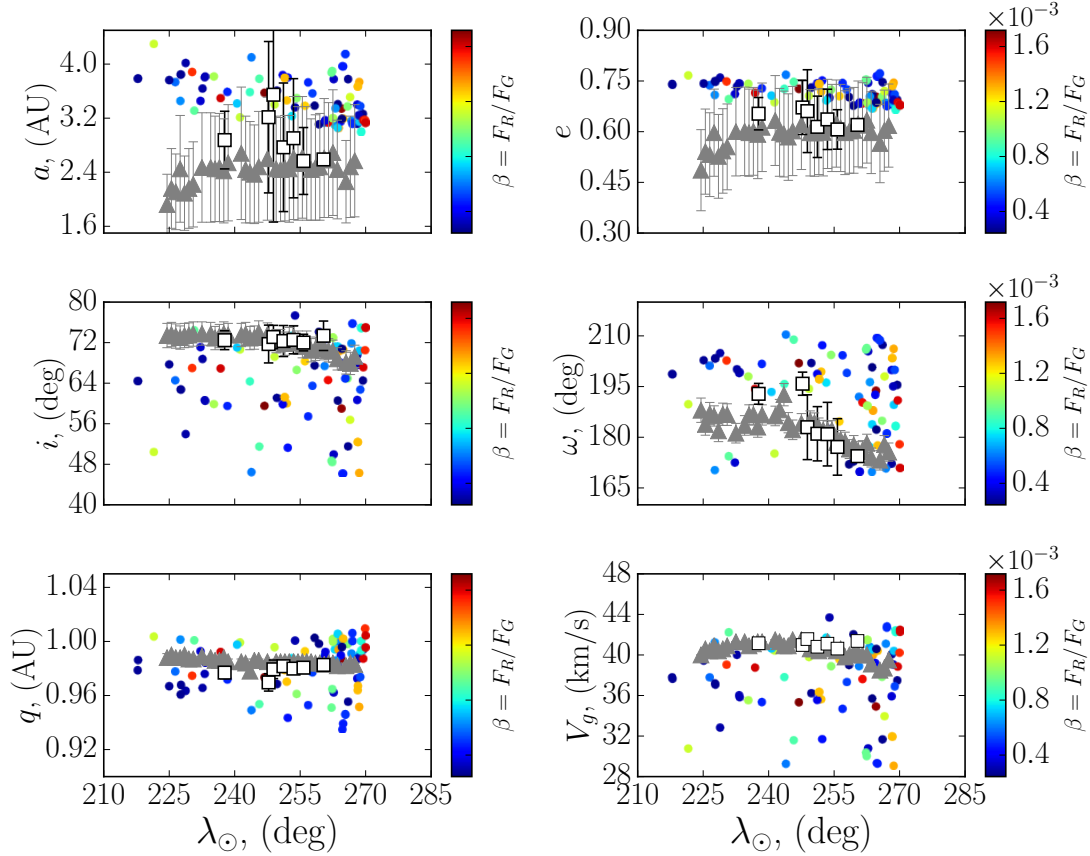

Figure 4.22: Simulated distribution of the orbital elements of the filament 1 (color dots) for assumed meteoroid ejection onset epoch in 18000 BC from comet 96P. The color coding is in terms of meteoroids' β-parameter (or equivalent to meteoroid size). Superimposed are the observed distributions by CAMS (open squares) and CMOR (grey triangles).

Filament 2

Filament 2 in our simulations is predicted to be a meteor shower with radiant location between $325° < (\lambda - \lambda_\odot) < 340°$ and $-10° < b < -4°$ (see Fig. 4.6), located south of the well known ARI. Using a 3D wavelet search in the CMOR database, we established that filament 2 exists and has an activity profile and radiant position resembling the daytime λ-Taurids (DLTs) (Brown et al., 2008, 2010). Unlike filament 1, the DLT appear to be stronger and well defined. Figure 4.23 shows the simulated activity profile, compared to radar observations by CMOR. The simulated maximum activity occurs at $\lambda_\odot = 82.5°$, while CMOR observations measure a peak activity at $\lambda_\odot = 82.5°$. We note that, at the time of preparation of this work, there were no available

optical observations of the DLT, perhaps mainly due to their daytime nature and significantly lower activity compared to the ARI.

Investigation of various meteoroid ejection onset times yielded a best match between the theoretical and observed shapes of the activity profiles, assuming 96P has been captured in a short period orbit circa 20000 BC. However, our residual analysis of the shape of the profiles did not converge to a minimum value, due to our limited simulations time window of 22000 years. That might indicate that the DLTs are even older, or that another body contributes to some portion of the activity profile. We note that there are a few degrees discrepancy between the observed and simulated extent of the wings of the activity profile, likely due to the activity level cutoff threshold of 3σ imposed by our 3D wavelet search (see Sec. 4.2). Furthermore, the FWHM of the simulated profile was somewhat narrower compared to the CMOR profile, which leads to hypothesize that perhaps there may be another body or bodies that may be contributing to the stream, though 96P seems to be the dominant parent.
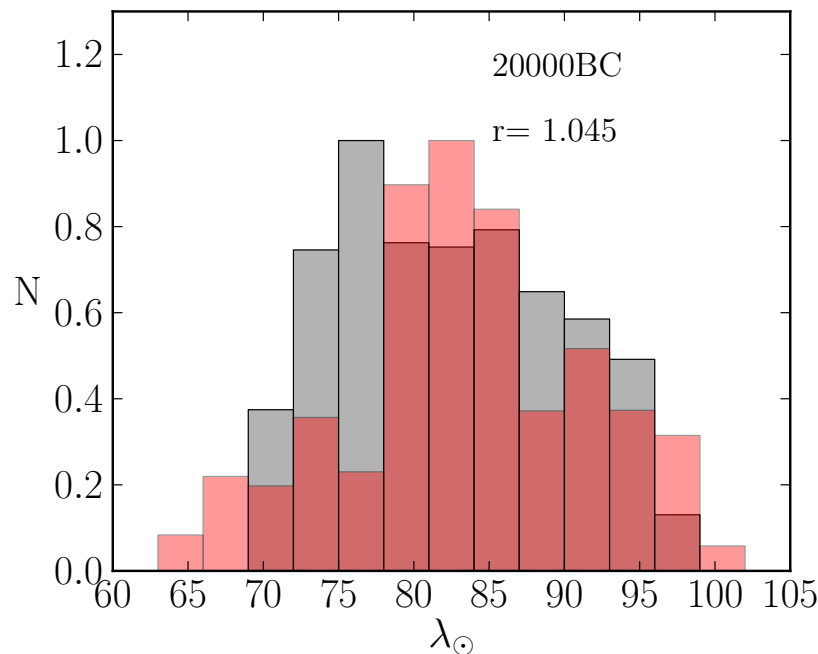

Figure 4.23: Simulated, weighted and normalized activity profile (red histogram) of filament 2, originating from 96P/Machholz with meteoroid ejection onset in 20000 BC. Superimposed are the observed normalized relative activity profiles by CMOR (grey histogram).

The simulated mean radiant location at $\lambda_\odot = 82.5°$ was $\lambda - \lambda_\odot = 333.4° \pm 1.3°$ and $b = -6.5° \pm 0.7°$. That corresponds to a mean difference of 2.8 degrees with the CMOR measured mean radiant (see Tab. 4.1 in Sec. 4.2 for details). Likely, the reason for the small difference is a result of the slightly different CMOR-derived peak location, as well as the uncertainties in our simulations.
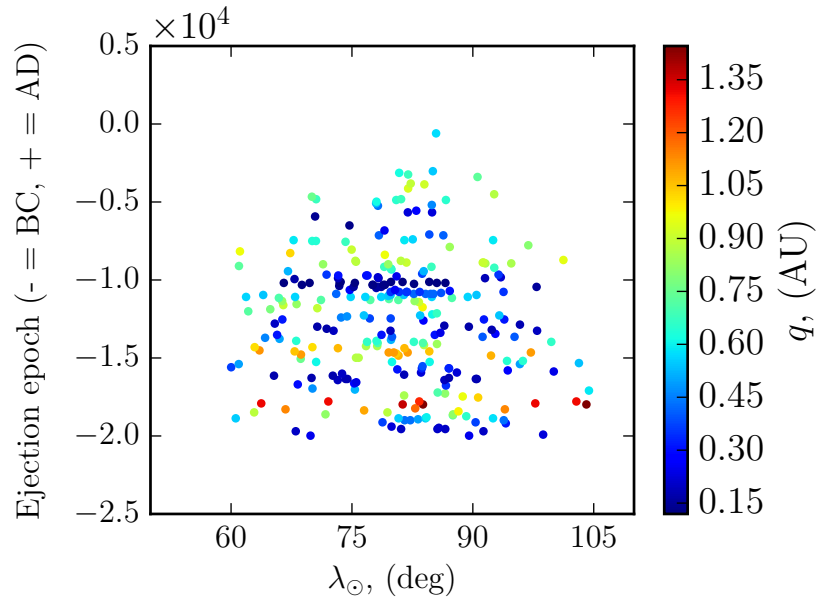
Figure 4.24: Solar longitude distribution of filament 2 as a function of meteoroid ejection epoch, from comet 96P/Machholz. Individual meteoroids are color coded in terms of their perihelion distance at time of ejection.

Figure 4.25 shows the simulated radiant drift of the DLTs, compared to the CMOR observations. The latter suggests a drift along the ecliptic of $\Delta(\lambda - \lambda_\odot) \approx 5°$ whereas the simulations yielded $\Delta(\lambda - \lambda_\odot) \approx 12°$ with slightly larger dispersion. The drift along the ecliptic latitude produced a better match, though the individual radiants also demonstrated a moderate scatter. However, these fits are relatively good given the long integration timescales and the chaos involved in the dynamics.
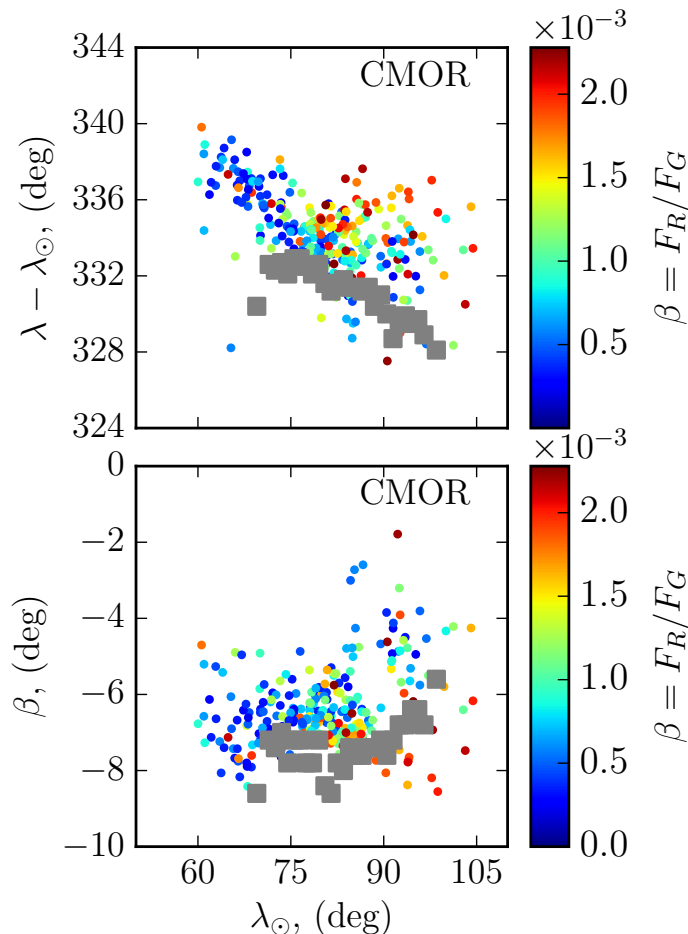
Figure 4.25: Simulated sun-centered radiant drift of filament 2, with assumed meteoroid ejection onset in 20000 BC from comet 96P. The color coding is in terms of meteoroid size. Superimposed is the observed radiant drift by CMOR (grey squares).

The distribution of the orbital elements of the resulting simulated stream are presented in Fig. 4.26. As in the previous cases, there was a substantial systematic offset between the simulated and the observed meteoroids' geocentric speeds, orbital semi-major axes and eccentricity. We recall that, unlike the ARI, there are no optical detections of the DLTs, and hence no orbital elements for comparison. However, apart from the poor fit in semi-major axis and eccentricity, the match in the angular orbital elements and the perihelion distance yield satisfactory results. Figure 4.26 shows that the simulated width of the shower is somewhat wider compared to radar observations. The reason may be that within the frames of our simulations, we do not impose an activity level threshold, whereas in the case of CMOR a shower is defined as activity level greater that 3σ above the median value of the sporadic background activity (see Sec. 4.2). The distributions of the orbital elements seem to change linearly during the activity period of the DLTs, where the simulated slope yields a good match to the observations.
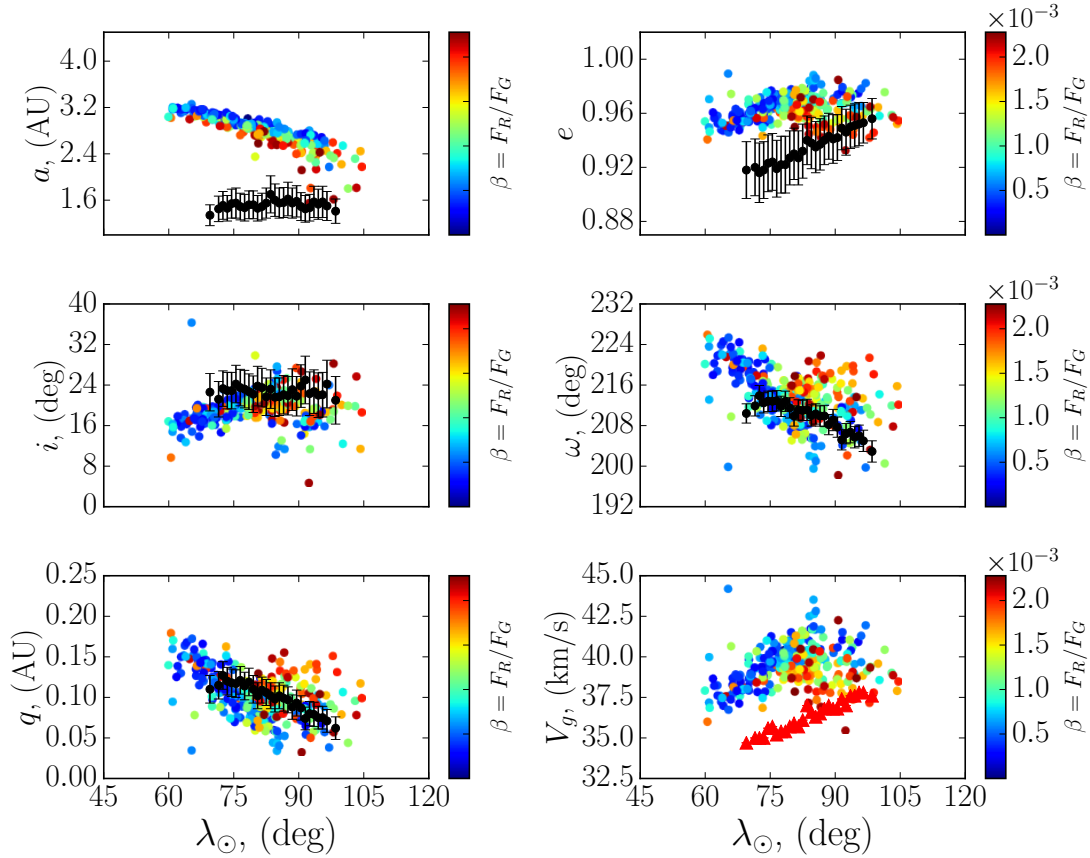
Figure 4.26: Simulated distribution of the orbital elements of the filament 2 (color dots) for assumed meteoroid ejection onset epoch in 20000 BC from comet 96P. The color coding is in terms of meteoroids' β-parameter (or equivalent to meteoroid size). Superimposed is the observed distributions by CMOR (black circles).

Filament 3

Filament 3 (see Fig. 4.6) is located deep in the southern hemisphere with a mean sun-centered radiant location $(\lambda - \lambda_\odot) = 279.3° \pm 3.1°$ and $b = -63.3° \pm 1.7°$. Similar to previous filaments, a 3D wavelet search in the SAAMER database (Janches et al., 2013, 2015) indicated a radiant location resembling the θ-Carinids. The simulated activity profile of the shower is presented in Fig. 4.27 and compared to the SAAMER-derived profile. While the timing of the maximum activity was well reproduced, the overall width of the shower profile was not. The simulations predict an activity extending $272° < \lambda_\odot < 283°$ with the main peak activity at $\lambda_\odot = 276°$ and a secondary maximum near $\lambda_\odot = 281°$, the association of which with a separate shower is uncertain. However, we note that the available SAAMER observations spans only 3 years and hence the shower might not be well defined due to small number statistics. Moreover, likely the shower is weak as well, as implied by the simulations (see Fig. 4.28). However, if the activity of the TCD is indeed only 5 days, that may well imply an extended activity of a few
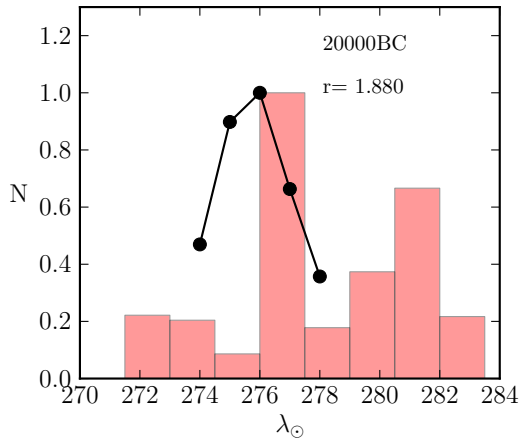
Figure 4.27: Simulated, weighted and normalized activity profile of filament 3, originating from 96P/Machholz (red histogram) with meteoroid ejection onset in 20000 BC. The black circles corresponds to the observed normalized activity profile by SAAMER.
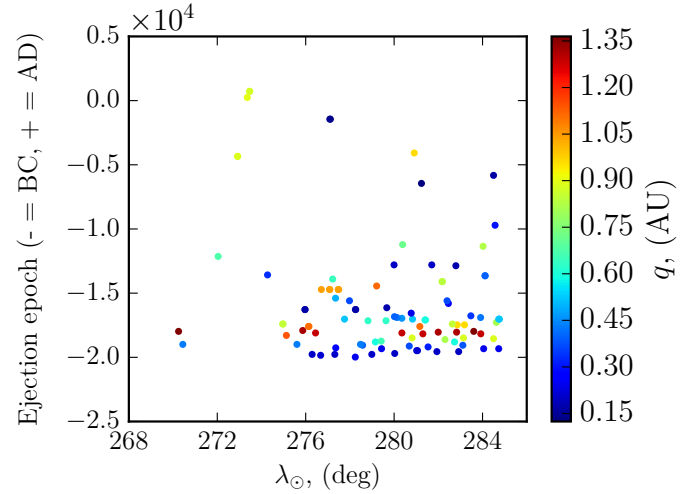
Figure 4.28: Solar longitude distribution of filament 3 as a function of meteoroid ejection epoch, from comet 96P/Machholz. Individual meteoroids are color coded in terms of their perihelion distance at time of ejection.

overlapping showers, a case similar to QUA and filament 1.

The best match between the predicted and observed activity profiles is obtained assuming initial meteoroid ejection onset from comet 96P circa 20000 BC. However, that epoch is the furthest we went back in our backward simulations. In fact, the residuals of the profile fit did not converge and perhaps the TCDs may be older than 22000 years. Figure 4.28 shows that meteoroids ejected after 15000 BC would result in a weak and scattered activity.

The simulated mean radiant location at $\lambda_\odot = 276°$ is $\lambda - \lambda_\odot = 279.1° \pm 3.0°$ and $b = -61.6° \pm 1.9°$. That corresponds to a mean difference of 4 degrees with the SAAMER-derived mean radiant (see Tab. 4.1 in Sec. 4.2 for comparison with SAAMER radiant), a difference also evident in the the simulated radiant drift (Fig. 4.29). Interestingly, the simulated radiant drift shows a large scatter between individual meteoroids ($\Delta(\lambda - \lambda_\odot) \approx 15°$), while SAAMER measures a drift of roughly 4 degrees along the ecliptic and almost none in the ecliptic latitude. That large scatter may suggest that 96P contributes to other nearby shower/showers, though we did not find a candidate in the SAAMER database.

Furthermore, the shower consists mainly of old ejecta, a result that is also clear from Fig. 4.28. There is no obvious mass segregation along the radiant, though the stream seems to be dominated by relatively larger particles (millimeter size). Perhaps, similar to the QUA there is a mechanism such as a MMR with Jupiter which preferentially scatters away smaller particles or the action of PR drag has decreased the orbits of small particles, so that they do not presently intersect the Earth.
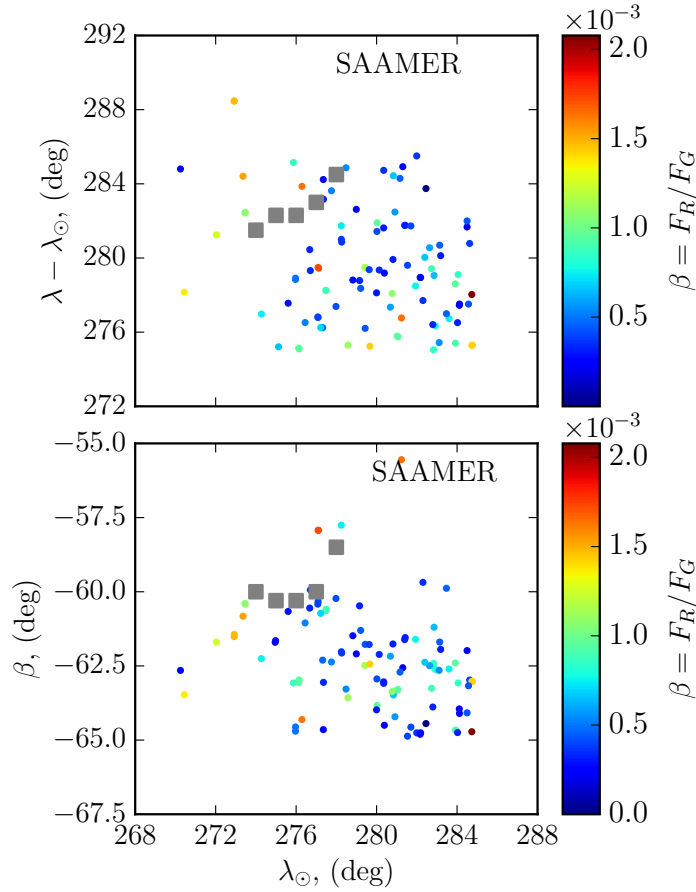
Figure 4.29: Simulated sun-centered radiant drift of filament 3, with assumed meteoroid ejection onset in 20000 BC from comet 96P. The color coding is in terms of meteoroid size. Superimposed is the observed radiant drift by CMOR (grey squares).

The fit to the observed distribution of the orbital elements of TCD is presented in Fig. 4.30. Our simulations predict systematically higher values of the orbital semi-major axis $a \approx 3$ AU, whereas SAAMER measures a mean value of about 2 AU. We note that we did not find optical observations of the TCD, in the literature, so we can not determine the reliability of our estimations and the degree of discrepancy with optical surveys. The simulated orbital eccentricity is also somewhat higher, though within the measurement uncertainties. A close inspection of Fig. 4.30 reveals a steep drop in all orbital elements except the inclination, beyond $\lambda_\odot = 276°$, which if real (not due to low meteor number statistics) likely suggest of existence of another nearby shower.
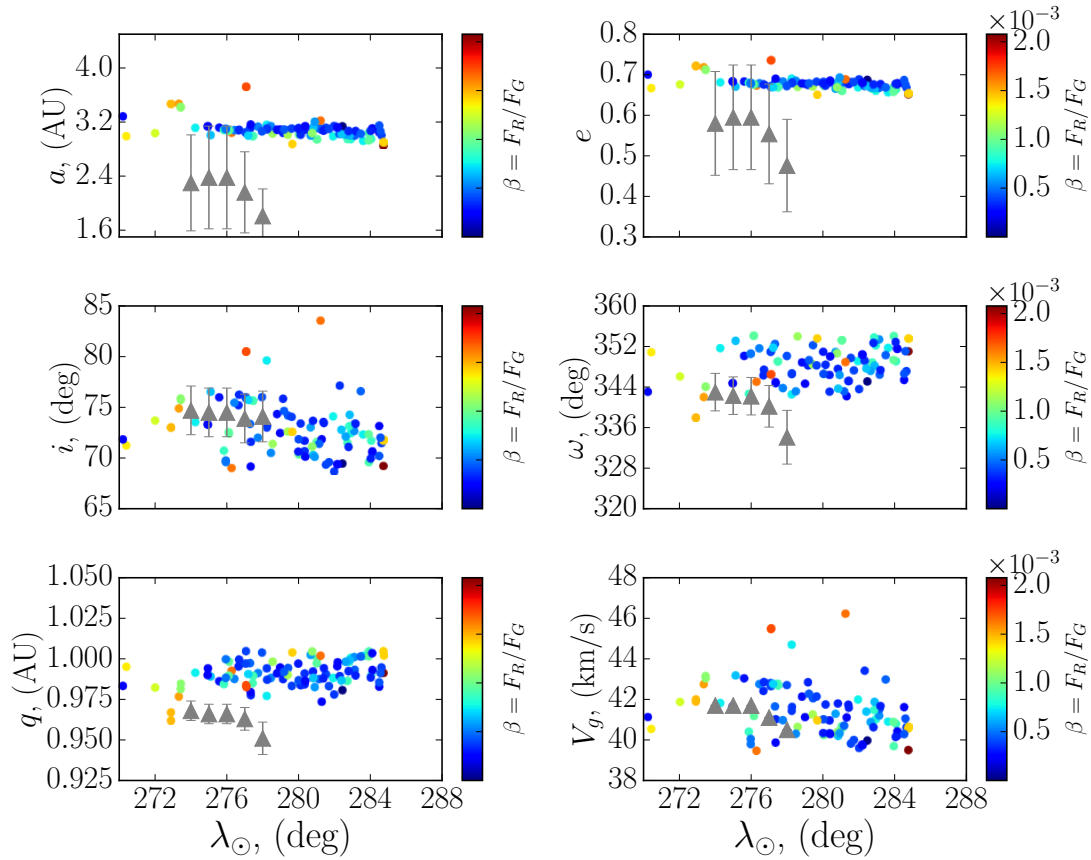
Figure 4.30: Simulated distribution of the orbital elements of the filament 3 (color dots) for assumed meteoroid ejection onset epoch in 20000 BC from comet 96P. The color coding is in terms of meteoroids' β-parameter (or equivalent to meteoroid size). Superimposed is the observed distributions SAAMER (grey triangles).

Filament 4

Filament 4, according to our simulation, corresponds to a meteor shower from a mean radiant position $(\lambda - \lambda_\odot) = 260.3° \pm 2.8°$ and $b = -62.6° \pm 1.9°$. A 3D wavelet search (see Sec. 4.2) in the SAAMER database indicated a radiant location resembling the KVE shower that is found the southern toroidal source. Figure 4.31 shows the simulated and weighted activity profile of the KVE, compared to SAAMER observations. Interestingly, this activity range is similar to that of filament 3, that was identified as the TCD. In fact, both filaments seem to have approximately the same duration and peak at the same time (see Fig. 4.27 for comparison), though their mean radiant positions are separated by about 20 degrees (see Tab. 4.1 in Sec. 4.2).
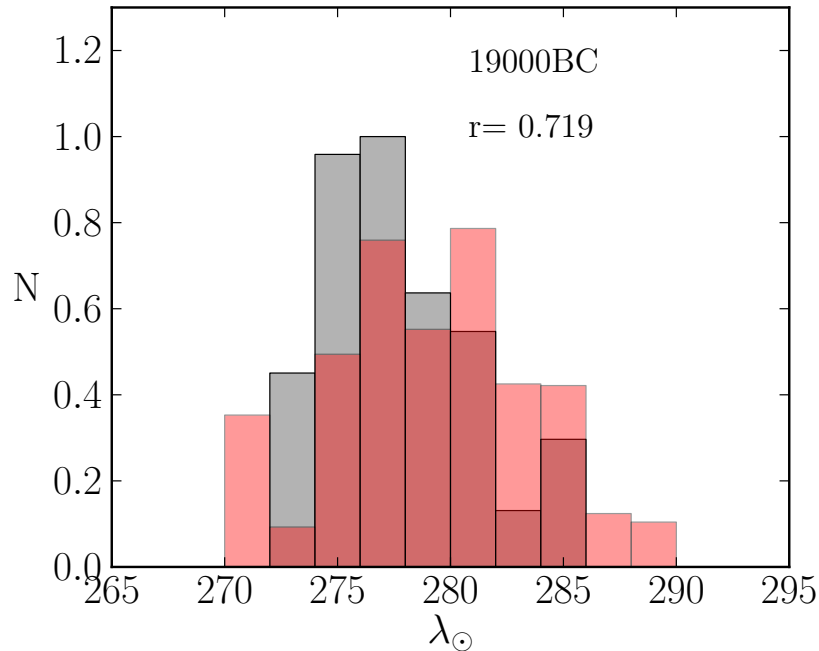
Figure 4.31: Simulated, weighted and normalized activity profile (red histogram) of filament 4, originating from 96P/Machholz with meteoroid ejection onset in 19000 BC. Superimposed are the observed normalized relative activity profiles by SAAMER (grey histogram). The quantity *r* denotes the sum of the residuals of the fit between the theoretical and SAAMER profile.

The best match between the theoretical and observed profiles is obtained assuming meteoroid ejection onset time circa 19000 BC. The fit is relatively good, though the simulations predict a slightly longer activity of $\Delta\lambda_\odot \approx 4$ days. Our modelling did not yield a clear peak, though an average maximum seems to be found near $\lambda_\odot \approx 277°$ or roughly 1 day later than the observed one. This small discrepancy may be due to uncertainties in our simulations or also may be indicate an older age. Generally, the orbital nodes regress with time for prograde orbits, so an older age may account for the difference in timing between the simulated and observed shower profile. However, the stream can not be younger than 20000 years, as meteoroids ejected prior to 19000 BC result in narrow profile and low activity, inconsistent with the observations (see Supplementary Material in Appendix A). Furthermore, as seen from Fig. 4.32, filament 4 seems to be mainly dominated by old ejecta. In fact, the bulk of the particles are released prior to 15000 BC, with only a small fraction of recent ejecta (2000 BC). Moreover, old particles released circa 13000 BC and 17000 BC, have been ejected from orbits of low perihelion distance, so these particles are weighted more, which results in a relatively wide profile.

The simulated radiant drift (Fig. 4.33) produced a good fit to the SAAMER observations. However, as with previous showers, we do not observe a strong mass segregation along the radiant, though it is evident that the showers is mostly dominated by old ejecta and large parti-
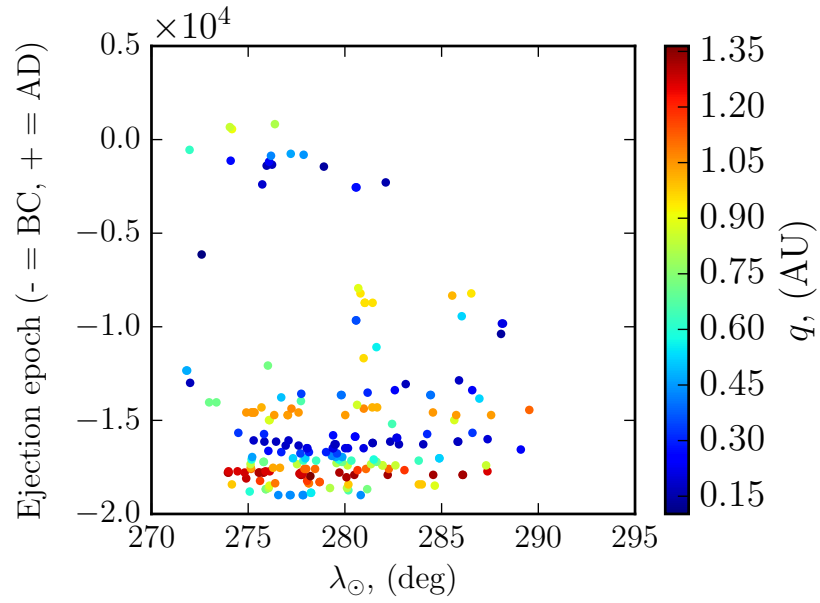
Figure 4.32: Solar longitude distribution of filament 4 as a function of meteoroid ejection epoch, from comet 96P/Machholz. Individual meteoroids are color coded in terms of their perihelion distance at time of ejection.
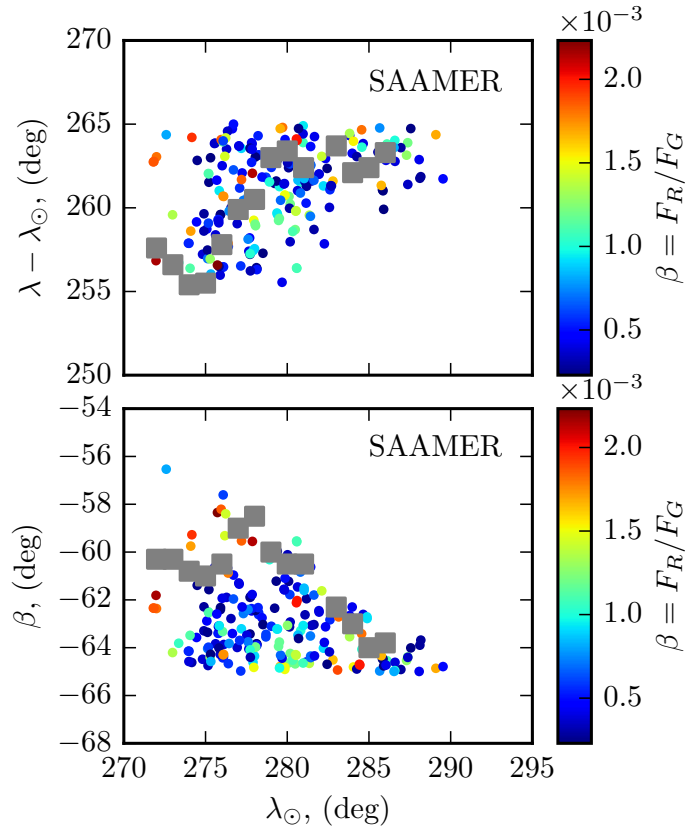
cles.

Figure 4.33: Simulated sun-centered radiant drift of KVE, with assumed meteoroid ejection onset in 19000 BC from comet 96P. The color coding is in terms of meteoroid size. Superimposed is the observed radiant drift by CMOR (grey squares).

Figure 4.34 shows the simulated distribution of the orbital elements of the KVE, assuming meteoroid ejection onset time circa 19000 BC. As with the previous showers, there is an obvious systematic shift in the predicted and measured geocentric speeds and thus the orbital semi-major axis and eccentricity, though the angular orbital elements produced a relatively good match. It is also noteworthy the systematic difference in the perihelion distance between the simulations and observations, a discrepancy also seen for the filament 3 (TCD) in Sec. 4.4.1 and whose nature is not clearly understood.
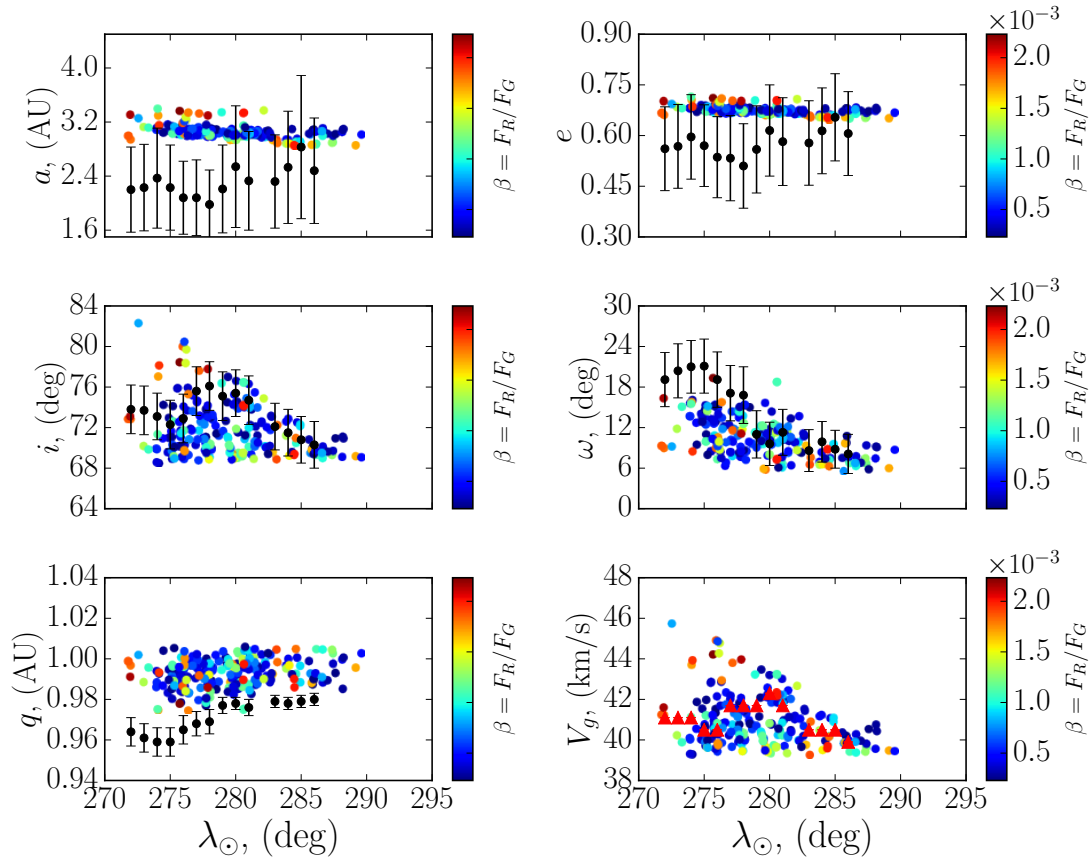
Figure 4.34: Simulated distribution of the orbital elements of the KVE (color dots) for assumed meteoroid ejection onset epoch in 19000 BC, from comet 96P. The color coding is in terms of meteoroids' β-parameter (or equivalent to meteoroid size). Superimposed are the observed distributions SAAMER (black circles).

4.4.2   The simulated meteor showers of parent candidate - P/1999 J6

In this section, we present our results of the meteoroid stream simulations, associated with the Marsden group of comets, assuming that P/1999 J6 can be taken as a representative parent body for the group as a whole. Following the scenario suggested by Sekanina and Chodas (2005), wherein a single large comet broke up between 100 AD and 950 AD, and formed the Marsden group of comets and the ARI, SDA, and NDA, we investigate the individual showers that comet P/1999 J6 may produce during its secular evolution. The resulting simulated showers are presented in Fig 4.35, where the individual showers are investigated below.

The Southern δ-Aquariids

Figure 4.36 shows the simulated activity profile of the SDAs, assuming a meteoroid ejection onset time circa 100 AD, from comet P/1999 J6. The predicted pre- peak portion of the profile
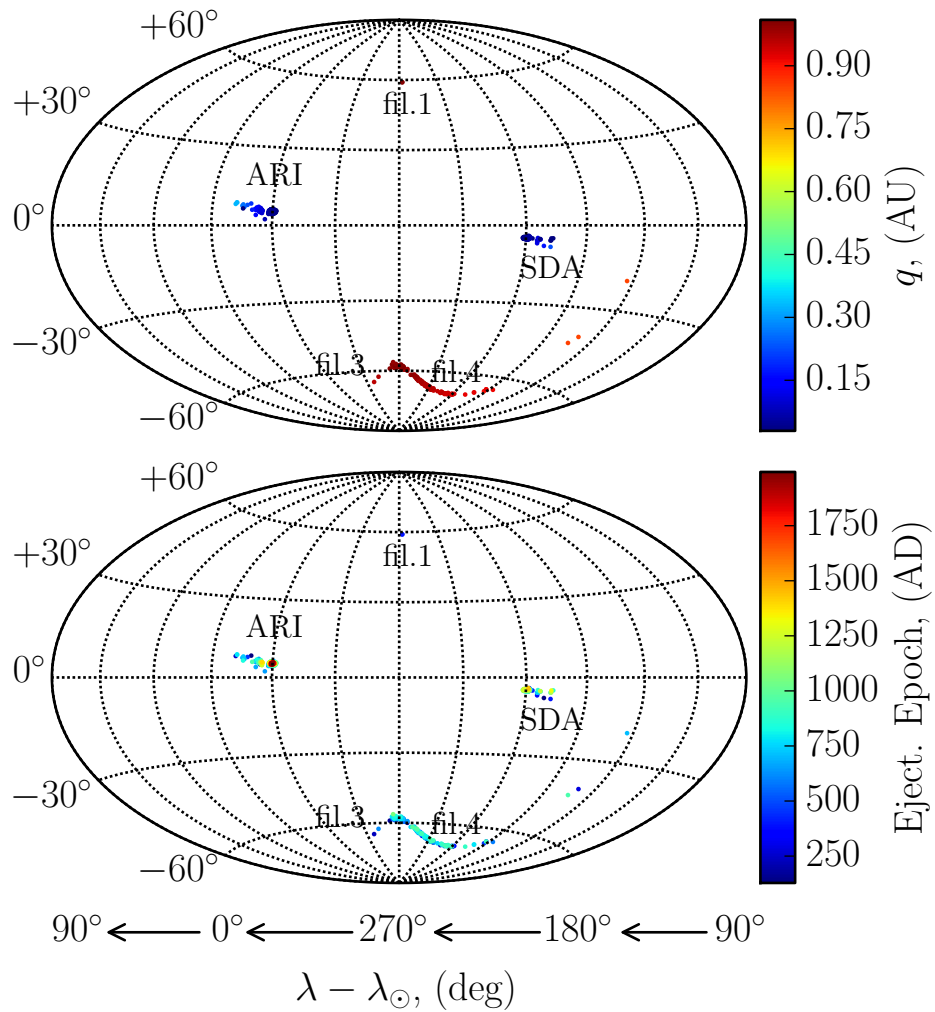
Figure 4.35: Resulting radiant distribution of meteoroids ejected from a single clone of comet P/1999 J6 with meteoroid ejection onset time 100 AD. The radiants in top panel are color coded in terms of meteoroids' present perihelion distance, and as a function of meteoroid ejection speed (lower panel).

and the timing of the peak activity ($\lambda_\odot = 123.5$) produced a good fit to the observations, though the overall width was too narrow compared to radar and visual observations. It is evident from Fig. 4.38 that mostly particles ejected between 700 AD and 1500 AD dominate the peak of the SDAs. However, if the contribution of 96P, assuming meteoroid ejection onset in 17000 BC, is added to the activity profile then the fit to the radar observation is significantly improved (see Fig. 4.37).
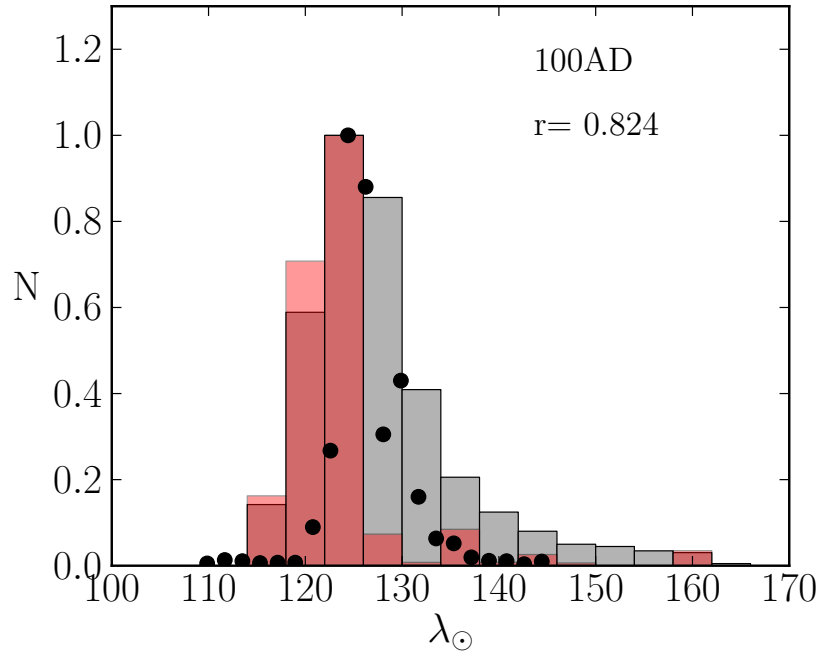

Figure 4.36: Simulated, weighted and normalized activity profile (red histogram) of the SDA, originating from comet P/1999 J6 with meteoroid ejection onset in 100 AD. Superimposed are the observed normalized relative activity profiles by CMOR (grey histogram) and IMO visual observations (black circles). The quantity r denotes the sum of the residuals of the fit between the theoretical and CMOR profile.

The simulated mean radiant location at $\lambda_\odot = 123.5°$ was $\lambda - \lambda_\odot = 209.2° \pm 0.4°$ and $b = -4.8° \pm 0.3°$. Although the simulated radiant was very narrow, overall it was systematically shifted by 3.5 degrees from the CMOR-derived mean radiant (see Tab. 4.1 in Sec. 4.2 for comparison). The simulated geocentric radiant drift of the SDA, originating from P/1999 J6 only, is presented in Fig. 4.39. The fit to the observations was good before $\lambda_\odot = 125°$, though beyond that point the simulated drift was higher than the measured one.

Figure 4.40 shows the simulated distribution of the orbital elements of the SDA originating from comet P/1999 J6, assuming meteoroid ejection onset time in 100 AD. As with previous showers, there was a systematic difference between the theoretical and the radar-derived geocentric speeds of the meteoroids, resulting in systematic discrepancy in the semi-major axis. More specifically, in the range $115° < \lambda_\odot < 125°$, where the best match between our simulated
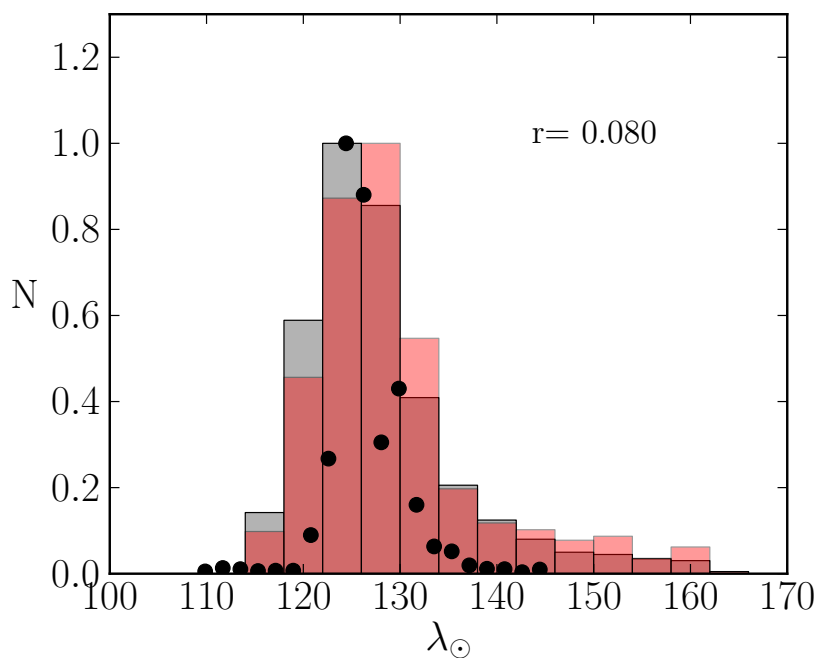
Figure 4.37: The combined simulated activity profile of the SDA (red histogram), assuming meteoroid contribution from both, 96P and P/1999 J6. The assumed meteoroid ejection onset of 96P/Machholz is 17000 BC, and meteoroid ejection onset of P/1999 J6 in 100 AD. The grey histogram corresponds to the observed activity profile by CMOR, while the circles are activity measured from visual observations of the IMO.
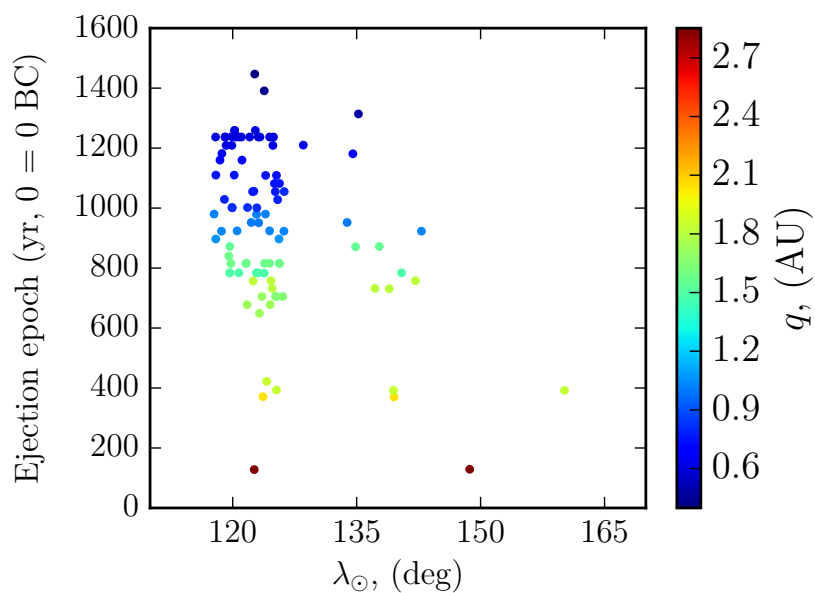

Figure 4.38: Solar longitude distribution of SDA as a function of meteoroid ejection epoch, from comet P/1999 J6. Individual meteoroids are color coded in terms of their perihelion distance at time of ejection.
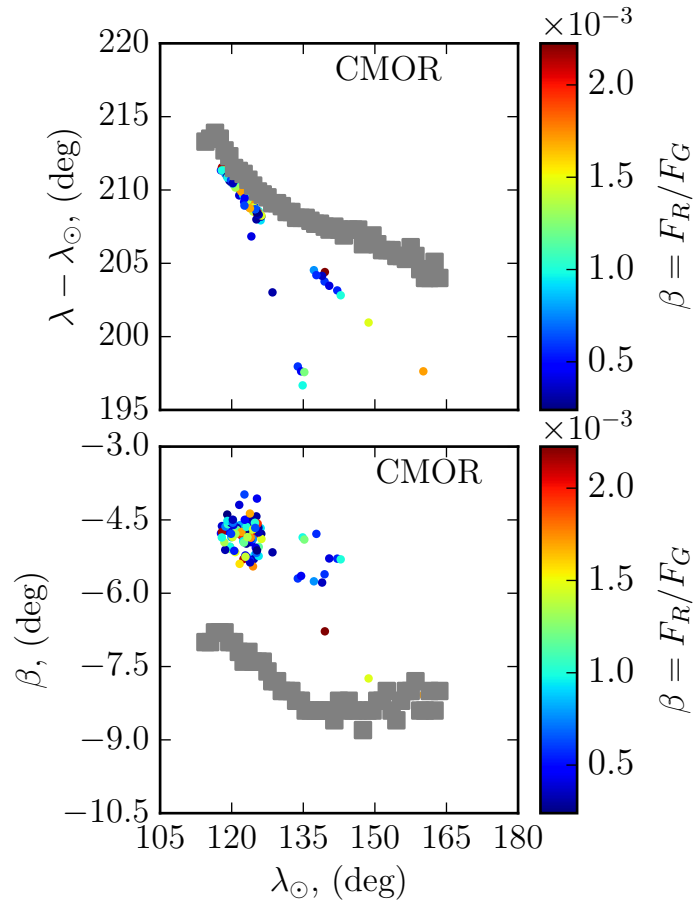
Figure 4.39: Simulated sun-centered radiant drift of SDA, with assumed meteoroid ejection onset in 100 AD from comet P/1999 J6. The color coding is in terms of meteoroid size. Superimposed is the observed radiant drift by CMOR (grey squares).

and the observed activity profile was observed, our predicted meteoroids' geocentric speeds were overestimated by $\Delta V_g \approx 1.5$ km/s compared to both CMOR and CAMS. However, the theoretical values of the meteoroids' semi-major axis were within the statistical uncertainty of the values measured by CAMS, though CMOR's values were underestimated by approximately 1 AU.
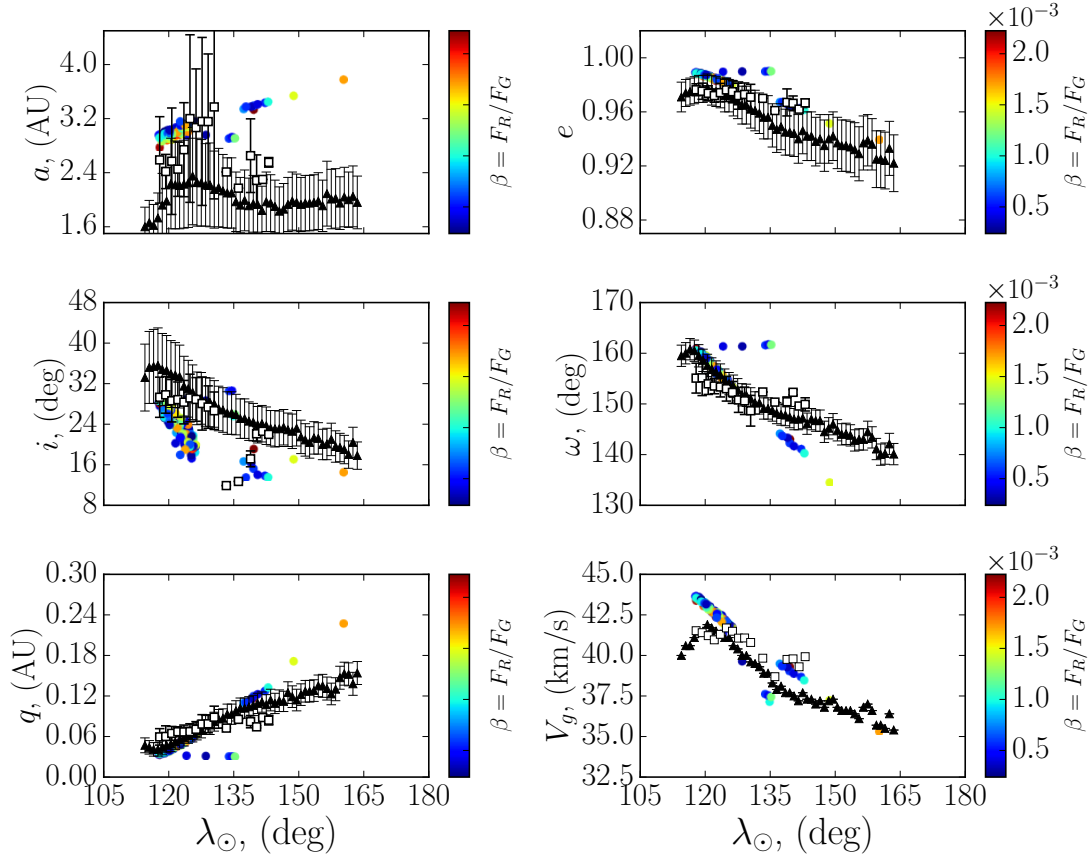

Figure 4.40: Simulated distribution of the orbital elements of the SDA (color dots) for assumed meteoroid ejection onset epoch in 100 AD from comet P/1999 J6. The color coding is in terms of meteoroids' β-parameter (or equivalent to meteoroid size). Superimposed are the observed distributions by CAMS (open squares) and CMOR (grey triangles).

Finally, considering the fit of our simulated activity profile to the observed one, the origin of the SDA as being solely due to ejections from P/1999 J6, between 100 AD and 950 AD, is not supported by our simulations. The resulting shower duration from P/1999 J6 is too short. Hence, we conclude the Marsden group of comets can not alone reproduce the observed profile features of the SDAs. The longer activity of the shower requires inclusion of older particles, consistent with much of the dust being related by 96P. In fact, the most plausible scenario according to our simulations, is that comet 96P was captured into a short period orbit circa 17000 BC, and suffered a major breakup in 100 AD, which resulted in the formation of the

Marsden group of comets. Comet 96P is the dominant parent of the SDAs, where the Marsden group of comets contribute mainly to the pre- peak portion of the stream.

Filament 1 and 3

According to our simulations, there is a minuscule contribution by P/1999 J6 to filament 1 and filament 3, in the northern and southern toroidal sources respectively. Using a 3D wavelet search, filament 1 seems to resemble the NID or DADs as described in Sec. 4.4.1. In contrast, the radiant location of filament 3 was in the proximity of the TCD (see Sec. 4.4.1). We omit the visual representation of these filaments here due to their low number of particles, in each of these radiants. The radiant of filament 1 consists of 2 particles, whereas 5 meteoroids contributed to filament 3. Perhaps, if our initial meteoroid ejection was earlier than 100 AD, the abundance of the particles in those filaments would be higher.

Filament 4

Our numerical simulations indicate that comet P/1999 J6 contributes to the KVE (filament 4 from Sec .4.4.1). The simulated activity profile is presented in Fig. 4.41. Similar to the SDA, the timing of the shower is reproduced well, while the overall width of the profile is not. The resulting FWHM of the profile corresponds to approximately 2 days, whereas SAAMER measures FWHM$\approx 10°$. The bulk of the meteoroids are old, in the sense they have been ejected between 100 AD and 1000 AD, but they did not have enough time to spread across the width of the stream (see Fig. 4.43). It is also evident that meteoroids released after 1000 AD do not presently reach the Earth.

Clearly, there is a need for older meteoroid supply or for an additional parent. In Sec. 4.4.1 we showed that the most of the observed characteristics of the KVE can be explained by meteoroid ejection onset time, from 96P after 19000 BC. Indeed, if the latter contribution is added, the overall simulated activity profile produces a better fit to the observations (see Fig. 4.42). Thus, the observed activity profile is consistent with a capture of 96P into a short period orbit around 19000 BC, followed by a major fragmentation of the comet near 100 AD, resulting in the formation of the Marsden group of comets. The subsequent independent evolution of the Marsden group of comets have supplied meteoroids mainly to the core of the KVE. We recall that, that a similar scenario was proposed by Sekanina and Chodas (2005), except that observed features of the activity profile of the KVE can not be explained by a cometary activity of the Marsden group of comets alone over only 2000 years.
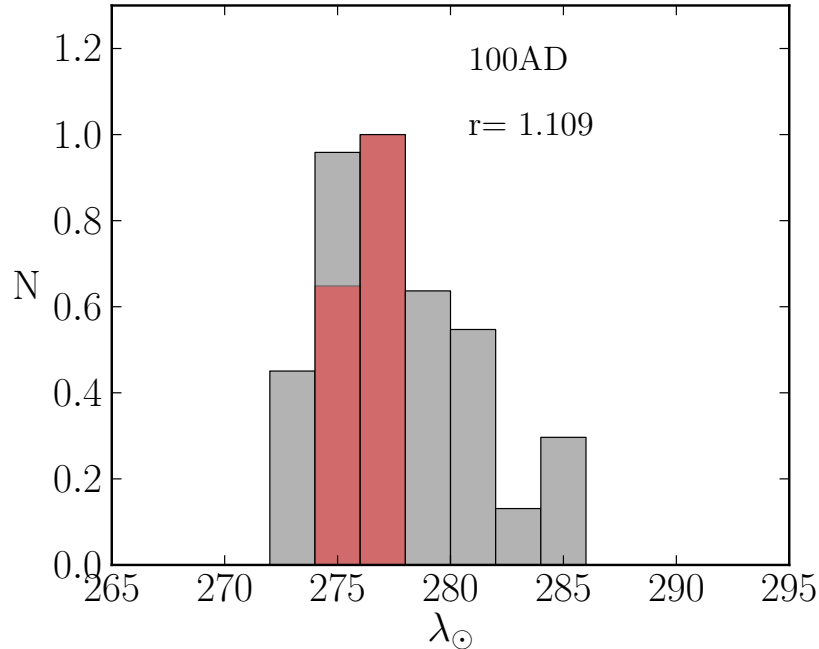
Figure 4.41: Simulated, weighted and normalized activity profile (red histogram) of filament 4, originating from comet P/1999 J6 with meteoroid ejection onset in 100 AD. Superimposed is the observed normalized relative activity profiles by SAAMER (grey histogram). The quantity *r* denotes the sum of the residuals of the fit between the theoretical and SAAMER profile.

The simulated sun-centered radiant (Fig. 4.44) drift yields a poor match to the SAAMER observations. The latter measures only a moderate drift, while the simulations predict a large motion in each dimension, $(\lambda - \lambda_\odot)$ and b, in the range of the simulated activity. Since, both the predicted and measured drifts intersect, they are only consistent over a short time, corresponding to the narrow peak of the activity profile. That clearly indicates that the Marsden group of comets are not the sole parent of the shower, where our simulations show that the dominant contributor to the shower is comet 96P (see Sec. 4.4.1).

Figure 4.45 shows the predicted distribution of the orbital elements of the KVE across the simulated activity period. Apart from the poor fit to the measured semi-major axis and eccentricity, the simulated angular orbital elements seem to be consistent with observations within a narrow time interval, corresponding to the predicted activity period of the shower, resulting from P/1999 J6. An interesting feature is that the simulated orbital elements split into two groups, a difference that is most noticeable in the $(i, \lambda_\odot)$, $(\omega, \lambda_\odot)$, $(q, \lambda_\odot)$ and $(V_g, \lambda_\odot)$ space. The simulations predict meteoroid with orbits that span a wide range of orbital elements values within a few days, a feature not supported by the SAAMER observations. The measured orbital elements by SAAMER do predict a drift as a function of the solar longitude, though moderate and more gradual. Due to the poor match of the simulations to the observed shower characteristics of the KVE, the Marsden group of sunskirters do not seem to be the dominant
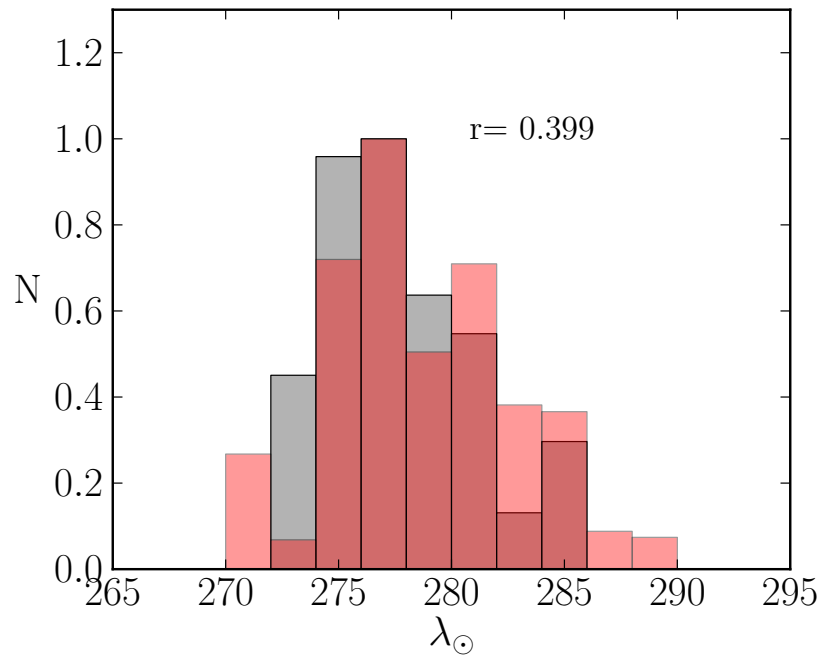
Figure 4.42: The combined simulated activity profile of the filament 4 (red histogram). The assumed meteoroid ejection onset of 96P/Machholz is 17000 BC, and meteoroid ejection onset of P/1999 J6 in 100 AD. The grey histogram corresponds to the activity profile as measured by SAAMER. The number "r" is sum of the residuals from the fit.
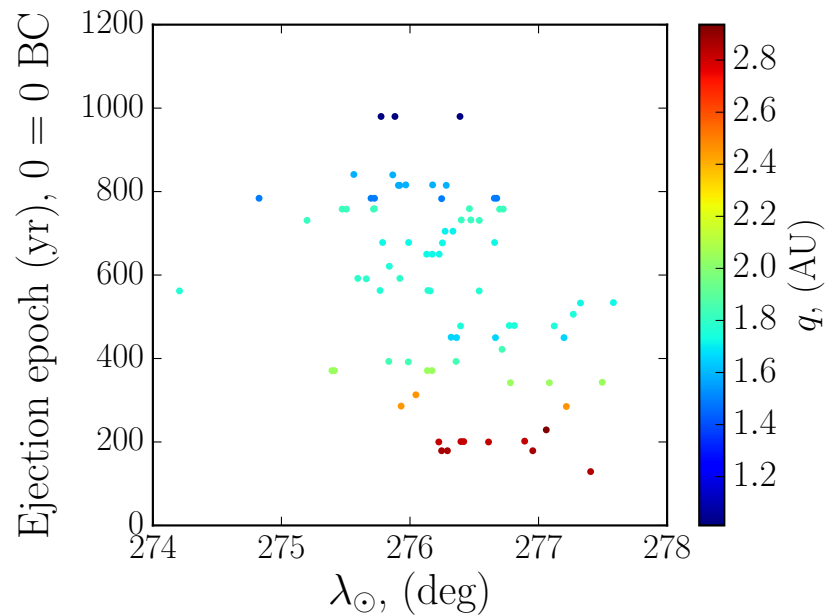
Figure 4.43: Solar longitude distribution of filament 4 as a function of meteoroid ejection epoch, from comet P/1999 J6. Individual meteoroids are color coded in terms of their perihelion distance at time of ejection.
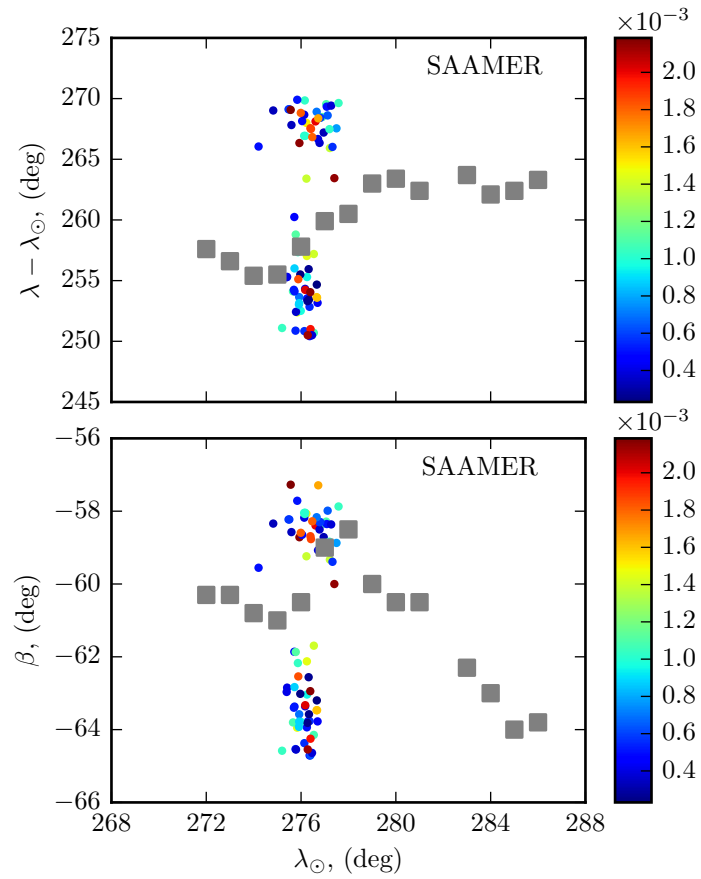
Figure 4.44: Simulated sun-centered radiant drift of KVE, with assumed meteoroid ejection onset in 100 AD from comet P/1999 J6. The color coding is in terms of meteoroid size. Superimposed is the observed radiant drift by CMOR (grey squares).

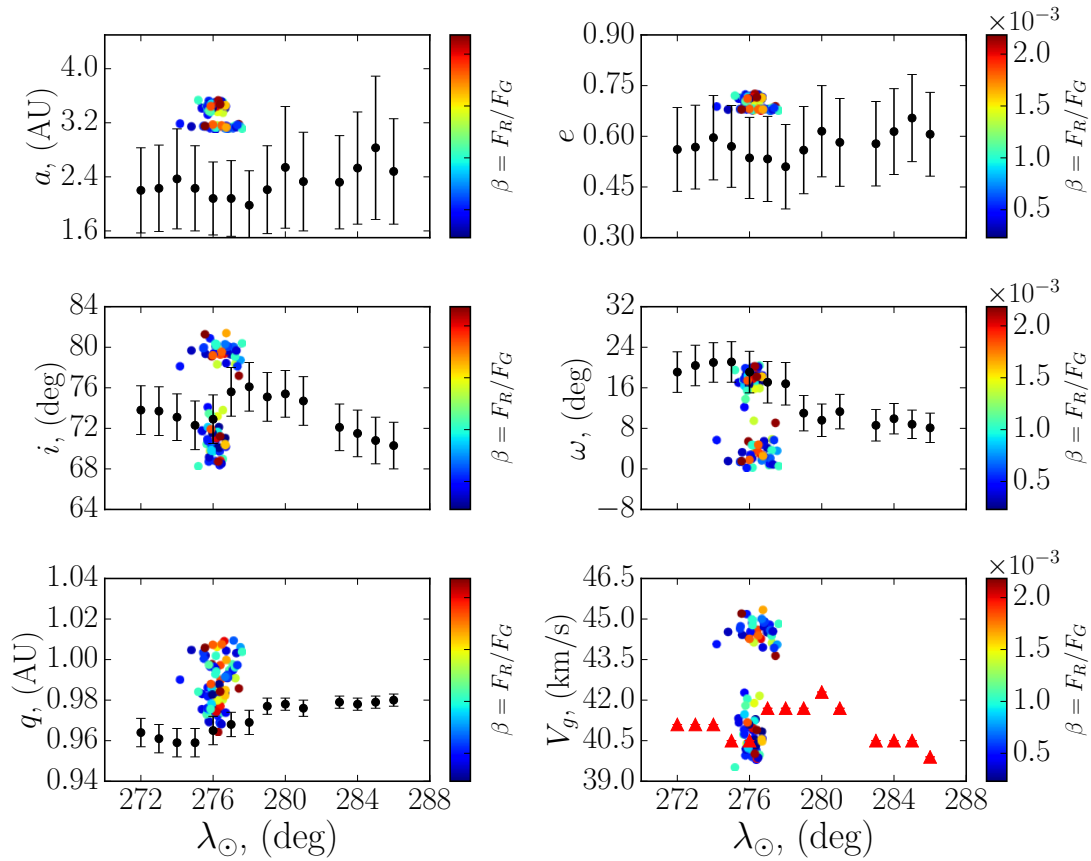parent of the shower, but may contribute to the core of stream.

Figure 4.45: Simulated distribution of the orbital elements of the KVE (color dots) for assumed meteoroid ejection onset epoch in 100 AD from comet P/1999 J6. The color coding is in terms of meteoroids' β-parameter (or equivalent to meteoroid size). Superimposed is the observed distributions by SAAMER (black circles).

4.5   Discussion and Conclusions

We performed numerical simulations to investigate the individual meteoroid streams of comets 96P/Machholz and the most prominent member of the Marsden group of comets, P/1999 J6. Our goal was to obtain a self-consistent scenario of the past dynamical evolution of the interplanetary bodies associated with comet 96P, and to determine the dominant parent of the complex. As a product of this study, we also aimed to establish a possible past fragmentation chronology of a single large first precursor, presumably giving rise to the Marsden group of sunskirting comets (Sekanina and Chodas, 2005). The relative contribution of each parent to the complex is determined, by simultaneous matching and investigation of the observed characteristics of their resulting showers. As observational shower constraints we used data from meteor surveillance by CMOR, SAAMER, CAMS and IMO.

Our simulations confirm the results of Babadzhanov and Obrubov (1992) and Neslušan et al. (2013b) that within one full Kozai circulation cycle, the ascending and descending nodes of comet 96P intersect the Earth's orbit in eight different locations, and thus result in eight different meteor showers. Four of these showers are in the ecliptic meteoroid source and four belong to the Northern and Southern toroidal sources, respectively. Furthermore, four of these showers are well known, the Quadrantids (QUA), the daytime Arietids (ARI), the Southern and Northern δ-Aquariids (SDA and NDA), whereas the remainder four showers are weak and less well constrained. We call these weak showers "filaments":

Filament 1 is found in the north toroidal source and is possibly associated with the "November ι-Draconids (NID)" or with the "December α-Draconids (DAD)". The two showers peak at the same time and have radiants partially overlapping, so their separation as individual showers was not possible in this work, a similar result initially suggested by Neslušan et al. (2013b). Filament 2 resembles the "daytime λ-Taurids (DLT)" that appears to be consistent with the long-sought southern branch of the daytime Arietids. Filament 3 and 4 likely corresponds to the θ-Carinids (TCD) and κ-Velids respectively, showers are found in the southern toroidal source. Similar to filament 1, the TCD and KVE appear to peak at the same time, though their radiant locations are separated by 20 degrees. However, the separation of filaments 3 and 4 is more obvious and and they appear to be two distinct showers. We note that the DLT, TCD and the DAD (or NID) were identified by Babadzhanov and Obrubov (1992) as the α-Cetids, Carinids and Ursids, respectively. Among these showers, the most active are the QUA, followed by the ARI, SDA, NDA, DLT, KVE, NID or DAD and the TCD.

We use the width of the wings and shape of the observed activity profile as a strong proxy as to the age of individual showers to fit to our simulated meteoroid streams. We find that ages of the eight showers, originating from 96P, range between 10000 BC and 20000 BC.

The best match between the duration of the simulated and observed activity profiles for the QUA is obtained assuming initial meteoroid ejection onset from 96P in 10000 BC. We did not attempt to match the narrow portion of the shower, which we showed in a previous work that it is associated with asteroid 2003 EH$_1$.

The simulated width of the ARI requires a meteoroid ejection onset time at least 12000 years ago (Abedin et al., 2016), whereas the bulk of the activity profile of the SDA is reproduced, assuming that 96P has been captured in a short period orbit circa 17000 BC. A similar result is obtained for the NDA, with a best fit between the simulated and observed duration of the shower for meteoroid ejection onset time in 17000 BC. The observed widths of the profiles of filament 1, 2, 3 and 4 can only be explained if the comet became active circa 19000 BC.

Assuming the scenario proposed by Sekanina and Chodas (2005) of formation of the Marsden group of comets, the ARI, SDA and NDA, in a major comet break-up event, between

100 AD and 950 AD, we simulated the possible showers associated with comet P/1999 J6, with the latter being a substitute of the Marsden group of comets as a whole. Our simulations confirm that the Marsden group of comets contribute to the ARI, SDA and three weak filaments (filament 1, 3 and 4 associated with 96P), though we find that P/1999 J6 is not the parent of the NDA, as opposed to previous suggestions (Ohtsuka et al., 2003; Sekanina and Chodas, 2005; Jenniskens, 2006). Furthermore, using a 3D wavelet search in the CMOR and SAAMER database, the three weak filaments are identified as part of the NID or DAD, the TCD and KVE, respectively. However, the contribution of the comet to filaments 1 and 3 is extremely low, with only a few particles approaching the Earth. Finally, assuming even the earliest fragmentation epoch, 100 AD, as suggested by Sekanina and Chodas (2005), our simulations indicate the Marsden group of comets can not alone explain the observed activity profile of the showers associated with it (ARI, SDA, NDA, KVE, TCD and NID or DAD). There is a need for meteoroids ejection of at least a few tens of millenia, in order for the observed width of the activity profiles to be explained.

In summary, the bulk of the observed characteristics of the meteor showers, associated with comet 96P, can be explained if the comet has been captured into a short period orbit circa 20000 BC and has been active until the present. Then there is a sufficient time for it to produce most of the features the QUA, ARI, SDA, NDA, DLT, KVE, TCD and the NID or DAD. However, a better match to the activity profiles is produced if we also add the scenario by Sekanina and Chodas (2005), namely brake up of 96P after 100 AD which has formed the Marsden group of comets, and perhaps other sungrazing comets. The meteoroid supply from the Marsden group of comets complement the observed features of these showers, though mainly contribute to their peak activity.

Bibliography

Abedin, A., Spurný, P., Wiegert, P., Pokorný, P., Borovička, J., Brown, P., 2015. On the age and formation mechanism of the core of the Quadrantid meteoroid stream. Icarus 261, 100–117. `1508.02418`.

Abedin, A., Wiegert, P., Pokorný, P., Brown, P., 2016. On the age and formation mechanism of the daytime Arietids meteoroid stream. Icarus .

A'Hearn, M.F., Millis, R.C., Schleicher, D.O., Osip, D.J., Birch, P.V., 1995. The ensemble properties of comets: Results from narrowband photometry of 85 comets, 1976-1992. Icarus 118, 223–270.

Babadzhanov, P.B., Obrubov, Y.V., 1992. P/Machholz 1986 8 and quadrantid meteoroid stream. Orbital evolution and relationship, in: Harris, A.W., Bowell, E. (Eds.), Asteroids, Comets, Meteors 1991, pp. 27–32.

Bailey, M.E., Chambers, J.E., Hahn, G., 1992. Origin of sungrazers - A frequent cometary end-state. A&A 257, 315–322.

Brown, P., Jones, J., 1998. Simulation of the Formation and Evolution of the Perseid Meteoroid Stream. Icarus 133, 36–68.

Brown, P., Weryk, R.J., Wong, D.K., Jones, J., 2008. A meteoroid stream survey using the Canadian Meteor Orbit Radar. I. Methodology and radiant catalogue. Icarus 195, 317–339.

Brown, P., Wong, D.K., Weryk, R.J., Wiegert, P., 2010. A meteoroid stream survey using the Canadian Meteor Orbit Radar. II: Identification of minor showers using a 3D wavelet transform. Icarus 207, 66–81.

Bruzzone, J.S., Brown, P., Weryk, R.J., Campbell-Brown, M.D., 2015. A decadal survey of the Daytime Arietid meteor shower using the Canadian Meteor Orbit Radar. MNRAS 446, 1625–1640.

Burns, J.A., Lamy, P.L., Soter, S., 1979. Radiation forces on small particles in the solar system. Icarus 40, 1–48.

Campbell-Brown, M., Brown, P.G., 2015. A 13-year radar study of the η-Aquariid meteor shower. MNRAS 446, 3669–3675.

Chambers, J.E., 1999. A hybrid symplectic integrator that permits close encounters between massive bodies. MNRAS 304, 793–799.

Delsemme, A.H., 1982. Chemical composition of cometary nuclei, in: Wilkening, L.L. (Ed.), IAU Colloq. 61: Comet Discoveries, Statistics, and Observational Selection, pp. 85–130.

Froeschle, C., Scholl, H., 1986. Gravitational splitting of Quadrantid-like meteor streams in resonance with Jupiter. A&A 158, 259–265.

Gonczi, R., Rickman, H., Froeschle, C., 1992. The connection between Comet P/Machholz and the Quadrantid meteor. MNRAS 254, 627–634.

Green, D.W.E., Rickman, H., Porter, A.C., Meech, K.J., 1990. The strange periodic comet Machholz. Science 247, 1063–1067.

Grun, E., Zook, H.A., Fechtig, H., Giese, R.H., 1985. Collisional balance of the meteoritic complex. Icarus 62, 244–272.

Janches, D., Close, S., Hormaechea, J.L., Swarnalingam, N., Murphy, A., O'Connor, D., Vandepeer, B., Fuller, B., Fritts, D.C., Brunini, C., 2015. The Southern Argentina Agile MEteor Radar Orbital System (SAAMER-OS): An Initial Sporadic Meteoroid Orbital Survey in the Southern Sky. ApJ 809, 36.

Janches, D., Hormaechea, J.L., Brunini, C., Hocking, W., Fritts, D.C., 2013. An initial meteoroid stream survey in the southern hemisphere using the Southern Argentina Agile Meteor Radar (SAAMER). Icarus 223, 677–683.

Jenniskens, P., 2004. 2003 EH$_1$ Is the Quadrantid Shower Parent Comet. Astron. Journ. 127, 3018–3022.

Jenniskens, P., 2006. Meteor Showers and their Parent Comets.

Jenniskens, P., Betlem, H., de Lignie, M., Langbroek, M., van Vliet, M., 1997. Meteor stream activity. V. The Quadrantids, a very young stream. A&A 327, 1242–1252.

Jenniskens, P., Duckworth, H., Grigsby, B., 2012. Daytime Arietids and Marsden Sunskirters (ARI, IAU #171). WGN, Journal of the International Meteor Organization 40, 98–100.

Jenniskens, P., Lyytinen, E., de Lignie, M.C., Johannink, C., Jobse, K., Schievink, R., Lang-broek, M., Koop, M., Gural, P., Wilson, M.A., Yrjölä, I., Suzuki, K., Ogawa, H., de Groote, P., 2002. Dust Trails of 8P/Tuttle and the Unusual Outbursts of the Ursid Shower. Icarus 159, 197–209.

Jenniskens, P., Nénon, Q., Albers, J., Gural, P., Haberman, B., Holman, D., Morales, R., Grigsby, B.J., Samuels, D., C., J., 2015 In Press. The established showers as observed by CAMS. Icarus .

Jenniskens, P., Nénon, Q., Albers, J., Gural, P.S., Haberman, B., Holman, D., Morales, R., Grigsby, B.J., Samuels, D., Johannink, C., 2016. The established meteor showers as observed by CAMS. Icarus 266, 331–354.

Jones, J., 2002. A Model of the Sporadic Meteoroid Complex. Technical report. The University of Western Ontario and NASA (MSFC) .

Jones, J., Jones, W., 1993. Comet Machholz and the Quadrantid meteor stream. MNRAS 261, 605–611.

Kinoshita, H., Nakai, H., 1999. Analytical Solution of the Kozai Resonance and its Application. Celestial Mechanics and Dynamical Astronomy 75, 125–147.

Klačka, J., 2004. Electromagnetic Radiation and Motion of a Particle. Celestial Mechanics and Dynamical Astronomy 89, 1–61. `astro-ph/0301138`.

Klačka, J., Kocifaj, M., 2008. Times of inspiralling for interplanetary dust grains. MNRAS 390, 1491–1495.

Kozai, Y., 1962. Secular perturbations of asteroids with high inclination and eccentricity. Astron. Journ. 67, 591.

Lamy, P.L., Toth, I., Fernandez, Y.R., Weaver, H.A., 2004. The sizes, shapes, albedos, and colors of cometary nuclei. pp. 223–264.

Leinert, C., Grun, E., 1990. Interplanetary Dust. p. 207.

Levison, H.F., Duncan, M.J., 1994. The long-term dynamical behavior of short-period comets. Icarus 108, 18–36.

Levison, H.F., Duncan, M.J., 1997. From the Kuiper Belt to Jupiter-Family Comets: The Spatial Distribution of Ecliptic Comets. Icarus 127, 13–32.

Licandro, J., Tancredi, G., Lindgren, M., Rickman, H., Hutton, R.G., 2000. CCD Photometry of Cometary Nuclei, I: Observations from 1990-1995. Icarus 147, 161–179.

McIntosh, B.A., 1990. Comet P/Machholtz and the Quadrantid meteor stream. Icarus 86, 299–304.

Neslušan, L., Hajduková, M., Jakubík, M., 2013a. Meteor-shower complex of asteroid 2003 EH1 compared with that of comet 96P/Machholz. A&A 560, A47.

Neslušan, L., Kaňuchová, Z., Tomko, D., 2013b. The meteor-shower complex of 96P/Machholz revisited. A&A 551, A87.

Ohtsuka, K., Nakano, S., Yoshikawa, M., 2003. On the Association among Periodic Comet 96P/Machholz, Arietids, the Marsden Comet Group, and the Kracht Comet Group. Publ. Astr. Soc. Japan 55, 321–324.

Schleicher, D.G., 2008. The Extremely Anomalous Molecular Abundances of Comet 96p/Machholz 1 from Narrowband Photometry. Astron. Journ. 136, 2204–2213.

Schulz, R., 2006. Compositional coma investigations: Gas and dust production rates in comets, in: Daniela, L., Sylvio Ferraz, M., Angel, F.J. (Eds.), Asteroids, Comets, Meteors, pp. 413–423.

Sekanina, Z., 1988. Outgassing asymmetry of periodic comet Encke. I - Apparitions 1924-1984. Astron. Journ. 95, 911–924.

Sekanina, Z., 1990. Periodic Comet Machholz and its idiosyncrasies. Astron. Journ. 99, 1268–1277.

Sekanina, Z., 1992. Sublimation rates of carbon monoxide and carbon dioxide from comets at large heliocentric distances, in: Harris, A.W., Bowell, E. (Eds.), Asteroids, Comets, Meteors 1991.

Sekanina, Z., 2002. Statistical Investigation and Modeling of Sungrazing Comets Discovered with the Solar and Heliospheric Observatory. ApJ 566, 577–598.

Sekanina, Z., Chodas, P.W., 2005. Origin of the Marsden and Kracht Groups of Sunskirting Comets. I. Association with Comet 96P/Machholz and Its Interplanetary Complex. ApJS 161, 551–586.

SonotaCo, 2009. A meteor shower catalog based on video observations in 2007-2008. WGN, Journal of the International Meteor Organization 37, 55–62.

Weryk, R.J., Brown, P.G., 2013. Simultaneous radar and video meteors-II: Photometry and ionisation. Planet. and Space Sci. 81, 32–47.

Whipple, F.L., 1950. A comet model. I. The acceleration of Comet Encke. ApJ 111, 375–394.

Whipple, F.L., 1951. A Comet Model. II. Physical Relations for Comets and Meteors. ApJ 113, 464.

Whipple, F.L., 1967. On Maintaining the Meteoritic Complex. NASA Special Publication 150, 409.

Wiegert, P., Brown, P., 2005. The Quadrantid meteoroid complex. Icarus 179, 139–157.

Wiegert, P., Vaubaillon, J., Campbell-Brown, M., 2009. A dynamical model of the sporadic meteoroid complex. Icarus 201, 295–310.

Williams, I.P., Wu, Z.D., 1993. The Quadrantid Meteoroid Stream and Comet 1491I. MNRAS 264, 659.

Chapter 5

Concluding remarks

The past evolution of the meteoroid streams associated with comet 96P/Machholz and the Marsden group of comets, was investigated. By simultaneous fitting large scale numerical simulations to the observed characteristics of these showers, a self-consistent scenario of a past capture of a large comet and its subsequent break-up history was obtained.

In the first part of this work, the age of the core of the Quadrantids and its association with asteroid 2003 EH_1 is investigated. The simulated shower characteristics reproduce the observations quite well, where age of the core of Quadrantids is consistent with being 200 years old. Furthermore, the derived age of the core is compatible with the meteoroids being released from 2003 EH_1 circa 1800 AD, as a result of normal cometary sublimation. That renders the nature of 2003 EH_1 enigmatic e.g., a recently dormant or extinct comet. Further observations of 2003 EH_1 are highly encouraged and are crucial for establishing the true nature of the asteroid.

The second part of this work is dedicated to the formation mechanism and age of the second strongest shower among the 96P complex - the daytime Arietids. The goal is to test which is the dominant parent of the shower, comet 96P or the recently proposed Marsden group of comets. The results revealed that the Marsden group of comets can not alone reproduce the oberved characteristics of the Arietids and hence can not be considered the immediate parent of the shower. Instead, the simulations suggested that the dominant parent of the shower is comet 96P, though the Marsden group of comets contribute mainly to the peak of the shower. Lastly, the observed characteristics of the shower were consistent with a possible capture of comet 96P into a short period orbit prior to 10000 BC and a subsequent fragmentation near 100 AD.

In the last part of this work, the origin of the Southern and Northern δ-Aquariids, κ-Velids, the θ-Carinids is investigated. In particular, the most likely age of individual showers is explored with an emphasis on establishing their dominant parents - comet 96P or the Marsden group of comets. The results of the work suggest that the Marsden group of comets are

not the immediate parent of the daytime Arietids and the Southern and Northern δ-Aquariids, as previously thought. Rather, the dominant parent of all eight showers seems to be comet 96P/Machholz. The the age of individual showers, associated with 96P, range between 12000-20000 years, which is much older than previous estimates. The Marsden group of comets do contribute, mainly to peak activity of the daytime Arietids and the Southern δ-Aquariids. Moreover, previous hypothesis that the Northern δ-Aquariids are linked to the Marsden group of comets was not supported by this work, though these sunskirting comets weakly contribute to the the northern and southern toroidal sources as well. Finally, two meteor showers were identified in the CMOR database, as potential candidates of the showers named by **?** as the α-Cetids and the Ursids. These showers are the daytime λ-Taurids (the counterpart of the Cetids) and the December α-Draconids misidentified as the Ursids.

In summary, this work suggests that most of the observed characteristics of the 96P complex showers can be explained if a large comet was first captured into a short period orbit circa 20000 BC. This comet continuously supplied meteoroids to the inner Solar system until it broke apart between 100 AD and 950 AD, which resulted in the formation of the Marsden and Kracht group of comets. Lastly, comet 96P/Machholz seems to be the largest surviving fragment of that past catastrophic disruption and is the dominant parent of the complex which includes dozens of smaller fragments, and which through thousands of years of dynamical evolution has produced at least eight meteor showers at the Earth.

Appendix A

Supplementary material to Chapter 4.

A.1 Meteor showers of comet 96P
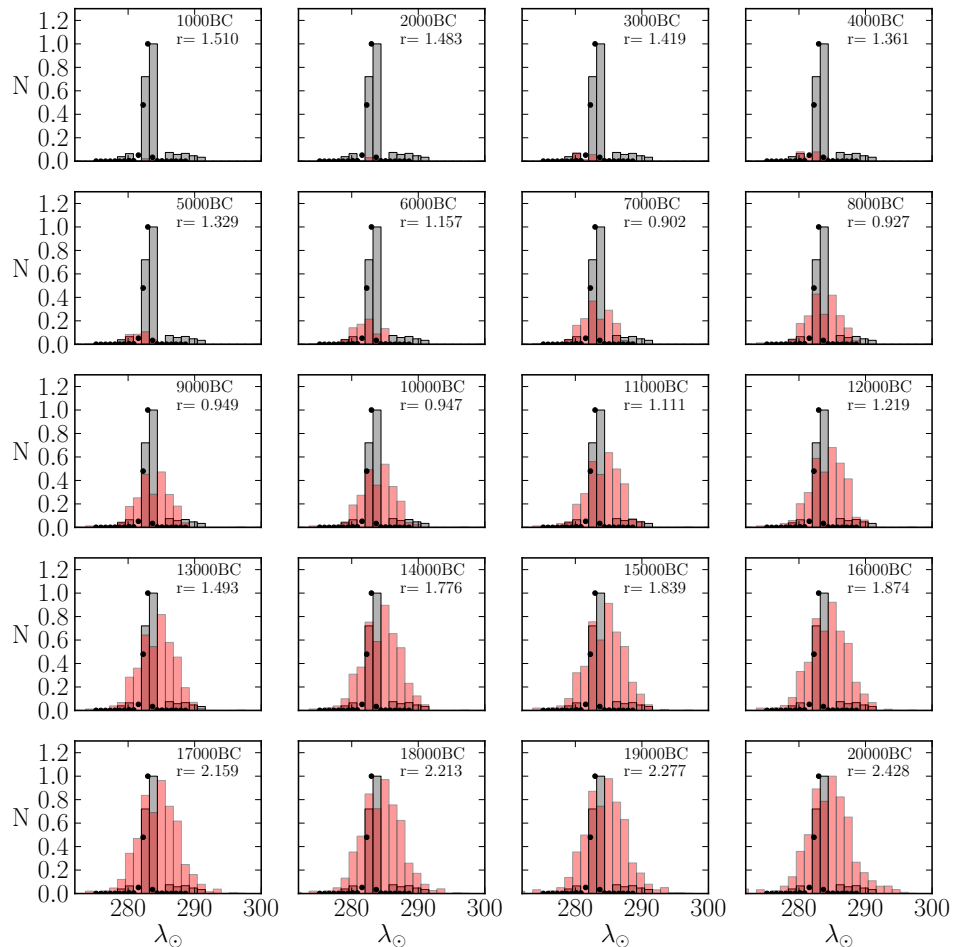
A.1.1 The Quadrantids (QUA)

Figure A.1: Simulated, weighted and normalized activity profile (red histogram) of QUA, originating from 96P/Machholz, for different initial meteoroid ejection onset times. Superimposed is the observed normalized relative activity profiles by CMOR (grey histogram).

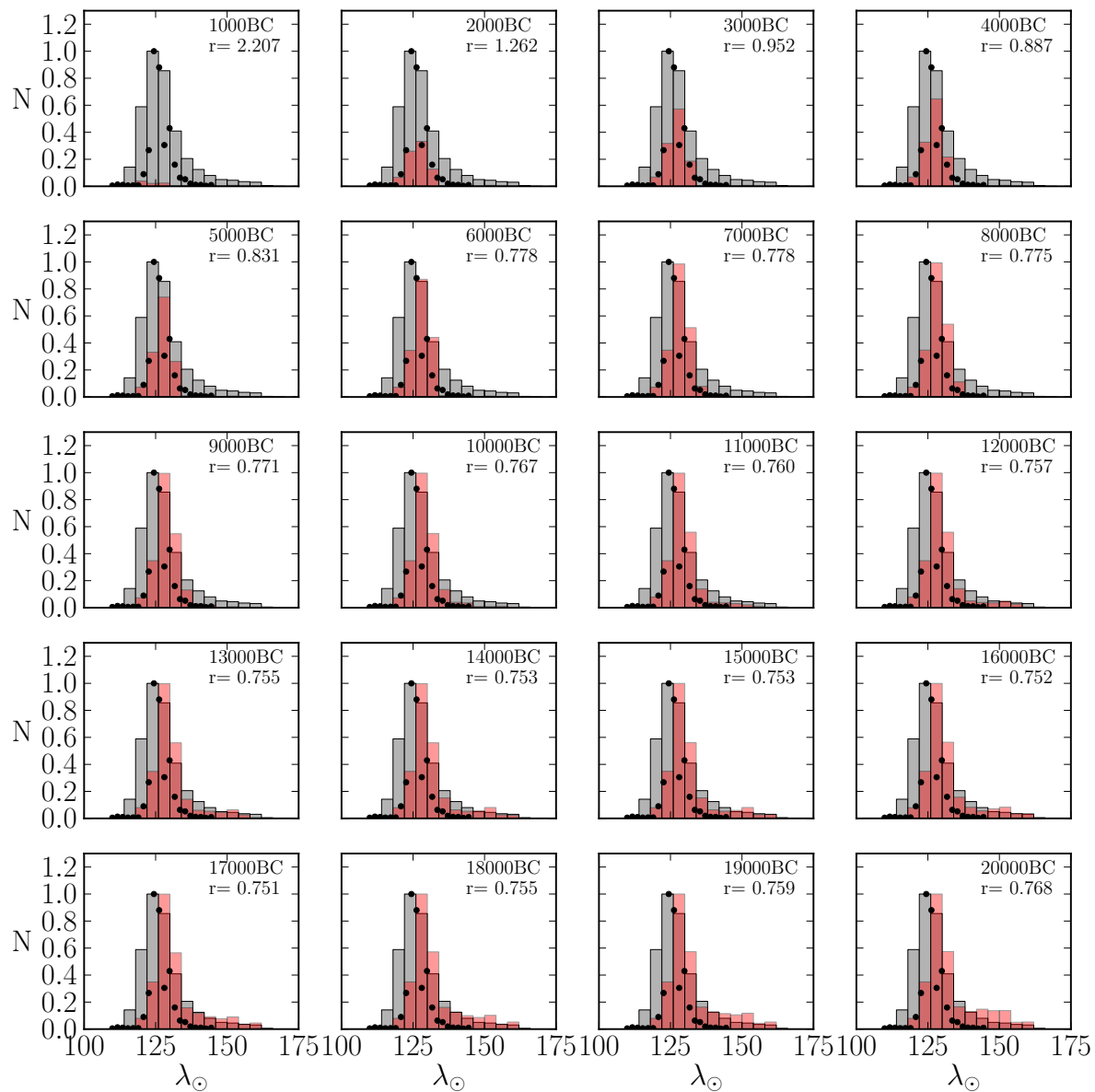## A.1.2   The Southern δ-Aquariids (SDA)

Figure A.2: Simulated, weighted and normalized activity profile (red histogram) of SDA, originating from 96P/Machholz, for different initial meteoroid ejection onset times. Superimposed is the observed normalized relative activity profiles by CMOR (grey histogram).
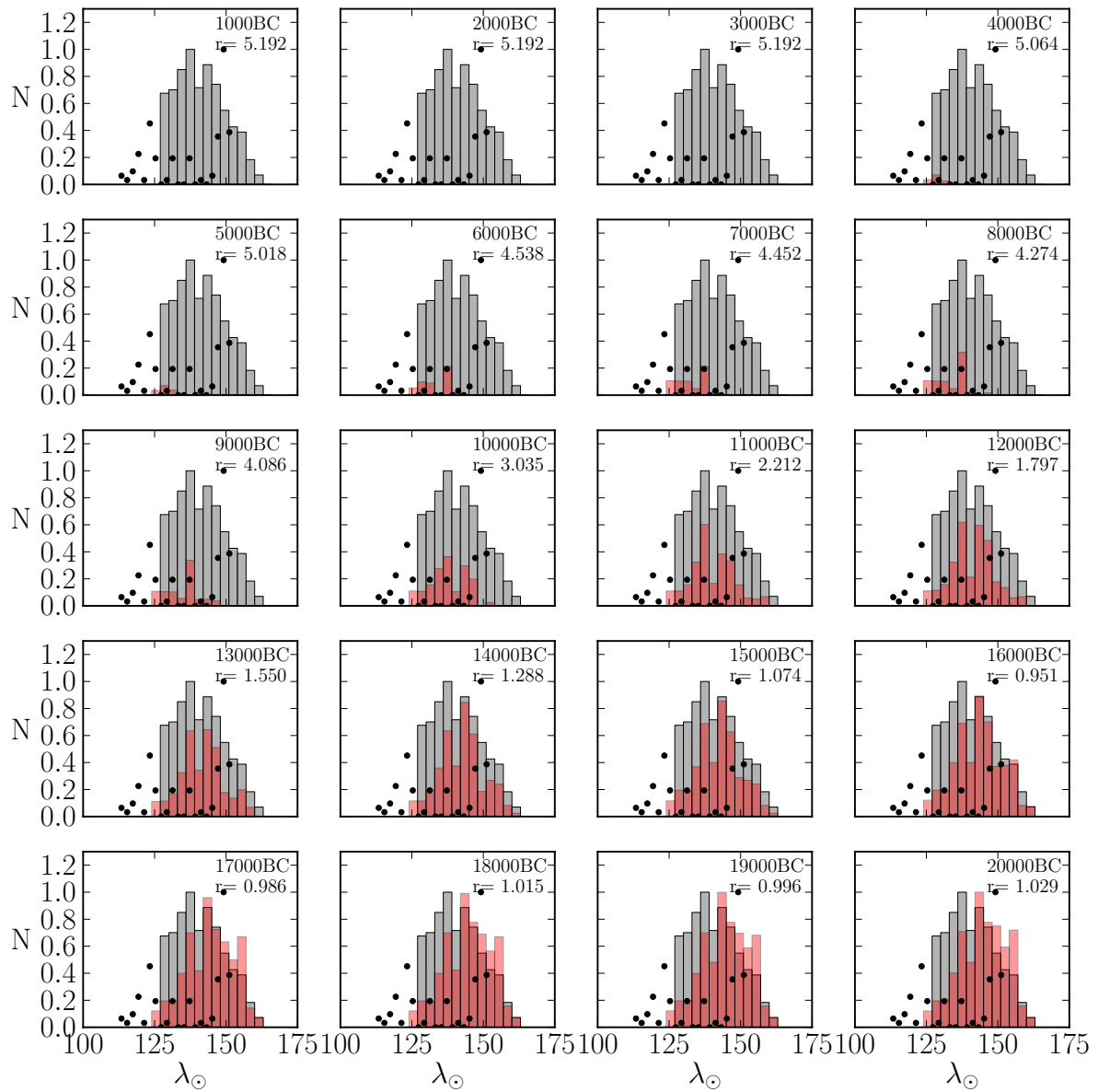
A.1.3 The Northern δ-Aquariids (NDA)

Figure A.3: Simulated, weighted and normalized activity profile (red histogram) of NDA, originating from 96P/Machholz, for different initial meteoroid ejection onset times. Superimposed is the observed normalized relative activity profiles by CMOR (grey histogram).

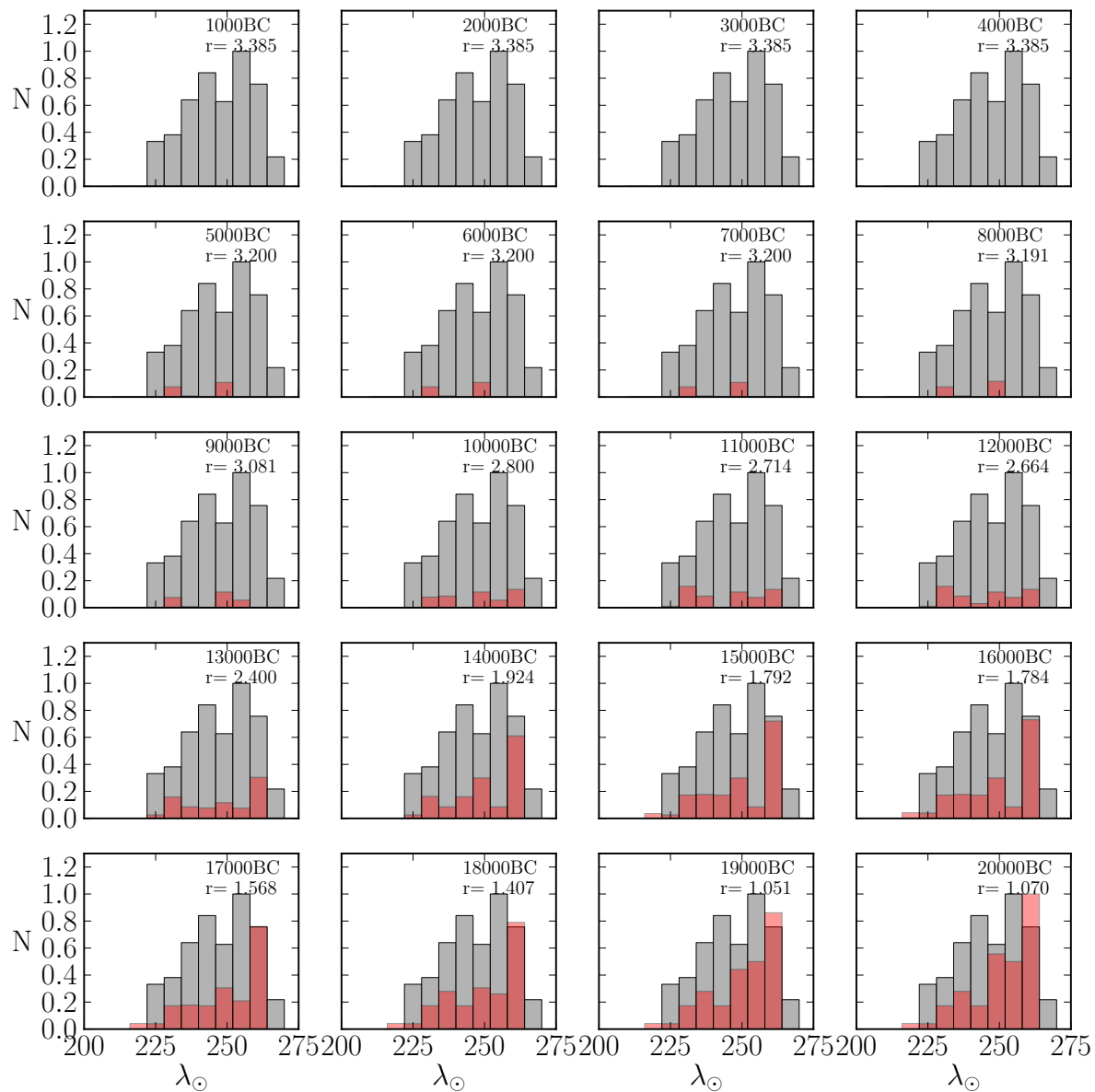## A.1.4   Filament 1 - The December α-Draconids (DAD)

Figure A.4: Simulated, weighted and normalized activity profile (red histogram) of filament 1 (or DAD), originating from 96P/Machholz, for different initial meteoroid ejection onset times. Superimposed is the observed normalized relative activity profiles by CMOR (grey histogram).

A.1.5   Filament 2 - The daytime λ-Taurids (DLT)

Figure A.5: Simulated, weighted and normalized activity profile (red histogram) of filament 2 (or DLT), originating from 96P/Machholz, for different initial meteoroid ejection onset times. Superimposed is the observed normalized relative activity profiles by CMOR (grey histogram).

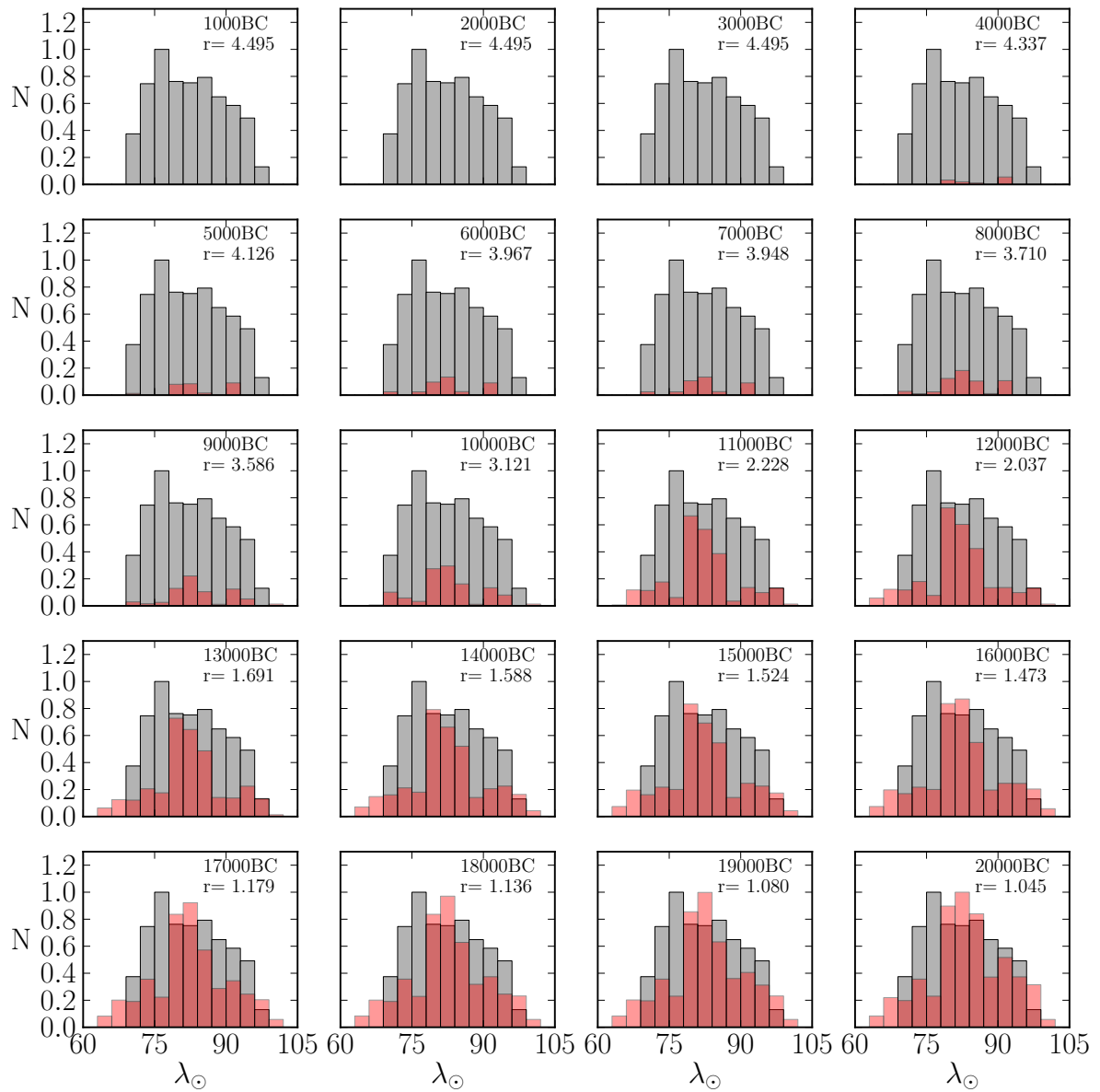## A.1.6   Filament 3 - The θ-Carinids (TCD)

Figure A.6: Simulated, weighted and normalized activity profile (red histogram) of filament 3 (or TCD), originating from 96P/Machholz, for different initial meteoroid ejection onset times. Superimposed is the observed normalized relative activity profiles by SAAMER (grey histogram).

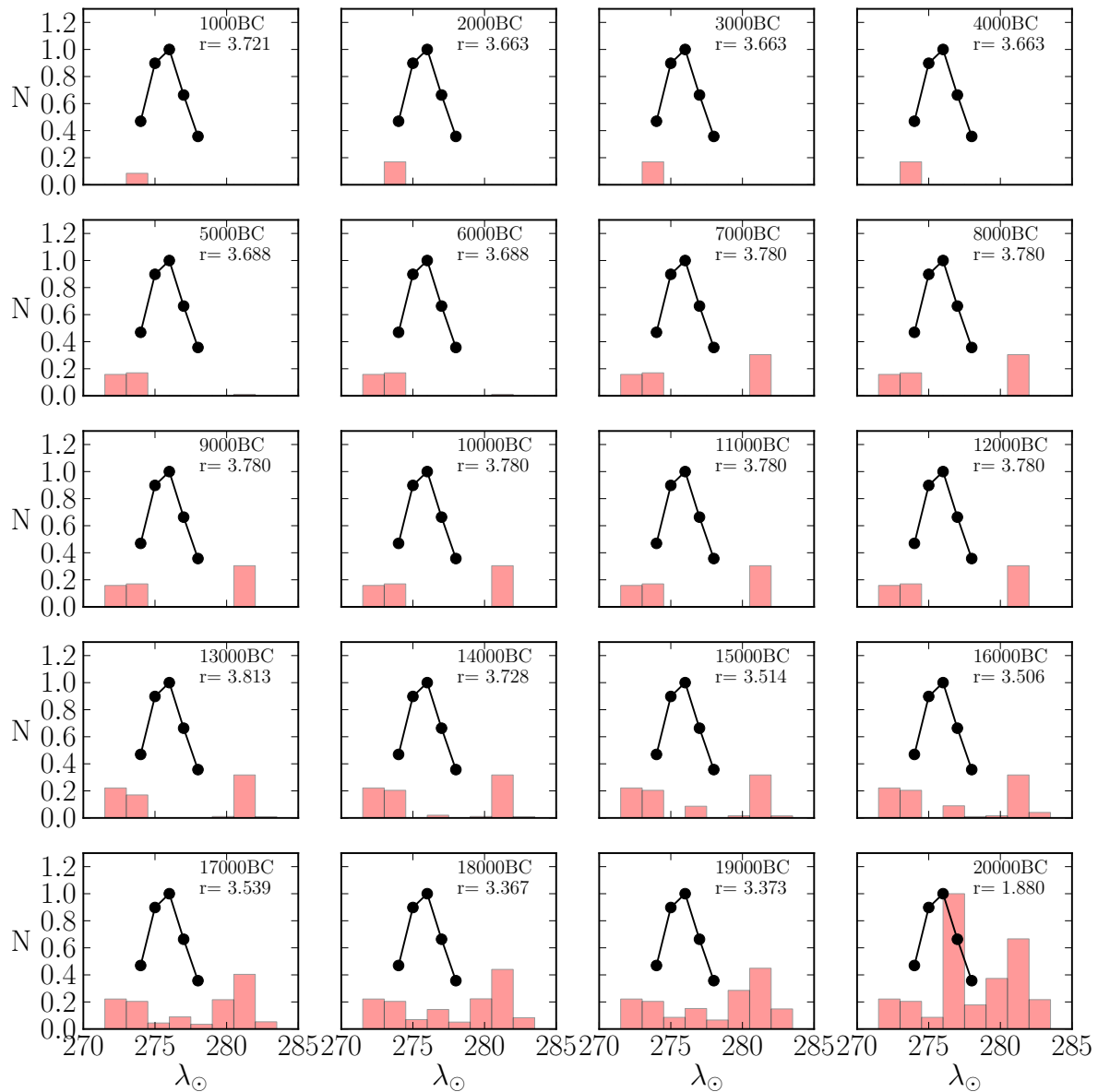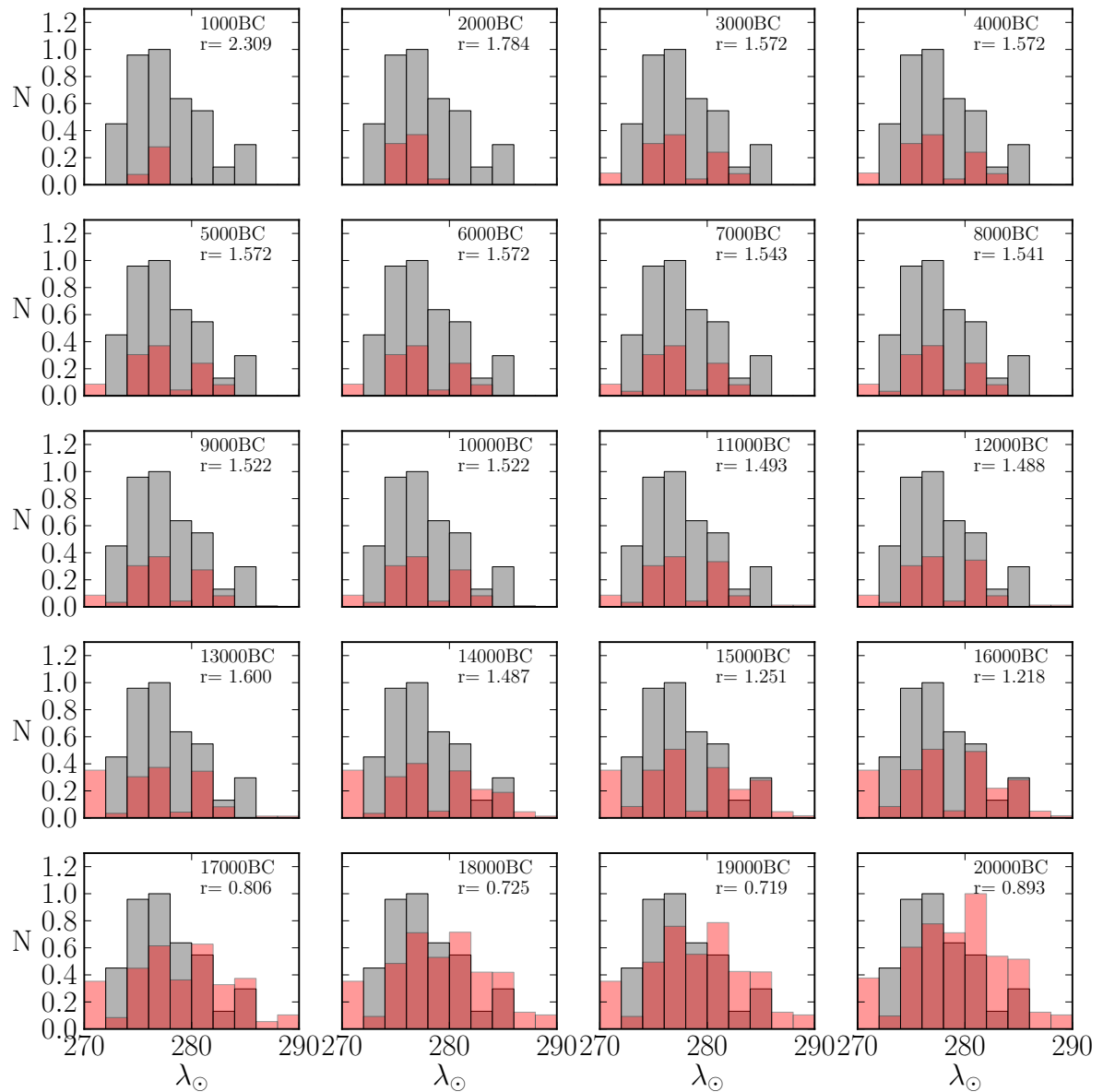## A.1.7 Filament 4 - The κ-Velids (KVE)

Figure A.7: Simulated, weighted and normalized activity profile (red histogram) of filament 4 (or KVE), originating from 96P/Machholz, for different initial meteoroid ejection onset times. Superimposed is the observed normalized relative activity profiles by SAAMER (grey histogram).

A.2   Meteor showers of comet P/1999 J6

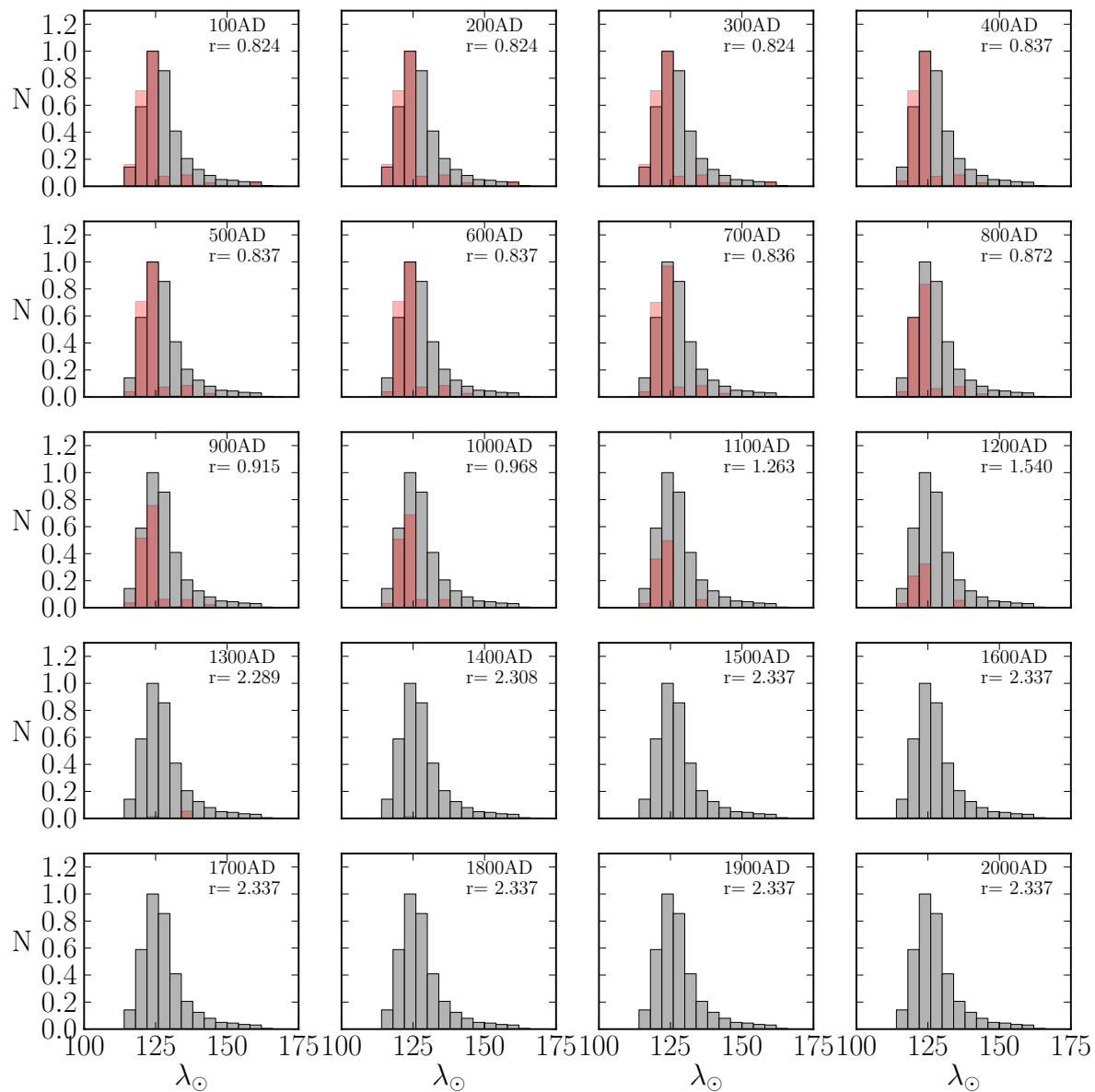### A.2.1   The Southern δ-Aquariids (SDA)

Figure A.8: Simulated, weighted and normalized activity profile (red histogram) of SDA, originating from P/1999 J6, for different initial meteoroid ejection onset times. Superimposed is the observed normalized relative activity profiles by CMOR (grey histogram).
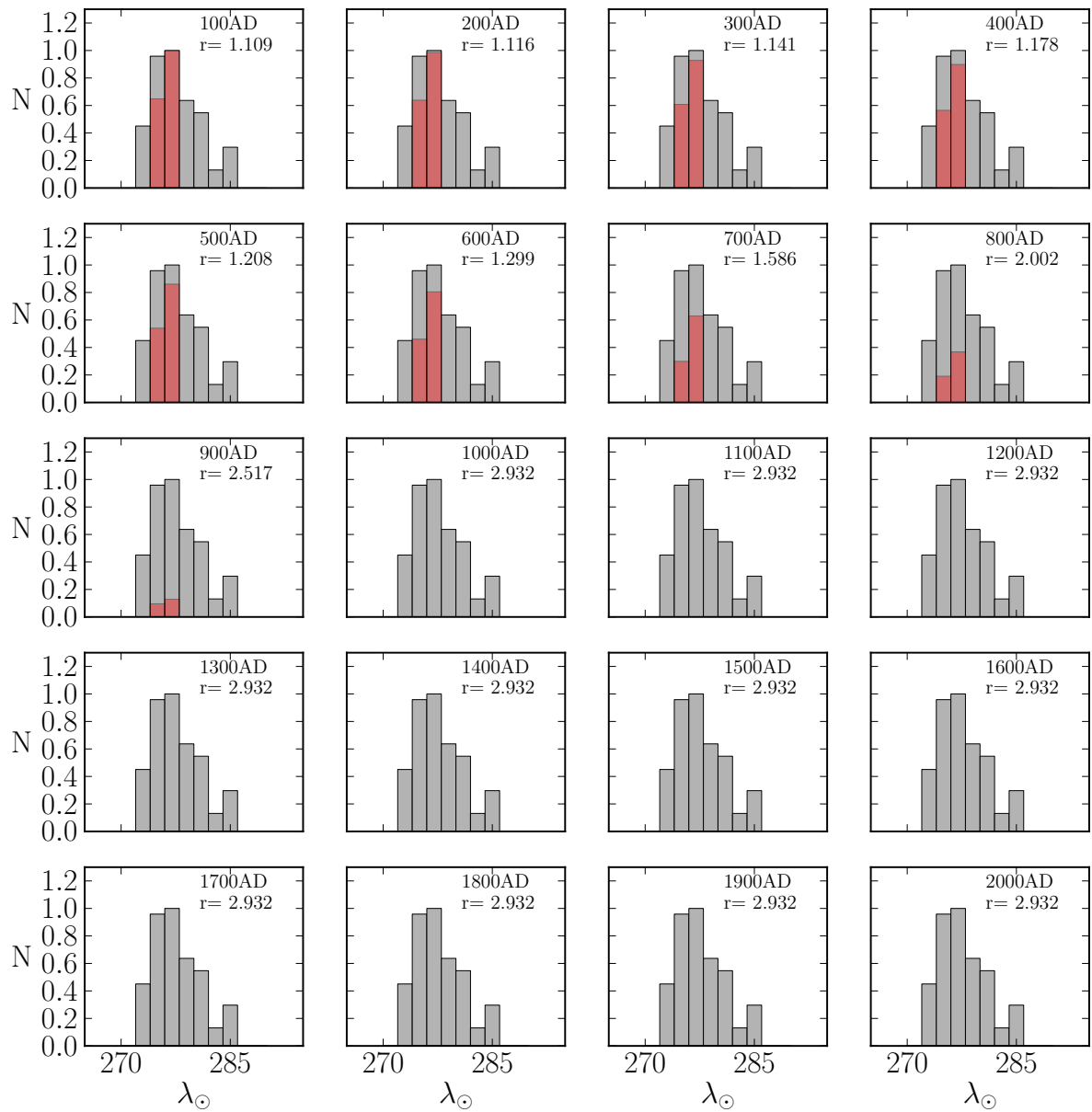
A.2.2 Filament 4 - The κ-Velids (KVE)

Figure A.9: Simulated, weighted and normalized activity profile (red histogram) of filament 4 (or KVE), originating from P/1999 J6, for different initial meteoroid ejection onset times. Superimposed is the observed normalized relative activity profiles by CMOR (grey histogram).

A.3   Combined activity of 96P and P/1999 J6

A.3.1   Southern δ-Aquariids
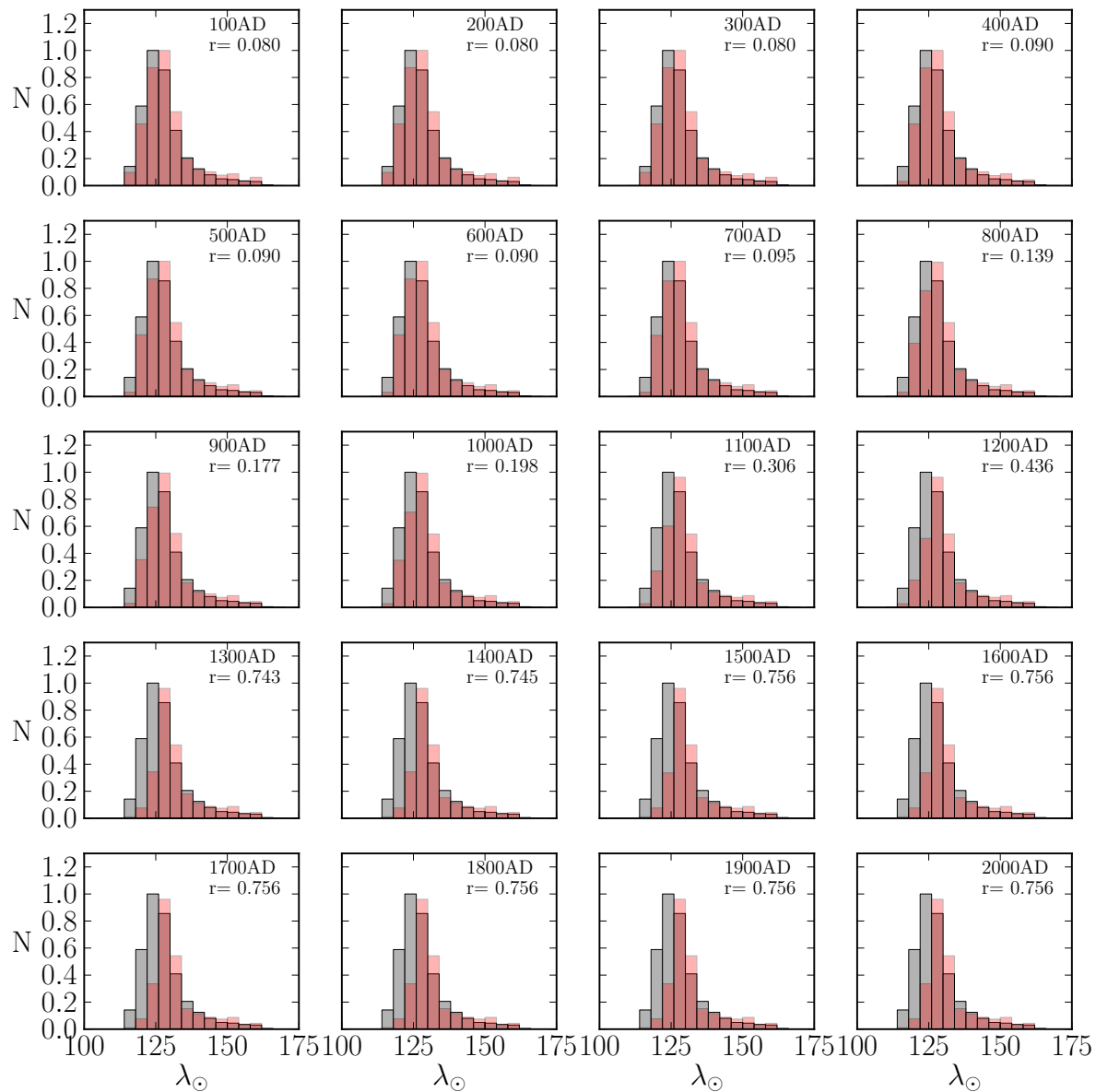

Figure A.10: Simulated, weighted and normalized activity profile (red histogram) of SDA, originating from P/1999 J6 and 96P, for different initial meteoroid ejection onset times. The cometary activity onset time for comet 96P is fixed to 17000 BC, as a best fit to observations (see Fig. A.2). Superimposed is the observed normalized relative activity profiles by CMOR (grey histogram).

A.3.2   Filament 4 - The κ-Velids (KVE)

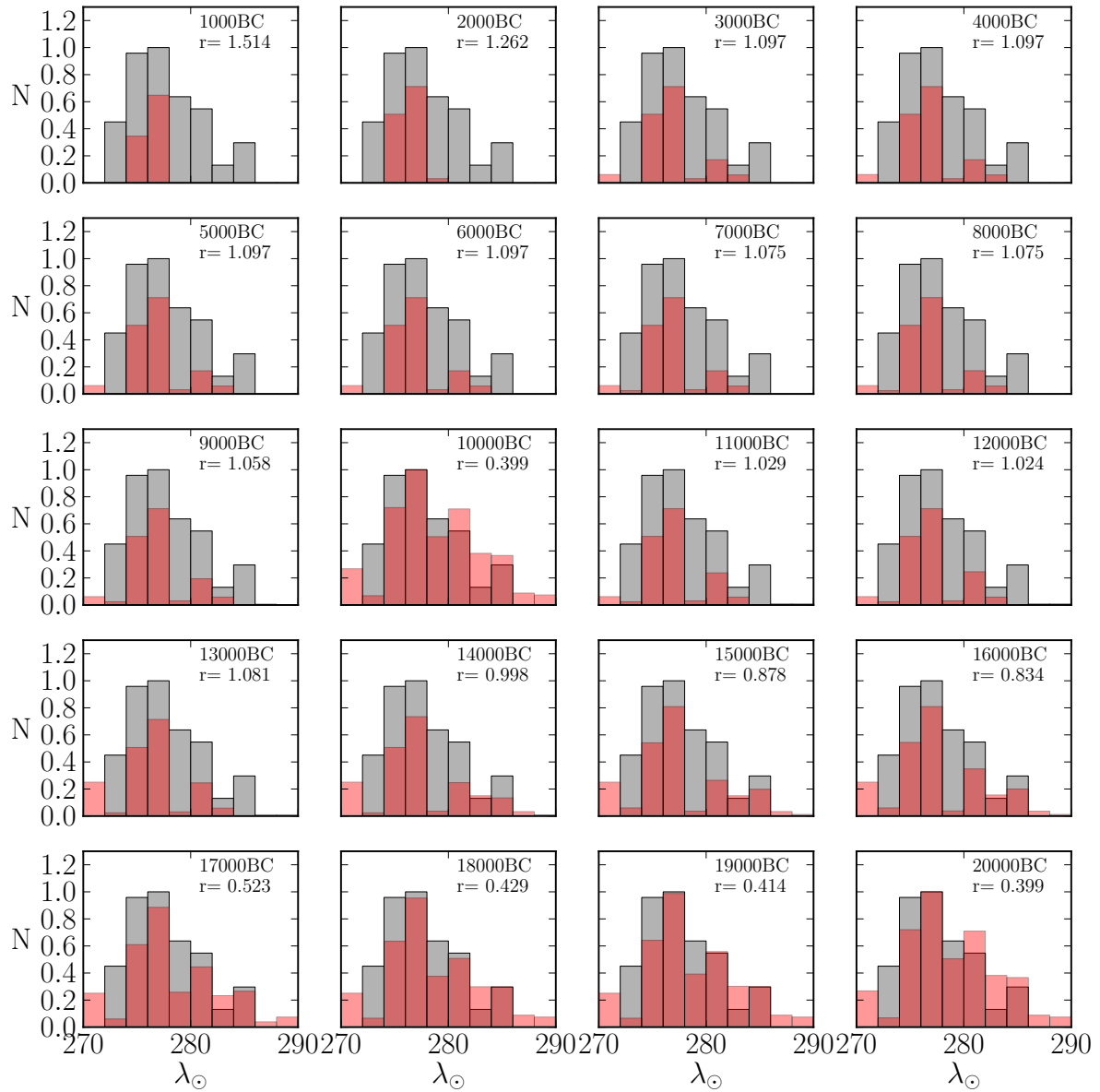Figure A.11: Simulated, weighted and normalized activity profile (red histogram) of filament 4 (or KVE), originating from P/1999 J6 and 96P, for different initial meteoroid ejection onset times. The cometary activity onset time for P/1999 J6 is fixed to 100 AD, as a best fit to observations (see Fig. A.9). Superimposed is the observed normalized relative activity profiles by SAAMER (grey histogram).

Appendix B

Celestial reference frames

B.1 Ecliptic and equatorial celestial coordinates

For an observer on the ground, the sky appears as a sphere with the observer at its center. This is referred to as a geocentric reference frame. However, the the Earth restricts the observations to only above the observer's horizon, making only the half of the celestial sphere available for the observation. For observers, at any point on the Earth's surface, only the sky above their local horizon will be observable.

The most used coordinates systems in observational astronomy, are the *equatorial* and *ecliptic* reference frames and to a lesser degree the *horizontal* coordinate system, which we ignore here. Figure B.1 illustrates the two reference frames. On the left hand-side the equatorial we illustrate the equatorial coordinate system. The origin of the system is at the Earth's center and the reference plane is the Earth's equator extended to intersect the celestial sphere, termed *celestial equator*. A cardinal direction of the equatorial reference frame is the *vernal equinox*, a point at infinity lying on the extension of the line, formed by the intersection of the celestial equator and ecliptic planes. Since a sphere is two dimensional, the position of an object on the sky is defined by two coordinates. The coordinates of an object O are defined by the *right ascension α* and *declination δ*. Often, in the literature, the Greek letters for these coordinates are substituted by their abbreviation as R.A. and Dec. The right ascension is the angle measured from the point γ (vernal equinox) to the celestial meridian M of the object on the celestial equator and varies from $0° < \alpha < 360°$. The declination is the altitude of the object relative to the celestial equator and varies from $-90° < \delta < 90°$, being positive for objects above the equator and negative for objects below it. However, if a unit vector $\hat{\mathbf{r}}$ to the objects is needed, then a coordinate system with three cardinal directions has to be specified. The positive X-axis points towards the vernal equinox, the Y-axis is in the equatorial plane and is $90°$ from the X-axis, and with the Z-axis being perpendicular to the equatorial plane with positive

direction coinciding with the north celestial pole (Fig. B.1, left panel). Thus, the coordinates of the unit vector $\hat{\mathbf{r}}$ are:

$$
\begin{aligned}
X &= \cos\delta\cos\alpha \\
Y &= \cos\delta\sin\alpha \\
Z &= \sin\delta
\end{aligned}
\tag{B.1}
$$

Similarly, the celestial ecliptic coordinate system is centered at the Earth, though the reference plain is the ecliptic. The position of an object in this reference frame is found by two coordinates, the *ecliptic longitude* λ and the *ecliptic latitude* b (Fig. B.1, right panel). The ecliptic longitude varies between $0° < \lambda < 360°$, where the latitude can take values between $-90° < b < 90°$. Again, before finding a unit vector to the object, three axis has to be defined. The positive X'-axis points towards the vernal equinox, the Y'-axis is in the ecliptic plane and is $90°$ from the X'-axis, and with the Z'-axis being perpendicular to the ecliptic plane with positive direction coinciding with the north celestial pole (Fig. B.1, left panel). The coordinates of the unit vector $\hat{\mathbf{r}}$ are thus given by:

$$
\begin{aligned}
X' &= \cos b\cos\lambda \\
Y' &= \cos b\sin\lambda \\
Z' &= \sin b
\end{aligned}
\tag{B.2}
$$

B.3 Any unit vector in one coordinate system can be transformed into the other, and vice-versa, by a rotation around the X-axis to an angle $-\epsilon$, the latter being the Earth's rotational axis tilt to the ecliptic, with $\epsilon \approx 23.44°$ (?). For example, the transformation of $\hat{\mathbf{r}}$ from the equatorial to ecliptic coordinate system is performed by the relation $\hat{\mathbf{r}} = \mathbf{R}_X(-\epsilon)\hat{\mathbf{r}}'$, where $\mathbf{R}_X(-\epsilon)$ is the rotation matrix around the X-axis with elements given by Eq. B.3. The rotation matrix is orthogonal, so the inverse transformations will be just $\hat{\mathbf{r}}' = \mathbf{R}_X^T(-\epsilon)\hat{\mathbf{r}}$.

$$
\mathbf{R}_X(-\epsilon) = \begin{bmatrix} 1 & 0 & 0 \\ 0 & \cos(-\epsilon) & -\sin(-\epsilon) \\ 0 & \sin(-\epsilon) & \cos(-\epsilon) \end{bmatrix}
\tag{B.3}
$$

In meteor observations the geocentric radiant is often given in equatorial coordinates α_g and δ_g. However, the diurnal motion of the Earth will cause the meteor shower radiant to elongate and the equatorial reference frame is not preferred. Meteor astronomers, use a quasi-inertial reference frame, subtracting the Earth's diurnal motion, to circumvent the radiant drift. This reference frame is called, the *sun-centered ecliptic* coordinate system with origin coinciding with the Earth's apex (the direction of the Earth's motion) and the reference plane being the
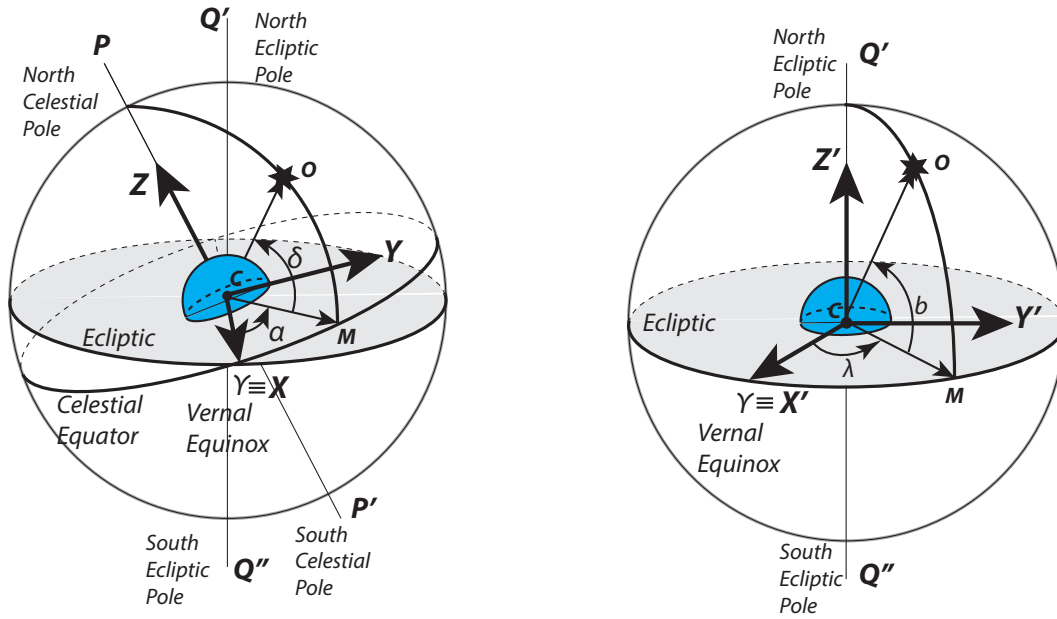
Figure B.1: Illustration of the equatorial (left) and ecliptic (right) celestial reference frames. The angle α (left) (right ascension) is measured along the celestial equator from the vernal equinox γ, anti-clockwise when looked from the north celestial pole. The angle δ (declination) is measured perpendicular to the equator. The angle λ (ecliptic longitude) (right) is measured from the vernal equinox γ, anti-clockwise when looked from the north equatorial pole. The angle b (ecliptic latitude) is measured perpendicularly to the ecliptic.

ecliptic.

Figure B.2 illustrates the ecliptic plane and the the Earth's orbit around the Sun. At a given instant of time the angular position of the Earth is given by its ecliptic longitude λ, whereas the angular projection of the Sun will be $\lambda_\odot = \lambda + 180°$. In fact, often in meteor astronomy the solar longitude is used to specify an instant of time, rather than the longitude of the Earth. Thus, for a meteor hitting the Earth's atmosphere, we know its ecliptic longitude λ (which can be found from the equatorial coordinate system) and we also know the solar longitude $\lambda_\odot$ for the instant when the meteor occurs. Then in order to account for the Earth's diurnal motion, and overcome the radiant from drifting, we have to subtract the solar longitude from the longitude of the meteor, i.e $(\lambda - \lambda_\odot)$ which is the basis of the sun-centered ecliptic reference frame, with the other coordinate being the ecliptic latitude b.
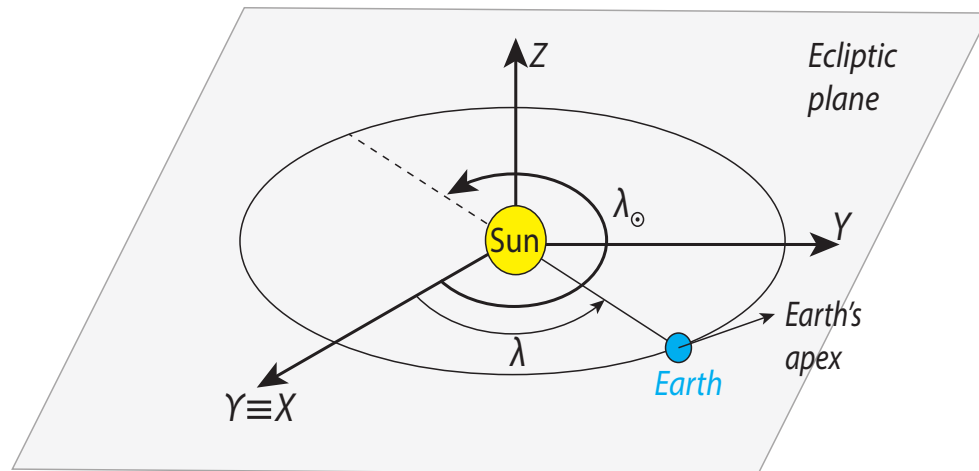
Figure B.2: Illustration of sun-centered ecliptic reference frame. Presented are the Earth's orbit and the angles λ (the longitude of the Earth), and the solar longitude $\lambda_\odot$.

Appendix C

Orbital elements

The motion of a celestial body around the Sun is defined by six orbital elements, *semi-major axis a*, *eccentricity e*, *inclination i*, *longitude of the ascending node* Ω, *argument of perihelion* ω and the *true anomaly* θ (Fig. C.1). The first two elements define the size and shape of the orbit, while (i, Ω and ω) define the orientation of the orbit in space. The last element θ indicates the position of the body on the orbit. It is has to be noted that in various celestial mechanics problems, the orbital elements are measured with respect to different reference planes. For example, when a motion of a body around the Sun is studied, the reference frame is centered at the Sun, where the orbital plane of the Earth, called the *ecliptic plane*, is generally accepted as a reference plane. When a motion of an artificial satellite is studied, generally the reference frame has its origin at the planet, which a satellite orbits. However, in this work we concern ourselves with motion of Solar System bodies around the Sun, so all the orbital elements are assumed to be with respect to the Sun and the ecliptic.

We define our coordinate system with an origin at the Sun, while the ecliptic will be the reference plane. This coordinate system is referred to as *heliocentric ecliptic* reference frame. The *X* and *Y* axes lie on the ecliptic plane, with the positive *X* direction towards the *vernal equinox* "γ". The *Y*-axis is perpendicular to *X*, while *Z* completes the right-handed system (Fig. C.1 top panel).

An ellipse is a curve with two focal points S and S', where one of them is always occupied by the Sun e.g., at S in this case. A circle, for example, is a special case of an ellipse where the two focal points coincide. The departure of an ellipse from circle is measured by the eccentricity e where eccentricity of $e = 0$ corresponds to a circle while $0 < e < 1$ denotes an ellipse. The higher the value of e, the more elongated the ellipse is. Eccentricity $e = 1$ describes a parabola, while $e > 1$ denotes a hyperbola.

The distance RP in Fig. C.1 (lower panel) is the major axis of the ellipse, while DE is referred to as the minor axis. The halves of the major and minor axes are called, the semi-
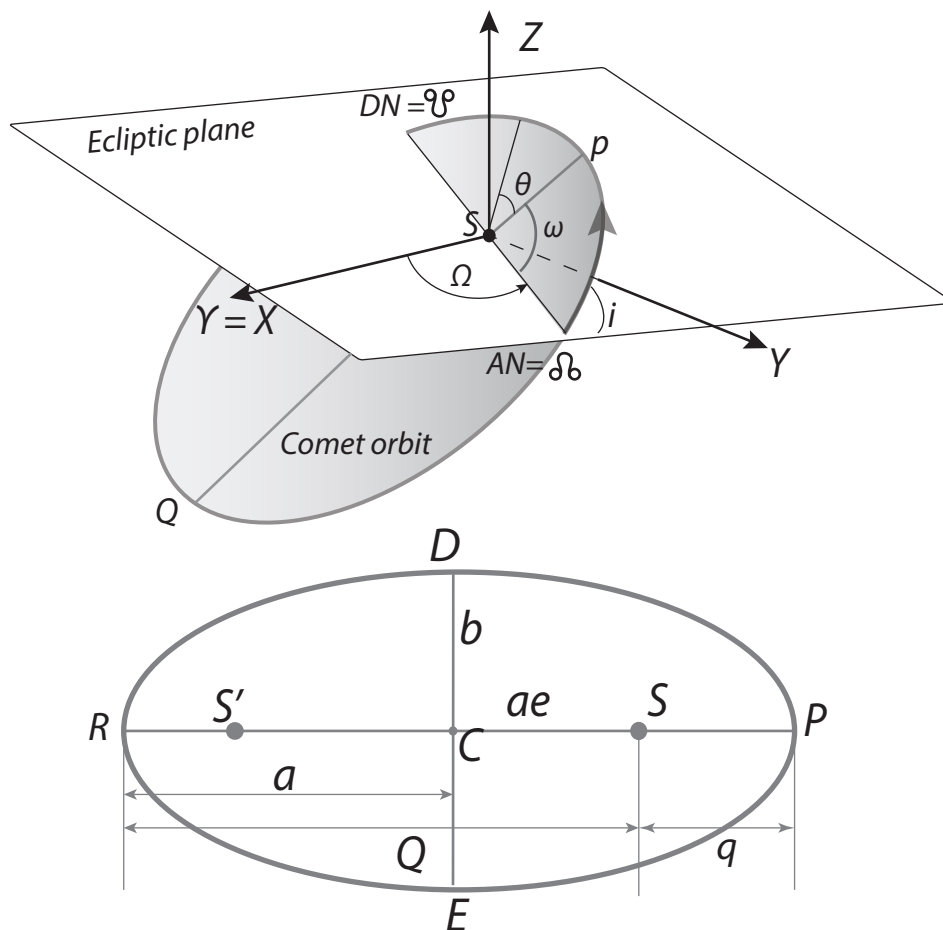
Figure C.1: Illustration the orbital elements. The top panel shows the orientation of the orbit with respect to the elliptic plane the position of a body on the orbit. The lower panel, shows the size and shape of the orbit and some relations between them (see text for details).

major $a \equiv RC$ and semi-minor axes $b \equiv DC$, respectively. The eccentricity relates the two quantities with the expression $b = a\sqrt{1 - e^2}$. Sometimes the major axis QP is referred to as the *line of apsides* or *apsidal line*.

Often in celestial mechanics, the closest and farthest points of the body from the Sun are of interest. These points are referred to as, the *perihelion* and the *aphelion* of the orbit, respectively. In Fig. C.1 (lower panel), the perihelion distance is the line SP and is usually denoted by q, while the aphelion distance is SR and denoted by Q. The perihelion and aphelion distances are expressed as: $q = a(1 - e)$, and $Q = a(1 + e)$. For elliptical orbits around the Sun, q, Q and the semi-major axis a, are measured in astronomical units (AU), where 1 AU$\approx 1.49 \times 10^8$ km.

The inclination i of the orbit is defined as the angle between the ecliptic plane and the orbital plane and can vary between $0° < i < 180°$. An orbit with inclination $i \leq 90°$ is called *prograde orbit*, in the sense that the body orbits the Sun counter-clockwise. Conversely, orbits with $90° < i \leq 180°$ is referred to as a *retrograde orbit* with the body orbiting the Sun clockwise.

The *ascending node* of an orbit *AN* is the point on the ecliptic plane, where the body pierces the ecliptic from south to north (from $-Z$ to Z axis). Conversely, the point where the body intersects the ecliptic from north to south is referred to as the *descending node* (*DN*). The line connecting the two nodes is called *nodal line*. Hence, the longitude of the ascending node Ω is the angle subtended from the positive $X \equiv \gamma$, to the ascending node, and varies between $0° < \Omega < 360°$.

The argument of the perihelion ω is the angle subtended from the ascending node *AN* to the perihelion point *P* of the orbit and is measured in the orbital plane. Similar to the longitude of the ascending node, it varies between $0° < \omega < 360°$.

The last element, the *true anomaly* θ defines the angular displacement of the body from the perihelion and is measured counter-clockwise for a prograde ($i \leq 90°$) orbit and opposite for a retrograde ($90° < i \leq 180°$) orbit. The true anomaly varies non-linearly from $0° < \theta < 360°$, where the rate of change is greatest at perihelion and slowest at aphelion. The distance of the body from the Sun is referred to as *heliocentric distance* and is given by:

$$r = \frac{a(1 - e^2)}{1 + e \cos \theta} \tag{C.1}$$

where a, e and θ are as above. Given the orbital elements and the heliocentric distance, the X, Y, Z coordinates of the body can be found at anytime using:

$$\begin{aligned}
X &= r \left[\cos \Omega \cos (\omega + \theta) - \sin \Omega \sin (\omega + \theta) \cos i \right] \\
Y &= r \left[\sin \Omega \cos (\omega + \theta) + \cos \Omega \sin (\omega + \theta) \cos i \right] \\
Z &= r \sin (\omega + \theta) \sin i
\end{aligned} \tag{C.2}$$

Appendix D

Definitions

- **Mean Motion Resonance (MMR)**

  In orbital mechanics, mean motion resonance refers to ratio of the orbital periods of two bodies orbiting a common central body. Two bodies are considered in a mean motion resonance if their orbital periods can be expressed as a ratio of two integers i.e., $p + q/p$. When the orbital periods of two bodies satisfy that condition (the first body will complete $p + q$ orbital revolutions for every p revolutions of the second body), the bodies are referred to be in mean motion resonance. There large number of cases of MMR in the Solar system. For example, Pluto and Neptune are in 2:3 MMR. The effect of this resonance is that Pluto's orbit has remained relatively stable over the age of the Solar System, ensuring that the two bodies never approach each other.

- **Minimum Orbit Intersection Distance MOID**

  The Minimum Orbit Intersection Distance (MOID) refers to the closest distance between two orbits. The analytical expression for the MOID is rather complicated and therefore it is generally computed numerically.

- **Kozai resonance**

  The Kozai resonance refers to distinct correlation between the orbital elements over a long period of time (a few thousand years). This type of resonance arises from the "three-body problem". Orbits with initial inclination near 90° and perihelion distance of $q \approx 2$ AU may experience specific orbital evolution, in which some orbital elements oscillate out of phase. For instance, in the Kozai resonance the semi-major axis of the orbit is approximately conserved, while the orbital eccentricity and inclination oscillate out of phase. Another quantity which is approximately conserved is the Kozai energy C_K.

- **Tisserand parameter**

  The Tisserand parameter is a quasi-constant arising from the "restricted three-body problem" and is expressed as a ratio of the orbital elements of a small body to a planet. It describes the shape, size and orientation of an orbit of a small solar system body with respect to a planet of interest. More precisely, the Tisserand parameter measures how strongly a small body's orbit or dynamics is coupled to a given planet. The most massive planet in the Solar System is Jupiter, and hence the Tisserand parameter of a small body is generally expressed with respect to Jupiter. It is denoted by T_J where the subscript stands for Jupiter. The Tisserand parameter with respect to Jupiter is given by:

  $$T_J = \frac{a_J}{a} \sqrt{\frac{a}{a_J}(1 - e^2)} \cos i, \tag{D.1}$$

  where a_J is the semi-major axis of Jupiter, a, e and i are the semi-major axis, eccentricity and orbital inclination of the small body.

  Jupiter family comets, whose dynamics is greatly controlled by Jupiter, have Tisserand parameter $2 < T_J < 3$. Halley-type comets have Tisserand parameter $T_J < 2$, whereas asteroids generally have $T_J > 3$.

Curriculum Vitae

Name:	Abedin Yusein Abedin
Education and Degrees:	2011 - present Ph.D. The University of Western Ontario, Department of Physics and Astronomy London, ON, Canada
	2005 - 2006 M.Sc. The University of Sofia - "St.Kliment Ohridski", Department of Physics Sofia, Bulgaria
	2001 - 2005 B.Sc. The University of Sofia - "St.Kliment Ohridski", Department of Physics Sofia, Bulgaria
Honours and Awards:	Ontario Trillium Scholarship 2011 - 2015
Related Work Experience:	Teaching Assistant The University of Western Ontario 2011 - 2015

Publications:

1. Formation and past evolution of the showers of 96P/Machholz complex: (2016) - **Abedin, Abedin**; Janches, Diego, Wiegert, Paul; Pokorný, Petr; Brown, Peter, Hormaechea, Jose Luis - *Icarus*, In press.

2. The age and the probable parent body of the daytime Arietid meteor shower: (2016) - **Abedin, Abedin**; Wiegert, Paul; Pokorný, Petr; Brown, Peter - *Icarus*, In press.

3. On the age and formation mechanism of the core of the Quadrantid meteoroid stream: (2015) - **Abedin, Abedin**; Spurný, Pavel; Wiegert, Paul; Pokorný, Petr; Borovička, Jiří; Brown, Peter - *Icarus*, Vol. 261, p. 100-117.

4. Meteoroid stream modeling at the University of Western Ontario (2014) - **Abedin, Abedin Y.**; Wiegert, Paul A. - *International Meteor Organization*, ISBN 978-2-87355-025-7, pp. 86

5. Orbital parameters of the high-mass X-ray binary 4U 2206+54: (2014) - Stoyanov, K. A.; Zamanov, R. K.; Latev, G. Y.; **Abedin, A. Y**.; Tomov, N. A. - *Astronomische Nachrichten*, Vol.335, Issue 10, p.1060

6. Cascading fragmentation of comet 73P/Schwassmann-Wachmann 3: (2011) - **Abedin, A.**; Bonev, T. - *International Meteor Organization*, ISBN 2978-2-87355-022-6, pp. 5-9